

**Neuronal Dendropathy in CNS
Degeneration: A new marker for
protection and recovery**



Ryan J. Bevan

2020

School of Optometry and Vision Sciences

Cardiff University

This dissertation is submitted for the degree of

Doctor of Philosophy

Acknowledgements

Firstly, I wish to thank Professor James E. Morgan and Professor B. Paul Morgan for giving me the opportunity to undertake this project and to become part of their research groups at Cardiff University. It has been a privilege to develop both as a person and as a competent researcher within these labs. Your enthusiasm, guidance, help and support during the project really helped with new ideas and queries along the way.

I am grateful to Dr Tim Hughes, who supported the project and without this the animal work would have been more difficult. I would also like to thank Tim for the helpful discussions over the years and for the opportunities that he helped set up. I would also like to thank Professor Mark Good, Dr Tom Davies and Dr Mat Clement with assistance and access to various animal models during this PhD. The work would not have been completed in such detail without the help. I would also like to thank Dr James Tribble for the helpful guidance who provided the valuable foundation for the experiments when I first arrived.

I am grateful to the UK Dementia Research Institute at Cardiff University for access to the imaging suite and the extensive time that was allowed on the confocal microscope. I would also like to thank Dr Anthony Hayes and Marc Issacs for the continued support and access to the Imaris imaging suite in the Bioscience imaging facility at Cardiff University. Without the access to the confocal microscope and Imaris the project would never have achieved its objectives within this timespan.

Lastly, I am eternally grateful for the continued support provided by friends and family during the course of this thesis.

iii

All the work presented in this thesis is my own except for the following contributions.

In all experimental chapters, Dr Tim Hughes and JBIOS (animal facility at Cardiff University) assisted with housing, maintenance and the transferring of animals.

Chapter 3 and 4:

- Professor Mark Good provided access to the Tg2576 model.

Chapter 5:

- 3xTg-AD mice treated with a complement inhibitor was approved by Professor B. Paul Morgan, Dr Tim Hughes, Dr Jonathan Winter and Dr Alison Costigan which were supported by GlaxoSmithKline (GSK) project.

Chapter 6:

- Dr Tim Hughes assisted with LPS i.p. injections
- Dr Mat Clement provided the wildtype and 3xTg-AD mice that were virally infected.

Chapter 7:

- Dr Tim Hughes and Dr Tom Davies provided access to 3xTg-AD mice treated with probiotics. This work was supported through a project with Cultech Ltd.

Publications

Bevan, R.J., Hughes, T.R., Williams, P.A., Good, M.A., Morgan, B.P., and Morgan, J.E. (2020) Retinal ganglion cell degeneration correlates with hippocampal spine loss in experimental Alzheimer's disease. *Acta Neuropathol Commun* **8**: 1–13.

Abstract

Neuronal dendritic and synaptic degeneration are early markers of neurodegeneration occurring in the brain of Alzheimer's disease (AD). AD is the most common type of dementia characterised by the accumulation of extracellular amyloid plaques and neurofibrillary tangles, accompanied by neuroinflammation leading to neurodegeneration. AD diagnosis is often complex, expensive and/ or invasive, and only detect late stages of pathological changes. The retina, an extension of the central nervous system (CNS), develops AD-like pathology and may reflect ongoing pathological changes in the AD brain. Retinal ganglion cells (RGCs), the output neurons of the retina, are vulnerable to degeneration and may offer as a potential target for detecting and monitoring AD pathology. However, it is unclear whether RGC degeneration is a consistent feature in the AD retina.

This thesis utilises DiOlistic labelling to investigate RGC dendritic pruning and hippocampal dendritic spine loss in the AD mouse models and assesses the impact of immune system modulation via deficiency of the complement system, elevated systemic inflammation (bacterial and viral) and dietary modulation (high fat diet and probiotics). All AD mouse models (Tg2576, 3xTg-AD and APP^{N-G-F}) displayed excessive RGC dendritic pruning that occurred contemporaneously with dendritic spine loss in the hippocampus. In the 3xTg-AD model, deficiency in the complement system offered neuroprotection against both RGC dendritic and hippocampal synaptic pruning whilst elevated systemic inflammation (bacterial and viral) and high fat dietary modulation exacerbated neurodegeneration. Probiotic dietary supplementation was also associated with synaptic protection in the hippocampus.

Overall, this thesis demonstrates that excessive RGC dendritic pruning is a common feature in the retina of AD mouse models and occurs at the time of ongoing synaptic loss in the hippocampus. These findings support the prospective use of retinal analysis to monitor AD progression and severity, providing an accessible measure that reflects pathology within the brain.

Contents

Contents	v
List of Figures	ix
List of Tables.....	xiv
Abbreviations	xv
Chapter 1. Introduction.....	1
1.1 Alzheimer’s disease.....	1
1.1.1 Overview	1
1.1.2 Amyloid, tau and microglia.....	3
1.1.3 Hippocampus and synapses.....	5
1.1.4 AD mouse models	9
1.2 The retina.....	12
1.2.1 Retina structure	12
1.2.2 Retina cell types and phagocytosis	12
1.2.3 Retinal ganglion cells.....	14
1.2.4 Retinal changes in AD	16
1.2.5 Retinal AD pathology in rodent models.....	18
1.3 The complement system in AD	21
1.3.1 Pathways, regulation, and disease.....	21
1.3.2 Classical, lectin and alternative pathway	23
1.3.3 Complement regulation, dysregulation and deficiencies	24
1.4 Synaptic pruning in AD.....	25
1.4.1 Synapses.....	25
1.4.2 Phagocytosis and link to synaptic elimination.....	26
1.5 Systemic inflammation.....	30
1.6 Aims and hypothesis	34
Chapter 2. Methods.....	35
2.1 Animals	35
2.2 DiOlistic Labelling	37
2.2.1 Retina and hippocampus dissection	38
2.2.2 DiOlistic Preparation.....	39
2.2.3 DiOlistic labelling	39
2.2.4 Confocal Imaging.....	40
2.3 RGC dendritic reconstruction and data acquisition.....	42
2.3.1 Dendritic reconstruction.....	42
2.3.2 Sholl analysis and associated parameters.....	45

2.3.3	Receptive field classification	47
2.3.4	Nuclei counts in the ganglion cell layer.....	48
2.4	Dendritic spine reconstruction and data acquisition.....	49
2.4.1	Dendritic spine reconstruction	49
2.4.2	Dendritic spine classification	49
2.5	Immunofluorescence	51
2.6	Statistical analysis	52
Chapter 3.	Retinal ganglion cell dendritic pruning in mouse models of Alzheimer's disease	53
3.1	Introduction	53
3.2	Experimental Setup	55
3.3	Results	57
3.3.1	Tg2576	57
3.3.1.1	Preservation of RGC density in the Tg2576 retina.....	57
3.3.1.2	RGC dendritic pruning in Tg2576 mice	57
3.3.1.3	ON-centre restricted RGC dendritic pruning in Tg2576 retina.	58
3.3.1.4	RGC dendritic pruning is not exacerbated with further aging in the Tg2576 mice.....	58
3.3.1.5	Figures	59
3.3.2	3xTg-AD	64
3.3.2.1	RGC dendritic pruning in 3xTg-AD mice.	64
3.3.2.2	Male 3xTg-AD mice show greater RGC dendritic pruning.	64
3.3.2.3	ON-centre RGCs show consistent dendritic pruning in both male and female 3xTg-AD mice.....	65
3.3.2.4	Age influences 3xTg-AD RGC dendritic pruning.....	65
3.3.2.5	Figures	66
3.3.3	APP ^{NL-G-F}	71
3.3.3.1	APP ^{NL-G-F} mice exhibit RGC dendritic atrophy.....	71
3.3.3.2	APP ^{NL-G-F} RGC degeneration is not dependant on gender	71
3.3.3.3	Classification of RGC based on sublamina projections reflects dendritic structure in APP ^{NL-G-F} mice.....	72
3.3.3.4	Figures	73
3.4	Discussion	77
Chapter 4.	Hippocampal dendritic spine loss in mouse models of Alzheimer's disease.	81
4.1	Introduction	81
4.2	Experimental Setup	83

4.3	Results	84
4.3.1	Tg2576	84
4.3.1.1	Dendritic spine loss in the hippocampus of Tg2576 AD mice	84
4.3.2	3xTg-AD	84
4.3.2.1	Dendritic spine loss in the hippocampus of 3xTg-AD mice	84
4.3.2.2	Female 3xTg-AD mice show greater spine loss	85
4.3.2.3	Dendritic spine loss occurs in older 3xTg-AD mice	85
4.3.3	APP ^{NL-G-F}	86
4.3.3.1	Dendritic spine loss in the hippocampus of APP ^{NL-G-F} mice.	86
4.3.3.2	Dendritic spines in APP ^{NL-G-F} mice are affected equally in males and females at 12 months	86
4.3.3.3	APP ^{NL-G-F} dendritic spine loss occurs by 7 months	86
4.3.3.4	Dendritic spines in APP ^{NL-G-F} mice are affected equally in males and females at 7 months	87
4.3.4	Comparison between CA1 spines and RGC dendrites	87
4.3.5	Figures	88
4.4	Discussion	97
Chapter 5.	The role of complement in modulating retinal ganglion cell dendritic complexity and CA1 dendritic spines in wildtype and 3xTg-AD mice	100
5.1	Introduction	100
5.2	Experimental Setup	102
5.3	Results	104
5.3.1	C1q ^{-/-} , C3 ^{-/-} , C3aR ^{-/-} and TREM2 ^{-/-} mice	104
5.3.2	3xTg-AD C3 ^{-/-} and 3xTg-AD C6 ^{-/-} mice	105
5.3.3	3xTg-AD C5 antibody therapeutic inhibition with BB5.1	106
5.3.4	Figures	107
5.4	Discussion	115
Chapter 6.	The impact of bacterial and viral infections on retinal ganglion cells and CA1 hippocampal dendritic spines in wildtype and 3xTg-AD mice	119
6.1	Introduction	119
6.2	Experimental Setup	121
6.3	Results	123
6.3.1	Systemic LPS	123
6.3.1.1	Weight Monitoring	123
6.3.1.2	Wildtype	124
6.3.1.3	3xTg-AD	126
6.3.1.4	Figures	128

6.3.2	MCMV	135
6.3.2.1	Wildtype.....	135
6.3.2.2	3xTg-AD.....	136
6.3.2.3	Figures	137
6.4	Discussion	141
Chapter 7.	The impact of probiotic supplementation on retinal ganglion cells and CA1 hippocampal dendritic spines in the 3xTg-AD model.	145
7.1	Introduction	145
7.2	Experimental Setup	147
7.3	Results	149
7.3.1	Chow Diet	149
7.3.2	HFD Diet.....	150
7.3.3	Figures.....	151
7.4	Discussion	157
Chapter 8.	Discussion	160
References	166

List of Figures

Figure 1.1 Overview of APP processing via nonamyloidogenic and amyloidogenic pathway.	3
Figure 1.2 Schematic of a mouse hippocampus slice highlighting the CA1 region, dendritic spines, and spine morphologies.	8
Figure 1.3 Tg2576 phenotypic characterisation.	11
Figure 1.4 3xTg-AD phenotypic characterisation.	11
Figure 1.5 APP ^{NL-G-F} phenotypic characterisation.	11
Figure 1.6 Schematic of the retina structure, highlighting the different retinal layers and neurons.	13
Figure 1.7 Illustration of RGC dendritic pruning.	15
Figure 1.8 The role of the complement system in the innate immune response.	22
Figure 1.9 Schematic of excessive synapse elimination.	29
Figure 2.1 Overview of DiOlistic labelling.	37
Figure 2.2 Overview of tissue dissection.	38
Figure 2.3 DiOlistic fluorescent wavelengths for confocal imaging.	41
Figure 2.4 RGC dendritic morphology is highly variable and is detected through the DiOlistic labelling process.	43
Figure 2.5 Reconstruction of RGC dendritic complexity using Imaris Filament Tracer module.	44
Figure 2.6 Sholl analysis of RGC dendritic arborisation.	46
Figure 2.7 RGC receptive field classification.	47
Figure 2.8 Reconstruction of hippocampal dendritic spines using Imaris Filament Tracer module and Spine Classifier.	50

x

Figure 2.9 Representation of dendritic spine morphologies.	51
Figure 3.1 Experimental overview for Chapter 3 addressing RGC dendritic arborisation in AD mouse models.	56
Figure 3.2 RGC loss is not a feature in the Tg2576 retina.	59
Figure 3.3 RGC dendritic atrophy in Tg2576 mice.	60
Figure 3.4 ON-centre RGC vulnerability in Tg2576 mice.	61
Figure 3.5 Stable RGC dendritic complexity with further ageing in Tg2576 mice.	62
Figure 3.6 Stable RGC dendritic complexity based on receptive field classification with further ageing in Tg2576 mice.	63
Figure 3.7 RGC dendritic atrophy in 3xTg-AD mice.	66
Figure 3.8 Greater RGC dendritic pruning in male 3xTg-AD mice.	67
Figure 3.9 RGCs based on receptive field and gender classification in wildtype and 3xTg-AD mice.	68
Figure 3.10 ON- and OFF-centre RGCs are affected in male 3xTg-AD mice whilst only ON-centre RGCs are impaired in female 3xTg-AD mice.	69
Figure 3.11 Progressive RGC dendritic pruning with age in 3xTg-AD mice.	70
Figure 3.12 RGC dendritic atrophy in APP ^{NL-G-F} mice.	73
Figure 3.13 Minimal effect of gender on RGCs in APP ^{NL-G-F} mice.	74
Figure 3.14 RGCs based on receptive field and gender classification in wildtype and APP ^{NL-G-F} mice.	75
Figure 3.15 RGC receptive field classification in APP ^{NL-G-F} mice.	76
Figure 4.1 Experimental overview for Chapter 4 addressing CA1 hippocampal dendritic spine coverage in AD mouse models.	83
Figure 4.2 CA1 dendritic spine loss in Tg2576 AD mice.	88

Figure 4.3 CA1 dendritic spine loss in 3xTg-AD mice.	89
Figure 4.4 Greater spine loss in female 3xTg-AD mice.	90
Figure 4.5 Progressive spine loss in 3xTg-AD mice.	91
Figure 4.6 CA1 dendritic spine loss in 3xTg-AD mice.	92
Figure 4.7 Gender effect on spine density in APP ^{NL-G-F} mice.	93
Figure 4.8 APP ^{NL-G-F} CA1 dendritic spines at 7 months.	94
Figure 4.9 Influence of gender on CA1 spines in APP ^{NL-G-F} mice.	95
Figure 4.10 CA1 dendritic spines correlate with RGC complexity in Tg2576, 3xTg-AD an APP ^{NL-G-F} .	96
Figure 5.1 Experimental overview of Chapter 5 addressing the impact of the complement system on RGC dendritic complexity and CA1 hippocampal dendritic spine coverage.	103
Figure 5.2 RGC dendritic complexity in C1q ^{-/-} mice.	107
Figure 5.3 RGC dendritic complexity in C3 ^{-/-} mice.	108
Figure 5.4 RGC dendritic complexity in C3aR ^{-/-} mice.	109
Figure 5.5 RGC dendritic complexity in TREM2 ^{-/-} mice.	110
Figure 5.6 CA1 dendritic spines in C1q ^{-/-} , C3 ^{-/-} , C3aR ^{-/-} and TREM2 ^{-/-} mice.	111
Figure 5.7 Complement C3 and C6 offers protection from RGC dendritic loss in 3xTg-AD mice.	112
Figure 5.8 Complement C6 rather than C3 offers protection from hippocampal CA1 dendritic spine loss in 3xTg-AD mice.	113
Figure 5.9 mAb inhibition of C5 protects CA1 dendritic spines in 3xTg-AD mice.	114
Figure 6.1 Experimental overview for Chapter 6 addressing the impact of systemic inflammation triggered by bacterial (LPS) and viral (MCMV) infection on RGC dendritic arborisation and CA1 hippocampal dendritic spines.	122

Figure 6.2 LPS triggers weight loss in wildtype and 3xTg-AD mice.	128
Figure 6.3 RGC dendritic complexity in LPS insulted wildtype mice.	129
Figure 6.4 ON-centre vulnerability in LPS insulted wildtype mice.	130
Figure 6.5 CA1 dendritic spine density in LPS insulted wildtype mice.	131
Figure 6.6 RGC dendritic complexity in LPS insulted 3xTg-AD mice.	132
Figure 6.7 RGC receptive field classification in LPS insulted 3xTg-AD mice.	133
Figure 6.8 Repeated LPS insults triggers CA1 dendritic spine loss in 3xTg-AD mice.	134
Figure 6.9 RGC dendritic complexity in MCMV infected wildtype mice.	137
Figure 6.10 CA1 dendritic spines in MCMV infected wildtype mice.	138
Figure 6.11 RGC dendritic complexity in MCMV infected 3xTg-AD mice.	139
Figure 6.12 CA1 dendritic spines in MCMV infected 3xTg-AD mice.	140
Figure 7.1 Experimental overview for Chapter 7 addressing the impact of probiotics in 3xTg-AD mice on a chow and a high fat diet for RGC dendritic complexity and CA1 hippocampal dendritic spine coverage.	148
Figure 7.2 Probiotic supplementation in 3xTg-AD mice: RGC dendrites at 9 months.	151
Figure 7.3 Probiotic supplementation in 3xTg-AD mice: RGC dendrites at 12 months.	152
Figure 7.4 Probiotic supplementation in 3xTg-AD mice: CA1 hippocampal dendritic spines at 9 months.	153
Figure 7.5 Probiotic supplementation in 3xTg-AD mice: CA1 hippocampal dendritic spines at 12 months.	154
Figure 7.6 Probiotic supplementation in 3xTg-AD mice on a high-fat diet: RGC dendrites at 6 months.	155

xiii

Figure 7.7 Probiotic supplementation in 3xTg-AD mice on a high-fat diet: CA1 hippocampal dendritic spines at 6 months.

156

List of Tables

Table 1 Further details on the animal models used in this thesis.

36

Abbreviations

%	Percent
µm	Micrometre
AD	Alzheimer's disease
AMD	Age-related macular degeneration
APOE	Apolipoprotein E
APP	Amyloid Precursor Protein
AUC	Area under Sholl curve
Aβ	Amyloid beta
BDNF	Brain-derived neurotrophic factor
C1inh	C1-inhibitor
C3aR	Complement component 3a receptor 1
CAA	Cerebral amyloid angiopathy
CMV	Cytomegalovirus
CNS	Central Nervous System
CP	Classical pathway of the complement system
CSF	Cerebral spinal fluid
DAF	Decay accelerating factor
DiI	1,1'-Dioctadecyl-3,3,3',3'-Tetramethylindocarbocyanine Perchlorate
DiO	3,3'Dioctadecloxacarbocyanine Perchlorate
DRI	Dementia Research Institute
EOAD	Early-onset AD
ETFE	Ethylene tetrafluoroethylene
FAD	Familial AD
fH	Factor H
fI	Factor I
GCL	Ganglion cell layer
GWAS	Genome wide association study

xvi

HBSS	Hank's balanced salt solution
HCV	Hepatitis C virus
HSV	Herpes simplex virus
i.p	Intraperitoneal injection
INL	Inner nuclear layer
IPL	Inner plexiform layer
LOAD	Late-onset AD
LPS	Lipopolysaccharides
LTP	Long-term potentiation
MAC	Membrane attack complex
MASP	MBL-associated serine protease
MBL	Mannan-binding lectin pathway
MCI	Mild cognitive impairments
MCP	Membrane cofactor protein
mg	Milligram
min	Minutes
NFL	Nerve fibre layer
NFTs	Neurofibrillary tangles
OCT	Optical coherence tomography
ONH	Optic nerve head
ONL	Outer nuclear layer
OPL	Outer plexiform layer
PBS	Phosphate buffered solution
PBST	0.1% Triton in PBS
PD	Parkinson's disease
PERG	Pattern electroretinogram
PET	Positron emission tomography
PFA	Paraformaldehyde
pH	Potential Hydrogen

xvii

psi	pound per square inch (pressure)
RBPMs	RNA-binding protein with multiple splicing
RGC	Retinal ganglion cell
ROI	Region of interest
SD	Standard Deviation
SEM	Standard Error of the Mean

Chapter 1. Introduction

1.1 Alzheimer's disease

1.1.1 Overview

Dementia covers a broad classification of progressive neurological conditions, including Alzheimer's disease (AD), vascular dementia, frontotemporal dementia, Parkinson's disease and motor neuron disease (Elahi and Miller, 2017). The incidence of dementia is around 850,000 people in the UK, representing 1 in every 14 of the population over the age of 65 and at the current rate of prevalence will affect 1.5 million people in the UK by 2040 (statistics from Alzheimer's Research UK; <http://www.alzheimersresearchuk.org/>). Dementia represents a major economic, social and health burden of the 21st century affecting roughly 50 million individuals worldwide (Prince *et al.*, 2013; Prince *et al.*, 2016). The discrimination of normal age-related cognitive decline and dementia requires in depth cognitive assessments alongside clinical examinations to rule out other conditions (Frisoni *et al.*, 2010). Some diagnostic criteria include medial temporal lobe atrophy, abnormal cerebrospinal fluid (CSF) inflammation, and altered glucose metabolism in the brain detected by positron emission tomography (PET) scans (Dubois *et al.*, 2007). Diagnosis typically comprises clinical evidence supporting cognitive deterioration, including memory loss, learning, language and motor deficits which are indicative of neuronal damage (Deture and Dickson, 2019). AD is by far the most common classification of dementia and is neuropathologically characterised by the presence of amyloid plaques and neurofibrillary tau tangles, accompanied by substantial neuronal loss (Serrano-Pozo *et al.*, 2011; LaFerla and Green, 2012; Scheltens *et al.*, 2016).

AD clinical disease progresses with time and is accompanied by the progression of underlying neuropathology (Dubois *et al.*, 2016). Age is the strongest risk factor for AD and therefore, in an ageing population, the disease is becoming more prominent (Niccoli and Partridge, 2012). Prior to cognitive decline the AD is associated with several decades of asymptomatic preclinical progression (Driscoll and Troncoso, 2011). During these stages, amyloid plaques and synaptic loss develop whilst, at a slower rate, tau pathology

occurs later in the disease (Spires-Jones and Hyman, 2014). With time, the condition develops to an extent where certain individuals will have early stages of cognitive deficits, referred to as mild cognitive impairment (MCI), of which some will convert to dementia (Langa and Levine, 2014). At this stage, amyloid plaques, tau pathology and synaptic loss become more abundant and associate with prominent brain atrophy (neuron loss) in the most vulnerable brain regions (Galasko *et al.*, 2019). Following this, the disease progresses with increasing cognitive decline to probable AD, accompanied by loss of synapses and neurons across considerable areas of the brain (Mukhin *et al.*, 2017). *In vivo* monitoring by imaging of vulnerable brain regions such as the hippocampus can provide evidence suggestive of AD (Johnson *et al.*, 2012); however, a definitive diagnosis requires neuropathological evidence (Leuzy *et al.*, 2018).

There are many subtypes of AD differing in age of disease onset, severity and progression (Olsen and Singhrao, 2020). Familial AD (FAD), representing fewer than 1% of the total AD cases, is caused by mutations in specific genes, notably the amyloid precursor protein (APP), presenilin 1 (PSEN1) and presenilin 2 (PSEN2) genes (Bekris *et al.*, 2010). Some individuals, approximately 5% of all AD cases, are recognised with early-onset AD (EOAD). In some individuals, approximately 5% of all AD cases, the disease occurs before the age of 65 and develops aggressive pathology; this is termed early-onset AD (EOAD) and carries a strong genetic component (Mendez, 2017). Late-onset AD (LOAD) is the most frequent classification; LOAD is considered sporadic, despite the identification of numerous genetic risk factors. Polymorphisms in the gene encoding apolipoprotein E (APOE) raise the risk of LOAD. The APOE4 polymorphisms is associated with increased disease risk and more severe disease; polymorphisms in this gene are also risk factors for other dementias (Bekris *et al.*, 2010; Safieh *et al.*, 2019; Neuner *et al.*, 2020). Genome-wide association studies (GWAS) have also identified further LOAD risk factors, including variants in TREM2, ADAM10, PLD3, CLU, CR1 and PICALM, with polymorphisms found that affect APP and tau directly as well as altering the immune response (Harold *et al.*, 2009; Kim *et al.*, 2009; Guerreiro *et al.*, 2013; Jonsson *et al.*, 2013).

1.1.2 Amyloid, tau and microglia

Amyloid

Amyloid plaques occur across the AD brain and contain extracellular accumulations of insoluble aggregates of A β peptides, A β 40 and A β 42, the latter being the primary component (Gu and Guo, 2013). Pathological A β peptides form as a consequence of abnormal APP processing by β - and γ -secretases and changes to the modulation of production/clearance pathways. Aggregation of A β peptides generates A β fibrils which establish amyloid plaques; the relevance of these to disease forms the basis of the amyloid hypothesis in AD (Hardy and Higgins, 1992). Figure 1.1 provides a summary of APP processing. For a detailed review of amyloid, Thal *et al.* provides several fundamental phenomena regarding amyloid, different plaque classifications and deposition in the AD (Thal *et al.*, 2006).

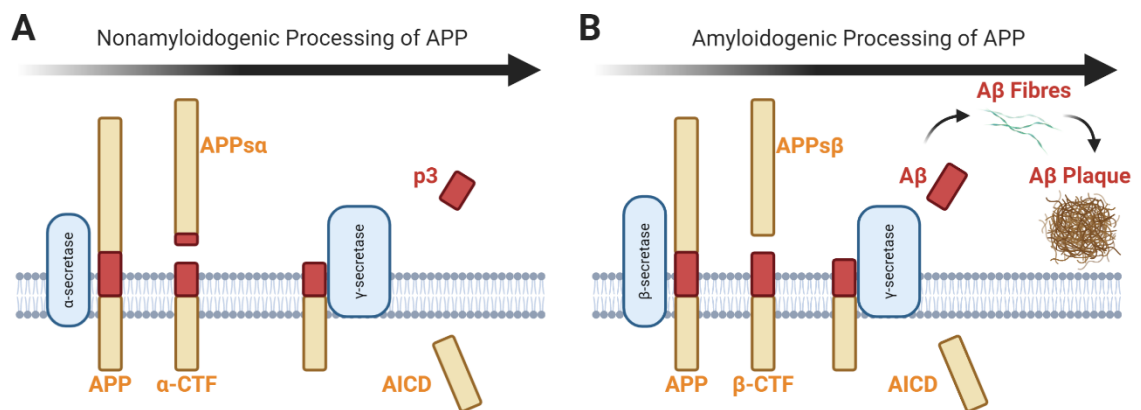


Figure 1.1 Overview of APP processing via nonamyloidogenic and amyloidogenic pathway. The nonamyloidogenic pathway (A), of which the majority of APP is processed, is catalysed by α -secretase for the formation of two fragments, an intracellular α -carboxyterminal fragment (α -CTF) and an extracellular secreted APP (APPs α). The cleavage site of APP by α -secretase is within the A β sequence and prevents A β peptide production. γ -secretase subsequently cleaves α -CTF generating a short fragment called P3 and the amino-terminal APP intracellular domain (AICD). In the amyloidogenic pathway (B), APP is cleaved by β -secretase releasing APPs β and the longer C-terminal fragment β -CTF. β -CTF fragment is cleaved by γ -secretase leading to the generation of AICD and A β peptides outside of the cell. An increased accumulation of toxic A β (A β 1-42), leads to the formation of A β oligomers which aggregate and overwhelm clearance and degradation processes triggering the formation of extracellular amyloid plaques.

Diffuse amyloid plaques occur in synaptically dense regions and weakly associate with glial activation and common amyloid stains. In contrast, dense-core senile amyloid plaques are tightly packed and strongly related to glial activation, contain higher amounts of A β filaments and stain with common amyloid markers (Serrano-Pozo *et al.*, 2011). Amyloid plaques also associate with tau pathology and synaptic markers, termed neuritic

plaques (Yasuhara *et al.*, 1994). *In vivo* techniques such as magnetic resonance imaging (MRI) have capabilities to detect the burden of amyloid deposition, although more likely to be detected once the disease has progressed (Nakada *et al.*, 2008). Growing evidence has supported the role for detecting blood-based biomarkers in AD. Measurement of A β 42, t-tau and p-tau are increased in AD and MCI, whereas factors including DYRK1A, BDNF and folic acid are reduced (Altuna-Azkargorta and Mendioroz-Iriarte, 2020). Additional biomarkers such as IL-10 and IL-12/23p40 have confirmed possibilities in detecting and predicting the abundance of amyloid in AD cases (Pedrini *et al.*, 2017).

Besides amyloid deposition in plaques, A β peptides, primarily A β 40, are also found in the cerebral blood vessels, termed cerebral amyloid angiopathy (CAA), in over 85% of cases (Bales *et al.*, 2016). Deposition of amyloid in the cerebrovascular system is a common finding in the elderly and was only recently linked with AD, although it may also be clinically distinct (Charidimou *et al.*, 2017). Interventions involving immunisation with amyloid peptides have successfully reduced the burden of amyloid plaques in patients; however, these led to an increase in CAA which impaired blood flow, increased inflammation and led to ischemic lesions and haemorrhages in severe cases (Boche *et al.*, 2010).

Tau

In addition to amyloid plaques, neurofibrillary tangles (NFTs) occur in the AD brain. NFTs contain abnormally folded hyperphosphorylated tau protein filaments in neurons. These result in tau unable to bind and stabilise axon microtubules (Binder *et al.*, 2005). During early stages of tau pathology, ‘pretangles’, hyperphosphorylated tau occurs in the neuron cell body and dendrites (Tatsumi *et al.*, 2014). Pretangles can mature and aggregate into filaments which displace cellular components giving neurons a ‘flame-shaped’ morphology. Mature tangles can trigger neuronal cell death, leading to extracellular insoluble tau filaments forming ‘ghost tangles’ (Deture and Dickson, 2019). Tau pathology also associates with microglial activation and can spread across the brain, formulating the tau-seeding hypothesis (Braak and Tredici, 2018; Perea *et al.*, 2018). The burden of NFTs is a better correlate of neuronal loss, disease severity and cognitive decline in AD than amyloid plaques, (Nelson *et al.*, 2012). There are also tau related polymorphisms in the *MAPT* tau gene, which feature in AD and in other neurodegenerative diseases (Iqbal *et al.*, 2010).

Microglia

Microglia cells, the phagocytes of the brain, survey and maintain homeostasis. Microglial activation has a crucial role in the pathologies of neurodegenerative diseases including AD (Galloway *et al.*, 2019). In response to A β fibrils, microglia shift to proinflammatory phenotypes, surround plaques and locally trigger excessive synaptic pruning and neurodegeneration (Hemonnot *et al.*, 2019). There are several microglial genetic risk factors identified in AD associated with TREM2, ABI3 and PLCG2; these alter microglial activation state and phagocytosis (Guerreiro *et al.*, 2013; Neuner *et al.*, 2020). Astrocytes, another type of glial cell, provide neuronal support by supplying nutrients and maintaining homeostasis (Siracusa *et al.*, 2019). In AD, astrocytes become reactive and respond to the proinflammatory environment and damaged neurons. Reactive astrocytes are neurotoxic and localise to amyloid plaques, particularly in the later stages of the disease (Matias *et al.*, 2019).

1.1.3 Hippocampus and synapses

Neurodegeneration, specifically synaptic loss, is the best correlator to cognitive impairment in AD (Scheff *et al.*, 2014). Amyloid and tau pathology may drive synaptic loss; however, synaptic remodelling is one of the first features of the disease. Neuronal and synaptic pruning occurs across the AD brain, particularly associated with the key neuropathological hallmarks of AD, for example localised around amyloid plaques, although it is most extensive in the hippocampus which is particularly affected in the early stages of the disease (O'Shea *et al.*, 2016).

Hippocampal Architecture

The hippocampus is essential for learning, emotions and the formation and storage of memories (Tyng *et al.*, 2017). Neurodegeneration occurring in the hippocampus is a feature in many neurological diseases and also with normal ageing (O'Shea *et al.*, 2016). The hippocampus is a dense neuron region that contains the dentate gyrus and hippocampal subfields (CA1-4) and connects to many areas of the brain such as the cortex (Dekeyzer *et al.*, 2017). The dentate gyrus acts as a pre-processor for incoming excitatory inputs from the cortex. CA4 region is considered part of the dentate gyrus and receive

inputs from the dentate gyrus. CA3 regions contain pyramidal neurons that receive inputs from the dentate gyrus and the entorhinal cortex. CA2 region is a small section located between the CA3 and CA1 subfields, although is often ignored due to the small size. Finally, the CA1 region contains pyramidal neurons and are the major output neuron of the hippocampus.

A major signalling pathway of the hippocampus is the perforant pathway from the entorhinal cortex. Axons arrive from the entorhinal cortex (layer III neurons) and directly synapse onto CA1 neurons, the output of the hippocampus. Alternatively, signal transmission can flow through the trisynaptic pathway where axons arrive from the entorhinal cortex (layer II neurons) and sequentially synapse through the hippocampus and out through the subiculum. There are many other reported hippocampal circuitries that are essential for transmission (Basu and Siegelbaum, 2015). These signalling pathways, both excitatory and inhibitory, degenerate in AD with the fewer dendritic spines (post-synaptic sites), dendritic retraction and neuronal loss (Strange *et al.*, 2014). Figure 1.2 provides an illustration of a mouse hippocampal slice indicating the CA1 neurons and dendritic spines.

Dendrites

Neurons have an intricate dendritic arbour which ensures efficient signal propagation. The morphology of the dendritic field is highly dynamic, with neurons structurally distinguishable between different regions in the CNS (Goillard *et al.*, 2020). Dendrites are cellular protrusions that increase a neuron's surface area to cover considerable distances and enable greater capacity to respond to changes. Dendrites contain cellular components including Golgi, endoplasmic reticulum, mitochondria and a supportive cytoskeletal structure (Silver, 2010; Emoto, 2011; Arikath, 2012). This compartmentalisation allows for localised protein synthesis and highly dynamic mitochondrial movement, which is particularly present during synaptogenesis (formation of synapses) (Ostroff *et al.*, 2002). Neurons can therefore respond to subtle changes through the elaborate dendritic arbour, and converts analogue signals to an effective digital action potential (Šišková *et al.*, 2014). The loss of dendrites (dendritic pruning/dendropathy) is a characteristic feature of neurodegeneration and in addition with synaptic loss is an early indication of neuron damage.

Synapses

Synapses communicating through pre- and post-synaptic sites and are the contact points for signal transmission between neurons. On the arrival of an action potential, stored neurotransmitters in the pre-synaptic terminal are released into the synaptic cleft, triggered by diffusion of Ca^{2+} into the presynapse neuron. Neurotransmitters bind to receptors on the post-synaptic neuron and based on the neurotransmitter will trigger an excitatory or inhibitory response. Disruption of generation, storage, release, recycling and, receptor binding of neurotransmitters the underlying cause many neurological diseases (Kavalali, 2015). Synapses that are used are appropriately strengthened and, continuous bursts of electrical stimuli, increase the synaptic response, necessary for the formation of memories, in a process termed long-term potentiation (LTP) (Kumar, 2011).

Dendritic spines and morphology

Dendritic spines are the sites for postsynaptic terminals of excitatory glutamatergic synapses; they are small protrusions from the dendritic shaft and the primary location for memory and synaptic plasticity (Sambasivarao, 2001; Berry and Nedivi, 2017). The dendritic spines are tightly regulated both in distribution and morphology along the dendrites. Since dendritic inputs pool to control the generation of action potentials, spines have a crucial effect on the computational characteristics of the neuron (Sambasivarao, 2001). Neuronal activity dictates the morphologies of dendritic spines and synapse functionality. Mushroom spines, responsible for long-lasting synaptic transmission, have a distinctive enlarged synaptic head, dense in AMPA receptors, corresponding to synaptic strength and memory retention (Kennedy, 2016).

In comparison, 'thin spines', which lack the enlarged spine head, but have long necks, are highly dynamic, responsible for the formation of new synapses and reflect synaptic plasticity (Bourne and Harris, 2008; Gipson and Olive, 2017). Stimulation and increased activity of thin spines triggers structural plasticity increasing GluR1 (glutamate receptor) insertion, PSD (postsynaptic density) expansion and increased AMPA receptor density, maturing the synapse (Ehlers *et al.*, 2007). Dendritic spines are vulnerable to pruning, with mushroom and thin spine loss associated with learning and memory deficits (Xu *et al.*, 2018). Small stubby spines lack the distinctive spine neck and spine head; these represent immature synapses and have the capacity, based on activity, to develop into

mature synapses (Gipson and Olive, 2017). In AD mouse models it is becoming increasingly evident that the loss of dendritic spines is a key pathological feature of the disease (Dorostkar *et al.*, 2015). In AD mouse models, the reduction in dendritic spine coverage is associated with the observed memory deficits, although studies report potential beneficial therapeutics that restore hippocampal synapses (Ricobaraza *et al.*, 2012). Figure 1.2 provides an illustration of the different dendritic spine morphologies.

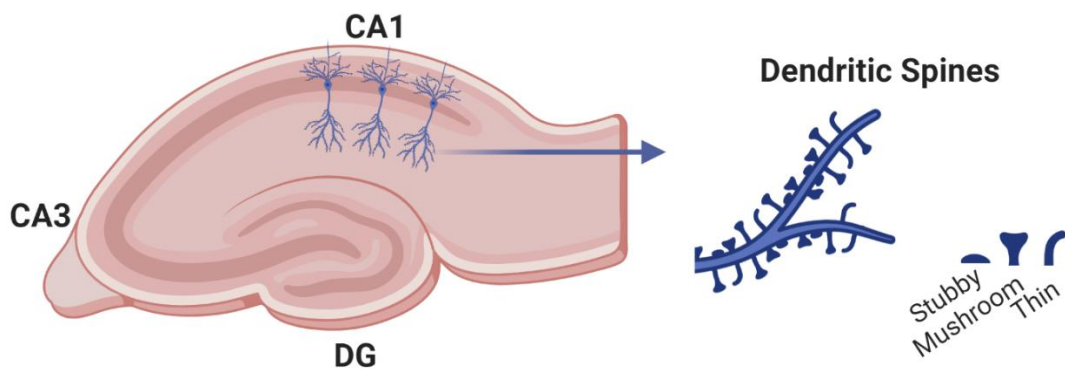


Figure 1.2 Schematic of a mouse hippocampus slice highlighting the CA1 region, dendritic spines, and spine morphologies. Abbreviations: DG, dentate gyrus. Figure created with BioRender.

1.1.4 AD mouse models

Rodent models present an ideal opportunity to study aspects of diseases in a living organism. These are under controlled environments and allow for the determination of possible mechanistic changes contributing to pathology. Many mouse models recapitulate aspects of AD pathology, and none are perfect models; in this thesis I analysed, two transgenic models (Tg2576 and 3xTg-AD) and one knock-in model (APP^{NL-G-F}).

Overexpression AD mouse models

Tg2576 (strain: B6;SJL-Tg(APP^{SWE})2576Kha) AD mice are one of the oldest and best-characterised amyloid-related AD mouse models (Hsiao *et al.*, 1996a). Tg2576 mice neuronally express the mutant form of human APP (isoform 695) containing the Swedish mutation (K670N and M671L) under the control of the hamster prion protein promoter (PrP) which dictates that it is expressed widely in the nervous system. Mutations increase the level of mutant APP, develop amyloid plaques, and are associated neuroinflammation which correlate with behavioural deficits (Hsiao *et al.*, 1996a; Hsiao *et al.*, 1996b). By the age of six months, mice develop deficits in spatial memory. By the age 14 months, Tg2576 mice show impairments in working memory and contextual fear conditioning (Jacobsen *et al.*, 2006). Amyloid plaques are numerous by 12 months in the cortex and hippocampus. Tg2576 mice also display dysfunction in synaptic plasticity, with hippocampal dendritic spine loss by 6 months (Irizarry *et al.*, 1997; Chapman *et al.*, 1999; Lanz *et al.*, 2003). Despite the abundant burden of amyloid, Tg2576 mice do not show neurofibrillary tangles and neuronal loss, therefore are expected to reflect only early stages of the human disease. Figure 1.3 provides an illustration of the disease hallmark time points.

The 3xTg-AD model expresses three AD familial mutations, APP Swedish, MAPT P301L and PSEN M146V under the control of the mouse Thy1.2 promoter (Oddo *et al.*, 2003). These mutations trigger age-dependent degeneration confined to the CNS. Amyloid plaques develop from 6 months and become more numerous in the cortex and hippocampus by 12 months. 3xTg-AD mice also develop intraneuronal amyloid which correlates with cognitive decline (Oddo *et al.*, 2003; Billings *et al.*, 2005). Besides amyloid pathology, 3xTg-AD mice develop tau associated pathology in the hippocampus. This is however a feature in older mice, similar to the human disease. Pathological

changes from the age of 6 months also correlate with deficits in learning and memory dysfunction (Stover *et al.*, 2015). In the advanced disease, ages over 12 months, 3xTg-AD mice are impaired in spatial learning acquisition and deficits in short-term and working memory (Blázquez *et al.*, 2014). Different lines of 3xTg-AD mice, however, known to display considerable variations in pathology with females displaying more consistent pathology, 3xTg-AD mice are also shown to have pathological drift shifting the onset of the disease later by several months (Carroll *et al.*, 2010; Blázquez *et al.*, 2014). Figure 1.4 provides an illustration of the disease hallmark time points.

Knock-in AD mouse models

Many transgenic AD mouse models overexpress mutant APP, which recapitulate amyloid deposition and the associated cognitive deficits. However, overexpression in transgenic AD models can lead to artificial phenotypes, therefore knock-in approaches are now widely adopted and are regarded to better reflect the human disease (Jankowsky and Zheng, 2017; Sasaguri *et al.*, 2017). APP^{NL-G-F} mice express APP in the relevant cell types and locations. This model features three familial AD mutations, Swedish (NL), Iberian (G) and Arctic (F) mutations, resulting in increased amyloid production, A β 42/A β 40 ratio and amyloid aggregation respectively (Saito *et al.*, 2014; Nilsson *et al.*, 2014). These increase the level of pathogenic A β while expressing APP at wildtype levels. APP^{NL-G-F} mice exhibit more severe pathology than other models, with amyloid plaques depositing in the subcortical and cortical regions from two months, reaching saturation by seven months. As with other models, amyloid plaques associate with local synaptic loss and neuroinflammation, correlating with age-dependent behavioural and cognitive deficits (Saito *et al.*, 2014; Masuda *et al.*, 2016). The APP^{NL-G-F} model display age-dependent memory impairment which is first detected at 6 months which worsens with greater impairments at 12 months based on Morris water maze, object recognition and fear condition tests (Sakakibara *et al.*, 2018; Mehla *et al.*, 2019). APP^{NL-G-F} mice are also found to display decreased levels of brain antioxidants, which increase inflammatory cytokines (Izumi *et al.*, 2020). APP^{NL-G-F} mice only reflect the amyloid component of AD and do not express tau pathology and neuronal loss. APP^{NL-G-F} mice are therefore likely to reflect the preclinical stages of the disease (Sasaguri *et al.*, 2017). Figure 1.5 provides an illustration of the disease hallmark time points.

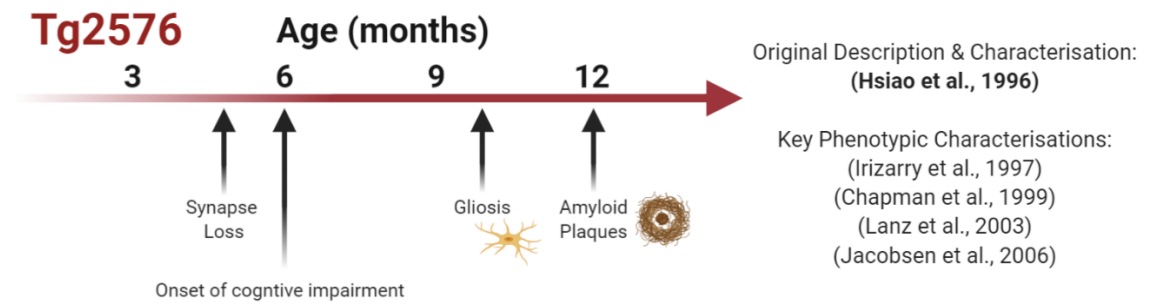


Figure 1.3 Tg2576 phenotypic characterisation. Synapse and cognitive impairment occur from around 6 months of age. Gliosis is detected from 10 months. Amyloid plaques are prominent by 12 months of age. Illustration created in BioRender.

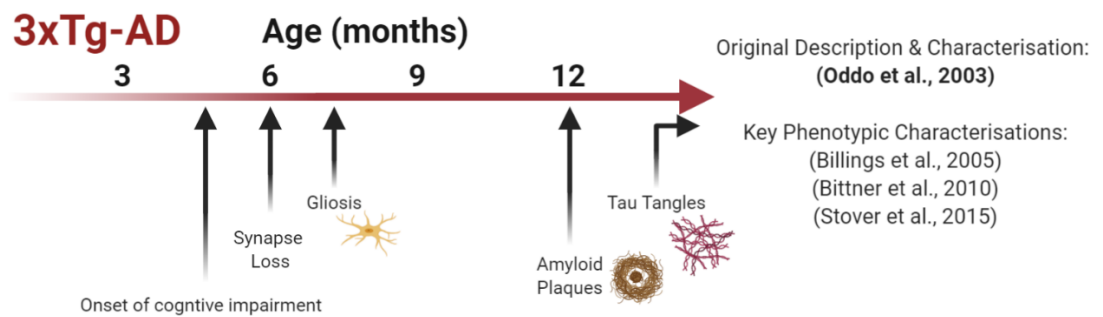


Figure 1.4 3xTg-AD phenotypic characterisation. Synapse and cognitive impairment occur from around 6 months of age. Gliosis is detected from 7-8 months. Amyloid plaques are prominent by 12 months of age with tau tangles later in disease around 15 months. Illustration created in BioRender.

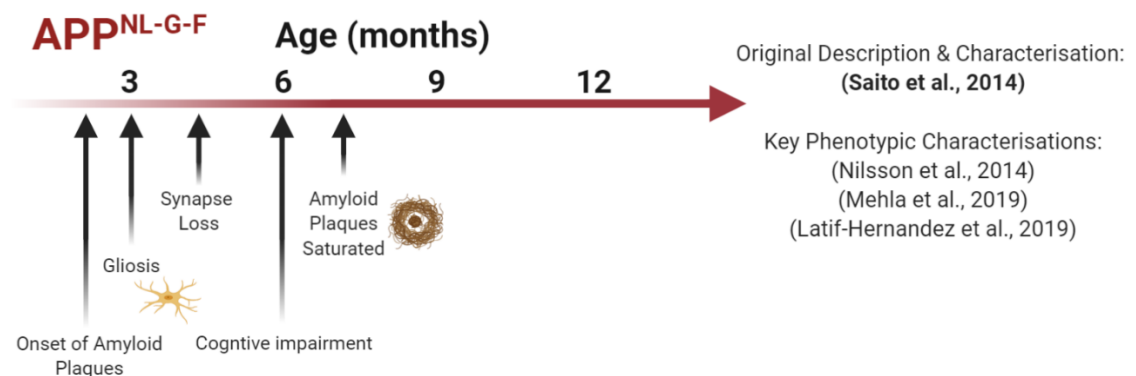


Figure 1.5 APP^{NL-G-F} phenotypic characterisation. Amyloid plaques deposit at 2-3 months with associated gliosis. Synapse and cognitive impairment occur by 6 months. Cortex and hippocampus fully saturated by around 7 months. Illustration created in BioRender.

1.2 The retina

1.2.1 Retina structure

The vertebrate retina is a developmental outgrowth of the embryonic diencephalon, and shares many similar features with the brain. The retina is the only part of the CNS that is not protected by bone. The main role of the retina is to convert light signals into neuronal impulses, which are transmitted to the brain for visual perception. The retina consists of three cellular layers, the outer nuclear layer (ONL), inner nuclear layer (INL) and ganglion cell layer (GCL). These are contacted by two synaptic layers the outer plexiform layer (OPL) and inner plexiform layer (IPL). Figure 1.6 illustrates the retinal layers.

1.2.2 Retina cell types and phagocytosis

The ONL contains the light-sensitive photoreceptors, rods and cones, which correspond to sensing sim light and colour vision respectively. Photoreceptors depolarise by light absorption and initiate phototransduction. The OPL provides dense synaptic connections that link the ONL and the INL. Within the INL, bipolar, horizontal and amacrine cells support the signalling processing. The GCL is the location of the retinal ganglion cells (RGCs) which receive inputs from the IPL, the region in which RGCs project their dendrites. RGCs project axons in the nerve fibre layer (NFL), which bundle together through the optic nerve head (ONH) to the brain (Masland, 2012; Hoon *et al.*, 2014). Therefore, the retina is physically connected to the brain via the optic nerve.

As in the brain, the retina contains of glial cells providing neuronal support and homeostasis. The retina has three types of glia, Müller cells, microglia and astrocytes. Müller cells are large retina spanning glia which protect against glutamate toxicity. Müller cells and microglia cross-talk during the process of phagocytosis. Müller cells are known to phagocytose cell debris; however the primary phagocytes in the retina are activated microglial cells which provide similar functions those occurring in the brain during development, homeostasis and pathological conditions (Vecino *et al.*, 2016). During development, microglia are found to phagocytose and eliminate RGCs that are tagged with complement proteins (Zhang *et al.*, 2019). In experimental axotomy with retrograde fluorescent dye labelling, microglia are found to contain RGC debris, likely of that linked

to pruning of vulnerable neurons (Thanos *et al.*, 1994). Similar to the brain, the retina is an area of high metabolic activity and is vulnerable to damage.

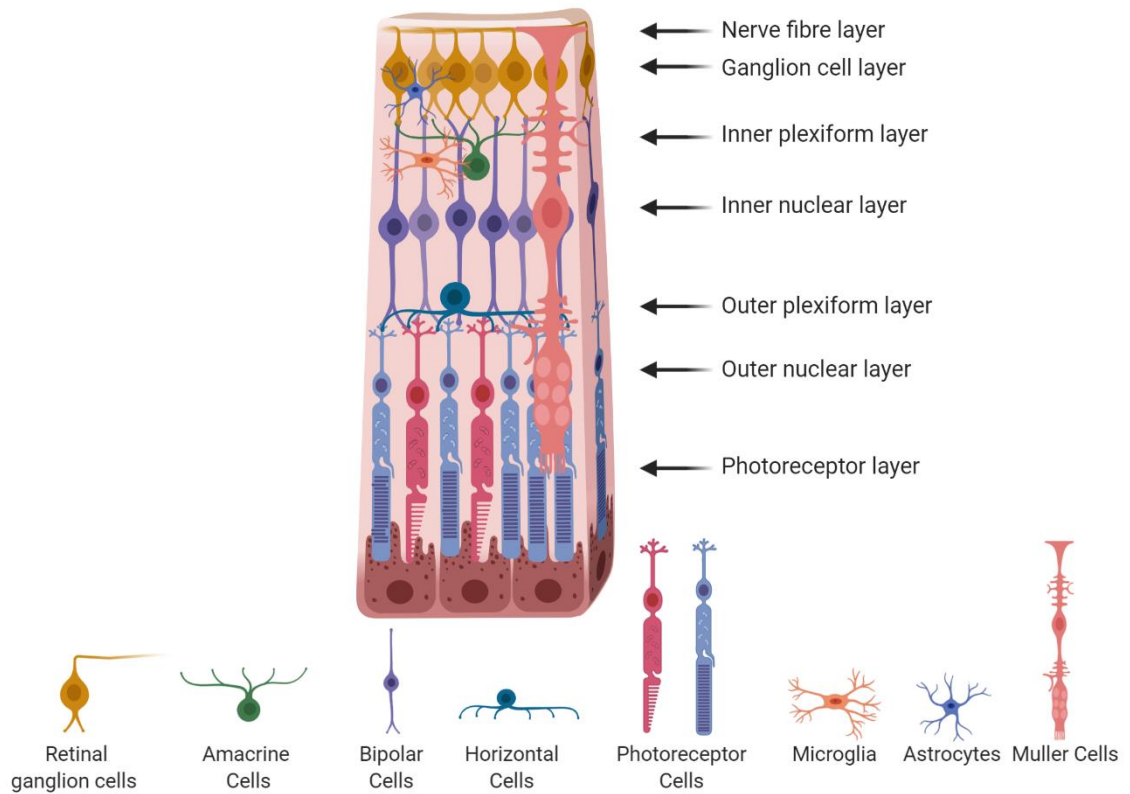


Figure 1.6 Schematic of the retina structure, highlighting the different retinal layers, neurons and glia. Created with BioRender.

1.2.3 Retinal ganglion cells

RGCs extend their dendrites into the IPL where they receive inputs. RGCs have distinctive dendritic architecture and are morphologically complex (Sanes and Masland, 2015). There are over 30 different functional types of RGCs in the mouse retina based on light responses and anatomical criteria (Baden *et al.*, 2016). Unlike neurons in the brain, synaptic input in the retina is situated directly on the dendritic shaft. Therefore, the function of an RGC is reliant on the coverage of the dendritic field. Dendritic lamination into the IPL also subtypes RGCs into those which respond to light (ON-centre) or to the absence of light (OFF-centre) (Bodnarenko and Chalupa, 1993; Wyk *et al.*, 2009). ON-centre RGCs ramify in sublamina b of the IPL synapsing (glutamatergic) with bipolar cells to form the light-sensitive pathway. Whereas OFF-centre RGCs project dendrites into the sublamina a of the IPL and synapse with amacrine cells (GABAergic) to form the dark sensitive pathway. The higher energy requirement of ON-centre RGCs marks these cells as more sensitive to degeneration (Sanes and Masland, 2015).

RGCs are susceptible to degeneration as they have a high energy demand, have long intraocular unmyelinated axon and a complex dendritic field. Neurodegenerative diseases that affect the retina, such as glaucoma, report RGC and axonal loss, changes that animal models also recapitulate (Buckingham *et al.*, 2008). RGC dendritic atrophy is unsurprising as dendrites reflect the majority of an RGC surface area and contain cellular components such as mitochondria essential for synapses (Ito and Di Polo, 2017). RGC excessive dendritic atrophy is an often-reported feature of many experimental glaucoma models, mainly triggered by an elevation of intraocular pressure, and of neurodegeneration in general. The process of RGC dendritic loss is both supported intrinsically driven events such as mitochondrial dysfunction and degeneration of axons, however dendritic loss is also supported by extrinsic factors such as elevated levels of retinal complement activation and microglial activation (Williams *et al.*, 2012; Williams *et al.*, 2016; Zhang *et al.*, 2019). These RGC dendritic changes reflect early stages of neurodegeneration, which appear before axon and neuron loss and highlight a reduction in the synaptic connectivity (Williams *et al.*, 2010; Williams, Thirgood, *et al.*, 2013). Figure 1.7 provides an illustration of RGC dendritic pruning, where the complex dendritic field is substantially reduced.

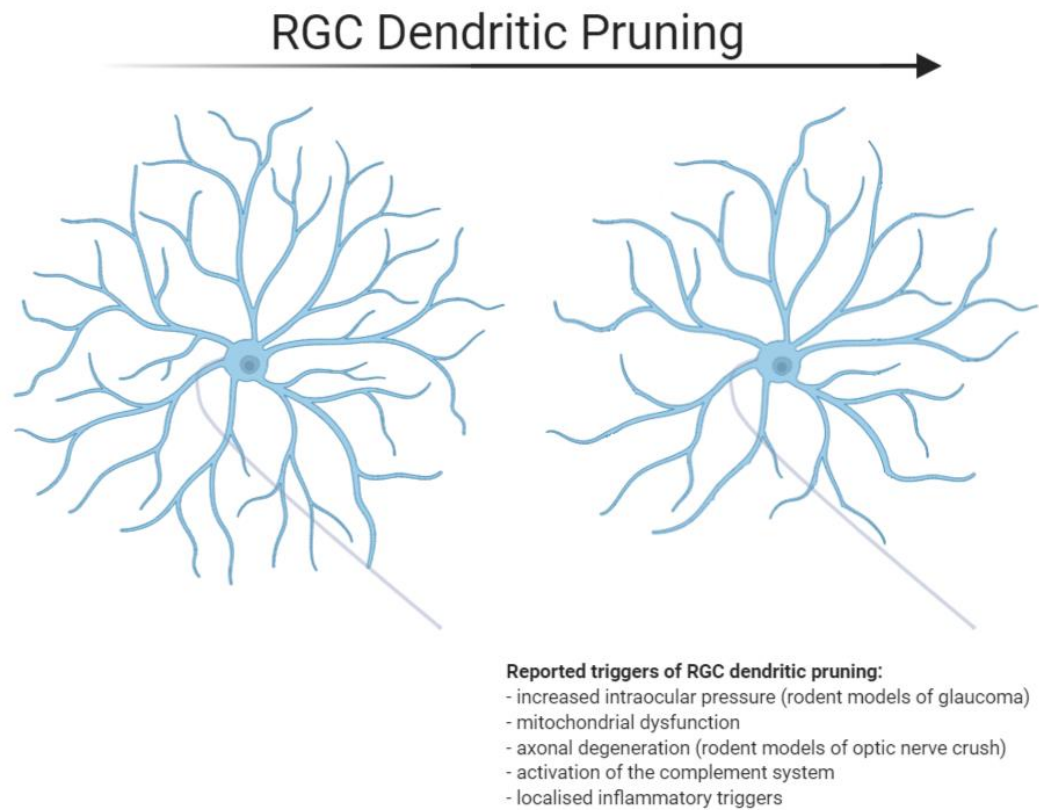


Figure 1.7 Illustration of RGC dendritic pruning. Left: representation of a healthy RGC with a complex dendritic field. Right: representation of an RGC that has undergone substantial dendritic pruning and is characterised by a loss of dendritic complexity. Axon indicated by faded blue line. Created with BioRender.

1.2.4 Retinal changes in AD

Background

AD diagnosis is difficult and requires expensive techniques, some of which are invasive. Standard methods include magnetic resonance imaging (MRI), positron emission tomography (PET) and analysis of cerebrospinal fluid to support cognitive assessments (Johnson *et al.*, 2012). Diagnosis typically takes place during the early stages of cognitive deterioration, which illustrate the initial clinical manifestations of the disease. However, at this stage, underlying pathology is already well advanced and on a downward trajectory. Therefore, there is an urgent need for a convenient technique that allows for population screening and the earlier detection of underlying pathology (Fiandaca *et al.*, 2014). Retinal changes could provide a surrogate marker, indicating and reflecting ongoing pathology in the CNS (London *et al.*, 2013). It is estimated that over 120,000 individuals in the UK display sight loss and also have dementia (statistics from Royal National Institute of Blind People; <https://www.rnib.org.uk/>). The retina is an extension of the CNS that has the advantage of easy non-invasive imaging at subcellular resolutions, and shares many similarities with the brain. Therefore, detection of retinal changes in the eyes of AD cases could offer potential avenues for monitoring the disease (Liao *et al.*, 2018).

Visual discrepancies are a feature in some AD cases with dysfunction noted in visual acuity, colour discrimination, contrast sensitivity and visual field loss, to name only a few (Javaid *et al.*, 2016). Post mortem analysis of retinas in human AD cases indicate damaged optic nerve head, neuronal loss and thinning of the retinal layers, along with other changes (Hinton *et al.*, 1986; Javaid *et al.*, 2016). Retinal function is also reduced, with decreased amplitudes on pattern electroretinogram (PERG) recordings in AD individuals, suggesting abnormal RGCs (Katz *et al.*, 1989; Krasodomska *et al.*, 2010). These retinal changes are not exclusive to AD and seen in other eye conditions and dementia. However, they could provide some useful targets. Visual dysfunction in AD, and other dementias, are challenging to identify and interpret from psychophysical experiments alone. These are due to confounding obstacles related to poor execution of tasks because of cognition rather than visual changes. Diagnosis of AD using the retina is likely to require structural techniques such as optical coherence tomography (OCT) and

measurement of electrophysiological parameters. OCT imaging provides an accessible non-invasive technology that is low cost and ideal for population screening (Doustar *et al.*, 2017). Recently, changes to light scattering parameters, a sign of degeneration, has been observed in the AD retina and in mouse models (More *et al.*, 2019; Song *et al.*, 2020). In some instances, mouse models, such as the 3xTg-AD model, report thinning of the retinal layers and nerve fibre layer (Song *et al.*, 2020). Despite several promising studies identifying AD retinal pathology, others are unable to detect such findings (Ho *et al.*, 2014; Williams *et al.*, 2017). These differences potentially arise from a lack of retina-brain comparisons within the same report, relatively low sample sizes and including AD subtypes or models that are not appropriate.

Retina AD Pathology

As in the brain, amyloid plaques and NFTs are a feature in the AD retina, although not always a consistent observation. The first description of amyloid plaques in the human AD retina occurred only one decade ago. Although plaques are smaller in size than the brain, similar morphologies are observed (Koronyo-Hamaoui *et al.*, 2011). These plaques were more prominent in the peripheral regions of the retina, notably in the superior and inferior quadrants (Koronyo *et al.*, 2017). Importantly, the observed retinal amyloid plaques correlate with the abundance of plaques in the brain, particularly in the primary visual cortex and entorhinal cortex (Koronyo *et al.*, 2017; Schultz *et al.*, 2020). Measurement of A β 40 and A β 42 in both the retina and hippocampus of AD individuals also correlate with the ApoE ϵ 4 carriers (Schultz *et al.*, 2020). Of note, A β immunoreactivity is detected in the sub-retinal pigment epithelium (RPE), and toxic amyloid oligomers in drusen deposits of in age-related macular degeneration (AMD) (Isas *et al.*, 2010). Amyloid plaques occur across the retina with higher depositions in the INL, NFL and GCL and are identified both in post-mortem and *in vivo* studies, the latter benefiting from fluorescent amyloid binding compounds such as curcumin (Koronyo *et al.*, 2017; den Haan *et al.*, 2018). Hyperspectral *in vivo* imaging of the AD retina also detects amyloid in the absence of fluorescence tagging. This method collects a series of images from various wavelengths of light that are stacked and combined. These provide spatial information and a reflectance spectrum related to the abundance and burden of amyloid deposition (More and Vince, 2015; Hadoux *et al.*, 2019). However, such imaging is technically challenging and hence under-used.

Abnormal tau, another key neuropathological hallmark of AD, is detected in the retinal layers mainly in the IPL, OPL and INL and is weakly observed in the GCL, NFL and photoreceptors (Loffler *et al.*, 1995; Leger *et al.*, 2011). In the AD retina, hyperphosphorylated tau is also described in post mortem tissue (Schön *et al.*, 2012). The presence of hyperphosphorylated tau is known to drive the formation of fibrillar tau inclusions and neurofibrillary tangles leading to neuronal dysfunction. However, only one study has identified NFT-like structures using Gallyas silver stain in the post mortem AD retina (Koronyo *et al.*, 2017).

Similarly, to the brain, the AD retina also demonstrates markers of retinal neuroinflammation with astrocyte and microglial activation localised around the plaques. These associate with an upregulation of IL-1 β , complement component 3 (C3) and TREM2 (Grimaldi *et al.*, 2019). Neurodegeneration is also a feature, with some post-mortem studies pinpointing decreased RGCs which coincide with axonal degeneration and thinning of the RNFL (Hart *et al.*, 2016). *In vivo* OCT imaging in AD individuals report degeneration across the retina, which correlate with cognitive impairment (Iseri *et al.*, 2006). RGC degeneration, specifically melanopsin-containing RGCs (mRGCs), which drive circadian photoentrainment, are significantly degenerated in the AD retina with dendritic and cell loss linked to the sites of amyloid plaque deposition (La Morgia *et al.*, 2016). Additionally, the AD retina also displays thinning of vessels and reduced blood flow indicative of vasculature changes (Frost *et al.*, 2013).

1.2.5 Retinal AD pathology in rodent models

Reports on retinal pathology in rodent models of AD have been inconsistent. Nevertheless, some reports suggest the mouse retina is affected in various AD models. In AD model mice, the retina displays an upregulation of APP, intracellular amyloid in RGCs and an age-associated amyloid plaque deposition across the retinal layers with the degree of pathology dependant on the animal model (Ning *et al.*, 2008). However, the expression of A β 42 in the retina is substantially lower than in the brain (Dutescu *et al.*, 2009). This is possibly a consequence of reduced retinal expression of BACE1, which is essential in the generation of the APP proteolytic products (Li *et al.*, 2016). Although the relative abundance of A β 42 peptides in the retina varies between the different transgenic AD models (Alexandrova *et al.*, 2011). Some studies also identify *in vivo* amyloid

signatures (hyperspectral imaging and amyloid tagging) in the mouse retina, supporting simultaneous plaque deposition with the brain (More and Vince, 2015). However, others fail to find amyloid pathology in the retinas of mouse AD models (Joly *et al.*, 2017).

Other classical AD neuropathology such as NFTs are less reported in AD models, mainly because of the absence of tau pathology in the commonly used amyloid models. However, hyperphosphorylated tau is a feature in the 3xTg-AD model, including in RGCs and increases with age (Chiasseu *et al.*, 2017). In tauopathy models (P301S), hyperphosphorylated tau is found to accumulate in the nerve fibre layer which aggregate to form inclusions in RGCs (Gasparini *et al.*, 2011). Similar to functional changes in the human AD retina, retinal physiology in AD mouse models also supports decreased signal amplitudes reflective of RGC activity in ERG and PERG studies (Gao *et al.*, 2015). A recent study analysed the retina of APP^{NL-G-F} mice and report the presence of soluble A β that with age develops into more mature plaques (Vandenabeele *et al.*, 2020). This study also reports changes to electrophysiological recordings in the absence deficits in the visual performance and identified that hyperspectral imaging was a quantitative measure of retinal amyloid (Vandenabeele *et al.*, 2020). Once again, these findings are inconsistent and highly reliant on age and model. Microglial activation is also a feature in the mouse AD model retina, with some studies indicating increased microglial density in the vicinity of plaques and tau pathology, morphological alterations and the expression of proinflammatory cytokines (Chen *et al.*, 2016). Again, these findings are not consistent across studies (Dutescu *et al.*, 2009; Chidlow *et al.*, 2017).

Evidence of RGC degeneration in mouse AD retina

The mouse AD retina also displays evidence supporting neurodegeneration. RGCs and cell density in the GCL are reduced in some studies, although more frequently, changes in the retinal thickness are detected in the RNFL, GCL and IPL (Chiquita, Campos, *et al.*, 2019). RGC loss is not an expected feature in the models given the lack of neuronal loss in the brains of AD models. Retinal neurons in AD mice also display evidence of apoptotic markers such as active caspase-3 and TUNEL-positive cells, as well as decreased choline acetyltransferase, axonal swelling and decreased axonal density in the optic nerves (Perez *et al.*, 2009; Parnell *et al.*, 2012; Eimer and Vassar, 2013; Gupta *et al.*, 2016). RGCs are one of the most damage-susceptible neurons in the CNS and are vulnerable to dendritic pruning which is an early feature of neurodegeneration. To date,

only one other study, the foundation of this thesis, provides evidence of RGC excessive dendritic pruning in the Tg2576 AD mouse model in the absence of RGC loss (Williams, Thirgood, *et al.*, 2013). It is therefore likely that measuring the burden of RGC dendritic complexity could provide a compelling measure of neurodegeneration in the retina of AD models.

1.3 The complement system in AD

1.3.1 Pathways, regulation, and disease

The immune response to invading pathogens and debris relies on an efficient complement system, a pathway that consists of circulating in the plasma and are expressed on cells. The complement system has the capacity for self-destruction. Both plasma and membrane-bound inhibitory proteins tightly regulate the complement system and maintain low-level activation to enable a rapid response. Three enzymatic cascades, classical, lectin and alternative pathways all converge on the terminal pathway contributing to opsonisation of targets and formation of the membrane attack complex (MAC) to trigger lysis on target cells (Morgan, 2003; Ricklin *et al.*, 2010). Figure 1.8 provides an overview of the different complement pathways involved in the innate immune response. Complement dysregulation leading to uncontrolled activation triggers tissue damage and is a feature of many inflammatory diseases, including joint, vascular and renal diseases (Morgan, 2003; Sarma and Ward, 2011; Xu and Chen, 2016). More recently, the role of complement in neurodevelopment and neurodegenerative diseases has become more transparent, including in the role of excessive microglial engulfment of synapses in AD (Stevens *et al.*, 2007).

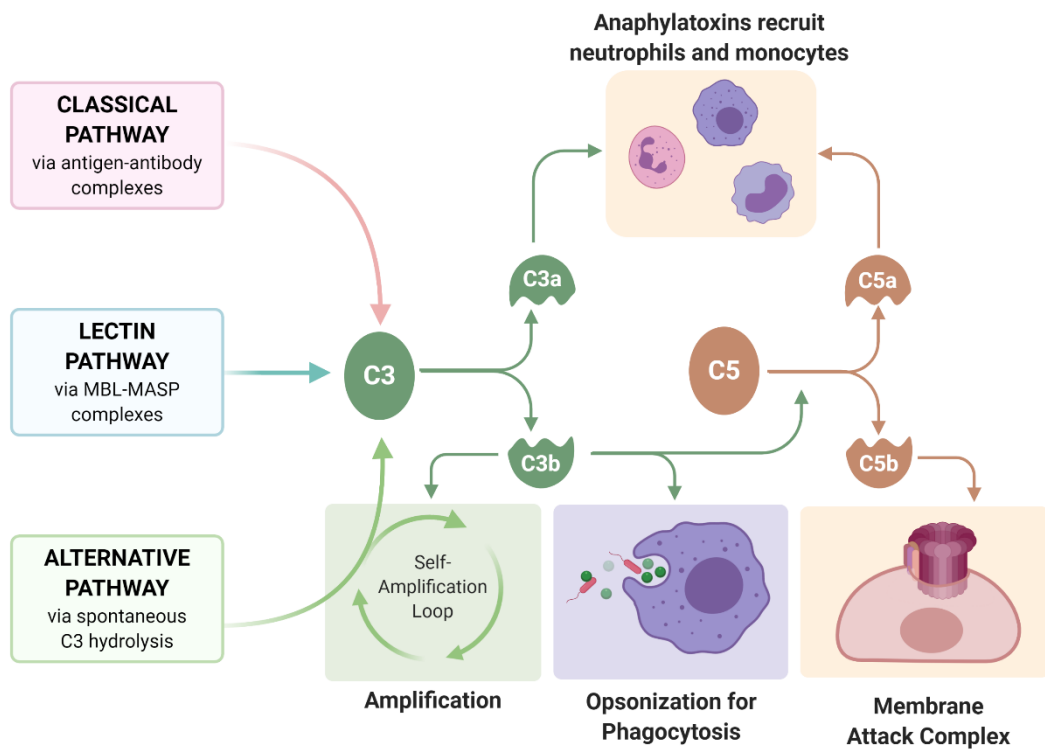


Figure 1.8 The role of the complement system in the innate immune response. The complement system is an integral part of the innate immune system and is comprised of three pathways, the classical, lectin and alternative pathways. The alternative pathway functions through a self-amplification loop through spontaneous C3 hydrolysis. These pathways converge onto C3, the most abundant serum complement component, releasing the anaphylatoxin C3a and C3b which has the capacity to opsonise target cells for phagocytosis. The C5 convertase binds plasma C5 which is cleaved into the anaphylatoxin C5a, and C5b. C5b feeds into the terminal pathway for the formation of the membrane attack complex (MAC) which triggers cell lysis. Created with BioRender.

1.3.2 Classical, lectin and alternative pathway

The classical complement pathway is initiated by the binding of C1q globular heads in the C1 complex (C1q, C1r and C1s) to the Fc region of IgM or aggregated IgG antibodies, or directly on invading pathogens expressing activators such as bacterial lipopolysaccharides and nucleic acids. Binding triggers conformation changes, in the presence of Ca^{2+} , which activate C1s to cleave plasma C4, a large protein encoded by two genes (C4A and C4B). C4 contains three disulphide-bound chains (α , β , and γ) and cleavage of C4 triggers the release of C4a and exposure of a previously buried thioester group on C4b which bind and locks onto target surfaces. The thioester in C4b is susceptible to inactivation by hydrolysis therefore restricting C4b deposition to the vicinity of the C1 complex. Bound C4b acts as a receptor for the plasma protein C2 which, in the presence of Mg^{2+} , is cleaved by C1s into C2a and C2b. C2a binds C4b forming the next enzyme in the pathway, C4b2a, the C3 convertase. C4b2a complex noncovalently binds C3, the most abundant serum complement component, and C2a in the complex mediates the cleavage of C3 into C3a and C3b; the latter binds C4b2a forming the C4b2a3b enzyme, C5 convertase. C5 convertase binds plasma C5, which is cleaved into C5a and C5b, the latter initiating the terminal pathway through binding C6 and the other terminal components. Both C3a and C5a fragments are anaphylatoxins, potent pro-inflammatory molecules that trigger an inflammatory response.

The lectin pathway is an antibody independent activation process that is activated by bacteria and microorganisms. The lectin pathway shares similarities to the classical pathway. Mannan-binding lectin (MBL), a serum lectin structurally similar to C1q, whilst MBL-associated serine protease (MASP) are functionally comparable to C1r and C1s. These form the MBL-MASP complex which activates C4, analogous to the C1 complex.

The alternative pathway differs from the classical and lectin pathways in that it rapidly activates on foreign surfaces in the absence of antibodies. Activation occurs spontaneously from low-level tick over. Plasma C3 is hydrolysed into $\text{C3}(\text{H}_2\text{O})$; this has similar activities to C3b, and binds factor B (fB) in the presence of Mg^{2+} . Factor D (fD) a plasma serine protease, cleaves fB to form Bb and generate the fluid phase C3 convertase $\text{C3}(\text{H}_2\text{O})\text{Bb}$. Properdin stabilises the C3 convertase and extends the lifetime

of the enzyme; enabling C3b molecules to bind onto foreign cells to form the C5 convertase, acting as a receptor for C5.

All these pathways converge on the terminal pathway. C5b fragments bound to C3b in the C5 convertase bind another plasma protein, C6, triggering stabilisation and binding of C7, causing the release of the complex to the fluid phase. The C5b67 complex binds membranes through a hydrophobic site; subsequent binding of C8 and multiple C9 molecules leads to the formation of MAC and the lysis of the target cell.

1.3.3 Complement regulation, dysregulation and deficiencies

The complement system is under tight regulation by many plasma and membrane-bound regulatory proteins acting across the pathways and preventing unnecessary activation and inflammation (Rodriguez de Cordoba *et al.*, 2012). Initiation of the classical pathway is controlled by the C1 inhibitor (C1inh), which binds to the C1 complex, removes C1r and C1s preventing cascade initiation. The fluid phase regulators Factor I (fI) and Factor H (fH) inactivate and break up the convertase enzymes in both the classical and alternative pathways. On cell surfaces, decay-accelerating factor (DAF; CD55) speeds up the decay of the convertases and membrane cofactor protein (MCP), acts as a cofactor for fI to bind and irreversibly inactivate the convertases. Complement receptor 1 (CR1) also uses fI to trigger the dissociation and decay of the convertases. In the alternative pathway, properdin stabilises the C3 convertase, preventing spontaneous decay and the effects of fH, DAF and CR1. The terminal pathway is controlled by fluid-phase factors such as vitronectin and clusterin with the lytic MAC complex controlled by CD59 on the membrane which blocks the incorporation of C9 into the forming MAC

Dysregulation of the complement system is a feature in many autoimmune diseases. Deficiencies in C1, C4 and C2 associate with increased susceptibility to immune complex diseases such as systemic lupus erythematosus (SLE) (Leffler *et al.*, 2014). Deficiency of C3, the central component of the complement system, or secondary C3 deficiencies as a consequence of fI and fH deficiency, causing insufficient opsonisation of bacterial pathogens, increasing the risk of reoccurring infections (Heesterbeek *et al.*, 2018). Terminal pathway deficiencies associate with an increase in susceptibility to *Neisseria* infection (Lewis and Ram, 2014).

1.4 Synaptic pruning in AD

1.4.1 Synapses

Background

Synapses are the connection point for neuron communication and are critical for signal transmission across the CNS. Neuronal loss is a prominent feature of neurodegenerative diseases, especially in the later stages of disease; however, the loss of synapses is one of the earliest detectable pathological changes (Scheff *et al.*, 2014). Synapses are susceptible to excessive pruning and this is a significant component in the pathology of AD. Indeed, synaptic loss is the best correlator with AD progression and severity. Reduced synaptic density is associated with amyloid deposition and occurs several years before the classical neuropathological hallmarks (Colom-Cadena *et al.*, 2020). Synaptic plasticity provides resilience against cognitive deterioration and is a potential target for the modulation of neurodegeneration (Boros *et al.*, 2017). In AD mouse models, synaptic and dendritic markers, although are reduced with ageing, in some regions these markers increase in the brain, through to be a compensatory mechanism to synaptic deficit and an attempt to repair itself (Baazaoui *et al.*, 2017). Figure 1.9 provides an illustration of excessive synapse elimination, indicated through the loss of dendritic spines and activation of glia.

Synaptic loss in AD

The loss of synapses associates with activation of the immune system and specifically the complement system and is a prominent feature in the pathology of AD (Morgan, 2018). Biomarker studies reinforce the role of the complement system in the AD brain, supported by immunohistochemistry evidence for deposition of C1q, C3, C4 and TCC (terminal pathway marker) around areas of pathology such as amyloid plaques (Eikelenboom and Veerhuis, 1996; Hakobyan *et al.*, 2016). GWAS studies also support the role of complement in AD; recent genetic hits include genes encoding complement proteins clusterin (*CLU*) and CR1 (*Cr1*) (Harold *et al.*, 2009). Microglial activation in the AD brain is important for the clearance of amyloid plaques. Microglia express complement receptor 3 (CR3) which is necessary for the removal of soluble A β . Several studies note that the absence of CR3, or blockage with small molecules such as Leukadherin 1, increases A β degradation, reducing the burden amyloid deposition (Czirr *et al.*, 2017).

Most of the supporting evidence of complement associating with AD pathology are from post-mortem studies that reflect end-stage disease. Therefore, to explore the roles of complement in early stages of the disease, AD animal models are necessary.

Synaptic loss in AD mouse models

Animal models of AD recapitulate features of the pathology, including synaptic loss (Sri *et al.*, 2019). In Tg2576 AD mice show age associated reductions in dendritic spine density on CA1 neurons in the hippocampus and occur prior to the amyloid plaque deposition (Lanz *et al.*, 2003; Spires *et al.*, 2005). Similar observations are reported in the 3xTg-AD mouse model with a reduction in dendritic spine coverage (Bittner *et al.*, 2010). Spine loss is also a feature in the amyloid knock-in models with a reduction in spine density and impaired synaptic function reported in the hippocampus (Zhang *et al.*, 2015). Dendritic spines, in AD mouse models, are also found to reduce in times of short term stress, highlighting the vulnerability of these structures (Baglietto-Vargas *et al.*, 2016).

1.4.2 Phagocytosis and link to synaptic elimination

Phagocytosis, a process undertaken by specialised cells (macrophages, neutrophils, monocytes, dendritic cells and osteoclasts), is responsible for the removal of microorganisms and other targets as part of the innate and adaptive immune response. Phagocytosis is separated into (i) the detection of the target, (ii) internalisation of the target, (iii) phagosome maturation and digestion. Particles are internalised into the phagosome, which then fuse with lysosomes and trigger the cargo to be degraded (Uribe-Querol and Rosales, 2020). Receptors mediate the recognition of target particles by phagocytes and subsequently initiate signalling pathways that trigger phagocytosis (Freeman and Grinstein, 2014). Non-opsonic receptors directly identify distinct molecular patterns on the particle including C-type lectins, lectin-like recognition molecules and scavenger receptors. Opsonic receptors detect host-derived proteins that label target particles destined for phagocytosis and include antibodies, fibronectin, complement, lactadherin and mannose-binding lectin. Phagocytic receptors initiate signalling pathways to remodel actin cytoskeleton and membranes, creating the phagosome for internalisation of the target particle (Freeman and Grinstein, 2014). Complement receptors, CR1-CR4 bind deposited complement molecules that decorate

target cells. CR3 (CD11b/CD18) is the most efficient phagocytic complement receptor and binds iC3b on the target destined for phagocytosis (Helmy *et al.*, 2006).

Microglia, the brain's professional phagocytes, are crucial for the clearance of apoptotic/necrotic cells and actively remove proteins, including amyloid. During development of the CNS, neuronal circuits are remodelled through the engulfment of synapses and axons through proposed 'eat-me' tagged targets (Schafer *et al.*, 2012). Microglial activation is one of the key makers of neuroinflammation in the CNS. Whilst post-mortem evidence is indicative in highlighting the accumulation/ increased localisation around areas of pathology and altered microglial morphologies, the extent of microglial activation relies on more sensitive cell-based assays. Microglial cell lines, stem cell-derived microglia and primary microglial cultures in the literature are pivotal in the attempts to decipher the underlying mechanistic changes particularly related to phagocytosis (Galloway *et al.*, 2019). Assays such as flow cytometry, time-lapse microscopy for phagocytosis assays and the expression of phagocytic markers are some of the most useful techniques that have enabled the identification of microglia activation to be crucial in the modulation of synaptic networks.

Synaptic tagging

In the developing CNS, phagocytosis is essential for the refinement of the neuronal networks whereby unwanted synapses are removed in course to aid in learning and memory (Schafer *et al.*, 2012). Microglia make physical contact with synapses, likely based on neuronal activity which reflect 'find me' signals directing phagocytosis to the relevant targets (Pocock and Kettenmann, 2007). In mice lacking the ADP receptor P2Y₁₂ or CX₃CR₁, the development of the visual cortex and hippocampal synaptic networks are severely impaired (Sipe *et al.*, 2016). The visual system provides an opportunity to assess synaptic pruning during the development of the CNS. Decreasing neuronal activity within the visual system (by visual deprivation), has aided the understanding of the 'find me' targets based on decreased neuronal activity (Schafer *et al.*, 2012). Recognition and microglial engulfment of synapses is reportedly linked to the activation of the complement system, primarily components of the classical complement pathway. C1q and C3 are found to tag synapses destined for phagocytosis, and likely through complement receptor 3 (CR3), are crucial for proper network refinement (Stevens *et al.*, 2007; Schafer *et al.*, 2012; Shi *et al.*, 2015). Live- cell imaging has supported the

concept of microglial-synaptic contacts, however it is unclear whether the entire synapse is phagocytosed or, as current evidence indicates, just presynaptic elements (Weinhard *et al.*, 2018).

Recent GWAS studies have pinpointed a number of microglial/phagocytic genes implicated in AD such as APOE, CLU, INPP5D, CD33, PLCG2, SPI1, and FCER1G. Additionally, several GWAS genes such as GPC2, TREML2, SYK, GRN, SLC2A5, SAMSN1, PYDC1, HEXB, RRBP1, LYN, and BLNK, are below genome-wide significance threshold become upregulated when exposed to A β (Sierksma *et al.*, 2020). TREM2, necessary for the expression of the scavenger receptor CD36 and required for phagocytosis, when absent leads to a reduction in microglial A β phagocytosis and a reduced apoptotic uptake capacity (Kim *et al.*, 2017). TREM2, along with APOE4 (APOE is a ligand for TREM2), are two of the most significant genetic risk factors in AD with their functional activity linked to microglia. The genetic risk of AD functionally translates into different microglial pathway responses which indicates the role of genetic factors downstream of amyloid. Therefore genetic findings, along with the post-mortem studies, further emphasise the key role of microglia in driving the underlying AD pathology.

Microglial-mediated synaptic engulfment in AD and link to the complement system

Microglia in areas of the brain such as the cortex and hippocampus localise around plaques and trigger microglial-synaptic engulfment; phagocytic vesicles contain synaptic markers such as PSD95 and synaptophysin. Importantly, complement is a prominent feature in the process of microglial-synaptic elimination (Hong *et al.*, 2016; Shi *et al.*, 2017). C1q labels synapses destined for removal both pathologically in AD and developmentally in the CNS. In development, complement plays roles in the remodelling of neuronal circuits essential for proper formation and maturation, as exemplified in the pruning of synapses in the retinogeniculate system (Stevens *et al.*, 2007).

The role of complement in AD models is supported through back-crossing to complement deficiencies and analysing the effects on the development of pathology. Deficiency of C1q in the Tg2576 AD model reduces the burden of synaptic loss and glial activation; however, the abundance of amyloid remained unchanged (Fonseca *et al.*, 2004). C1q blocking antibodies also inhibited microglial activation and protection against synaptic elimination (Dejanovic *et al.*, 2018). Deficiency of C3 in APP/PS1 mice improved

cognitive function and reduced microglial activation and dysfunctional neurons near amyloid plaques (Shi *et al.*, 2017). However, in the J20 model, deficiency of C3 increased the burden of amyloid pathology (Maier *et al.*, 2008).

These studies indicate that C3, or subsequent downstream complement activation fragments, may have both damaging and protective roles in AD pathology. Increased C3a signalling, in response to amyloid plaques was shown to activate NfκB and disrupt neuronal morphology and function; blockage of C3aR restores these neuronal changes and rescue cognitive deficits in AD models (Lian *et al.*, 2015). Microglia phagocytic signalling in an activity-dependent manner involving CR3 and C3b/iC3b, is important for the postnatal development and remodelling of synapses in the retinogeniculate system (Schafer *et al.*, 2012). Fibrinogen, an blood based coagulation protein that binds to CR3 is found to induce microglial activation leading to excessive spine elimination in transgenic AD mouse models (Merlini *et al.*, 2019). Although not in an AD model, blockage of the complement system, targeted at C1q, also protects against microglial pruning of retinal ganglion cell dendrites in chronic models of glaucoma (Williams *et al.*, 2016). In the developing retina similar finding have also been reported with complement also involved in the targeting of newly born retinal ganglion cells which are eliminated through microglial phagocytosis. Despite all these studies, the exact mechanisms of synaptic remodelling in development and in disease remain unclear.

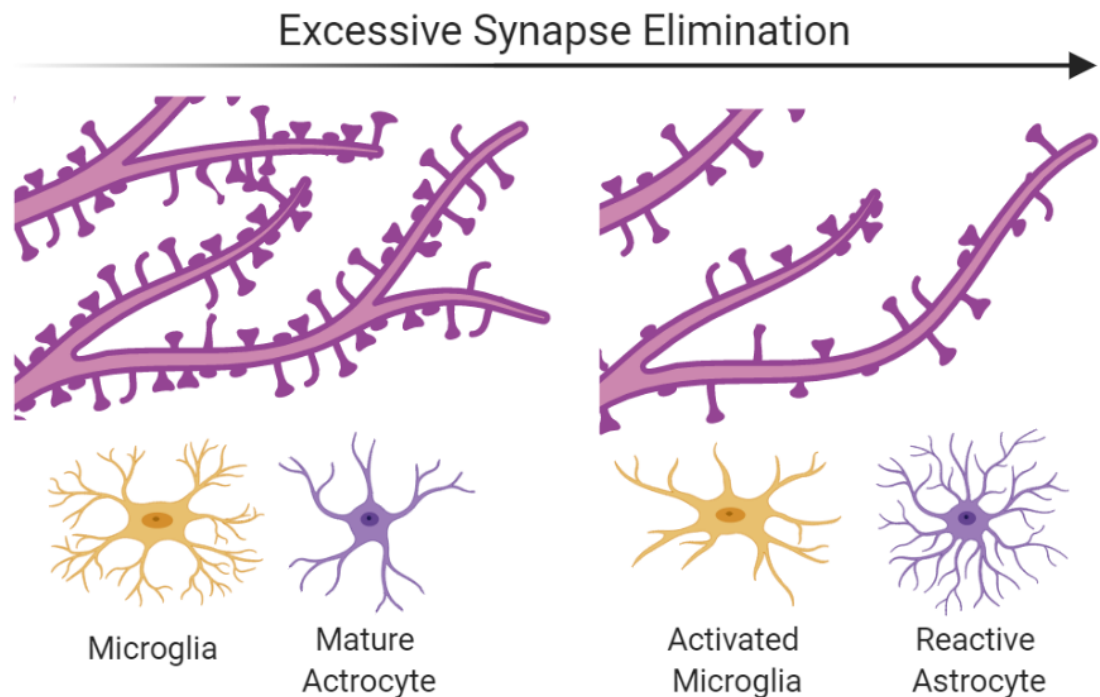


Figure 1.9 Schematic of excessive synapse elimination. Left: In healthy neurons, dendrites are decorated with dendritic spines, the site of the postsynaptic region. Spines vary in morphology, some display larger spine heads, reflecting stronger synaptic regions highlighting more stable and functionally relevant synapses. Microglia and astrocytes in the ‘healthy’ brain display morphology typical of surveying homeostatic glial cells. Right: In contrast, in conditions of neurodegeneration, neurons are substantially pruned for the dendritic spines. Microglia and astrocytes are activated and display proinflammatory phenotypes. Created with BioRender.

1.5 Systemic inflammation

Inflammation is crucial for the response to cellular damage. Acute inflammatory events aim to restore homeostasis and trigger an appropriate inflammatory response. However, with ageing and in certain diseases, infections become more common and lead to chronic bouts of dysregulated inflammation (Chovatiya and Medzhitov, 2014). Neuropathology underpinning dementia associates with co-morbidities, often linked to chronic inflammation (Cunningham and Hennessy, 2015).

Neuroinflammation associates with glial cell activation, an elevation of proinflammatory cytokines such as IL-1 β , IL-6 and TNF- α , and complement activation; together these lead to disruption of homeostasis in the CNS. Chronic inflammation both in periphery and in the brain which persists over long periods correlates with increased neurodegeneration by impairing protein clearance, increasing accumulation of APP and triggering of synaptic

elimination (Cunningham and Hennessy, 2015). Therefore, the role of chronic inflammation in the periphery to influence in the development of neurodegeneration and cognitive impairment needs addressing. Elevated levels of proinflammatory markers have been reported in the plasma of AD individuals, even before the onset of AD symptoms (Walker *et al.*, 2017; Keenan A. Walker *et al.*, 2019).

Infections

Bacterial and viral infections in the periphery influence the CNS and are associated with enhanced cognitive impairments in AD (Giridharan *et al.*, 2019). Although the blood-brain barrier (and blood-retina barrier) protect the CNS by blocking the entry of large pathogens, inflammation in the periphery can lead to CNS effects, including the triggering of inflammation within the CNS. Although the exact mechanisms are unclear. In cases where barriers are disrupted, leukocytes and peripheral immune cells infiltrate into the CNS (Varatharaj and Galea, 2017). Therefore, uncontrolled chronic inflammation in the periphery associates with neuroinflammation and detrimental effects in neurodegenerative diseases.

Bacterial infections contribute to the burden of neurodegeneration, and in the case of sepsis can trigger delirium and cognitive impairment (van Gool *et al.*, 2010). Animal models can recapitulate and mimic bacterial infections, commonly through the use of Gram-negative bacterial endotoxin, lipopolysaccharide (LPS). LPS triggers systemic inflammation which induces neuroinflammation, likely through microglial priming, and associates with chronic neurodegeneration and cognitive impairment (Qin *et al.*, 2007; Brown, 2019). Gram-negative infections are associated with the progression of AD and contribute to amyloid deposition. Recently, chronic infections driven through periodontal disease have been linked to low-grade systemic inflammation and increased risk of AD (Olsen and Singhrao, 2015). AD models administered with LPS showed increased activity of amyloid secretase, intraneuronal APP deposits, amyloid deposition and tau pathology (Sheng *et al.*, 2003; Kitazawa *et al.*, 2005; Lee *et al.*, 2008). In models involving chronic LPS exposure, inflammatory microglial phenotypes induced and maintained the upregulation of complement components such as C3 and complement receptors like CD11b which when ligated triggers microglial production of neurotoxic reactive oxygen species and neurodegeneration (Qin *et al.*, 2013; Bodea *et al.*, 2014). In support of the roles of complement, deficiency of C3 protected against the LPS-driven

inflammation (Bodea *et al.*, 2014). In a recent study, a single dose of LPS intraperitoneally injected in a mouse model of tauopathy (P301S) caused acute motor deficits and contributed to the acceleration of disease, including increased tau pathology (Torvell *et al.*, 2019). Peripheral LPS challenge is found to trigger microglial hyperactivity and age-associated microglial priming which induces exaggerated neuroinflammation (Henry *et al.*, 2009).

Viral infections, notably herpes simplex virus (HSV), through reactivation of latent infection associate with brain regions affected in the early stages of AD (Mangold and Szpara, 2019). Antibodies against viruses such as HSV are present in 80% of the population and asymptomatic latent reactivation is common (Sochocka *et al.*, 2017). In compromised individuals, such as those suffering from AD, viral reactivation triggers cascades of intracellular changes that associate with neurodegeneration. Viral DNA are also observed in senile plaques. The identification of viral DNA in the brain is more frequent in elderly individuals, thought to be due to compromised brain barriers and impaired immune responses (Wozniak *et al.*, 2009). Other viruses such as Cytomegalovirus (CMV) and Hepatitis C virus (HCV) can also infect neurons and enter latency. CMV seropositivity is associated with an increased risk of AD and cognitive impairment (Chiu *et al.*, 2014; Barnes *et al.*, 2015). In animal models, viral infections increase the inflammatory response, triggering increases in IL-1 β and type I interferon, which exacerbate pathology in AD mice (Krstic and Knuesel, 2013).

Other sources of inflammation

Although infections are one of the factors that can lead to peripheral inflammation, diet also impacts and can cause increasing proinflammatory markers. Obesity and a high-fat diet both associate with peripheral inflammation and the triggering of neuroinflammation accompanied by reduced neurotrophic agents such as BDNF, excessive synaptic pruning and cognitive deficits (Knight *et al.*, 2014; Miller and Spencer, 2014). Recently, changes associated with the gut-brain axis leading to dysbiosis were also linked to cognitive impairments (Ma *et al.*, 2019). In a healthy gut, the microbiome is essential in maintaining homeostasis and provides a protective barrier (Belkaid and Hand, 2014). Bacteria such as *Bifidobacteria* and *Lactobacillus* are beneficial to the host and are the main bacterial strains used in probiotic supplements (Fijan, 2014). The composition of the gut microbiome has a key role in modulating circulating inflammation (Grigg and

Sonnenberg, 2017). *Lactobacillus* probiotics have been successful in rescuing behaviours and neuroinflammation in mouse models (Lebovitz *et al.*, 2019). In situations of gut dysbiosis, induced either through diet, antibiotics or stress, changes to the microbiome can trigger long-term sustained chronic levels of proinflammatory cytokines which associates with dysfunction synaptic plasticity and impact on the progression of neurological diseases including AD (Saiyasit *et al.*, 2020). It is possible that modulation of the gut microbiome, potentially through probiotics, might offer a therapeutic option to decrease circulating peripheral inflammation with beneficial effects on AD pathology and disease progression.

1.6 Aims and hypothesis

This thesis explores changes in RGC dendritic structure and CA1 hippocampal dendritic spine density in mouse models related to AD. The work primarily utilises the DiOlistic neuron labelling technique accompanied by the reconstruction of individual RGC dendrites and of dendritic spines. These provide sensitive indicators of early stages of neurodegeneration in the retina and brain. In addition to AD mouse models, this thesis also explores the impact on RGCs and hippocampal spines of deficiencies in the complement system, inflammatory challenges, diet and probiotics.

The work in this thesis tests the hypotheses that RGC dendritic pruning is a robust readout to reflect changes in synaptic density in the hippocampus in mouse models of AD, complement deficiency, peripheral inflammation and dietary interventions.

This thesis focuses on five key aims presented as separate experimental chapters.

1. To assess whether RGC dendritic pruning is a consistent feature of AD mouse models (Tg2576, 3xTg-AD and APP^{NL-G-F}).
2. To determine the extent of synaptic loss (dendritic spines) on CA1 neurons in the hippocampus in AD mouse models (Tg2576, 3xTg-AD and APP^{NL-G-F}).
3. To establish whether complement deficiency impacts the fate of RGC dendrites and CA1 hippocampal dendritic spines.
4. To gauge whether systemic inflammation (bacterial and viral infections) triggers an exacerbation of RGC dendritic pruning and CA1 hippocampal spine loss in wildtype and AD mice (3xTg-AD).
5. To evaluate whether probiotic dietary supplementation offers neuronal protection against RGC dendritic pruning and CA1 hippocampal spine loss in AD mice (3xTg-AD).

Chapter 2. Methods

2.1 Animals

The use of animals was crucial for the acquisition of data and the completion of this thesis. Where possible, both the eyes and brain were analysed from individual animals to limit the number used in experiments. In all instances, the health and wellbeing of all animals were the priority. All protocols were conducted under the ethical guidelines at Cardiff University under the following project licences: PPL 30/3313, PPL 30/3038, PPL 30/3120, PF4167C0A, and P0EA855DA.

All animals in this study were group-housed where possible in standard environmentally enriched cages in a 12-hour light-dark cycle. Mice used for the analysis of the impact of viral infection and probiotic supplementation were housed pathogen-free in scintainer ventilated cages. All animals had unlimited access to standard chow food or high-fat diet as appropriate and water. All animals were frequently health checked; where necessary, additional health checks were included such as the monitoring of ageing and expected adverse effects of administered agents. In all instances, experiments required the use of fresh tissue samples, rather than fixed. Therefore, animals were transferred from the housing facility to the specific experimental rooms. All animals were health checked before transfer and moved under regulations in place at Cardiff University. This thesis analysed the following models: Tg2576 (gifted by Professor Mark Good), 3xTg-AD (The Jackson Laboratory), APP^{NL-G-F} (RIKEN, Japan), 3xTg-AD C3^{-/-} (crossed in house by Dr Tim Hughes), 3xTg-AD C6^{-/-} (crossed in house by Dr Tim Hughes), C1q^{-/-} (gifted by Professor Marina Botto through a collaboration with Professor B. Paul Morgan), C3^{-/-} (gifted by Professor Mike Carroll through a collaboration with Professor B. Paul Morgan), C3aR^{-/-} (gifted by Professor Craig Gerard through a collaboration with Professor B. Paul Morgan), TREM2^{-/-} (gifted by Professor Peter St. George Hyslop through a collaboration with Professor B. Paul Morgan) and C57BL/6 (in house colony). Table 1 provides further details on the animal models.

Table 1 Further details on the animal models used in this thesis.

Mouse Model	Genetic Background	Number of backcrosses	Breeding regimes	Genotyping methods	Primer sequences	Catalogue number	Original paper
Tg2576	Mixed	-	Heterozygous	Ear biopsy-PCR	1502: GTGGATAACCCCTCCCCAGCC TAGACCA 1503B: CTGACCACTCGACCAGGTTCTGGGT 1501: AGCGGCCAAAGCCTGGAGGGTGAACA (Hall <i>et al.</i> , 2016)	In house colony	(Hsiao <i>et al.</i> , 1996a)
3xTg	Mixed	-	Homozygous	Ear biopsy-PCR	https://www.jax.org/Protocol?stockNumber=004807&protocolID=6115 https://www.jax.org/Protocol?stockNumber=004807&protocolID=23370 Combined with test breeding to generate the complement crosses (c3 and C6) https://www.jax.org/Protocol?stockNumber=004807&protocolID=35216	34830-JAX	(Oddo <i>et al.</i> , 2003)
APP NLGF	B6/J	-	Homozygous	Ear biopsy-PCR	Exon 16 WT: ATCTCGAAGTGAAGATG WT: TGTAGATGAGAACTTAAC Exon 16 Mut: ATCTCGAAGTGAATCTA Lox P: CGTATAATGTATGCTATACGAAG	RBRC06344 RIKEN, Japan	(Saito <i>et al.</i> , 2014)
WT	B6/J	-	-	-	-	In house colony	-
3xTg C3 ^{-/-}	Mixed	Single Backcross	Homozygous	Ear biopsy-PCR	See above for 3xTG combined with C3 per below	In house colony	-
3xTg C6 ^{-/-}	Mixed	Single backcross	Homozygous	Ear biopsy-PCR	See above for 3xTG combined with C6 SNP per assay (Thermo)	In house colony	-
C1q ^{-/-}	B6/J	-	Homozygous	Ear biopsy-PCR	mC1qA/5': GGGCCTGTGATCCAGACAG mC1qIN/2': TAACCATTGCCTCCAGGATGG Neo3: GGGGATCGGCAATAAAAAGAC	Professor Marina Botto through a collaboration with Professor B. Paul Morgan	(Cook <i>et al.</i> , 2002)
C3 ^{-/-}	B6/J	-	Homozygous	Ear biopsy-PCR	Common oIMR1325: ATCTTGAGTGACCAAGCC Wild type oIMR1326: GGTTGACAGCTCTATGAAGG Mutant oIMR7415: GCCAGAGGCCACTTGTGTAG	Professor Mike Carroll through a collaboration with Professor B. Paul Morgan Jackson Laboratory B6;129S4-C3tm1Crr/J Stock No: 003641	(Cook <i>et al.</i> , 2002)
C3aR ^{-/-}	B6/J	-	Homozygous	Ear biopsy-PCR	Forward: GCTTCCTGGTGCCGTTTTTC Reverse: GTTTTGTTCCGAGACTTGGTGAA	Professor Craig Gerard through a collaboration with Professor B. Paul Morgan Jackson Laboratory C.129S4-C3ar1tm1Cge/J Stock No: 005712	(Humbles <i>et al.</i> , 2000)
Trem2 ^{-/-}	B6/J	-	Homozygous	Ear biopsy-PCR	Forward: CAGTGCAGAGTCTCCGAGG Reverse: CACAGGATGAAACCTGCCTGG	Gifted by Professor Peter St. George Hyslop through a collaboration with Professor B. Paul Morgan	-

2.2 DiOlistic Labelling

Morphological labelling of neurons typically relies on the expression of fluorescent markers. However, these techniques are problematic when assessing degenerating tissue. Therefore, this thesis primarily used DiOlistic labelling, a method that relies on membrane dye diffusion. DiOlistic labelling is a robust technique for evaluating neuronal morphology in the retina and brain (Gan *et al.*, 2000; Kima *et al.*, 2007; Staffend and Meisel, 2011; Cheng *et al.*, 2014). The technique requires expert and speedy dissection of fresh tissue samples to minimise the impact of tissue damage and degeneration. In brief, tungsten particles coated with lipophilic dyes are pressure-blasted onto retinal explants and hippocampal slices. Dyes diffuse in membranes and reveal randomly labelled RGCs and hippocampal neurons capable of identifying structural morphology. Labelled neurons are confocally imaged and reconstructed for quantitative analysis. These provide a sensitive readout for dendritic arborisation and dendritic spine coverage in the retina and hippocampus respectively. Figure 2.1 provides an overview of the DiOlistic experimental setup.

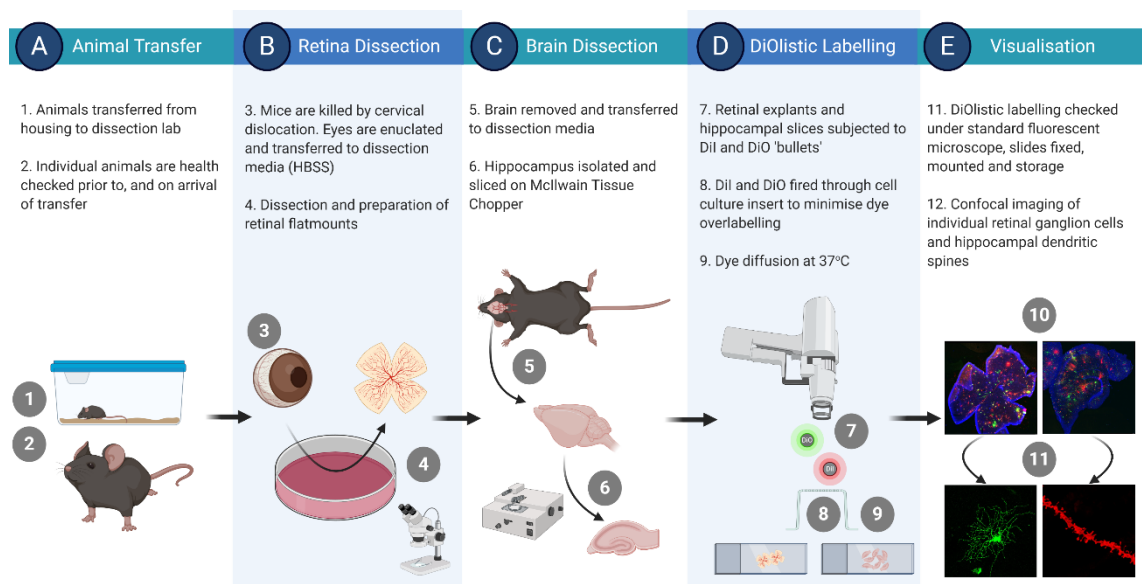


Figure 2.1 Overview of DiOlistic labelling. (A) Animals are transferred to the dissection lab following the necessary health checks. (B) Mice are killed by cervical dislocation with the eyes enucleated with the retinas dissected and flat mounted, ganglion cell layer up. (C) The hippocampus is then isolated from the mouse brain and sliced on a McIlwain tissue chopper. (D) Both retinal explants and hippocampal slices are subjected to DiOlistic labelling with tungsten coated with lipophilic dyes. (E) After dyes diffuse along the neuronal membranes, both RGCs and hippocampal dendritic spines are visualised and confocally imaged. Illustration created in BioRender.

2.2.1 Retina and hippocampus dissection

Mice were killed by cervical dislocation followed by the removal of the eyes and brains into chilled (4°C) in HBSS (Hank's balanced salt solution; ThermoFisher) dissection medium. For isolation of the retina, eyes were needle punctured at the limbus to enable the removal of the cornea, lens, sclera and vitreous with the retina orientated GCL up. For isolation of the hippocampus, brains were sagittally cut and the hippocampus removed. A McIlwain tissue chopper, set at 200 µm, sliced the hippocampus into consistent slices, approximately 10-15 per hippocampal hemisphere. Tissue for storage was fixed in 4% paraformaldehyde (PFA; Sigma). Retinal explants and hippocampal slices were transferred to separate histology slides, positioned centrally and allocated for DiOlistic labelling. Optimum dye diffusion required fresh tissue samples; therefore, dissection time was critical. The total time from tissue removal to DiOlistic labelling was less than 10 minutes per animal. Figure 2.2 provides a summary of the dissection.

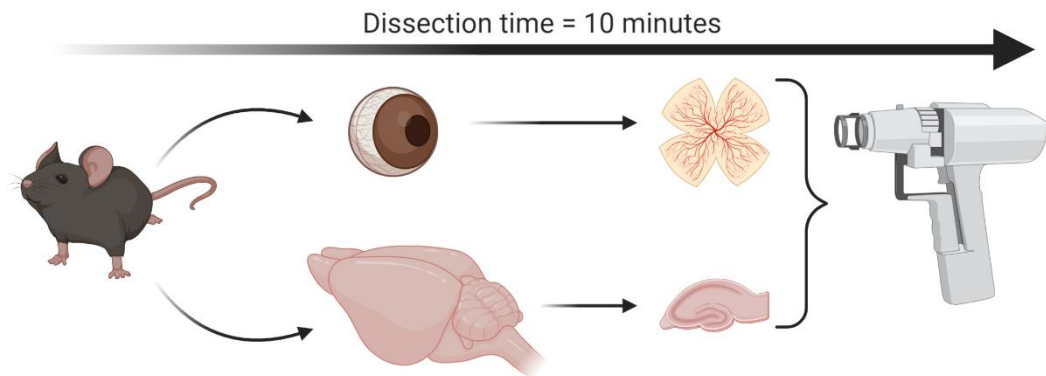


Figure 2.2 Overview of tissue dissection. The total time from eye and brain dissection to the DiOlistic labelling station per mouse was no greater than 10 minutes. Created with BioRender.

2.2.2 DiOlistic Preparation

DiOlistic labelling relies on the preparation of tungsten particles coated in fluorescent lipophilic dyes, with the relative amount of label determining, in part, the extent of neuronal labelling. Typically, 2 mg of 1,1'-Diocadecyl-3,3,3',3'-Tetramethylindocarbocyanine Perchlorate (DiI, Life Technologies) and 4 mg of 3,3'-Diocadecloxacarbocyanine Perchlorate (DiO, Life Technologies) were separately dissolved in 200 μ l of methylene chloride (Sigma) and applied dropwise to a glass slide covered in an even distribution of 40 mg of 1.7 μ m diameter tungsten particles (BioRad). Methylene chloride evaporated enabling the drying of the dyes onto the tungsten particles. To ensure efficient multicolour labelling, dye-coated particles were mixed after drying. Coated tungsten particles were then funnelled into 30 cm of Ethylene tetrafluoroethylene (ETFE) tubing (BioRad) ensuring an even distribution in the tubing. Dye covered ETFE 'bullets' were cut at 1.2 cm and stored in the dark at room temperature until use. Typically, the creation of the 'bullets' was ad hoc; however, excess was stored and used for up to two months.

2.2.3 DiOlistic labelling

DiOlistic 'bullets' were loaded into the Helios gene gun (BioRad) and primed at 100 psi. Histology slides containing the retinal explants and hippocampal slices were placed beneath the gene gun. DiOlistic bullets were fired at a pressure of 100-120 psi for retinal explants and 80-100 psi for hippocampal slices through a BD falcon cell culture insert with a pore size of 3 μ m (BD Biosciences) to minimise dye aggregation. These pressures provided the optimal degree of labelling; heavier coated bullets and/or higher pressure resulted in over-labelling of the tissue, while lightly coated bullets and/or low pressure resulted in under labelling. It was noted that hippocampal slices required a lower pressure in comparison to retinal explants. The distance between the tissue samples and the gene gun, including the cell culture insert was approximately 10 cm. Post-labelling, tissue samples were transferred on the histology slides to 10 cm culture dishes and submerged in Neurobasal-A medium (Life Technologies). Care was taken to prevent flipping of the tissue, especially hippocampal slices, as it was not possible to image flipped tissue slices. Dyes were allowed to diffuse along randomly labelled neurons in the tissue by incubating at 37°C with 5% CO₂ for 25 minutes. Labelling was checked briefly under a standard

fluorescence microscope (Zeiss) to ensure sufficient labelling. Tissues were fixed in 4% PFA for at least 30 minutes, under-fixation was associated with dye leakage whereas over fixation did not impede dye imaging once labelled. Both retinal explants and hippocampal slices were nuclear stained with Hoechst 33342 (1:1000, ThermoFisher) for 10 minutes and coverslipped using the FluorSave (MilliporeSigma) mounting agent. Slides were stored in the dark at 4°C to prevent further dye quenching and confocally imaged the next day for optimal acquisition of morphology.

2.2.4 Confocal Imaging

All images in this thesis were collected using a Leica SP8 lightning confocal microscope. Imaging setups consisted of three channels, Hoechst, DiO and DiI at the necessary wavelengths. Figure 2.3 provides the spectral wavelengths for the imaging Hoechst, DiI and DiO fluorescence.

It was optimal to collect RGC images before dendritic spines due to the vulnerability of RGC staining to increased dye leakage. Each retina was screened and marked for RGCs on the LASX software, typically marking 8-10 cells per retina. Due to the variation in the labelling, some retinas yielded higher cell densities whereas others revealed fewer cells. Neuronal morphology and the relative position in the retina i.e. in the GCL, a typical dendritic field and a clear axon projecting towards the optic nerve head, differentiated RGCs from other cell types. Overlapping dendritic fields that prevented single-cell delineation were excluded from imaging. RGC dendritic fields were collected using the HC PL APO CS2 20x/0.75 dry objective under the resonant imaging set up with a scan speed of 8,000 Hz. Photomultiplier tube (PMT) detector collected Hoechst 33342 and DiO fluorescence signal with gains set at 550 and laser intensity up to 30%, dependent on the signal intensity. A HyD detector collected DiI fluorescence signal with gain set at 10 (minimal) and laser intensity up to 1%. All RGC images were 1024 x 1024 with a pixel size of 0.455 μm and a z-axis interval of 1 μm . Line averaging improved signal to noise and was typically at 2-4. Each image, including the full dendritic field depth into the IPL, required typically 30 seconds of acquisition. A balance between resolution and scan time required compromise as typically, image acquisition for both retinas from a mouse took 30 minutes. Therefore, a cohort of 10 animals required ~5 hours of confocal time for RGC analysis alone.

Following imaging of RGCs, hippocampal slices were imaged for CA1 hippocampal spines of apical dendrites. Each mouse generated up to 15 hippocampal slices, from each of which typically 8 neurons were imaged. Hippocampal slices were more susceptible to over labelling; therefore, it was beneficial to under label during the DiOlistic labelling. Dendritic spines were imaged on CA1 apical dendrites and selected based on the clear identification of dendritic segments originating from CA1 neurons and minimal overlapping of other neurons. DiI labelling was analysed at the necessary wavelengths using the HC PL APO CS2 63x/1.40 oil objective in the resonant imaging set up with a scan speed of 8,000 Hz. A HyD detector collected DiI fluorescence signal with gain set at 10 (minimal) and laser intensity up to 1%. All spines images were 1024 x 1024 with a pixel size of 0.144 μm and a z-axis interval of 0.184 μm . Line averaging improved signal to noise and typically set at 2-4. All spine images were lightning deconvolved using default settings to enhance the distinction of spine morphologies. Typically, image scanning for a single dendritic segment took 1 minute of acquisition, with a balance achieved for resolution and scan speed. A total image session for all stages per mouse totalled 20 minutes, which corresponded in a cohort of 10 animals to 3.5 hours of spine confocal imaging.

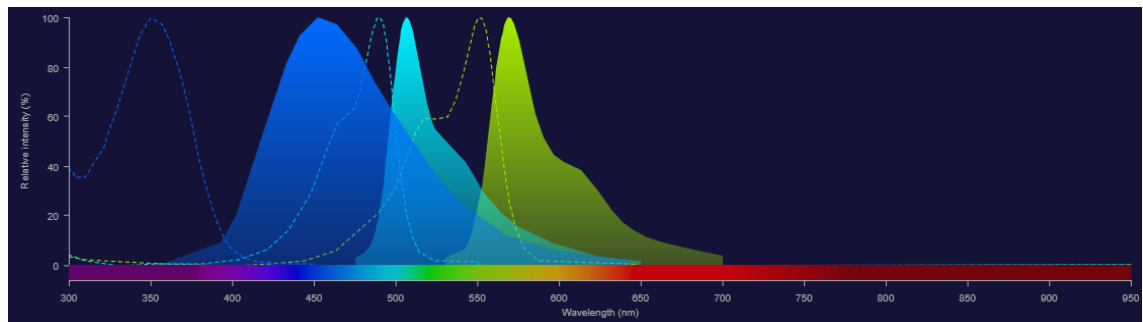


Figure 2.3 DiOlistic fluorescent wavelengths for confocal imaging. Dashed line corresponds to excitation, solid line corresponds to emission spectrum. From left to right: Hoechst 33342, DiO and DiI. Created with ThermoFisher Fluorescence SpectraViewer.

2.3 RGC dendritic reconstruction and data acquisition

2.3.1 Dendritic reconstruction

RGC dendritic morphology across the different subtypes is reflected by the diversity of the dendritic arborisation (Figure 2.4). Therefore, it is important to sample a wide range of RGCs from each group in order to account for the variation in complexity. Measurement of the dendritic arborisation is a reliable measure for early stages of neurodegeneration, with typically a reduction in complexity indicative of pathological conditions. Dendritic reconstruction is achievable in many programs; however, these often rely on individual bias, compression of images into 2D or loss of hierarchical dendrite branching and require a lot of time. ImageJ, routinely used with tracing plugins takes around 20 minutes of manual tracing per cell, which translates to many days of continued tracing for entire groups. Newer, more advanced technologies are available, including Imaris (Bitplane) featuring FilamentTracer, which rapidly delivers dendrite reconstructions and improved data output compared to other commonly used alternatives.

RGC dendritic fields were reconstructed using an optimised protocol within Imaris (v9.3.1, Bitplane) (Figure 2.5). Raw confocal images were imported into Imaris and converted to the native Imaris file format (Figure 2.5A). The channel of interest, i.e. the DiI or DiO labelled channel, was selected (Figure 2.5B) and a 'region of interest' (ROI) was positioned around the dendritic field (Figure 2.5C). Absence of an ROI prompted tracing of the entire image regardless of adjacent cells. Based on the relative thresholding, Imaris determined the cell body and a starting point for dendritic tracing (Figure 2.5D). In the calculations, 'seed points' are positioned on potential dendrites (Figure 2.5E). It was advantageous to remove the seed points near the cell body approximately 10-30 μm radius to improve tracing capability proximal to the cell. Using measures such as dendrite diameter, Imaris calculates the relative thickness of the dendrites to determine dendritic hierarchy and branching patterns (Figure 2.5F). These stages ultimately lead to the dendrite tracing of an individual RGC (Figure 2.5G), with the data exported for analysis. In all stages, default and relative automatic thresholding offered the best tracing capability. However, in weakly labelled images or overlapping of adjacent cells, manual adjustments were required. For a 'clean' image, in absence of dye debris and adjacent

overlapping cells, tracing an entire dendritic field required 2 minutes, 10-fold quicker than manual techniques.

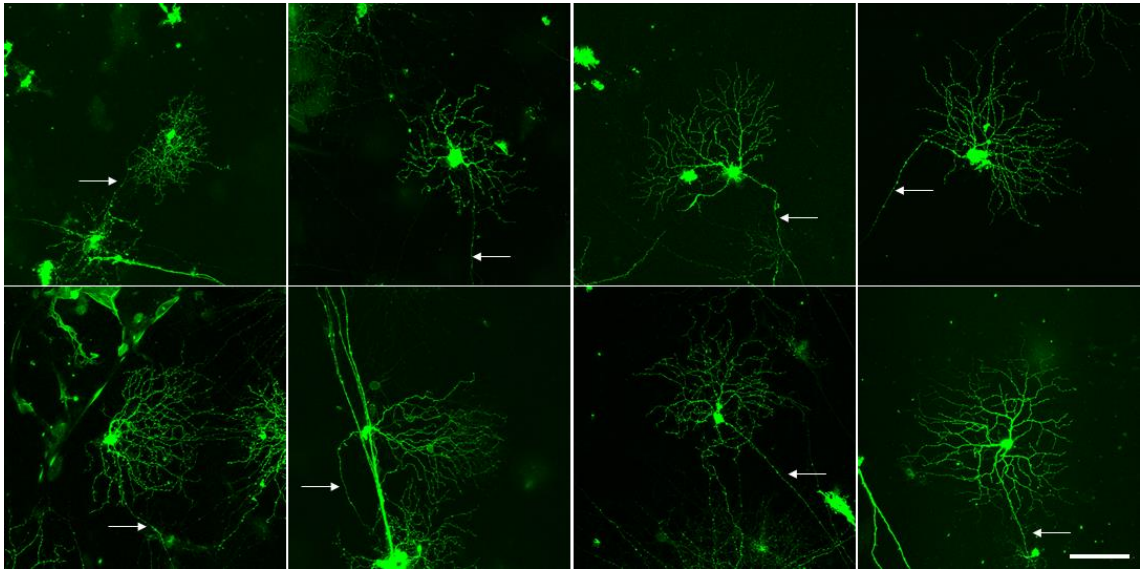


Figure 2.4 RGC dendritic morphology is highly variable and is detected through the DiOlistic labelling process. Arrows indicate RGC axon. Scale bar 50 μ m

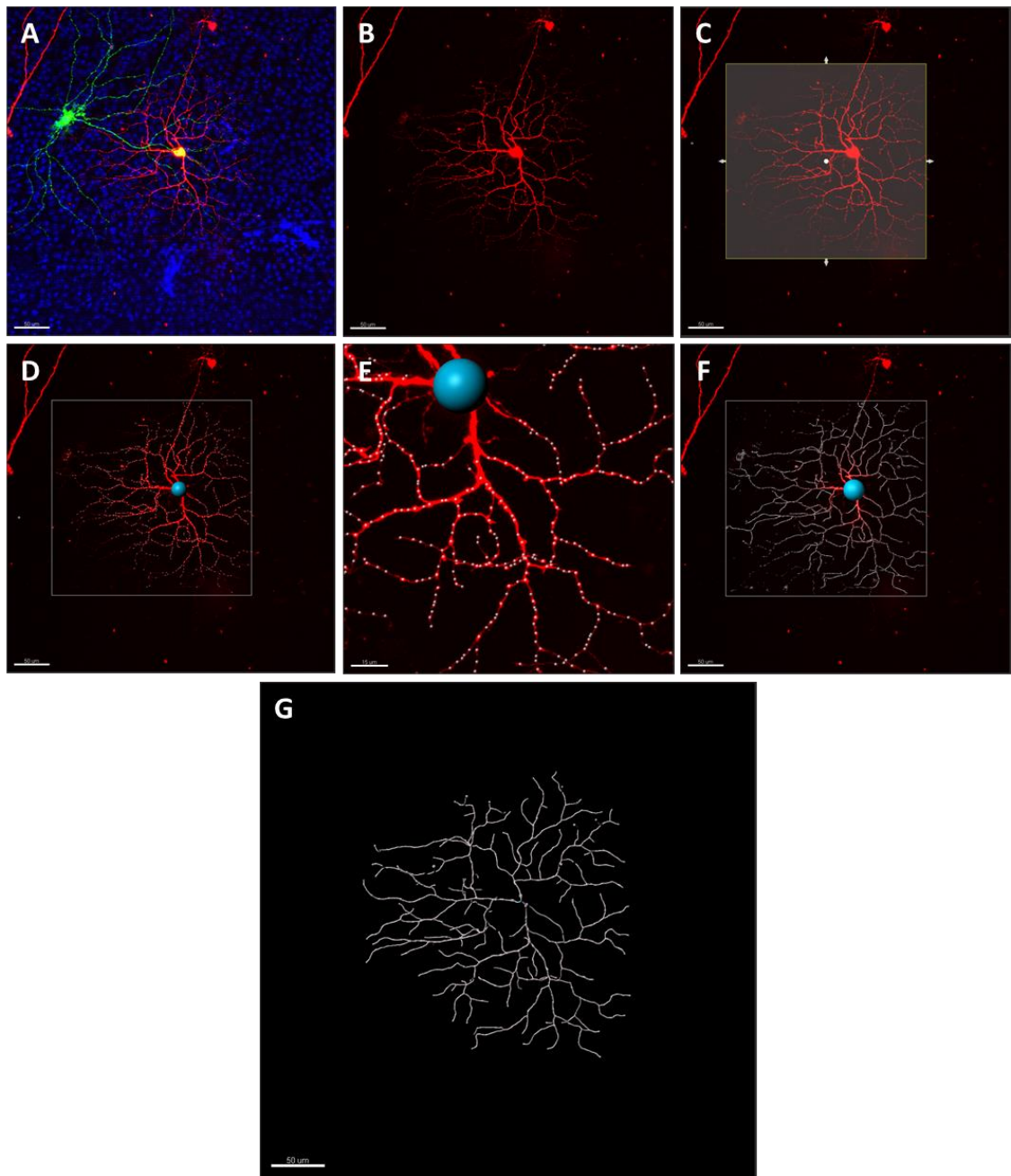


Figure 2.5 Reconstruction of RGC dendritic complexity using Imaris Filament Tracer module. (A) Raw confocal RGC images are imported into Imaris. (B) Channel of interest is selected, in this example the red channel. (C) A region of interest is positioned around the dendritic field. If the region was not specified Imaris would attempt to trace the entire image. (D) Imaris calculates the cell body based on thresholding. (E) Dendrites are detected and labelled with ‘seed points’ to indicate areas used in the calculation of dendritic branching. (F) In the calculation of the dendritic branching, Imaris calculates relative diameters of dendrites. (G) This process results in the 3D reconstruction of the dendritic arborisation of an individual RGC. Scale bar 50 μm for A-D and F-G, scale bar 15 μm in E.

2.3.2 Sholl analysis and associated parameters

Dendritic arborisation is generally assessed by Sholl analysis (Sholl, 1953), an appropriate technique for demonstrating the morphology of neurons both in the retina and brain (Figure 2.6). A shift in the Sholl profile indicates changes in the overall dendritic architecture. Imaris automatically determines the Sholl analysis for each reconstruction created with FilamentTracer and expresses the morphology in 3D; information usually lost in other programs.

Sholl analysis is a measure of dendritic complexity as a function of distance from the cell body. A Sholl curve is generated by quantification of the number of dendrites that intersect set interval concentric rings (10 μm for RGCs) (Figure 2.6A). An RGC with more dendrites, larger and more complex dendritic field is mirrored by an increase in the number of Sholl intersections. Typical wildtype RGC from an adult mouse exhibits a peak Sholl curve at around 60 μm from the cell body with around 20 intersections. Until the peak, the dendrites typically correspond to primary-quaternary branches. The Sholl curve then steadily declines after the peak. A shift in the Sholl profile shows alterations to the dendritic arborisation, often corresponding to dendritic pruning (Figure 2.6B). In models of neurodegeneration, dendritic complexity is decreased, which is reflected by a smaller peak of the Sholl curve and fewer total number of intersections for the entire Sholl curve. Dendritic loss generally appears in distal dendrites around and after the peak, whilst maintaining the number of proximal dendrites.

Besides the Sholl curve, other parameters provide further details on the extent of dendritic arborisation. The area under the Sholl curve (AUC) is a measure of overall dendritic complexity. AUC takes into account the total number of Sholl intersections and is an effective representation of overall variations in the Sholl curve. In models of excessive dendritic pruning, AUC is reduced. The maximum number of Sholl intersections/ peak of the Sholl, provide a reflection on the point of the highest complexity. In models of substantial dendritic loss, it reduces the peak of the Sholl curve. Another method useful in assessing dendritic complexity is the overall length of all the reconstructed dendrites, in models of dendritic loss, this measure is reduced.

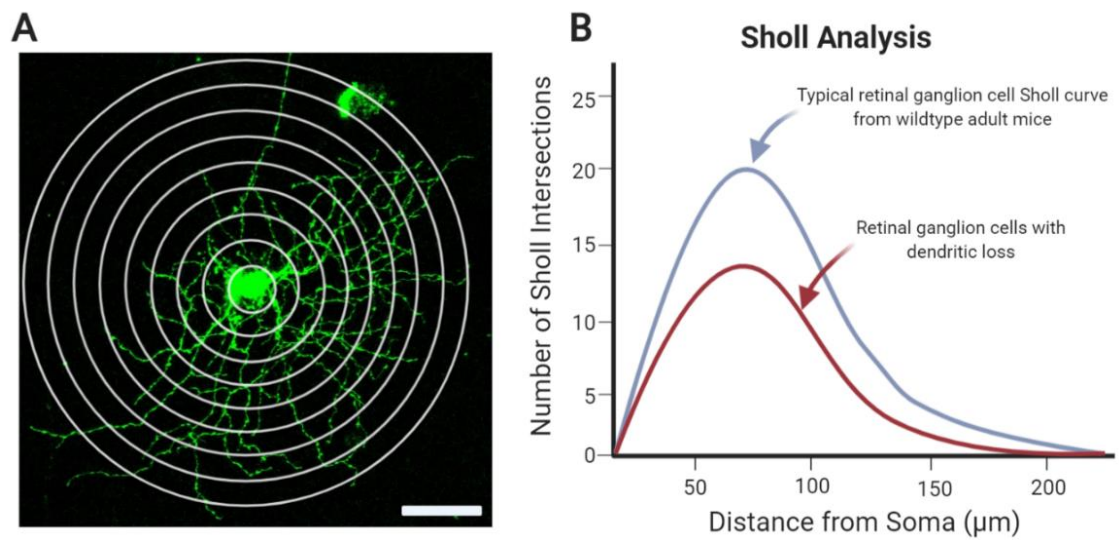


Figure 2.6 Sholl analysis of RGC dendritic arborisation. (A) Typical example of an RGC that have been imaged following DiOlistic labelling to reveal the dendritic arborisation. In the process of performing the Sholl analysis, Imaris calculates the number of dendrites in 3D on the original confocal raw image and records the number of dendrites that intersect concentric circles at set intervals, 10 μm for RGCs. Scale bar 100 μm (B) Typical example Sholl profile representing the number of intersections at the set intervals from the cell body. Adult wildtype mice (blue line), on average, display RGCs with highest complexity (peak of the Sholl curve) at around 60 μm from the cell body and around 20 intersections. After the peak of the curve, the number of intersections gradually decrease further away from the cell body. Dendritic loss (red line), even in cases of subtle pruning, is detected by a shift in the Sholl curve with fewer intersections compared to the wildtype levels. In RGCs with substantial dendritic loss, the peak of the Sholl curve is typically reduced to around 10-15 followed by fewer intersections after the peak.

2.3.3 Receptive field classification

As previously discussed, RGCs extend their dendrites into the IPL; those terminating in sublamina b close to the GCL are termed ON-centre, whereas dendrites terminating in sublamina a are termed OFF-centre. In contrast, RGCs with dendrites laminating in both layers are termed ON-OFF centre (Wyk *et al.*, 2009; Williams *et al.*, 2010; Baden *et al.*, 2016). The prevalence of ON and OFF RGCs are comparable, whereas ON-OFF RGCs are less frequent. This thesis only analysed ON and OFF RGCs. An RGC is categorised as ON centre when the dendrites start in close proximity to the cell body often within a few micrometres in the dendritic field (Figure 2.7A). In contrast, OFF-centre RGCs laminate further away and are distinguishable with a substantial gap (10-20 μm) between the end of the cell body and the start of dendritic branching (Figure 2.7B). It is occasionally challenging to establish dendritic depth due to retinal folds occurring during dissection or compression of the retinal explant.

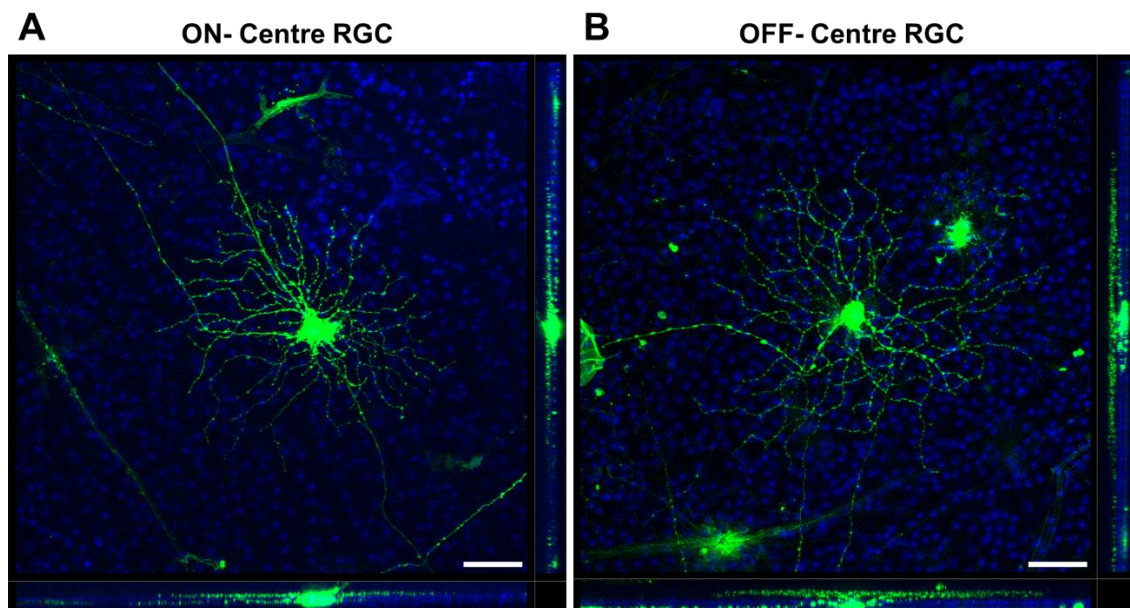


Figure 2.7 RGC receptive field classification. (A) Typical example of an RGC that is classified as ON-centre. Dendrites project in the sublamina b of the IPL and occur close to the cell body. (B) Typical example of a RGC classified as OFF-centre. Dendrites project into the sublamina b of the IPL with a distinctive gap between the cell body and the start of dendritic lamination. Scale bar 100 μm . Abbreviations: IPL, inner plexiform layer.

2.3.4 Nuclei counts in the ganglion cell layer

In models of retinal degeneration, the loss of nuclei in the GCL (reduced RGCs) is described. Although in models of AD, cell loss is not an expected feature, this thesis quantified the number of nuclei in the GCL using Hoechst 33342 labelling on the DiOlistic images. In Imaris, nuclei were enumerated using the Spots function to obtain an average GCL nuclei count per animal. In all conditions the parameters were kept consistent and based on relative automatic thresholding in Imaris.

2.4 Dendritic spine reconstruction and data acquisition

2.4.1 Dendritic spine reconstruction

Quantification of dendritic spines provides the number of postsynaptic sites on dendrites. Many approaches to quantify dendritic spines rely on manual counting, which is time-consuming and involves considerable human judgment. Imaris, using the FilamentTracer module, evaluates the density of dendritic spines and runs an inbuilt MATLAB Spine Classifier extension to determine spine morphology (Figure 2.8) (Basu *et al.*, 2018; M *et al.*, 2018).

Raw, lightning deconvolved dendritic spine images were imported into Imaris with several ROI positioned along dendritic segments typically stretching 30 μm (Figure 2.8A-B). Imaris determines potential starting points to establish the base dendrite by relative thresholding (Figure 2.8C). At this stage, several possible starting positions are proposed with the desired option manually selected. In comparison to RGCs which are decorated with ‘seed points’ along the dendrites, the base dendrites for spine analysis are manually controlled with seed points located at the end of the segment (highlighted by the arrows) (Figure 2.8D). Imaris determines the relative diameters and traces the base dendrite (Figure 2.8E-F), and automatically positions spine seed points decorating the traced dendrite (Figure 2.8G). Imaris calculates the relative diameters and sizes of the dendritic spines from the positioned spine seed points, (Figure 2.8H), and reconstructs dendritic spines (Figure 2.8I). Spine seed points with spine heads greater than 0.45 μm provided the optimum determination of dendritic spines. For all data, spine density is displayed per 10 μm of dendrite.

2.4.2 Dendritic spine classification

Following the reconstruction of all the dendritic spines on the traced dendritic segment, spines were morphologically classified Using the Spine Classifier MATLAB extension based on parameters associated to size of spine heads and spine necks (Figure 2.8J). Several rounds of optimisation were performed that matched manual recording. Stubby spines were best classified when spine length was less than 0.8 μm , and mushroom spines when the length of the spine was less than 3 μm , and the spine head was larger than the

spine neck. Any spines that were greater than 3 μm were classified as filopodia, these were very infrequent. The remaining spines, featuring a long spine neck and a relatively small spine head were classified as thin spines. All criteria were consistent throughout the analysis for all groups. An overview of the various spine types is represented in Figure 2.9.

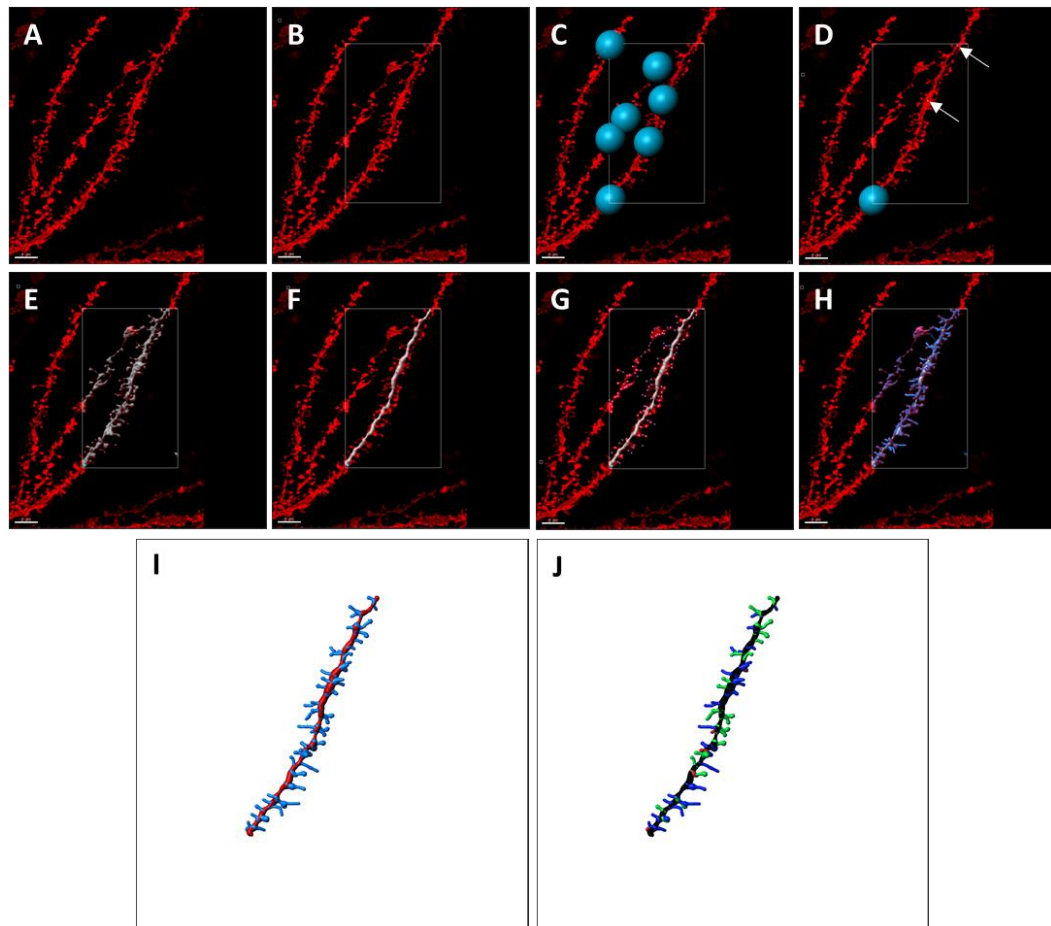


Figure 2.8 Reconstruction of hippocampal dendritic spines using Imaris Filament Tracer module and Spine Classifier. (A) Raw confocal hippocampal dendritic image imported into Imaris, image is magnified on a dendritic segment for reconstruction. (B) A region of interest is positioned around the dendritic segment. If the region was not specified Imaris would attempt to trace the entire image. (C) Imaris calculates starting points. (D) A single starting point is selected and 'seed points' are positioned on the dendritic segment, indicated by the arrows. (E) Imaris determines the diameter of the dendrites used for tracing. (F) The dendrite is traced. (G) 'Seed points' are positions on regions Imaris calculates are related to dendritic spine protrusions. Note in the determination of spine coverage seed points at a distance away from the traced dendrite are temporary calculations used to determine the position of dendritic spines. (H) Imaris determines the relative sizes and diameters of the dendritic spines, crucial for spine classification. (I) Traced dendritic segment with the associated dendritic spine coverage. (J) Dendritic spines are classified using the MATLAB Spine Classifier extension into stubby (red), mushroom (green) and thin (blue) spines. Scale bar 5 μm .

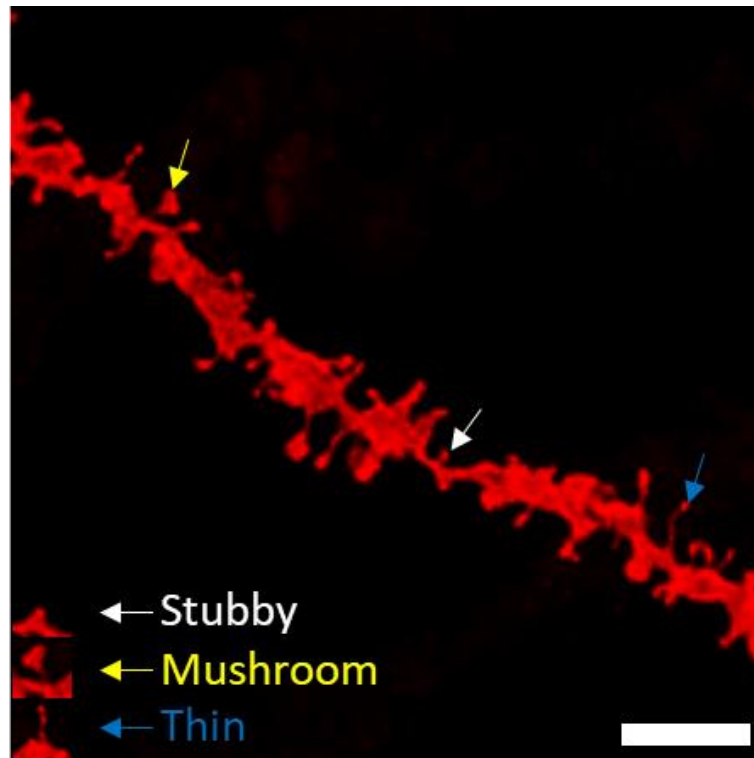


Figure 2.9 Representation of dendritic spine morphologies. Dendritic spines are morphologically classified based on spine head and neck. Stubby (white arrows) spines are identified by short protrusions from the dendritic shaft that do not have a distinctive spine neck. Mushroom (yellow arrows) spines have a distinctive enlarged spine head and a thin spine neck. Thin (blue arrows) spines are long and thin, lacking the enlarged spine head. Scale bar 5 μm .

2.5 Immunofluorescence

There are only a few antibodies that reliably identify RGCs, in preparation of this thesis several antibodies were assessed; however, only RBPMS (RNA-binding protein with multiple splicing, NBP2-20112, Novus, dilution of 1:1000), which exclusively identified RGCs was included.

Eyes allocated for immunofluorescence were fixed overnight in 4% PFA followed by 30% sucrose and cryopreserved in Optimal Cutting Tissue solution. Frozen tissue blocks were sectioned at 15 μm using a cryostat and stored at -80°C . For immunofluorescence staining, sections were defrosted and hydrated in 0.1% Triton in PBS. Sections were subjected to heat-induced antigen retrieval (Sodium Citrate Buffer (10mM Sodium Citrate, 0.05% Tween 20, pH 6.0)) for optimal staining. Sections were blocked in 5% normal serum for 30 minutes, followed by overnight primary antibody incubation. Sections were washed in PBS, and detection of primary antibody binding was achieved with fluorescent conjugated secondary antibodies (Alexa Fluor Plus). Sections were

washed in PBS and nuclei stained with Hoechst 33342 followed by mounting in FluorSave. Sections were stored at 4°C in the dark and confocally imaged within one week. RBPMS staining was imaged using the Leica SP8 confocal using similar parameters to those applied for imaging of DiOlistic labelling of RGCs.

2.6 Statistical analysis

All data was collected using Imaris v 9.3 (Bitplane, Zurich, Switzerland) with statistical analyses performed using GraphPad Prism 8. Data sets were checked for normality with two group analyses, normally distributed data were analysed using unpaired t-test, and non-normally distributed data were analysed using the non-parametric Mann-Whitney-U test. For Sholl analysis, the number of intersections were compared at each interval using the non-parametric Mann-Whitney-U test. For three or more group analyses, data sets were analysed using one-way ANOVA and/or Kruskal–Wallis test. To test for statistical difference between groups (e.g. the effect of genotype and gender), two-way ANOVA was used with Tukey’s post hoc test. All Sholl analysis are displayed as mean values \pm standard error of the mean (SEM). For all other data, unless stated, data is displayed as mean values \pm standard deviation of the mean (SD). Significance is denoted as * = $p < 0.05$, ** = $p < 0.01$, *** = $p < 0.001$, **** = $p < 0.0001$.

Chapter 3. Retinal ganglion cell dendritic pruning in mouse models of Alzheimer's disease

3.1 Introduction

Alzheimer's disease (AD) pathology is characterised by extracellular amyloid plaques and neurofibrillary tangles accompanied by neuroinflammation and synaptic loss that ultimately result in severe brain atrophy and cognitive deficits (Hardy and Higgins, 1992; Querfurth and Laferla, 2010; Serrano-Pozo *et al.*, 2011; De Strooper and Karran, 2016). Synaptic loss, rather than amyloid and tau, are the stronger correlators with AD severity. Synaptic changes are detectable even in the early stages of neurodegeneration, and are a potential therapeutic target (Tampellini, 2015; De Strooper and Karran, 2016). The detection of neurodegeneration, before cell loss, is challenging from human studies and relies on observations from animal models that recapitulate features of the disease.

Others have described visual impairment as an early symptom in some individuals diagnosed with neurodegenerative disease, including AD (Lemos *et al.*, 2012; Graewe *et al.*, 2013). Visual deficits such as reduced acuity, field defects, changes in contrast sensitivity, impaired object recognition, altered face perception and delayed visual processing are found (Marquié *et al.*, 2019). While of importance, these observations have not pinpointed specific locations in the visual pathway that consistently account for a reduction in visual performance. The retina has been suggested as an avenue for *in vivo* detection and monitoring of the CNS, since the retina is an extension of the brain and accessible for imaging (Ran *et al.*, 2009; London *et al.*, 2013; Mahajan and Votruba, 2017). AD retinal pathology mirrors that identified in the brain, including neuronal cell loss, wherein retinal ganglion cells (RGCs) are vulnerable (Chiquita, Rodrigues-Neves, *et al.*, 2019). However, loss of RGCs, thinning of the retinal nerve fibre layer and other features related to AD pathology have not been a consistent finding and when described have not correlated with pathological CNS changes (Ho *et al.*, 2014; Williams *et al.*, 2017).

RGCs are particularly susceptible to degeneration because of their intraocular unmyelinated axons, high energy demand and complex dendritic arbours. RGC dendritic

morphology associates with neuronal function, whereby dendritic atrophy correlates with visual decline. RGC dendritic pruning is characterised by the loss of dendritic complexity and is a feature in retinal neurodegeneration models (Williams, Howell, *et al.*, 2013; Williams *et al.*, 2016). The underlying mechanism of dendritic loss is uncertain; however, it is a crucial feature in the early stages of neurodegeneration. RGC dendritic loss has been reported in one AD mouse model (Tg2576) (Williams, Thirgood, *et al.*, 2013). However, it is not yet clear whether these findings are reproducible across other AD mouse models and, if so, whether they correspond with degenerative events in the CNS.

To address these issues, in this chapter, I characterised the RGC dendritic morphology in overexpressing (Tg2576, 3xTg-AD) and knock-in (APP^{NL-G-F}) AD mouse models. RGCs were morphologically assessed using DiOlistic labelling which is an approach that is not contingent on cell health (Schlamp *et al.*, 2001; Huang *et al.*, 2006; Williams, Howell, *et al.*, 2013). I also assessed whether the RGC receptive field, age and gender associate with RGC dendritic complexity. This chapter provides consistent evidence that RGC degeneration exists in both overexpressing and knock-in AD models, and reinforces the possibilities of exploiting the retina to observe early stages of neurodegeneration in AD.

3.2 Experimental Setup

In this chapter I assessed the dendritic arborisation of RGCs in the Tg2576, 3xTg-AD and APP^{NL-G-F} mouse models of AD in comparison to wildtype mice. Chapter 2 provides a detailed description of the protocols used to assess RGC dendritic complexity. Figure 3.1 presents an overview of the methods used in this chapter for the assessment of RGC dendritic complexity in the AD models by DiOlistic labelling.

Previously, only the Tg2576 strain had been assessed and compared to wildtypes, displayed increased RGC dendritic pruning in the retina of 14-month-old mice (Williams, Thirgood, *et al.*, 2013). I re-evaluated the Tg2576 AD model for RGC dendritic loss at 12 and 15 months. Due to animal availability, only male mice were included. In order to determine whether RGC dendritic pruning is common in AD mouse models, two additional well characterised models were analysed. The 3xTg-AD model has demonstrated retinal pathology in other studies; however the impact on RGC dendritic complexity is uncertain (Grimaldi *et al.*, 2018; Salobar-García *et al.*, 2020). In this chapter I assessed 3xTg-AD mice at ages 3, 6, 9, 12 and 15 months and both male and female mice. A third AD model was included as others report that transgenic models may exhibit potential artefacts that cause retinal pathology (Saito *et al.*, 2014; Jankowsky and Zheng, 2017; Sasaguri *et al.*, 2017). I assessed the APP^{NL-G-F} knock-in model at 7 and 12 months for both genders. These AD models were compared to wildtype mice from both genders at 12 months, which depict typical RGC dendritic complexities. Additional littermate wildtypes were included when analysing the Tg2576 cohort; these littermate wildtypes are the same control line used in the original report (Williams, Thirgood, *et al.*, 2013), whereas all other wildtypes are C57BL/6J.

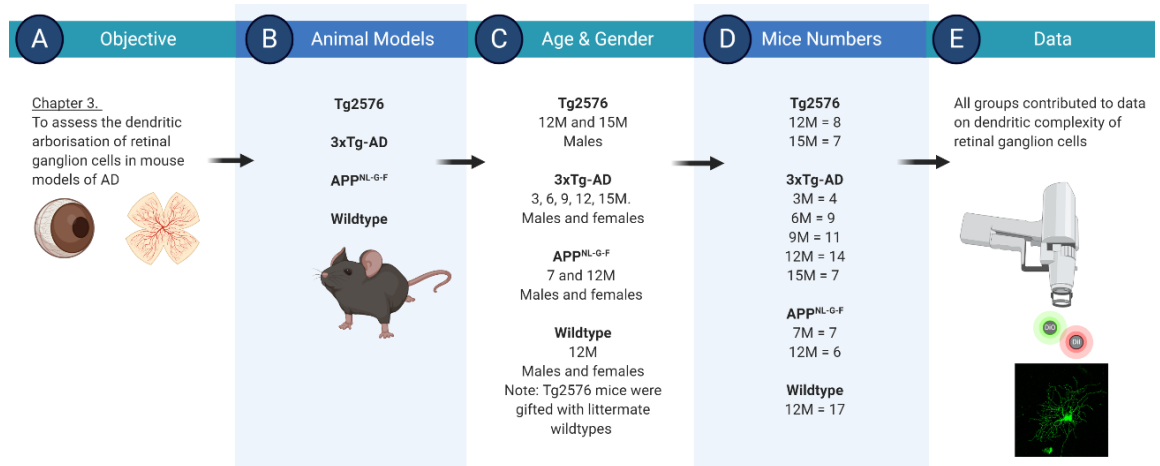


Figure 3.1 Experimental overview for Chapter 3 addressing RGC dendritic arborisation in AD mouse models. (A) Main objective for Chapters 3. (B) The different animal models used in this chapter. (C) Details on the animal models including the ages analysed and genders available. (D) Total number of mice analysed that were subjected to DiOlistic labelling. (E) All groups in Chapter 3 were analysed for RGC dendrites and hippocampal dendritic spine coverage. Illustration created in BioRender.

3.3 Results

3.3.1 Tg2576

3.3.1.1 Preservation of RGC density in the Tg2576 retina

The first series of analyses tested whether the retina in the Tg2576 AD mouse model showed global loss of RGCs using the antibody RBPMS (RNA-binding protein with multiple splicing) on retinal sections (Figure 3.2A-B). There were no changes in the number of RBPMS-positive RGCs in the GCL in Tg2576 retinas compared to wildtype at 12-months (Figure 3.2C). Further analysis to determine the proportion of RBPMS-positive cells relative to the number of nuclei in the GCL, confirmed that the densities of RGCs were also proportionate to wildtype (~ 40%; Figure 3.2D). These initial data demonstrate that RGC loss, indicative of neurodegeneration, is not a feature in the retinas of Tg2576 mice at 12 months.

3.3.1.2 RGC dendritic pruning in Tg2576 mice

Despite the absence of RGC loss in the retina of Tg2576 mice, I further explored whether RGCs retained their dendritic complexity. To assess RGC dendritic morphology, individual RGCs were reconstructed from DiOlistically labelled cells in wildtype and Tg2576 mice at 12 months (representative examples, Figure 3.3A-B). As expected, RGCs from wildtype mice were morphologically complex and highly variable in their dendritic field, representing a typical RGC dendritic arborisation pattern (Figure 3.3A). In contrast, in the Tg2576 retina, RGCs showed an obvious reduction in the dendritic complexity, apparent even before quantitative analyses (Figure 3.3B). Measurement of the dendritic structure of RGCs based on Sholl analysis revealed significant dendritic pruning in the Tg2576 mice (up to 100 μm , $p < 0.05$; Figure 3.3C). The dendrites proximal to the cell body (primary and secondary dendrites) were unaffected. However, significantly fewer tertiary and quaternary dendrites were detected in RGCs from Tg2576 mice (Figure 3.3D). Morphological parameters including the area under the Sholl curve (AUC, Figure 3.3E), the peak of the Sholl intersections (Figure 3.3F), and the total length of all measured dendrites (Figure 3.3G) all showed significant reductions. As noted above, these dendritic differences occurred in the absence of cell loss in the GCL based on

Hoechst labelling (Figure 3.3H). These results show that excessive RGC dendritic pruning is a feature in the retina of 12-month-old Tg2576 mice.

3.3.1.3 ON-centre restricted RGC dendritic pruning in Tg2576 retina.

To test whether RGC dendritic pruning occurred in both ON and OFF-centre RGCs, data were divided based on the dendritic sublamina projection into the IPL (Figure 3.4A). ON-centre RGCs were classified when dendrites terminated in sublamina b nearest to the GCL. In contrast, OFF-centre RGCs were classified when dendrites terminated in sublamina a, deeper in the IPL. Analysis of RGCs in Tg2576 mice showed that dendritic pruning was restricted to ON-centre classification RGCs, with significant dendritic loss affecting the majority of the dendritic field (up to 110 μm , $p < 0.05$; Figure 3.4B-F). Conversely, dendritic complexity in OFF-centre RGCs in Tg2576 mice was comparable to wildtype (Figure 3.4B-F). These observations demonstrate that RGC dendritic pruning in the Tg2576 mice is restricted to ON-centre specific cells, potentially due to the higher energy demand required for this subtype to function (Williams *et al.*, 2010).

3.3.1.4 RGC dendritic pruning is not exacerbated with further aging in the Tg2576 mice.

I further considered whether RGC dendritic pruning progressively deteriorated in the Tg2576 mice at 15 months. RGCs did not exhibit any further dendritic loss between 12 and 15 months. Sholl analysis suggested that dendritic complexity was increased in the RGCs from 15-month mice at distal dendrites (between 110 and 140 μm , $p < 0.05$; Figure 3.5A). However, when analysing the number of proximal dendrites, the Sholl AUC, the peak of the Sholl intersections and the total dendritic length all showed no significant differences were noted (Figure 3.5B-E). The number of nuclei in the GCL was likewise unaffected with ageing (Figure 3.5F). RGCs were split based on their ON-/OFF-centred classification. For either subgroup, there was no significant difference in Sholl curves or derived parameters in the 15-month Tg2576 mice compared to 12-months (Figure 3.6A-D). These data imply that RGC dendritic pruning does not progressively decline between the ages of 12 and 15 months in Tg2576 mice.

3.3.1.5 Figures

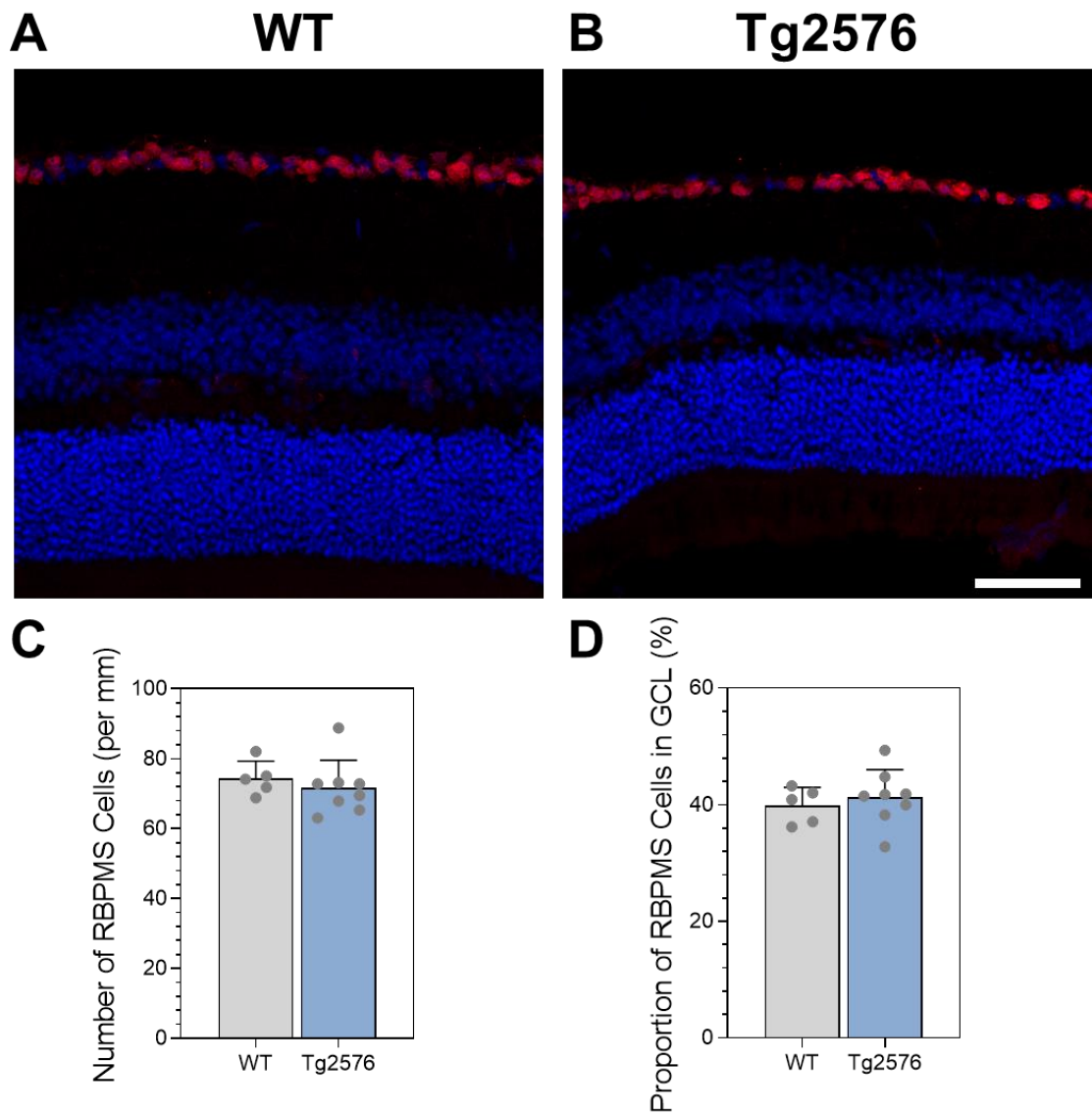


Figure 3.2 RGC loss is not a feature in the Tg2576 retina. (A-B) RBPMS (red) immunofluorescence labelling for RGCs and Hoechst nuclei stain (blue) from WT and Tg2576 retina cryosections. Scale bar 50 μm . (C) Number of RBPMS-positive cells per mm of GCL. (D) Proportion of RBPMS-positive cells relative to the number of Hoechst nuclei in the GCL. WT: $n = 5$ mice and Tg2576: $n = 8$ mice. All male mice aged twelve months. Two group comparisons, Mann-Whitney U test: (C) $p = 0.2844$, (D) $p = 0.7242$. Data points represent individual mice and error bars correspond to SD. Abbreviations: WT, wildtype; RBPMS, RNA-binding protein with multiple splicing; GCL, ganglion cell layer.

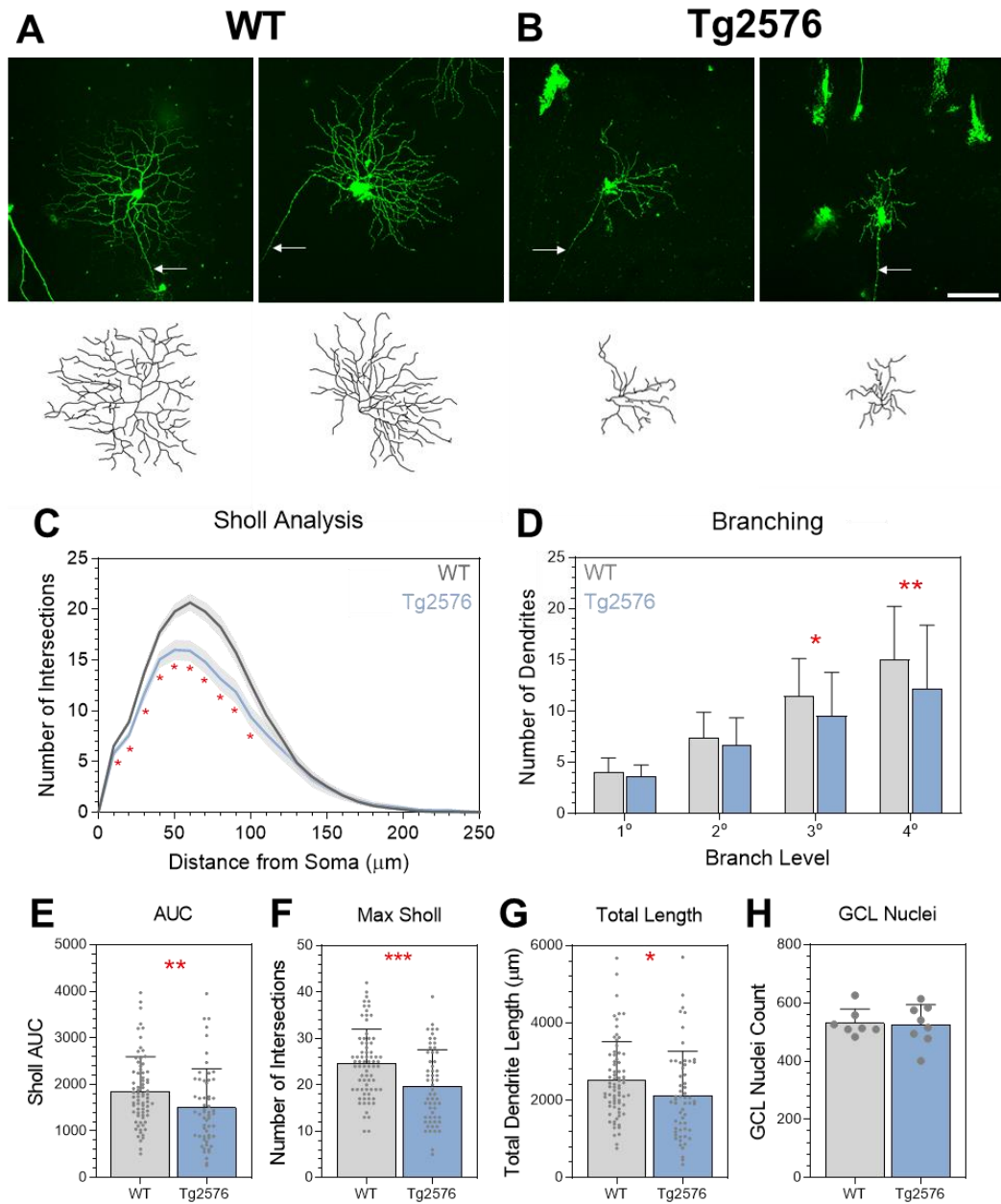


Figure 3.3 RGC dendritic atrophy in Tg2576 mice. (A-B) DiOlistic labelled RGCs with corresponding Imaris dendritic reconstructions from WT and Tg2576 mice aged at twelve months. Arrows indicate RGC axon. Scale bar: 100 μm . (C) Sholl analysis of reconstructed RGCs. Line represents mean of group at each interval, shaded error zones \pm SEM. Two-tailed Mann-Whitney U test at each interval distance, * = $p < 0.05$. (D) Number of dendrites at each branching level proximal to the cell body. (E) Area under the Sholl curve. (F) Maximum number of Sholl intersections. (G) Total length of all dendrites. (H) Number of nuclei in the GCL. Column plot (D): bars represent mean from individual cells and error bars correspond to SD. Column Scatterplots (E-G): bars represent mean, data represent individual cells and error bars correspond to SD. Column Scatterplots (H): bar represent mean of group from at least three images per mouse, data points represent the mean and error bars represent SD. WT: $n = 72$ cells (7 mice) and Tg2576: $n = 58$ cells (8 mice). Two group comparisons, Mann-Whitney U test: * = $p < 0.05$, ** = $p < 0.01$, *** = $p < 0.001$, **** = $p < 0.0001$. Abbreviations: WT, wildtype; AUC, area under the Sholl curve; GCL, ganglion cell layer.

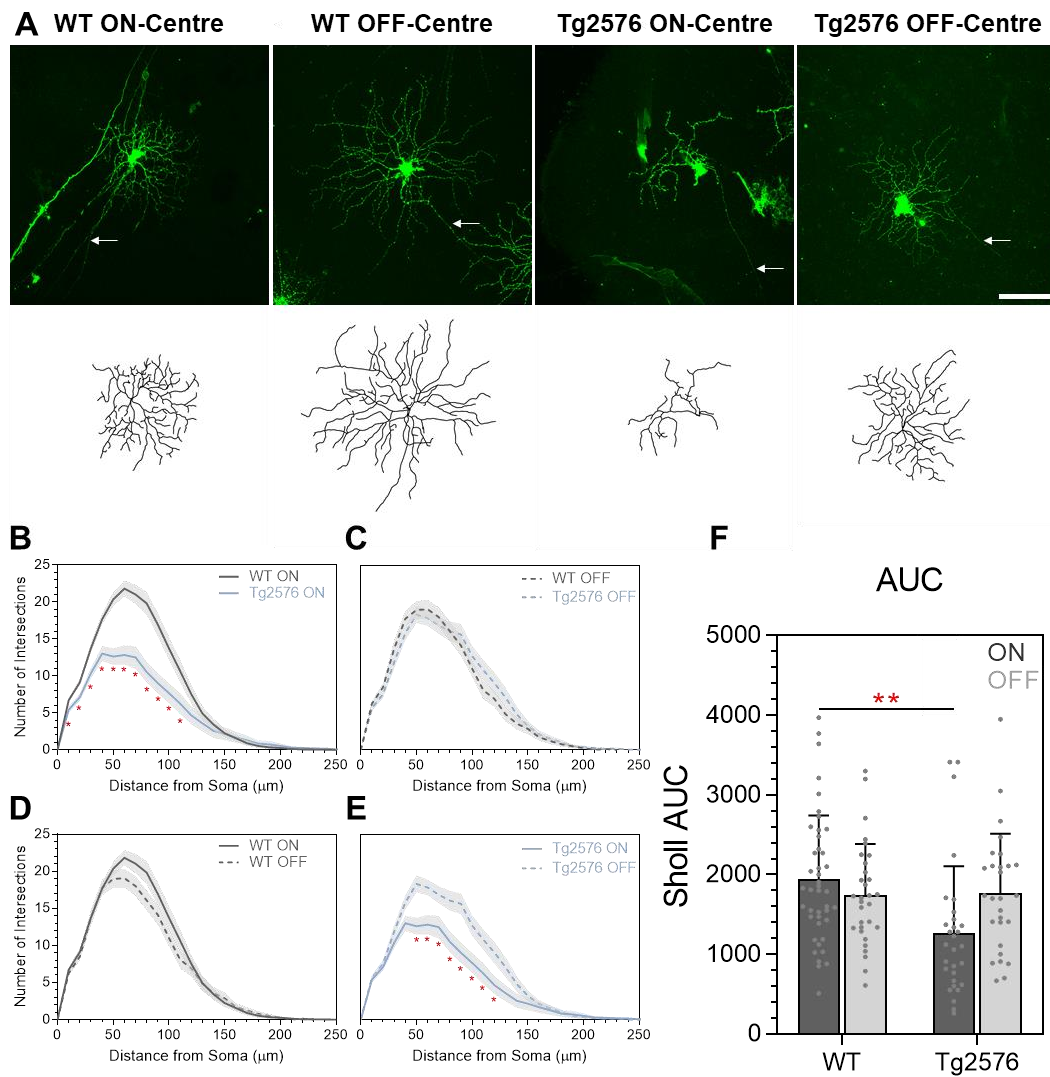


Figure 3.4 ON-centre RGC vulnerability in Tg2576 mice. (A) Representative examples and Imaris reconstructions of ON- and OFF-centre RGCs from WT and Tg2576 mice. Arrows indicate RGC axon. Scale bar: 100 μm. (B-E) Sholl analysis of ON-centre and OFF-centre RGCs. Line represents mean of group at each interval, shaded error zones ± SEM. Two-tailed Mann-Whitney U test at each interval distance, * = $p < 0.05$. (F) Area under the Sholl curve. Two-way ANOVA was used to determine interaction between two factors (genotype and RGC classification) and Tukey's post hoc test to determine statistical significance. Column Scatterplot (F): data represent individual cells and error bars correspond to SD. WT ON-centred: $n = 43$ cells (7 mice), WT OFF-centred: $n = 31$ cells (7 mice), Tg2576 ON-centred: $n = 65$ cells (8 mice) and Tg2576 OFF-centred: $n = 43$ cells (8 mice). All male mice aged twelve months. * = $p < 0.05$, ** = $p < 0.01$, *** = $p < 0.001$, **** = $p < 0.0001$. Abbreviations: WT, wildtype; AUC, area under the Sholl curve; ON, ON-centre RGCs; OFF, OFF-centre RGCs.

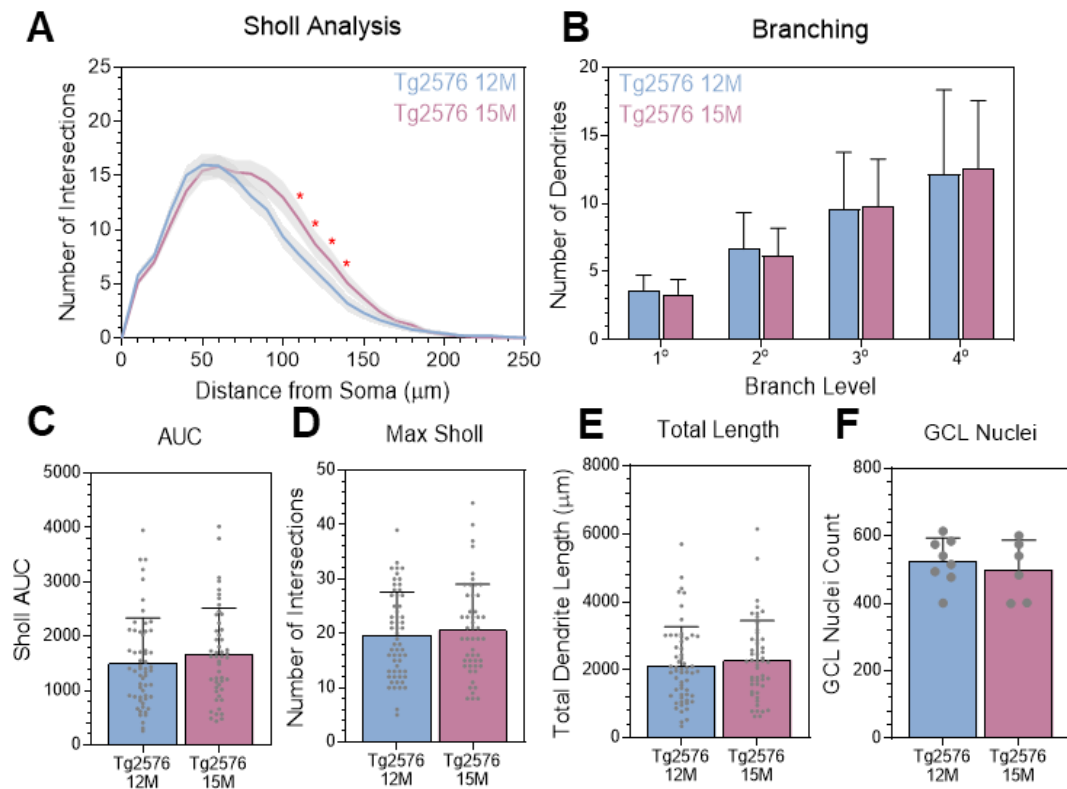


Figure 3.5 Stable RGC dendritic complexity with further ageing in Tg2576 mice. (A) Sholl analysis of Imaris reconstructed RGCs from Tg2576 mice aged twelve and fifteen months. Line represents mean of group at each interval, shaded error zones \pm SEM. Two-tailed Mann-Whitney U test at each interval distance, * = $p < 0.05$. (B) Number of dendrites at each branching level proximal to cell body. (C) Area under the Sholl curve. (D) Maximum number of Sholl intersections. (E) Total length of all dendrites. (F) Number of nuclei in the GCL. Column Scatterplots (B-E): data represent individual cells and error bars correspond to SD. Tg2576 12M: $n = 58$ cells (8 mice) and Tg2576 15M: $n = 50$ cells (7 mice), Tg2576 12M ON-centred: $n = 30$ cells (8 mice), Tg2576 12M OFF-centred: $n = 28$ cells (8 mice), Tg2576 15M ON-centred: $n = 35$ cells (7 mice) and Tg2576 15M OFF-centred: $n = 15$ cells (7 mice). All male mice aged either twelve or fifteen months old. Two group comparisons, Mann-Whitney U test. * = $p < 0.05$, ** = $p < 0.01$, *** = $p < 0.001$, **** = $p < 0.0001$. Abbreviations: WT, wildtype; AUC, area under the Sholl curve; ON, ON-centred RGCs; OFF, OFF-centred RGCs, 12M, twelve-months; 15M, fifteen-months; GCL, ganglion cell layer.

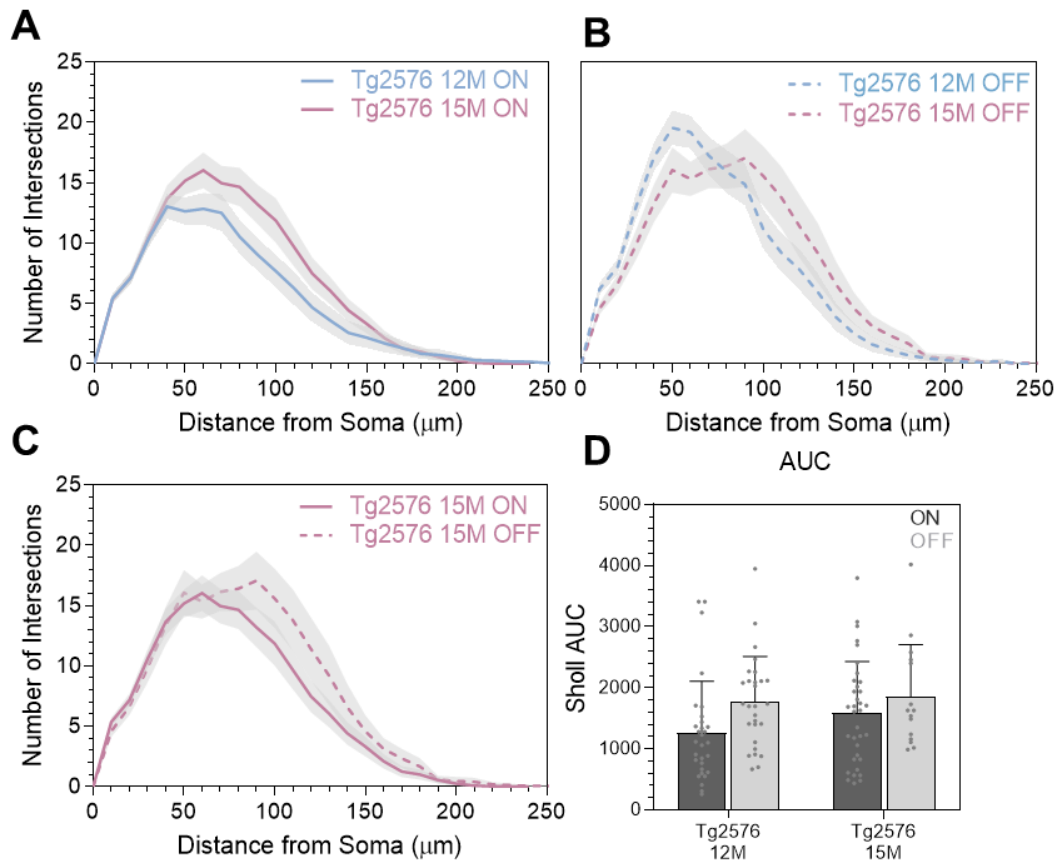


Figure 3.6 Stable RGC dendritic complexity based on receptive field classification with further ageing in Tg2576 mice. (A-C) Sholl analysis of Imaris reconstructed RGCs from Tg2576 mice aged twelve and fifteen months based on ON- and OFF-centre classification. Line represents mean of group at each interval, shaded error zones \pm SEM. Two-tailed Mann-Whitney U test at each interval distance, * = $p < 0.05$. (D) Area under the Sholl curve. Two-way ANOVA with Tukey multiple comparisons test. Column Scatterplot (D): data represent individual cells and error bars correspond to SD. Tg2576 12M ON-centre: $n = 30$ cells (8 mice), Tg2576 12M OFF-centre: $n = 28$ cells (8 mice), Tg2576 15M ON-centre: $n = 35$ cells (7 mice) and Tg2576 15M OFF-centre: $n = 15$ cells (7 mice). All male mice aged either twelve or fifteen months. * = $p < 0.05$, ** = $p < 0.01$, *** = $p < 0.001$, **** = $p < 0.0001$. Abbreviations: WT, wildtype; AUC, area under the Sholl curve; ON, ON-centre RGCs; OFF, OFF-centre RGCs, 12M, twelve-months; 15M, fifteen-months.

3.3.2 3xTg-AD

3.3.2.1 RGC dendritic pruning in 3xTg-AD mice.

To establish whether RGC dendritic pruning is a feature across AD mouse models, I investigated the 3xTg-AD model. Dendritic morphology of RGCs was analysed from 3xTg-AD retinas from both male and female mice at 12 months and compared to wildtype. Excessive dendritic pruning was confirmed in the RGCs of 3xTg-AD mice (Figure 3.7A-B) with significantly fewer dendrites reflecting the majority of the Sholl curve (up to 180 μm , $p < 0.05$; Figure 3.7C). Not only distal but also proximal dendrites, covering primary and secondary dendrites, were decreased in the RGCs from 3xTg-AD mice (Figure 3.7D). The analysis confirmed reductions in the Sholl AUC (Figure 3.7E), the peak of the Sholl curve (Figure 3.7F) and the total dendritic length (Figure 3.7G). These differences to the RGC dendritic complexity occurred in the absence of cell loss in the GCL based on Hoechst (Figure 3.7H). These results provide the first evidence of RGC dendritic pruning in the 3xTg-AD mouse model.

3.3.2.2 Male 3xTg-AD mice show greater RGC dendritic pruning.

Separating the 3xTg-AD mice into males and females, enabled the quantification of changes in both genders. Male 3xTg-AD mice displayed prominent RGC dendritic pruning compared to male wildtypes. However, female 3xTg-AD mice only showed modest dendritic pruning (Figure 3.8A). In both genders, the number of primary dendrites was unaffected. However, males displayed significantly greater dendritic loss from the secondary dendritic level, which deteriorated further with distance from the cell body. Female 3xTg-AD mice showed small but significant reductions in tertiary and quaternary dendrites (Figure 3.8B). Both male and female 3xTg-AD mice revealed a reduction (37% $p < 0.0001$ and 17% $p = 0.0248$, respectively) in the Sholl AUC compared to sex-matched wildtype mice, with the former marking more significant reductions (Figure 3.8C). In line with the reduced Sholl AUC, the peak number of intersections was lowest in male 3xTg-AD mice (Figure 3.8D). Determining the total length of all the dendrites confirmed that dendritic pruning was more prominent in male 3xTg-AD mice (Figure 3.8E). These differences occurred irrespective of nuclei changes in the GCL (Figure 3.8F). These

results provide evidence that RGC dendritic pruning, in this 3xTg-AD cohort, is more prominent in male mice.

3.3.2.3 ON-centre RGCs show consistent dendritic pruning in both male and female 3xTg-AD mice.

To analyse whether RGC dendritic pruning occurred in both ON and OFF-centre RGCs, data was split based on the dendritic sublamina projection into the IPL. Representative examples with dendritic tracings are shown in Figure 3.9. ON-centre RGCs were classified when dendrites restricted to sublamina b nearest to the GCL. In contrast, OFF-centre RGCs were classified when dendrites projected further into the IPL. ON-centre classified RGC dendritic pruning was found in both male and female 3xTg-AD mice; more marked in males (47% $p < 0.001$ and 27% $p = 0.0024$, respectively; Figure 3.10). Female 3xTg-AD mice displayed an ‘intermediate’ profile sitting between male 3xTg-AD and wildtype (Figure 3.10A-B). Conversely, in OFF-centre classified RGCs, dendritic pruning was only found in male 3xTg-AD mice (reduction of 27%, $p = 0.0060$); in females these were comparable to wildtype and did not reveal any dendritic changes (Figure 3.10C-D). These results demonstrate that ON-centre RGCs in the 3xTg-AD retina show consistent excessive dendritic pruning in both male and female mice. In contrast, OFF-centre RGC degeneration is only observed in male 3xTg-AD mice.

3.3.2.4 Age influences 3xTg-AD RGC dendritic pruning

I further tested whether ageing impacted RGC dendritic pruning in the 3xTg-AD mice. Male 3xTg-AD mice were assessed at 3, 6, 9, 12 and 15-months. RGC dendritic complexity in 3 and 6 month 3xTg-AD mice was comparable to wildtype. RGC dendritic pruning increased stepwise from 6 to 9 to 12 months, then plateaued between 12 and 15 months (Figure 3.11A). For all age groups, the number of proximal dendrites remained constant with dendritic pruning detected at the tertiary dendritic level (Figure 3.11B). Quantification of the related parameters confirmed a stepwise age-dependent dendritic pruning in the Sholl AUC, the peak number of Sholl intersections and the total dendritic length (Figure 3.11C-E). These results demonstrate that age increases the burden of RGC dendritic loss in 3xTg-AD mice.

3.3.2.5 Figures

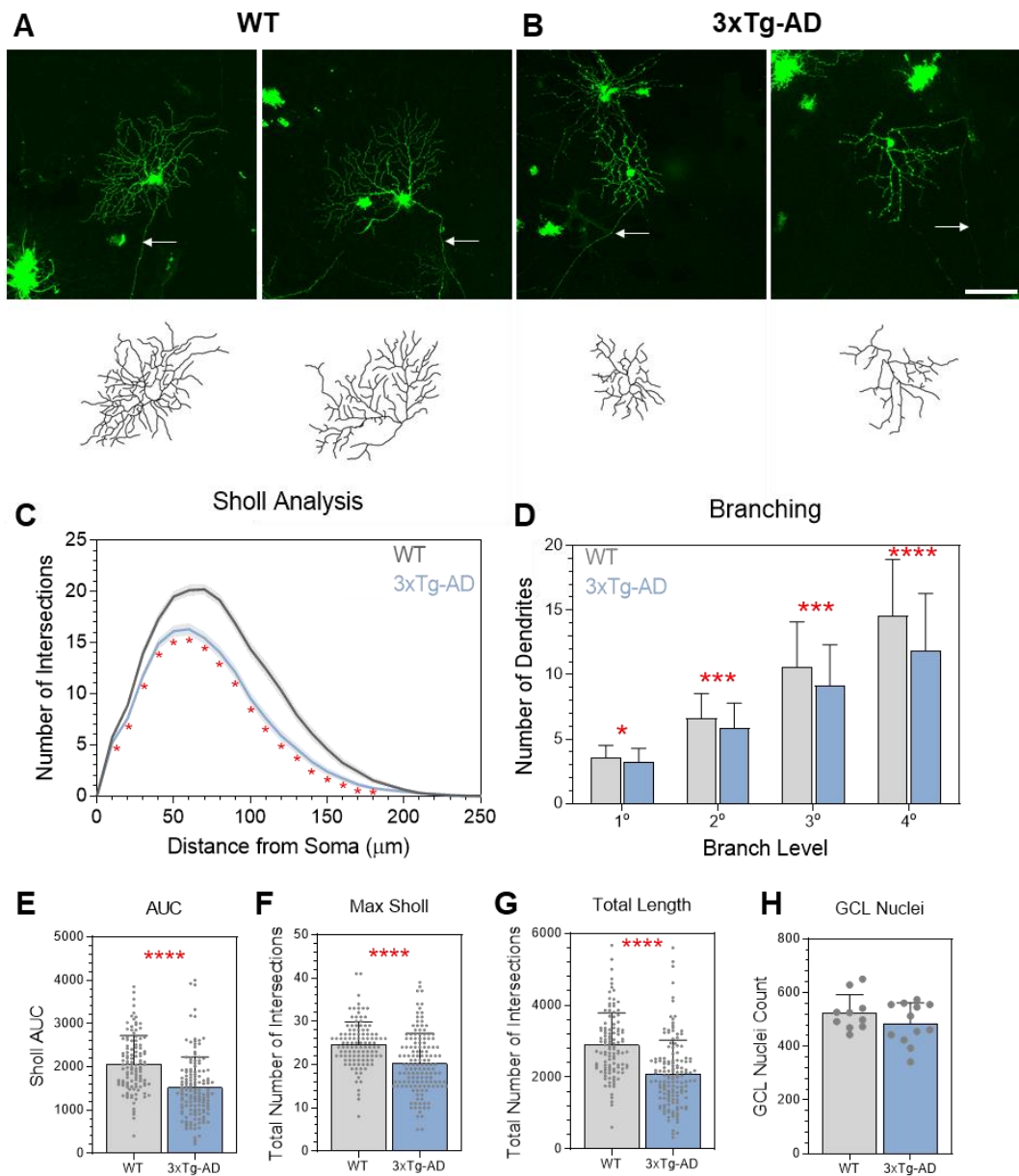


Figure 3.7 RGC dendritic atrophy in 3xTg-AD mice. (A-B) DiOlistic labelled RGCs from WT and 3xTg-AD mice at twelve months. Arrows indicate RGC axon. Scale bar 100 μm. (C) Sholl analysis of reconstructed RGCs. Line represents mean of group at each interval, shaded error zones ± SEM. Two-tailed Mann-Whitney U test at each interval distance, * = $p < 0.05$. (D) Number of dendrites at each branching level proximal to cell body. (E) Area under the Sholl curve. (F) Maximum number of Sholl intersections. (G) Total length of all dendrites. (H) Number of nuclei in the GCL. Column scatterplots (D-G): data points represent individual cells and error bars correspond to SD. Column scatterplots (H): data represent individual mice and error bars correspond to SD. WT: $n = 114$ cells (10 mice, 5 male/5 female) and 3xTg-AD: $n = 144$ cells (12 mice, 6 male/6 female). Two group comparisons were made using the Mann-Whitney U test. * = $p < 0.05$, ** = $p < 0.01$, *** = $p < 0.001$, **** = $p < 0.0001$. Abbreviations: WT, wildtype; AUC, area under the Sholl curve; GCL, ganglion cell layer.

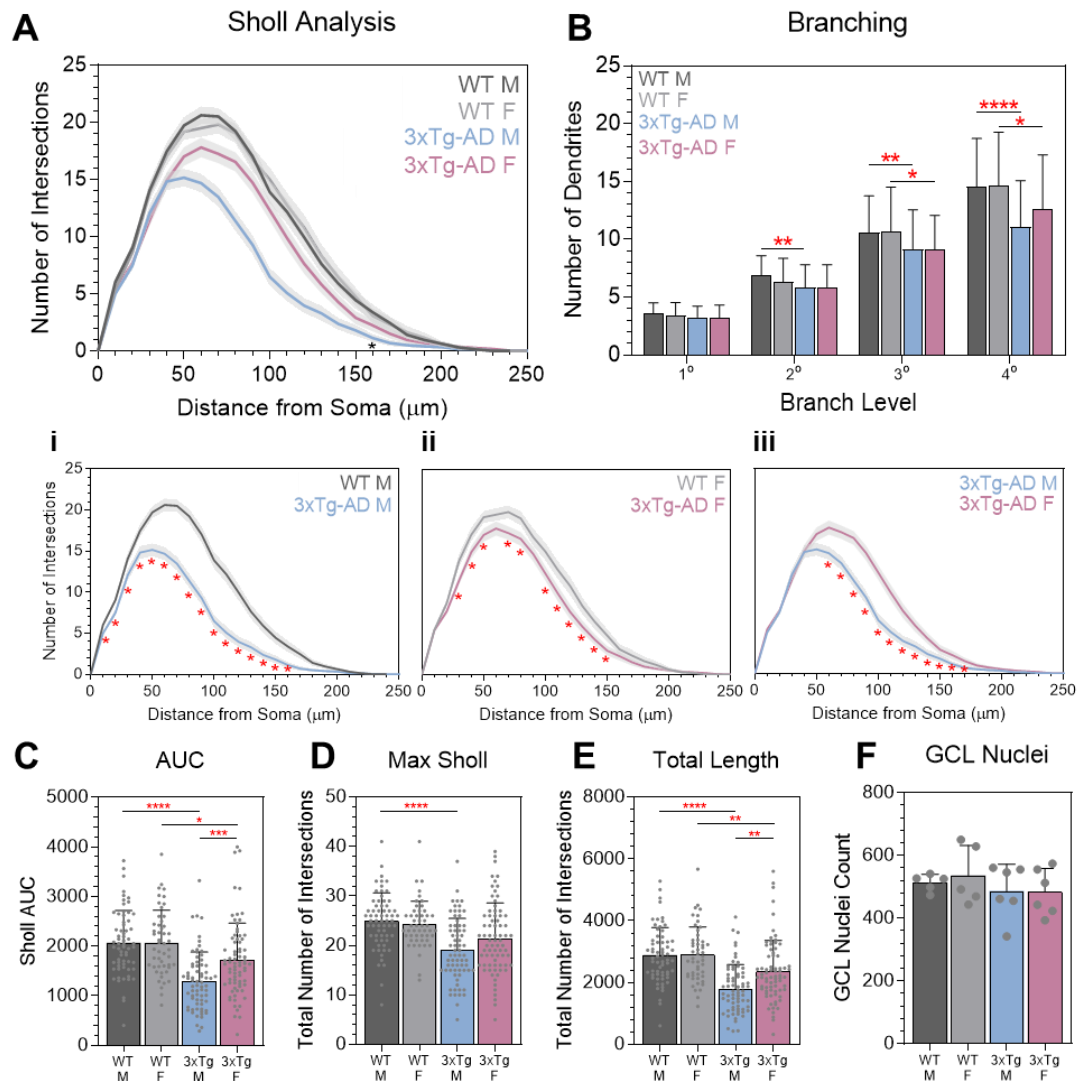


Figure 3.8 Greater RGC dendritic pruning in male 3xTg-AD mice. (A) Sholl analysis of Imaris reconstructed RGCs from WT and 3xTg-AD retinal explants separated based on gender. Line represents mean of group at each interval, shaded error zones \pm SEM. Two-tailed Mann-Whitney U test at each interval distance, $* = p < 0.05$. (B) Number of dendrites at each branching level proximal to cell body. (C) Area under the Sholl curve. (D) Maximum number of Sholl intersections. (E) Total length of all dendrites. (F) Number of nuclei in the GCL. Column Scatterplots (B): bars represent mean from individual cells and error bars correspond to SD. Column Scatterplots (C-E): data represent individual cells and error bars correspond to SD. Column Scatterplot (F): data represent individual mice and error bars correspond to SD. WT-M: $n = 64$ cells (5 mice), WT-F: $n = 50$ cells (5 mice), 3xTg-AD M: $n = 69$ cells (6 mice) and 3xTg-AD-F: $n = 75$ cells (6 mice). All mice aged twelve months. Two-way ANOVA was used to determine interaction between two factors (genotype and gender) and Tukey's post hoc test to determine statistical significance. $* = p < 0.05$, $** = p < 0.01$, $*** = p < 0.001$, $**** = p < 0.0001$. Abbreviations: WT, wildtype; M, male; F, female; AUC, area under the Sholl curve; GCL, ganglion cell layer.

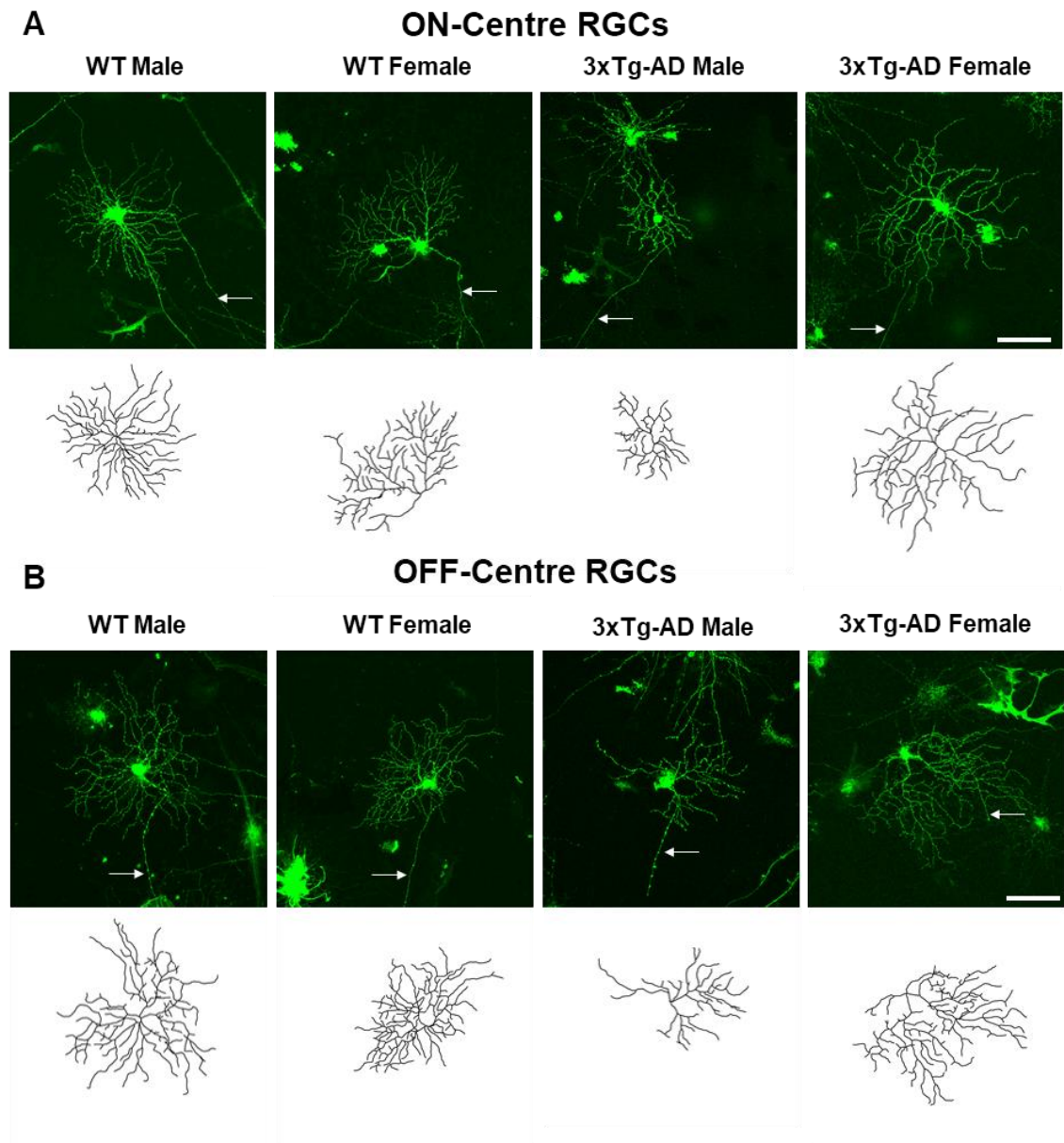


Figure 3.9 RGCs based on receptive field and gender classification in wildtype and 3xTg-AD mice. All mice aged at twelve months old. Arrows indicate RGC axon. Scale bar: 100 μ m. WT, wildtype.

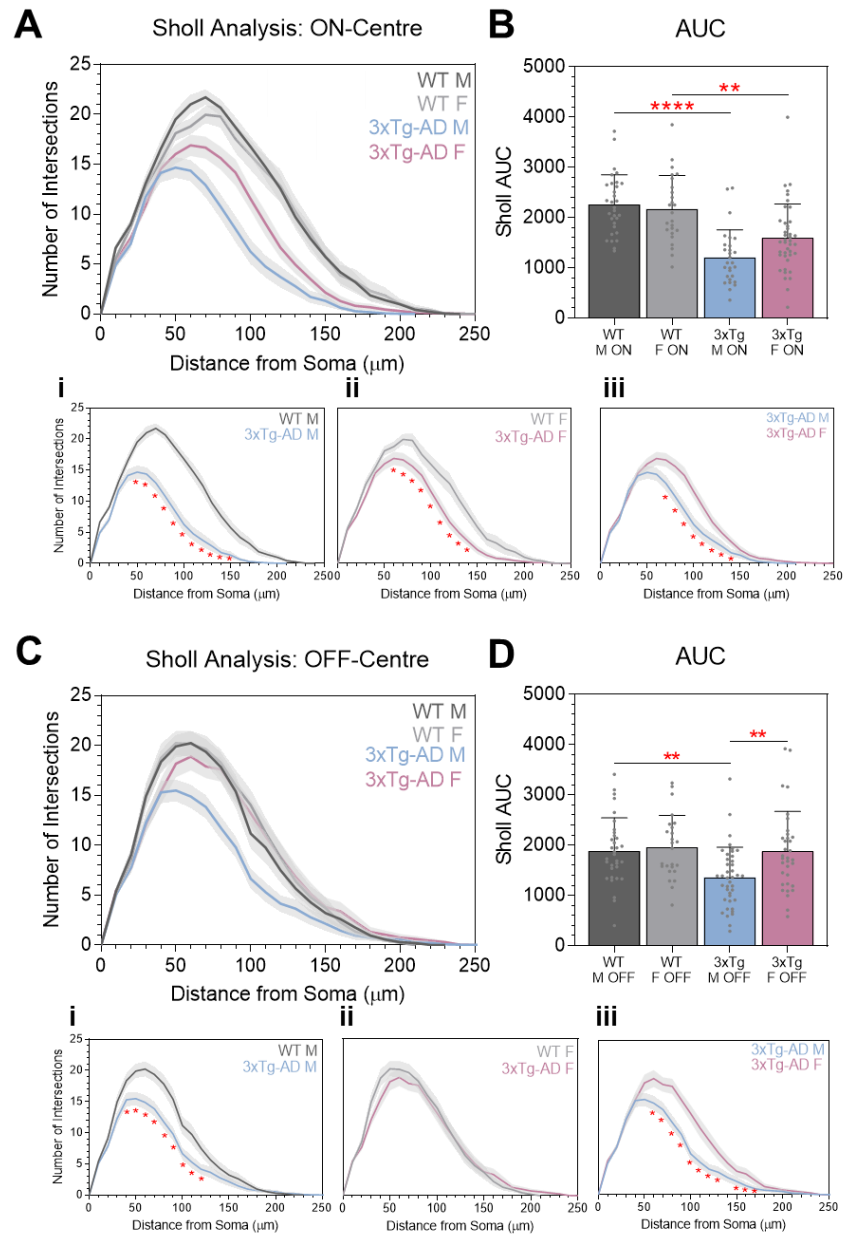


Figure 3.10 ON- and OFF-centre RGCs are affected in male 3xTg-AD mice whilst only ON-centre RGCs are impaired in female 3xTg-AD mice. (A) Sholl analysis of reconstructed ON-centred RGCs. Line represents mean of group at each interval, shaded error zones represent \pm SEM. Two-tailed Mann-Whitney U test at each interval distance, $* = p < 0.05$. (B) Area under the Sholl curve for ON-centred RGCs. (C) Sholl analysis of Imaris reconstructed OFF-centred RGCs. Line represents mean of group at each interval, shaded error zones represent \pm SEM. Two-tailed Mann-Whitney U test at each interval distance, $* = p < 0.05$. (D) Area under the Sholl curve for OFF-centred RGCs. Column Scatterplots (B, D): data represent individual cells and error bars correspond to SD. WT-M ON-centre: $n = 31$ cells/ 5 mice, WT-M OFF-centre: $n = 33$ cells/ 5 mice, WT-F ON-centre: $n = 25$ cells/ 5 mice, WT-F OFF-centre: $n = 25$ cells/ 5 mice, 3xTg-AD-M ON-centre: $n = 28$ cells/ 6 mice, 3xTg-AD-M OFF-centre: $n = 41$ cells/ 6 mice, 3xTg-AD-F ON-centre: $n = 41$ cells/ 6 mice and 3xTg-AD-F OFF-centre: $n = 34$ cells/ 6 mice. All mice aged at twelve months old. Two-way ANOVA was used to determine interaction between two factors (genotype and gender) and Tukey's post hoc test to determine statistical significance. $* = p < 0.05$, $** = p < 0.01$, $*** = p < 0.001$, $**** = p < 0.0001$. Abbreviations: WT, wildtype; M, male; F, female; AUC, area under the Sholl curve; ON, ON-centre RGCs; OFF, OFF-centre RGCs.

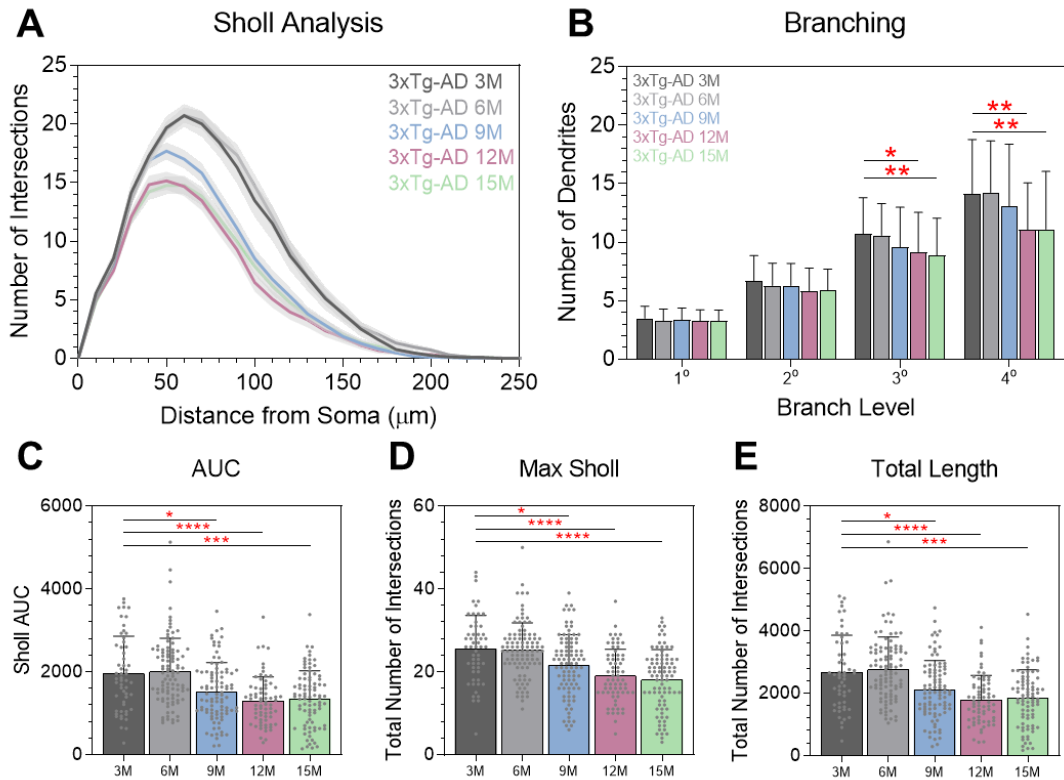


Figure 3.11 Progressive RGC dendritic pruning with age in 3xTg-AD mice. (A) Sholl analysis of reconstructed RGCs from 3xTg-AD male mice at the ages of 3, 6, 9, 12 and 15 months. Line represents mean of group at each interval, shaded error zones \pm SEM. Two-tailed Mann-Whitney U test at each interval distance, $* = p < 0.05$. (B) Number of dendrites at each branching level proximal to cell body. (C) Area under the Sholl curve. (D) Maximum number of Sholl intersections. (E) Total length of all dendrites. Column Scatterplots: data represent individual cells and error bars correspond to SD. 3xTg-AD 3M: $n = 55$ cells (4 mice), 3xTg-AD 6M: $n = 99$ cells (9 mice), 3xTg-AD 9M: $n = 93$ cells (6 mice), 3xTg-AD 12M: $n = 69$ cells (6 mice) and 3xTg-AD 15M: $n = 86$ cells (7 mice). Three or more groups were compared by nonparametric one-way analysis of variance (Kruskal–Wallis test) using Dunn multiple comparisons post-test. $* = p < 0.05$, $** = p < 0.01$, $*** = p < 0.001$, $**** = p < 0.0001$. Abbreviations: 3M, three months; 6M, six months; 9M, nine months; 12M, twelve months; 15M, fifteen months; AUC, area under the Sholl curve.

3.3.3 APP^{NL-G-F}

3.3.3.1 APP^{NL-G-F} mice exhibit RGC dendritic atrophy

The data presented in the previous sections provide evidence for excessive RGC dendritic pruning in AD transgenic overexpression models. I further explored whether RGC dendritic complexity was altered in the knock-in APP^{NL-G-F} AD model (Figure 3.12A-B). RGCs were morphologically quantified from APP^{NL-G-F} mice at 7 and 12 months. Excessive RGC dendritic pruning was observed in both 7 and 12 month APP^{NL-G-F} mice, with the latter demonstrating greater dendritic loss (Figure 3.12C). Proximal dendrites, from the secondary branching level, were significantly decreased ($p < 0.05$) in the 12-month APP^{NL-G-F} mice compared to wildtype. No statistical differences were found between the two APP^{NL-G-F} ages up to the tertiary dendrites. However, at the quaternary dendritic level, pruning was significantly greater in the 12-month APP^{NL-G-F} mice compared to 7-months (16% $p < 0.01$; Figure 3.12D). These differences in RGC dendritic complexity also coincided with reductions in the Sholl AUC (Figure 3.12E), the peak of the Sholl intersections (Figure 3.12F) and the total dendritic length (Figure 3.12G). These results describe the first evidence of excessive RGC dendritic pruning in a knock-in AD model, the only report in APP^{NL-G-F} mice.

3.3.3.2 APP^{NL-G-F} RGC degeneration is not dependant on gender

I further studied whether there was a gender difference for RGC dendritic pruning in the APP^{NL-G-F} mice. Although male APP^{NL-G-F} RGCs showed significantly greater dendritic pruning in proximal dendrites (between 20 and 50 μm , $p < 0.05$) when compared to female mice (Figure 3.13A). Despite this, the number of primary to quaternary dendrites was not different between the genders (Figure 3.13B). No statistical differences were found in the Sholl AUC (Figure 3.13C) or the total dendritic length (Figure 3.13E). However, males demonstrated significantly fewer intersections at the peak of the Sholl curve (reduction of 15% $p = 0.0442$; Figure 3.13D). These results suggest that excessive RGC dendritic pruning occurs in both male and female APP^{NL-G-F} mice at twelve months, although pruning is worse in males.

3.3.3.3 Classification of RGC based on sublamina projections reflects dendritic structure in APP^{NL-G-F} mice.

To assess whether excessive RGC dendritic pruning occurred in both ON and OFF-centre RGCs (Figure 3.14A-B), data were split based on the dendritic sublamina projection into the IPL. ON-centre RGCs were classified with dendrites confined to the sublamina nearest to the GCL. In contrast, OFF-centre RGCs were classified when dendrites extended further in the IPL. ON-centre RGCs from both male and female APP^{NL-G-F} mice showed similar excessive dendritic pruning (38% $p < 0.0001$ and 45% $p < 0.0001$, respectively; Figure 3.15A-B). Conversely, OFF-centre RGC dendritic pruning more evident in males than females (50% $p < 0.0001$ and 34% $p = 0.0035$, respectively; Figure 3.15C-D). Both male and female APP^{NL-G-F} mice displayed reduced Sholl curves and Sholl AUC compared to their respective wildtypes. These results indicate that dendritic loss is not restricted to a single RGC receptive field classification type in APP^{NL-G-F} mice.

3.3.3.4 Figures

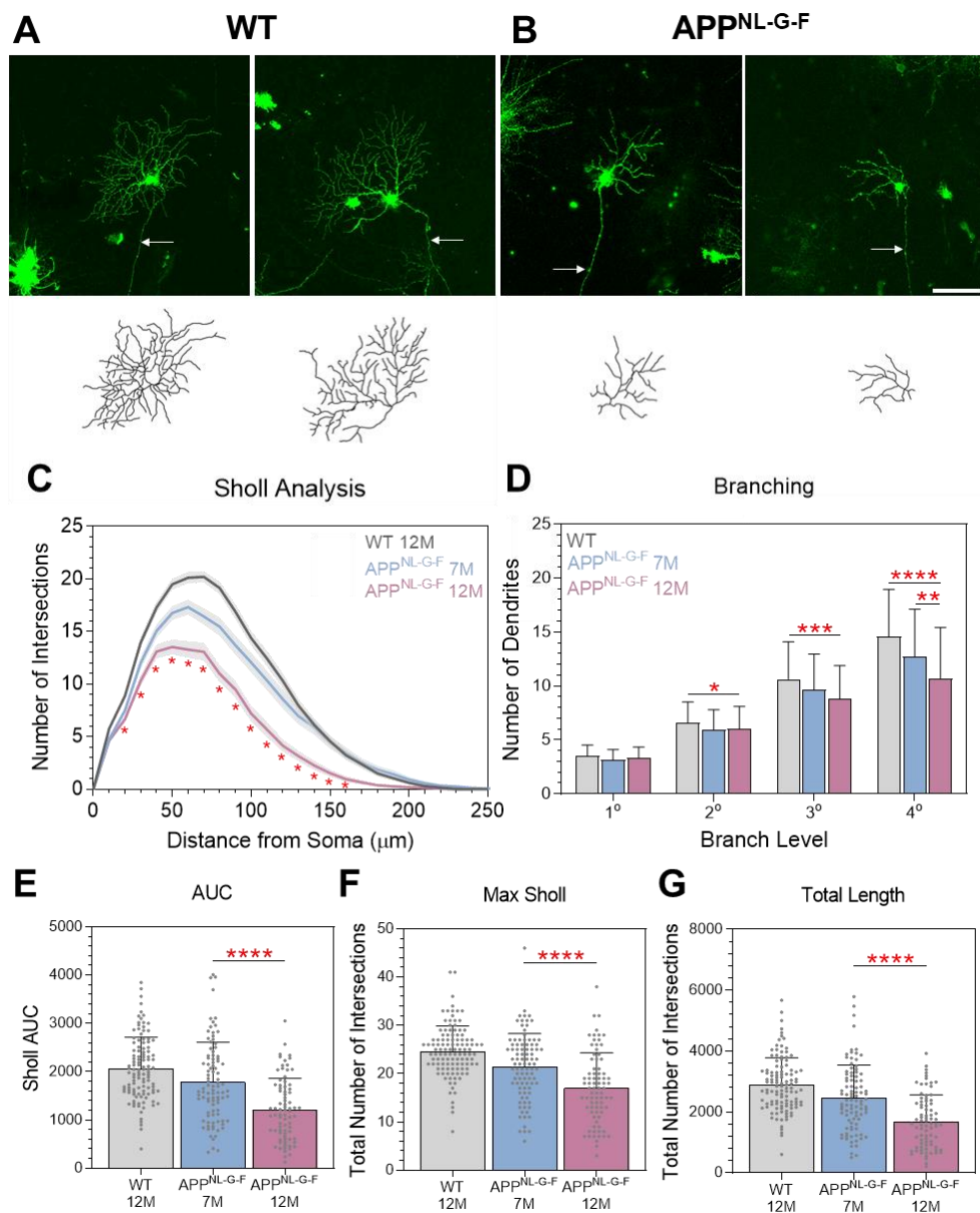


Figure 3.12 RGC dendritic atrophy in APP^{NL-G-F} mice. (A-B) DiOlistic labelled RGCs from WT and APP^{NL-G-F} mice from mice aged 12 months. Arrows indicate RGC axon. Scale bar: 100 μm . (C) Sholl analysis of reconstructed RGCs from WT, APP^{NL-G-F} at 7 months and 12 months. Line represents mean of group at each interval, shaded error zones \pm SEM. Two-tailed Mann-Whitney U test at each interval distance, * = $p < 0.05$. (D) Number of dendrites at each branching level proximal to cell body. (E) Area under the Sholl curve. (F) Maximum number of Sholl intersections. (G) Total length of all dendrites. Column Scatterplots: data represent individual cells and error bars correspond to SD. WT: $n = 114$ cells (10 mice, 5 male/5 female), APP^{NL-G-F} 7M: $n = 94$ cells (7 mice, 4 male/3 female) and APP^{NL-G-F} 12M: $n = 80$ cells (6 mice, 3 male/3 female). Two group comparisons were made using the Mann Whitney U test. * = $p < 0.05$, ** = $p < 0.01$, *** = $p < 0.001$, **** = $p < 0.0001$. Abbreviations: WT, wildtype; M, male; F, female; AUC, area under the Sholl curve; 7M, seven months; 12M, twelve months.

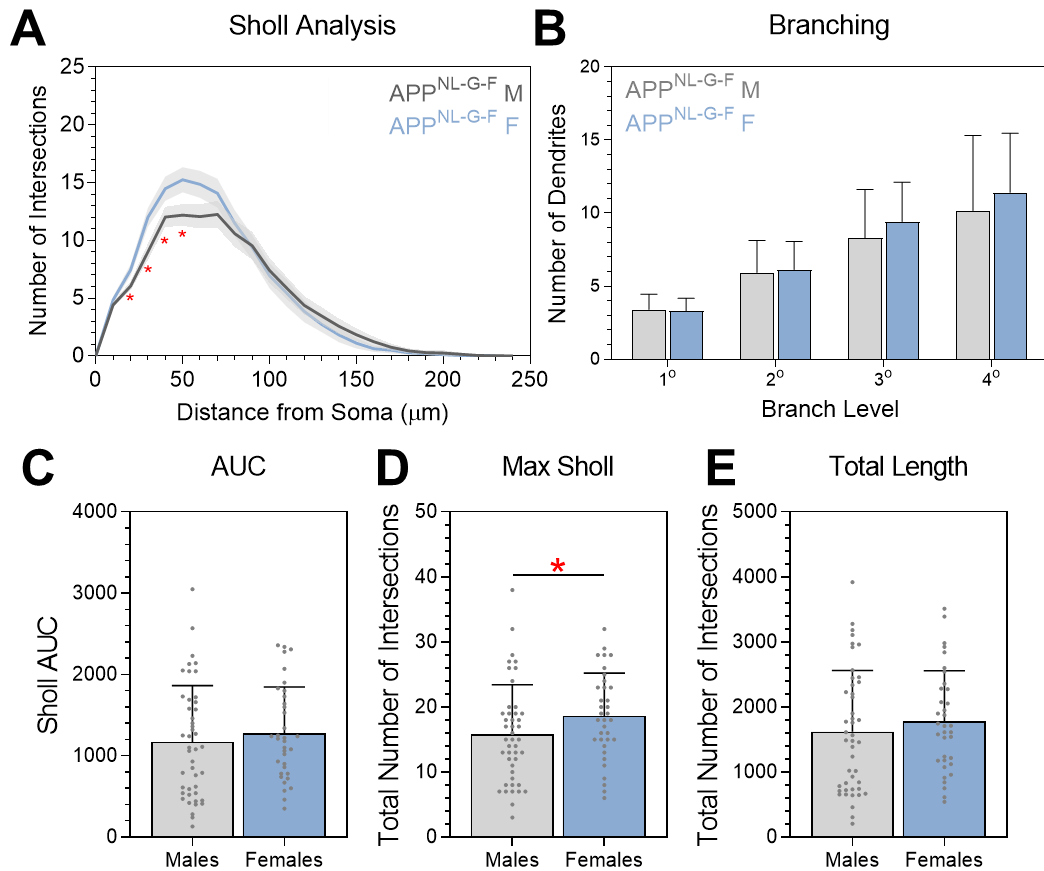


Figure 3.13 Minimal effect of gender on RGCs in APP^{NL-G-F} mice. (A) Sholl analysis of reconstructed RGCs from APP^{NL-G-F} at twelve months separated into males and females. Line represents mean of group at each interval, shaded error zones \pm SEM. Two-tailed Mann-Whitney U test at each interval distance, $* = p < 0.05$. (B) Number of dendrites at each branching level proximal to cell body. (C) Area under the Sholl curve. (D) Maximum number of Sholl intersections. (E) Total length of all dendrites. Column Scatterplots: data represent individual cells and error bars correspond to SD. Male APP^{NL-G-F} at 12 months: $n = 45$ cells (3 mice) and female APP^{NL-G-F} at 12 months: $n = 35$ cells (3 mice). All mice aged at twelve months. Two group comparisons were made using the Mann-Whitney U test. $* = p < 0.05$, $** = p < 0.01$, $*** = p < 0.001$, $**** = p < 0.0001$. Abbreviations: M, males; F, females; AUC, area under the Sholl curve.

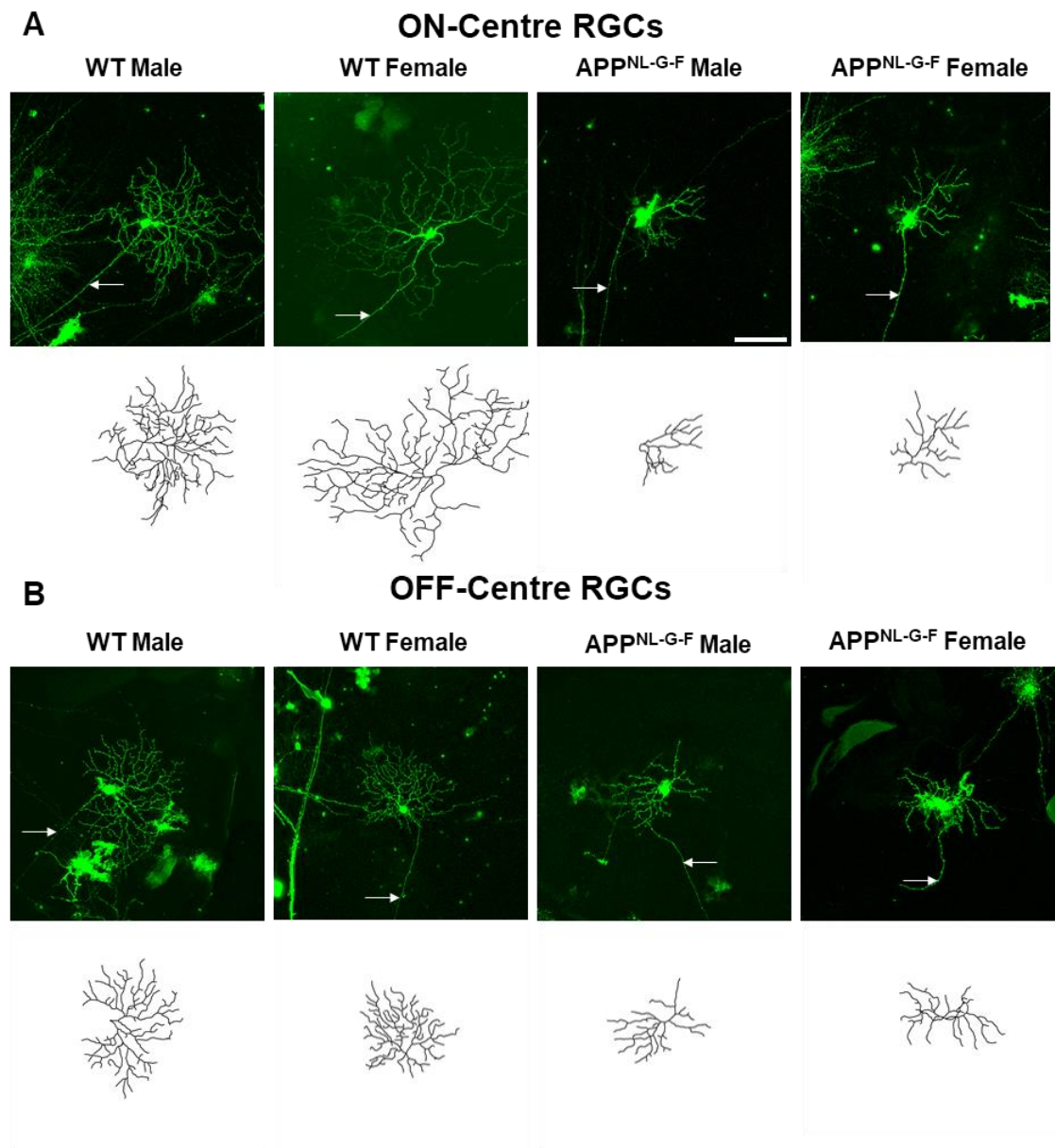


Figure 3.14 RGCs based on receptive field and gender classification in wildtype and APP^{NL-G-F} mice. All mice aged at twelve months old. Arrows indicate RGC axon. Scale bar: 100 μ m. WT, wildtype.

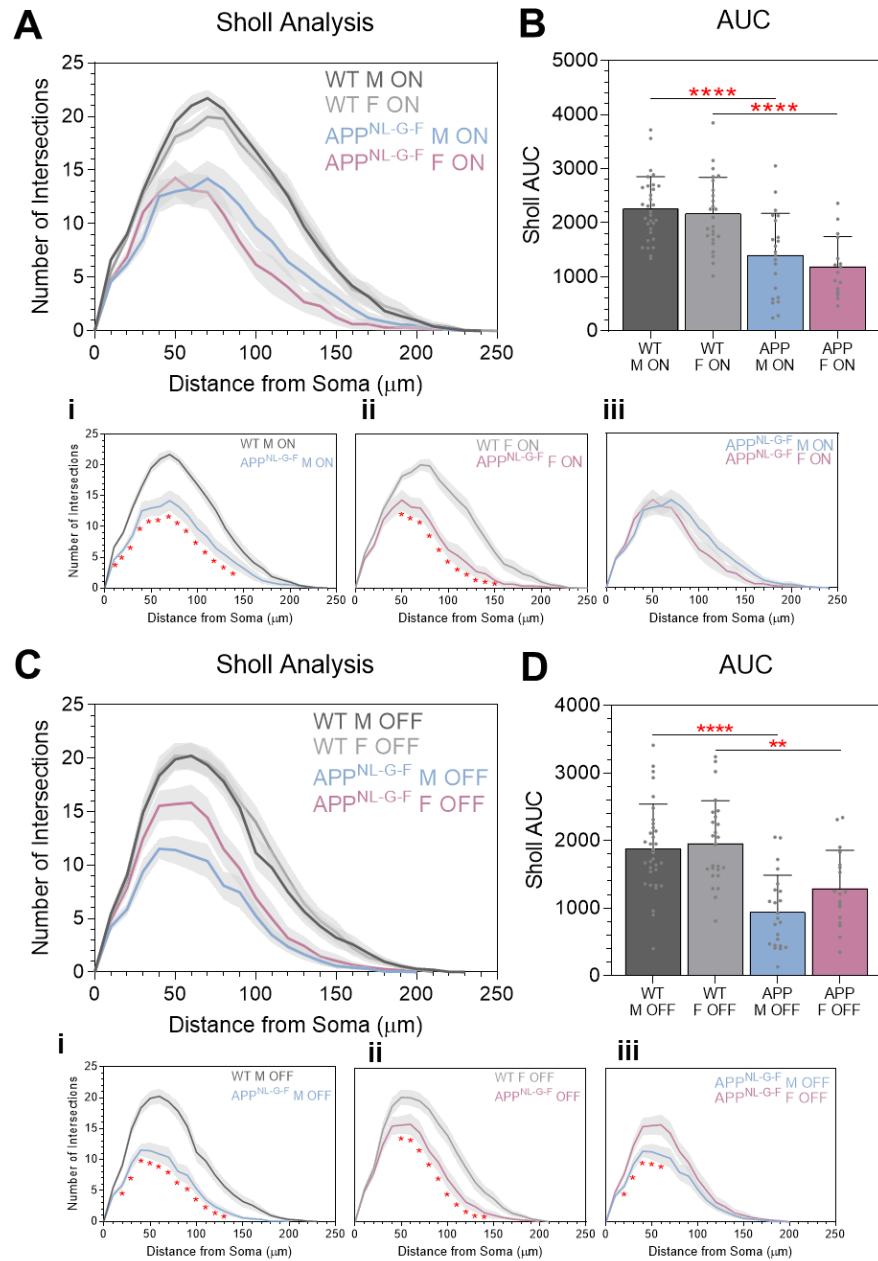


Figure 3.15 RGC receptive field classification in APP^{NL-G-F} mice. (A) Sholl analysis of reconstructed ON-centre RGCs. Line represents mean of group at each interval, shaded error zones \pm SEM. Two-tailed Mann-Whitney U test at each interval distance, * = $p < 0.05$. (B) Area under the Sholl curve for ON-centre RGCs. (C) Sholl analysis of reconstructed OFF-centre RGCs. Line represents mean of group at each interval, shaded error zones \pm SEM. Two-tailed Mann-Whitney U test at each interval distance, * = $p < 0.05$. (D) Area under the Sholl curve for OFF-centred RGCs. Column Scatterplots (B, D): data represent individual cells and error bars correspond to SD. WT-M ON-centre: $n = 31$ cells, WT-M OFF-centre: $n = 33$ cells, WT-F ON-centre: $n = 25$ cells, WT-F OFF-centre: $n = 25$ cells, APP^{NL-G-F}-M ON-centre: $n = 22$ cells, APP^{NL-G-F}-M OFF-centre: $n = 23$ cells, APP^{NL-G-F}-F ON-centre: $n = 16$ cells and APP^{NL-G-F}-F OFF-centre: $n = 18$ cells. All mice aged at twelve months old. Two-way ANOVA was used to determine interaction between two factors (genotype and gender) and Tukey's post hoc test to determine statistical significance. * = $p < 0.05$, ** = $p < 0.01$, *** = $p < 0.001$, **** = $p < 0.0001$. Abbreviations: WT, wildtype; ON, ON-centre RGCs; OFF, OFF-centre RGCs; AUC, area under the Sholl curve; M, males; F, females.

3.4 Discussion

RGCs are the exclusive output neurons of the retina and are vulnerable to degeneration across various pathologies, including AD (Blanks *et al.*, 1989; Blanks *et al.*, 1996; Williams, Thirgood, *et al.*, 2013). In this chapter, I demonstrate that excessive RGC dendritic pruning is a consistent feature in the retina of AD mouse models. Using both amyloid overexpressing (Tg2576, 3xTg-AD) and APP knock-in (APP^{NL-G-F}) AD models, I show that RGCs display substantial excessive dendritic pruning at the age of 12-months in all models. Additionally, the extent of RGC dendritic pruning was associated with age, gender, and receptive field classification in the models. This chapter reinforces the prospective value of retinal analysis as an indicator of neurodegeneration associated with pathology in AD.

The Tg2576 AD mouse model has previously been noted to display retinal pathology and specifically increased RGC dendritic pruning (Williams, Thirgood, *et al.*, 2013); I was able to replicate these initial results and found that excessive RGC dendritic loss was present at 12-months, two months earlier than previously described (14-months). In agreement with the first study, dendritic atrophy and cell loss in the GCL were not major factors in the model. It is therefore likely that changes at a dendritic level reflect the early stages of detectable neurodegeneration.

To further expand on the published work (Williams, Thirgood, *et al.*, 2013), RGCs were divided into ON- and OFF- centre subtypes based on the sublamina dendritic projections into the inner plexiform layer. ON- centre RGCs respond to light stimuli, whereas OFF- centre RGCs respond to dark stimuli. In the Tg2576 AD model, RGC dendritic pruning was more pronounced in ON- centre subtypes, not previously described for the Tg2576 mouse model. ON-centre specific degeneration is a reported feature in other RGC degeneration models, and is likely due to the higher energy demand and number of excitatory glutamatergic synapses for this subtype (Williams *et al.*, 2010). ON-centre RGCs laminate in sublamina b of the IPL, which using *in vivo* scans such as OCT can be delineated from the rest of the IPL. Therefore, monitoring sublamina *b* of the IPL, could provide a more sensitive marker of RGC changes in the AD retina. However, in other eye diseases that feature an increase intraocular pressure OFF-RGCs are more vulnerable (Della Santinaa and Ou, 2017).

To determine whether excessive RGC dendritic pruning is a robust retinal finding in mouse AD models, I next analysed the 3xTg-AD model. This model is well characterised and over expresses transgenes to develop both amyloid and tau pathology (Oddo *et al.*, 2003). Previously, the retinas of 3xTg-AD mice have been shown to display amyloid plaques and neuroinflammation (Grimaldi *et al.*, 2018). The retinas of 3xTg-AD mice are known to display prominent glial activation, particularly in aged mice (Edwards *et al.*, 2014; Salobarar-García *et al.*, 2020). For the first time, I here report that excessive RGC dendritic pruning is also a feature in the retina of aged 3xTg-AD mice. Similar to the Tg2576 retina, RGC dendritic loss was more pronounced in ON- centre subtypes, reinforcing the potential for monitoring sublamina b of the IPL. The 3xTg-AD model has exhibited variation between males and females, with the latter displaying more consistent brain pathology (Carroll *et al.*, 2010; Belfiore *et al.*, 2019). In contrast to these reports, overall, in 3xTg-AD mice, RGC dendritic loss was more prominent in males. However, on closer inspection of the RGC receptive field data, dendritic loss in ON-centre RGCs was similar between males and females. These discrepancies highlight the importance of analysing both genders in transgenic AD mouse models.

To date, AD models have addressed pathology using transgenic overexpression. However, the possibility remains that some reported features may be a confounding effect of overexpression and not reflective of the human disease (Chintapaludi *et al.*, 2020). Knock-in approaches have enabled the development of models that likely better reflect the human disease; APP^{NL-G-F} mice are a promising amyloidosis model (Saito *et al.*, 2014). In line with the findings in Tg2576 and 3xTg-AD models, I here demonstrate that excessive RGC dendritic pruning occurs at 12-months in APP^{NL-G-F} mice. The extent of dendritic loss was consistent between males and females. In contrast to the transgenic models, the burden of dendritic atrophy was similar for ON- and OFF- centre subtypes. These are the first reported data demonstrating RGC dendritic pruning in the retina of APP^{NL-G-F} mice and provide further evidence supporting the contention that RGC changes are a consistent feature in AD mouse models.

AD mouse models develop age-associated pathology and cognitive deficits that reflect to some degree those seen in the human disease; RGC changes were also age-dependent in the three models. In 3xTg-AD mice between the ages of 3- and 6-months, RGC dendritic complexity was comparable to typical wildtype levels; however, at 9-months excess

dendritic loss was detected, which worsened at 12 months and plateaued between 12 and 15 months. Similar age effects were observed in Tg2576, again plateauing after 12 months. The time points at which excessive dendritic loss occurred in the 3xTg-AD and Tg2576 AD mouse models coincide with the reported timing of cognitive impairments and pathology in the brain (Jacobsen *et al.*, 2006). The Tg2576 and 3xTg-AD models have similar timelines for the development of the disease; however, APP^{NL-G-F} mice develop pathology much earlier with amyloid plaques featuring from 2 months, reaching saturation at 7 months (Saito *et al.*, 2014). In the APP^{NL-G-F} model, excessive RGC dendritic pruning was detected earlier (7 months) than in the other two models. These observations suggest that the time course of excessive RGC degeneration reflects that of amyloid pathology and is a consistent feature of AD mouse models.

The underlying mechanisms that trigger to the observed RGC dendritic degeneration in the mouse AD retina are unclear, although, the consistent occurrence of toxic amyloid expression across the three AD models tested potentially highlights its role in driving these events. The relative abundance of amyloid in the retina is known to be far lower than the brain, therefore RGC dendritic loss is unlikely to occur due to the presence of retinal amyloid plaque deposition (Alexandrova *et al.*, 2011). The APP^{NL-G-F} model mice, a model with severe brain amyloid saturation, only displays detectable retinal amyloid plaques in the very old mice (around 18 months) (Vandenabeele *et al.*, 2020). Although the exact function of amyloid is unclear, recent findings highlight the role in synaptic function (Kent *et al.*, 2020). As retinal ganglion cells are one of the most energy demanding and vulnerable neuronal subpopulation in the CNS (Yu *et al.*, 2013), and there is evidence of ON-centre specific RGC vulnerability (Williams *et al.*, 2010), it remains plausible that the expression of toxic amyloid in the retina can drive synaptic/dendritic loss in the AD retina.

Nevertheless, it must not be excluded that retrograde signal transmissions along RGC axons results in RGC degeneration due to the substantial pathology occurring across the brain. RGCs, are susceptible to pathology outside of the retina as their axons terminate in the brain. Due to the high abundance of amyloid plaque pathology and activate status of neuroinflammation activity in the brains of the AD models, the lack of amyloid plaques in the retina and the timeline of retinal degeneration (RGC dendritic loss occurring after synaptic loss in the hippocampus), may indicate that the retina pathology is, at least in

part, a consequence of the pathology in the brain. Despite this, the detection of retinal changes may reflect ongoing pathology in the brain.

This chapter provides valuable guidance for future translation to the human disease and further studies in AD models. Other have demonstrated the impairment of the visual system in AD transgenic mice that in some cases occurs before neuronal dysfunction in the brain (Criscuolo *et al.*, 2018). *In vivo* imaging, using broad-spectrum light sources such as optical coherence tomography (OCT), has the capacity to detect changes in the optical scattering of the retina (Song *et al.*, 2020). Changes to RGC dendritic arborisation can alter the optical scattering characteristics in the IPL, reflective of degeneration (Jáñez-Escalada *et al.*, 2019; Liu *et al.*, 2019; Nunes *et al.*, 2019). Therefore, *in vivo* imaging to assess the status of RGC dendrites may provide a potential insight into the burden of RGC degeneration in the AD retina.

It is currently unclear whether the burden of RGC changes are reflective of the pathology in the brain; this is a critical question that needs to be addressed. In the next Chapter, I will address this question by measuring synaptic densities (dendritic spines) in the three AD models.

Chapter 4. Hippocampal dendritic spine loss in mouse models of Alzheimer's disease.

4.1 Introduction

Neuronal loss in the AD brain is a feature of late disease and is accompanied by amyloid and tau pathology. In the AD brain, the burden of neuronal loss influences the status of cognitive function. During the asymptomatic stages of the disease, which can last several decades, excessive synaptic pruning is detected in areas of the brain susceptible to pathology long before other neuropathological hallmarks (Driscoll and Troncoso, 2011). Indeed, quantification of synaptic loss, rather than neuronal loss, best correlates with the burden of cognitive impairment and disease severity (Spires-Jones and Hyman, 2014). Therefore, it is necessary to obtain a better understanding of synaptic changes related to AD pathology in models and man.

The hippocampus is crucial for the development and storage of memories, learning and emotions; however, it is also the region of the brain that is most susceptible to AD pathology (Van Strien *et al.*, 2009; Mu and Gage, 2011). In severe AD cases, the hippocampal pathology can be detected on a macroscopic level with extensive atrophy reflective of neuronal loss (Henneman *et al.*, 2009). Similar to other affected brain regions, the hippocampus features the characteristic neuropathological hallmarks of AD. In early stages of neurodegeneration, while the neuronal cell body remains intact, the cells display dendritic retraction and excessive pruning of synapses. In the hippocampus the CA1 neuronal subfield, the output neurons of the hippocampus, is particularly affected by degeneration, demonstrated in numerous human and animal AD studies (Jaworski *et al.*, 2011; Li *et al.*, 2020). Animal models have enabled more detailed analysis; indeed, transgenic AD models reveal dendritic and synaptic pruning in the hippocampus in the vicinity of amyloid plaques associated with microglia-mediated synaptic engulfment (Price *et al.*, 2014; Spires-Jones and Hyman, 2014; Shi *et al.*, 2017).

Synapses are the contact sites for communication between neurons and are continuously refined based on neuronal activity. Synapses comprise pre- and post-synaptic terminals. On excitatory neurons, post-synaptic sites are structured as dendritic spines, small

protrusions from the dendritic shaft. Synapses are highly dynamic with the relative size of the postsynaptic density related to the capacity of memory storage (Chklovskii, 2004). The loss of synapses is a frequent observation in AD mouse models, especially in the hippocampus and other areas of pathology. Dendritic spines are classified based on morphology which gives an indication of their functional roles. Larger, mushroom-shaped spines are important for the development of stable, long-term memory storage and are capable of generating the largest excitatory response. Long and thin spines reflect extremely plastic synapses capable of forming mature stable synapses. It is believed that thin spines denote synaptic resilience and the capacity to adjust to neuronal activity (Boros *et al.*, 2017). Small and stubby spines reflect immature synapses that have the potential to develop into more robust synapses. The loss of mushroom and thin spines is a feature of AD mouse models, likely due to amyloid altering F-actin cytoskeletal proteins that regulate the postsynaptic site (Lanz *et al.*, 2003; Zhang *et al.*, 2015).

In this chapter, I characterise CA1 hippocampal dendritic spine density and morphology in overexpressing (Tg2576, 3xTg-AD) and knock-in (APP^{NL-G-F}) AD mouse models. The findings in the chapter provide further evidence for synaptic pruning in the hippocampus of AD mouse models which occur alongside the previous reported evidence of excessive RGC dendritic pruning.

4.2 Experimental Setup

In this chapter I assessed the density and morphology of CA1 hippocampal dendritic spines in the Tg2576, 3xTg-AD and APP^{NL-G-F} mouse models of AD. See Chapter 2 for a detailed description of the protocols used to assess dendritic spine coverage and morphological classification. Figure 4.1 presents an overview of the methods used in this chapter for the assessment of CA1 dendritic spine coverage in AD models by DiOlistic labelling.

Dendritic spines were analysed in Tg2576, 3xTg-AD and APP^{NL-G-F} mice, the same cohorts used in Chapter 3 for assessing RGC dendrites. For the Tg2576 model, male mice were analysed at 12 and 15 months. For the 3xTg-AD model, dendritic spines were analysed at 3, 6, 9, 12 and 15 months, key time-points in the disease progression. Where possible, both male and female 3xTg-AD mice were analysed. APP^{NL-G-F} mice were analysed at 7 and 12 months for both genders. All models were compared to wildtype mice at 12 months, however, additional littermate wildtypes were included when assessing the Tg2576 cohort.

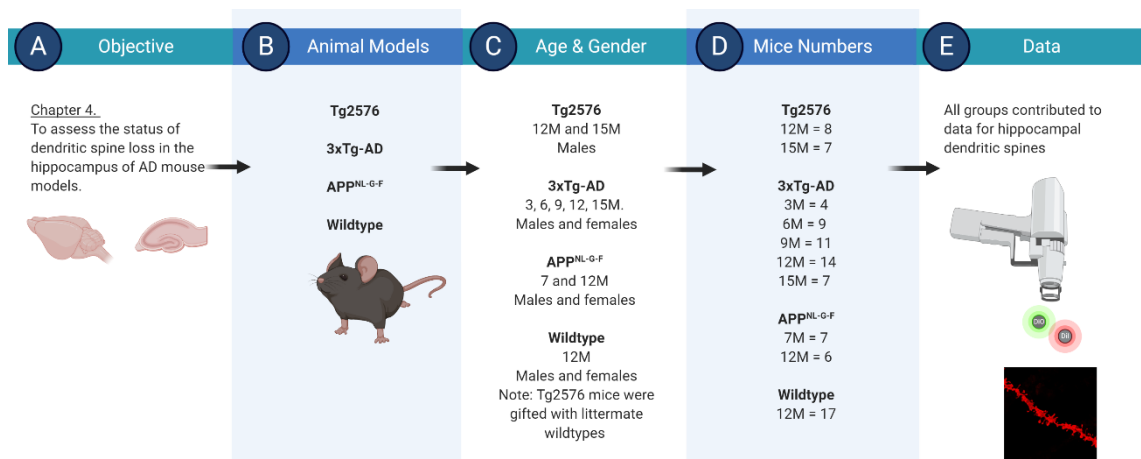


Figure 4.1 Experimental overview for Chapter 4 addressing CA1 hippocampal dendritic spine coverage in AD mouse models. (A) Main objectives for Chapter 4. (B) The different animal models used in these chapters. (C) More details on the animal models including ages analysed and genders available. (D) Number of total mice analysed that were subjected to DiOlistic labelling. (E) All groups in Chapter 4 were analysed for hippocampal dendritic spine coverage. Illustration created in BioRender,

4.3 Results

4.3.1 Tg2576

4.3.1.1 Dendritic spine loss in the hippocampus of Tg2576 AD mice

First, I assessed the Tg2576 AD model for the dendritic spine density on CA1 hippocampal neurons. DiOlistic labelled dendritic segments from wildtype and Tg2576 mice were reconstructed and quantified for dendritic spines (Figure 4.2A-C). Comparing all the segments revealed a significant reduction (13%, $p = 0.0012$) in the spine density of Tg2576 mice compared to wildtype at 12 months (Figure 4.2D). Ageing the Tg2576 model to 15 months, revealed age-associated progressive spine loss (further 17% reduction vs 12 months, $p = 0.0018$; Figure 4.2D). Classification of spines into their respective morphological groups showed that thin spines were the most affected spine type (Figure 4.2E-G). Significant mushroom spine loss was also evident in the Tg2576 mice at 15 months, while stubby spines remained constant between groups. Separating the dendritic segments by mouse further reinforced the observed loss of dendritic spines (Figure 4.2H-K). These results demonstrate that CA1 neurons in the hippocampus of Tg2576 mice display progressive dendritic spine loss.

4.3.2 3xTg-AD

4.3.2.1 Dendritic spine loss in the hippocampus of 3xTg-AD mice

Next, the 3xTg-AD model was assessed for dendritic spine density of hippocampal CA1 neurons (representative examples, Figure 4.3A-B). There was significant reduction in the spine density in 3xTg-AD mice compared to wildtype at 12 months (23%, $p < 0.0001$; Figure 4.3C). For the different spine types (Figure 4.3D-F), stubby and thin spines were the most affected in the 3xTg-AD mice. In contrast, the number of mushroom spines were not different between the groups. Separating the dendritic segments by mouse further reinforced the observed loss of dendritic spines (Figure 4.3G-J). These findings demonstrate that the hippocampus in 3xTg-AD mice displays dendritic spine loss.

4.3.2.2 Female 3xTg-AD mice show greater spine loss

The data from 3xTg-AD mice were divided based on gender. Both male and female 3xTg-AD mice exhibited significantly reduced spine densities compared to respective gender-matched wildtypes. However, female 3xTg-AD mice were significantly worse than male 3xTg-AD mice (reduction of 14% in female 3xTg-AD mice, $p = 0.0014$; Figure 4.4A). Classification of the dendritic spines into their respective morphological groups (Figure 4.4B-D) revealed that loss of thin spines was predominant for both males and females. Mushroom spines were significantly lower in number in female 3xTg-AD mice compared to males. In contrast, stubby spines were reduced in male 3xTg-AD mice due to higher baseline densities in wildtype males. Separating the dendritic segments by mouse further reinforced the observed loss of dendritic spines (Figure 4.4E-H). These results indicate that hippocampal dendritic spine loss occurs in both genders in the 3xTg-AD model, with females the most affected.

4.3.2.3 Dendritic spine loss occurs in older 3xTg-AD mice

The data above show that 3xTg-AD mice at 12 months display dendritic spine loss on CA1 neurons; to learn more about the time-course of spine loss, 3xTg-AD were assessed across various ages. Quantifying synapse number across all the dendritic segments collected from 3xTg-AD mice at 3, 6, 9, 12 and 15 months demonstrated progressive spine loss (Figure 4.5A). Up to 6 months of age, 3xTg-AD mice did not exhibit any overall spine loss when compared to wildtype aged 12 months; at 9 months, significant spine loss was found. Morphological classification showed that both mushroom and thin spines were the most affected in the 3xTg-AD mice at different ages, while stubby spines remained constant (Figure 4.5B-D). Separating the dendritic segments by mouse further reinforced the observed loss of dendritic spines (Figure 4.5E-H). These results show that dendritic spine loss occurs in the 3xTg-AD model and increase with age.

4.3.3 APP^{NL-G-F}

4.3.3.1 Dendritic spine loss in the hippocampus of APP^{NL-G-F} mice.

APP^{NL-G-F} AD model mice displayed CA1 hippocampal dendritic spine loss at 12 months compared to wildtypes at the same age (representative examples, Figure 4.6A-B). Dendrites from all the segments analysed displayed a marked and significant reduction (17%, $p < 0.0001$) in spine density of APP^{NL-G-F} mice compared to wildtype at 12 months (Figure 4.6C). Classification into their respective spine morphological groups (Figure 4.6D-F) demonstrated that only thin spines were altered in the APP^{NL-G-F} mice compared to wildtype. Both mushroom and stubby spines were comparable to wildtype. Separating the dendritic segments by mouse further reinforced the observed loss of dendritic spines (Figure 4.6G-J). These results demonstrate that APP^{NL-G-F} mice at 12 months display significant hippocampal dendritic spine loss.

4.3.3.2 Dendritic spines in APP^{NL-G-F} mice are affected equally in males and females at 12 months.

The APP^{NL-G-F} dataset was separated by gender to determine whether there was a difference between males and females. This analysis demonstrated that there were no differences between male and female APP^{NL-G-F} mice; both genders showed significantly reduced dendritic spine density indicating overall spine loss compared to gender-matched wildtypes (15% for males $p = 0.0034$ and 20% for females $p = 0.0012$; Figure 4.7A-H). Spine classification demonstrated that thin spines were decreased in both genders compared to wildtype; stubby spines were reduced in males but not females, while mushroom spines were not different between groups. These data demonstrate that CA1 hippocampal neuron dendritic spine densities are reduced in male and female APP^{NL-G-F} mice.

4.3.3.3 APP^{NL-G-F} dendritic spine loss occurs by 7 months

Next, I assessed whether spine loss occurred at an earlier age in the APP^{NL-G-F} AD model. APP^{NL-G-F} mice were analysed at 7 and 12-month-old. Overall spine density was significantly decreased in the 7-month APP^{NL-G-F} mice compared to at 12 months (7%

reduction $p = 0.0393$; Figure 4.8A). Morphological classification revealed that only thin spines were reduced in the 7 month APP^{NL-G-F} mice; the numbers of stubby and mushroom spines were comparable between the two groups (Figure 4.8B-D). Separating the dendritic segments by mouse further reinforced the observed loss of dendritic spines (Figure 4.8E-H). These observations demonstrate significant CA1 hippocampal neuron dendritic spine loss in 7-month-old APP^{NL-G-F} mice compared to 12 months.

4.3.3.4 Dendritic spines in APP^{NL-G-F} mice are affected equally in males and females at 7 months.

The results prompted the question whether APP^{NL-G-F} spine loss displayed any gender disparities. Reconstructed spines were grouped based on gender for both the 7 and 12-month APP^{NL-G-F} dataset. Analysis of dendritic spine density from all segments showed a significant reduction in overall spine density between male APP^{NL-G-F} mice at 7 and 12 months (Figure 4.9A). Classification by spine type revealed that thin spines were decreased with age in males with stubby and mushroom spines unchanged (Figure 4.9B-D). Separating the dendritic segments by mouse did not display any significant changes between the groups (Figure 4.9E-H). These results indicate that gender does not influence CA1 dendritic spine density in the APP^{NL-G-F} model.

4.3.4 Comparison between CA1 spines and RGC dendrites

In light of these data highlighting CA1 spine loss in the same AD mouse models in which I had earlier demonstrated RGC dendrite loss, I explored whether these two events correlated in the same mice. Correlations analyses were performed on the average AUC of the Sholl profiles of the RGCs compared with the overall spine density in each of the three AD mouse models and wildtype mice at twelve months. These revealed weak correlation between the overall dendritic spine density and RGC complexity, which was only significant in the APP^{NL-G-F} model ($r = 0.615$, $p = 0.028$) (Figure 4.10A). Interestingly, the density of thin spines better correlated with RGC dendritic complexity in all three models, most notably in 3xTg-AD ($r = 0.696$, $p = 0.005$) and APP^{NL-G-F} mice ($r = 0.670$, $p = 0.015$) (Figure 4.10B). These data demonstrate that the reduction in CA1 hippocampal spine density correlated with the dendritic complexity of RGCs in all three AD models.

4.3.5 Figures

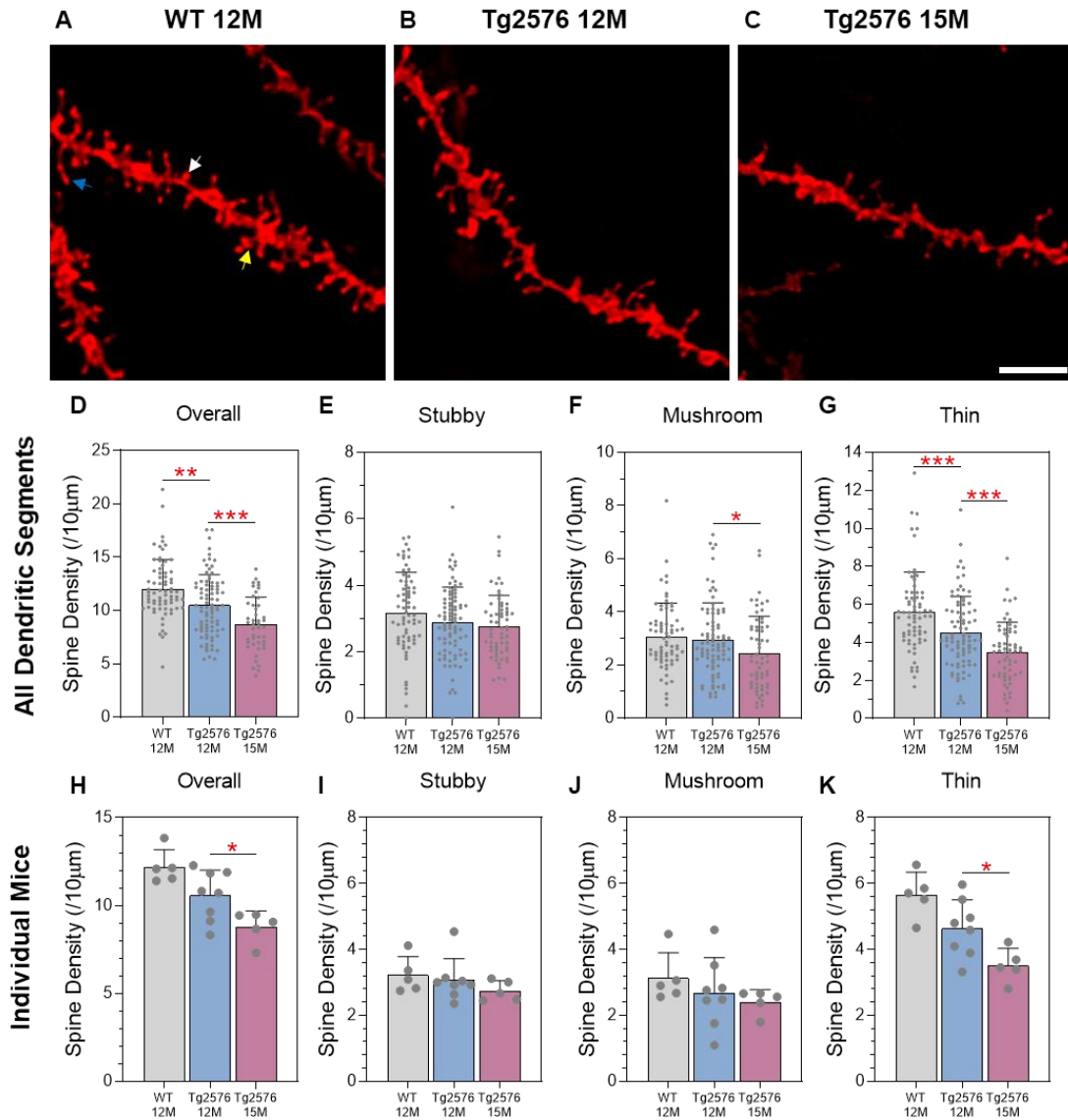


Figure 4.2 CA1 dendritic spine loss in Tg2576 AD mice. (A-C) DiO1istic labelled CA1 apical dendrites from WT aged at twelve months and Tg2576 mice aged at twelve and fifteen months. Arrows indicate spine morphology: stubby (white arrows), mushroom (yellow arrows), thin (blue arrows). Scale bar 5 µm. (D-G) Spine densities across all dendritic segments and (H-K) spine densities across all individual mice for overall, stubby, mushroom and thin groups. WT: $n = 71$ dendrites (5 mice), Tg2576 twelve-months old: $n = 85$ dendrites (8 mice) and Tg2576 fifteen-months old: $n = 61$ dendrites (5 mice). All mice were male with spine densities collected from an average of 30 µm dendritic segments. Column Scatterplots (D-G): data represent individual dendritic segments and error bars correspond to SD. Column Scatterplots (H-K): data represent the mean spine density from individual mice and error bars correspond to SD. Two group comparisons were made using the Mann-Whitney U test or unpaired T-test based on normality testing. * = $p < 0.05$, ** = $p < 0.01$, *** = $p < 0.001$, **** = $p < 0.0001$. Abbreviations: WT, wildtype; 12M, twelve-months old; 15M, fifteen-months old.

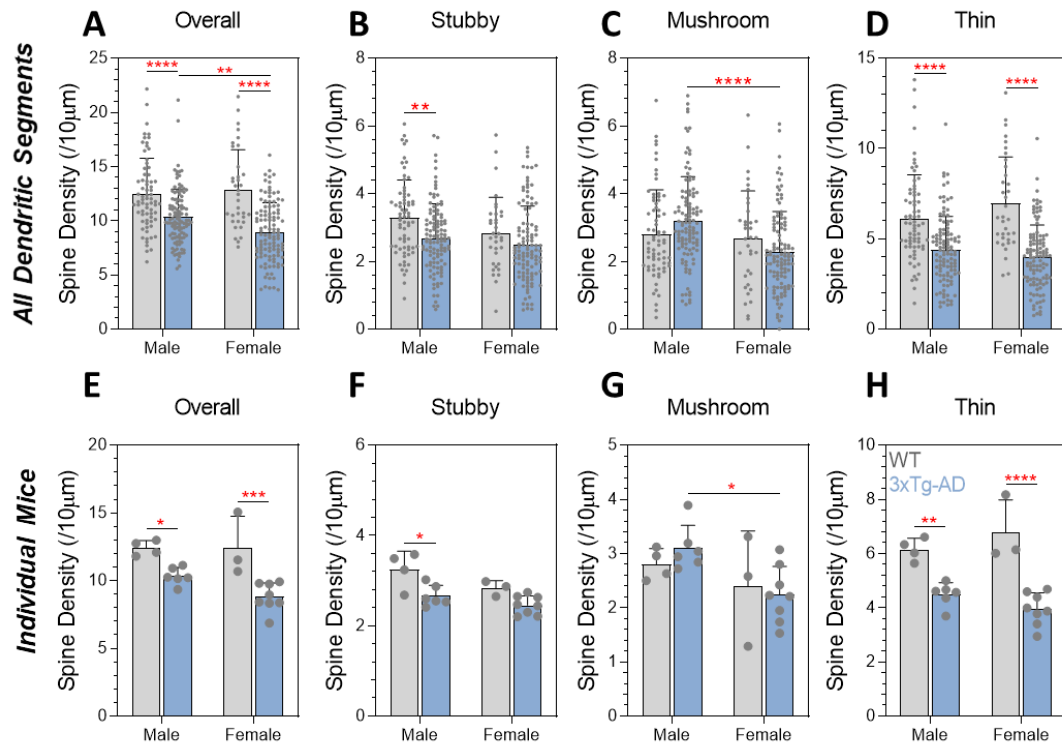


Figure 4.4 Greater spine loss in female 3xTg-AD mice. (A-D) Spine densities across all dendritic segments and (E-H) spine densities across all individual mice for overall, stubby, mushroom and thin groups. WT M: $n = 71$ dendrites (4 mice), WT F: $n = 35$ dendrites (3 mice), 3xTg-AD M: $n = 112$ dendrites (6 mice), 3xTg-AD F: $n = 111$ dendrites (8 mice). Spine densities collected from an average of 30 μm dendritic segments. Column Scatterplots (A-D): bars, mean of group; data represent individual dendritic segments and error bars correspond to SD. Column Scatterplots (E-H): data represent the mean spine density from individual mice and error bars correspond to SD. Two-way ANOVA was used to determine interaction between two factors (genotype and gender) and Tukey's post hoc test to determine statistical significance. * = $p < 0.05$, ** = $p < 0.01$, *** = $p < 0.001$, **** = $p < 0.0001$. Abbreviations: WT, wildtype.

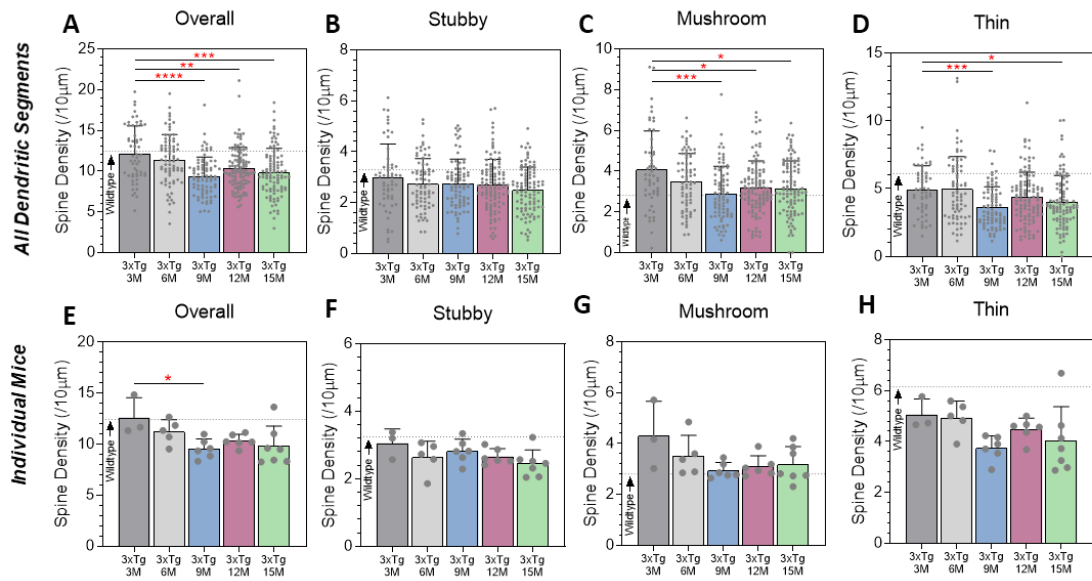
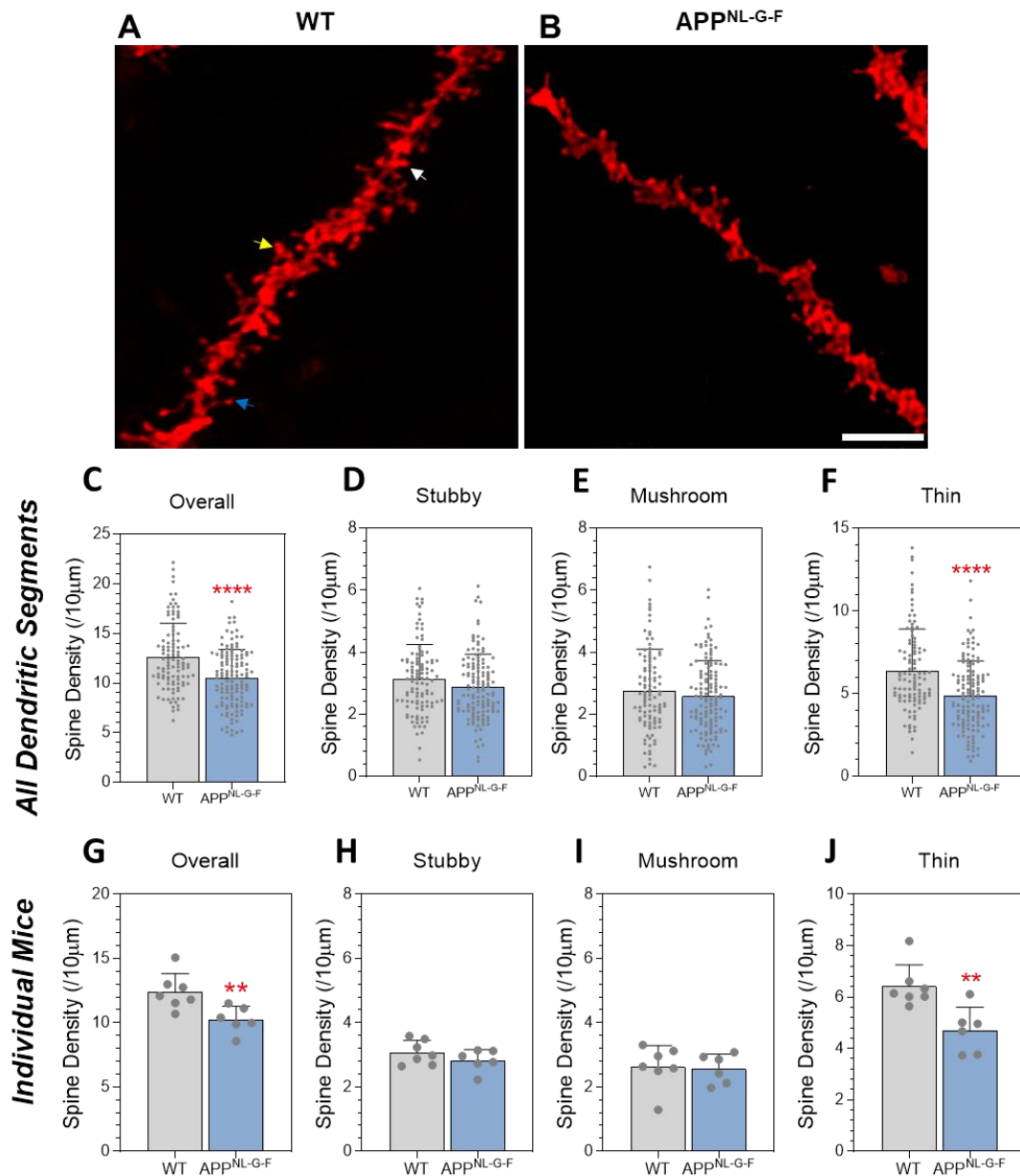


Figure 4.5 Progressive spine loss in 3xTg-AD mice. (A-D) Spine densities across all dendritic segments and (E-H) spine densities across all individual mice for overall, stubby, mushroom and thin groups. WT 12M: $n = 71$ dendrites (4 mice), 3xTg-AD 3M: $n = 56$ dendrites (3 mice), 3xTg-AD 6M: $n = 71$ dendrites (5 mice), 3xTg-AD 9M: $n = 81$ dendrites (6 mice), 3xTg-AD 12M: $n = 112$ dendrites (6 mice), 3xTg-AD 15M: $n = 100$ dendrites (7 mice). Spine densities collected from an average of 30 μm dendritic segments. Column Scatterplots (A-D): bars, mean of group; data represent individual dendritic segments and error bars correspond to SD. Column Scatterplots (E-H): bars, mean of group; data represent the mean spine density from individual mice and error bars correspond to SD. Multiple groups were compared by nonparametric one-way analysis of variance (Kruskal–Wallis test) using Dunn multiple comparisons post-test. * = $p < 0.05$, ** = $p < 0.01$, *** = $p < 0.001$, **** = $p < 0.0001$. Abbreviations: WT, wildtype.



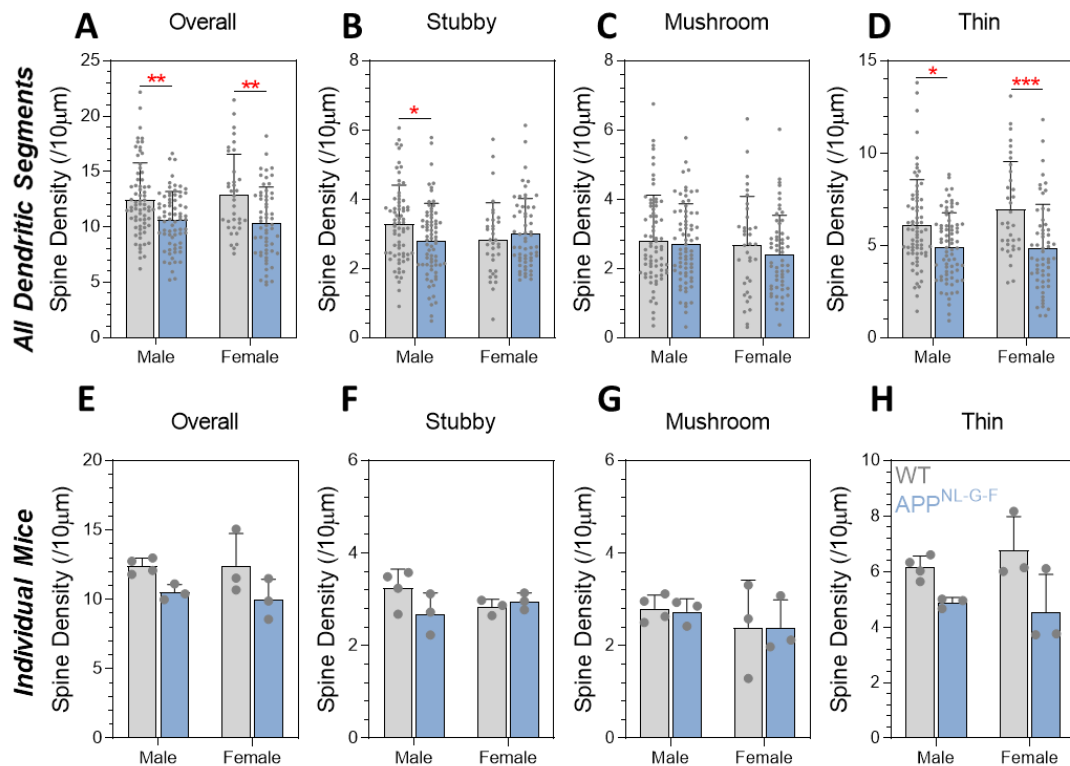


Figure 4.7 Gender effect on spine density in APP^{NL-G-F} mice. (A-D) Spine densities across all dendritic segments and (E-H) spine densities across all individual mice for overall, stubby, mushroom and thin groups. WT 12M M: $n = 71$ dendrites (4 mice), WT 12M F: $n = 35$ dendrites (3 mice), APP^{NL-G-F} 12M M: $n = 72$ dendrites (3 mice), APP^{NL-G-F} 12M F: $n = 58$ dendrites (3 mice). Spine densities collected from an average of 30 μm dendritic segments. Column Scatterplots (A-D): data represent individual dendritic segments and error bars correspond to SD. Column Scatterplots (E-H): data represent the mean spine density from individual mice and error bars correspond to SD. Two-way ANOVA was used to determine interaction between two factors (genotype and gender) and Tukey's post hoc test to determine statistical significance. * = $p < 0.05$, ** = $p < 0.01$, *** = $p < 0.001$, **** = $p < 0.0001$. Abbreviations: M, males; F, females; 12M, twelve months. WT, wildtype.

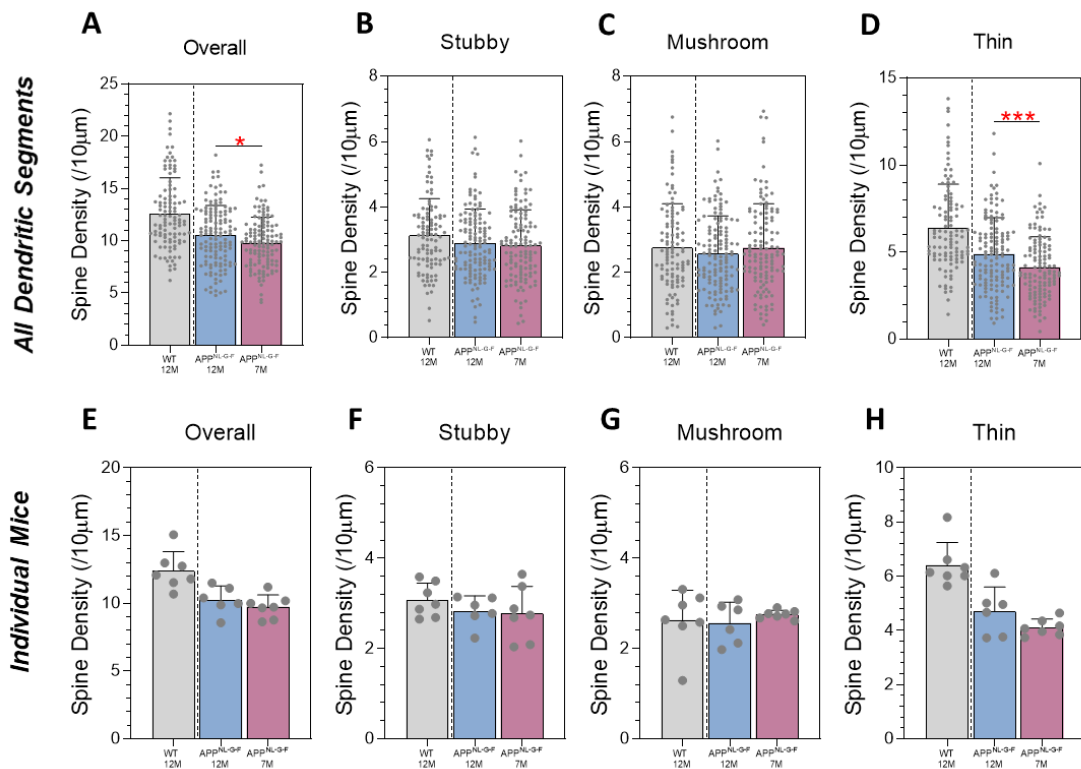


Figure 4.8 APP^{NL-G-F} CA1 dendritic spines at 7 months. (A-D) Spine densities across all dendritic segments and (E-H) spine densities across all individual mice for overall, stubby, mushroom and thin groups. WT: $n = 106$ dendrites (7 mice, 4 males/3 females), APP^{NL-G-F} 12M: $n = 130$ dendrites (6 mice, 3 males/3 females), APP^{NL-G-F} 7M: $n = 122$ dendrites (7 mice, 4 males/3 females). Spine densities collected from an average of 30 μ m dendritic segments. Column Scatterplots (A-D): data represent individual dendritic segments and error bars correspond to SD. Column Scatterplots (E-H): data represent the mean spine density from individual mice and error bars correspond to SD. Two group comparisons were made using the Mann-Whitney U test or unpaired t-test based on normality testing. * = $p < 0.05$, ** = $p < 0.01$, *** = $p < 0.001$, **** = $p < 0.0001$. Abbreviations: WT, wildtype.

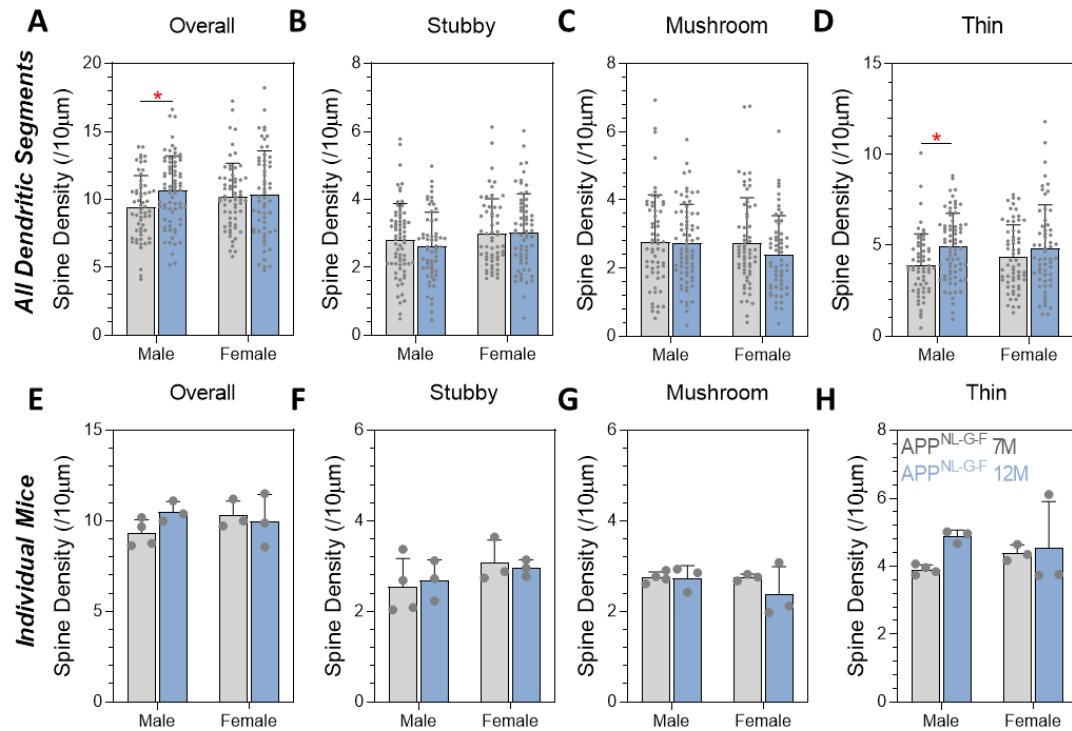


Figure 4.9 Influence of gender on CA1 spines in APP^{NL-G-F} mice. (A-D) Spine densities across all dendritic segments and (E-H) spine densities across all individual mice for overall, stubby, mushroom and thin groups. APP^{NL-G-F} 7M M: $n = 59$ dendrites (4 mice), APP^{NL-G-F} 7M F: $n = 63$ dendrites (3 mice), APP^{NL-G-F} 12M M: $n = 72$ dendrites (3 mice), APP^{NL-G-F} 12M F: $n = 58$ dendrites (3 mice). Spine densities collected from an average of 30 μm dendritic segments. Column Scatterplots (A-D): data represent individual dendritic segments and error bars correspond to SD. Column Scatterplots (E-H): bars, mean of group; data represent the mean spine density from individual mice and error bars correspond to SD. Two-way ANOVA was used to determine interaction between two factors (genotype and gender) and Tukey's post hoc test to determine statistical significance. * = $p < 0.05$, ** = $p < 0.01$, *** = $p < 0.001$, **** = $p < 0.0001$. Abbreviations: M, males; F, females; 7M, seven months; 12M, twelve months.

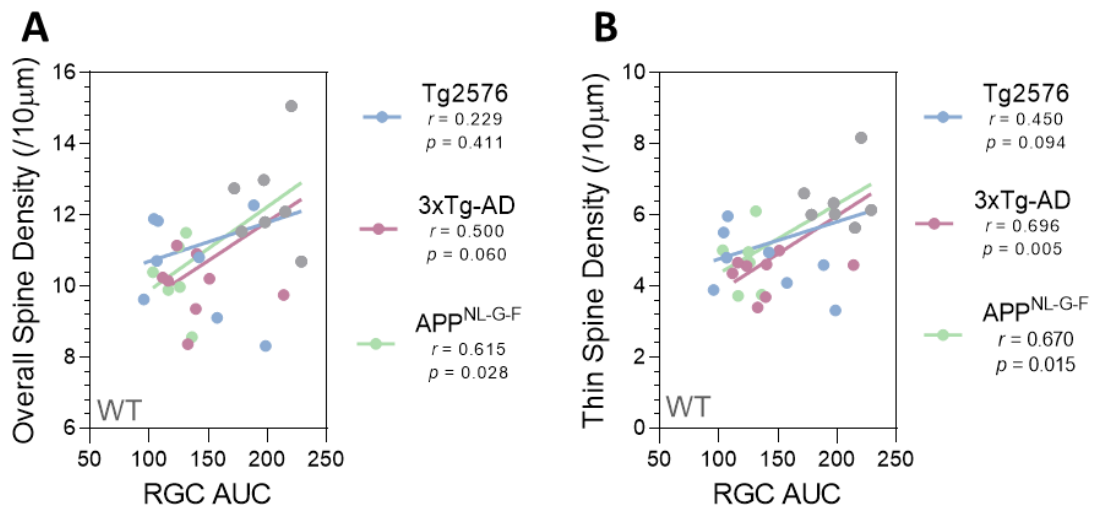


Figure 4.10 CA1 dendritic spines correlate with RGC complexity in Tg2576, 3xTg-AD and APP^{NL-G-F}. Spearman r correlations. All mice twelve months. WT $n = 7$ mice, Tg2576 $n = 8$ mice, 3xTg-AD $n = 8$ mice, APP^{NL-G-F} $n = 6$ mice. Abbreviations: WT, wildtype; AUC, Area under the Sholl curve.

4.4 Discussion

Neurodegeneration is a prominent feature in the AD brain and the extent of synaptic loss corresponds to the progression and severity of the disease (Colom-Cadena *et al.*, 2020). Dendritic spines are the sites of excitatory glutamatergic synaptic contacts and plasticity for memory function; reduced spine density is therefore a measure of synaptic loss in the AD brain. In this chapter, I demonstrate that CA1 hippocampal neurons demonstrate excessive pruning of dendritic spines in AD mouse models. Using the Tg2576, 3xTg-AD and APP^{NL-G-F} AD models, I observed significant age-associated dendritic spine loss, mainly corresponding to reduced thin spine density. In all three AD models, dendritic spine loss in comparison to wildtypes, with spine loss in the 3xTg-AD and AP^{PNL-G-F} mice correlating with the extent of loss of RGC dendritic complexity shown in earlier Chapters. This chapter reinforces the importance of dendritic spine loss and the susceptibility to excessive pruning in the hippocampus of AD mouse models and shows that these are mirrored by RGC dendritic loss in the same models.

The hippocampus is vulnerable to degeneration in age-related cognitive decline and in neurodegenerative diseases, including AD (O'Shea *et al.*, 2016). Previously, others reported that hippocampal pathology is common and coincides with age-dependent synaptic loss in the Tg2576 AD model (Lanz *et al.*, 2003; Spires *et al.*, 2005; Bittner *et al.*, 2010). The extent of dendritic spine coverage on CA1 neurons was closely associated with amyloid plaque deposition (Spires *et al.*, 2005). In agreement with these studies, I report that dendritic spine density is reduced on CA1 neurons in the hippocampus at 12 months in the Tg2576 AD model, and to a greater extent at 15 months. Spine loss in the Tg2576 model occurs at the time of onset of memory and learning impairments (Jacobsen *et al.*, 2006). Besides the overall reduction in dendritic spine density in the hippocampus, thin spines were identified as the major subtype most affected in Tg2576 AD mice, present at 12 and 15 months. Mushroom spine loss was significant only in the 15-month-old Tg2576 mice. These data overlap with reported behavioural and cognitive changes in the Tg2576 AD mice, with the loss of thin spines during initial stages of the disease and mushroom spines later in the disease at a time of substantial memory impairment (Evans *et al.*, 2020).

In the 3xTg-AD mouse model, others have reported similar cognitive deficits that coincide with synaptic loss in the brain (Belfiore *et al.*, 2019). In agreement with findings in the Tg2576 model, 3xTg-AD mice also displayed a reduction in the dendritic spine coverage on CA1 neurons in the hippocampus. In the 3xTg-AD model, mice displayed reduced spine densities from after 6 months and spine loss increased with age and prominent at 12 months. These observations were congruent with the expected timeline for pathology in the 3xTg-AD model (Oddo *et al.*, 2003). Detection of dendritic spine loss in the 3xTg-AD model is consistent with reports that pathology in these mice is most severe in the hippocampus (Mastrangelo and Bowers, 2008). Mendel *et al.* also report that the 3xTg-AD model displays spine loss and a reduction in the hippocampal dendritic branching (Mendell *et al.*, 2020).

Others have reported a gender discrepancy in the 3xTg-AD mice, whereby females develop more consistent and severe pathology (Carroll *et al.*, 2010). My findings support these studies; female 3xTg-AD mice exhibited greater spine loss indicative of neurodegeneration compared to age-matched males. Female 3xTg-AD mice showed greater loss of mushroom spines, predictive of greater cognitive deficits than in males. The detection of dendritic spine loss after 6 months concurs with similar reports that demonstrate detectable cognitive deficits at this stage (Stover *et al.*, 2015).

As discussed earlier, transgenic models overexpressing amyloid may display artificial phenotypes. Therefore, knock-in approaches such as APP^{NL-G-F} mice may better reflect the human disease (Saito *et al.*, 2014). In this chapter, I demonstrate that excessive dendritic spine loss occurs in the hippocampus of APP^{NL-G-F} mice; compared to the transgenic models, spine loss was detected earlier in APP^{NL-G-F} mice, significantly reduced at the age of 7 months. These differences are congruent with pathology in the model; amyloid plaques are present in the brains of APP^{NL-G-F} mice earlier than the other models, reaching saturation by 7 months (Jankowsky and Zheng, 2017). At 3-4 months APP^{NL-G-F} mice begin synaptic impairment in the cortex, this worsens 6-8 months and extended to the hippocampus, with primarily impairment of postsynaptic sites (Latif-Hernandez *et al.*, 2020). APP^{NL-G-F} mice are reported to display subtle changes to behaviour, which may be reflected by these synaptic changes, occurring before amyloid deposition (Latif-Hernandez *et al.*, 2019). Similar to findings in the Tg2576 and 3xTg-AD models, thin spines were the most affected spine subtype in the APP^{NL-G-F} mice. This

is in contrast to some studies on the APP^{NL-G-F} mouse line which reported the loss of mushroom spines (Zhang *et al.*, 2015). Dendritic spine loss in the hippocampus, especially loss of thin spines, is reported to coincide with onset of deficits in spatial learning and memory during normal ageing (Xu *et al.*, 2018). Thin spines are responsible for the formation of new synapses in an activity-dependent manner and are highly dynamic. Therefore, it is reasonable to propose that the loss of thin spines highlight the earliest and detectable synaptic modification in the AD mouse hippocampus, that is followed by the loss of more established mushroom spines as the disease develops.

Gender discrepancy in the APP^{NL-G-F} model was less apparent than in the 3xTg-AD model; no significant gender differences in synaptic loss were seen in the model. This is in agreement with the current literature (Saito *et al.*, 2014), although as this is a novel AD model it remains possible that gender variation may arise. Collectively, the identification of early dendritic spine loss in the APP^{NL-G-F} model, provides further evidence supporting the role of amyloid in the early stages of neurodegeneration.

Although there are numerous reports of retinal changes in AD models (Grimaldi *et al.*, 2018; Salobar-García *et al.*, 2020), to date, few have compared retinal changes with pathology in the brain in the same mice. The lack of this comparison has created inconsistencies in addressing the importance of retinal changes in AD models. In this chapter I was able to demonstrate excessive synaptic elimination in the hippocampus in AD mice and show that thin spine density correlated in the 3xTg-AD and APP^{NL-G-F} mice with reductions in RGC dendritic complexity. Linking retinal and brain changes will be crucial to further the aim of using the retina to aid in the diagnosis and monitoring of disease severity and progression in AD.

To conclude, I demonstrate that excessive loss of CA1 hippocampal dendritic spines, primarily thin spines, is a consistent feature in AD mouse models in an age-dependent process. A reduction in spine coverage coincided with reduced RGC dendritic complexity in the same mice. These findings provide supporting evidence for ongoing synaptic changes in the mouse AD brain which are mirrored by degeneration in the retina.

Chapter 5. The role of complement in modulating retinal ganglion cell dendritic complexity and CA1 dendritic spines in wildtype and 3xTg-AD mice.

5.1 Introduction

The complement system has a central role in the immune response to protect against infection and injury. In brief, activation of complement can arise through the classical, lectin and alternative pathways, triggering the generation of anaphylatoxins, opsonisation of target surfaces and the formation of the lytic membrane attack complex (Morgan, 2003). Dysregulation of the complement system leads to uncontrolled activation and is a feature of many inflammatory conditions, including neurodegenerative diseases.

During development, components of the classical complement pathway, particularly C1q, localise at synapses triggering microglial-mediated synaptic elimination, essential for the network refinement (Stevens *et al.*, 2007). Complement activation is tightly regulated to ensure normal pruning of synapses in the CNS. However, dysregulation and excessive complement activation leads to excessive synaptic elimination which is a core feature in AD. As discussed earlier, synaptic loss in AD is the strongest correlator to disease severity and progression. It is currently uncertain why and how particular synapses are tagged and eliminated. Therapeutic interventions will likely target neurodegeneration at the earliest possibly opportunity; synaptic loss is a key pathological event in the early stages of the disease.

In AD, synapse loss occurs in the early stages of the disease, potentially during the several years of asymptomatic progression before the appearance of classical hallmark pathologies. Amyloid plaques are deposited across the AD brain and are associated with glial activation producing several complement components (C1q, 'activated' C3, and C4) (Fonseca *et al.*, 2011). Amyloid beta peptides have the capacity to upregulate the production of complement proteins such as C3, recruiting and triggering further glial activation. Through iC3b and the receptor CR3, amyloid plaques are cleared by microglia. In AD mouse models deficient in C3, microglial activation is reduced and leads to synaptic protection which improves cognition (Shi *et al.*, 2015). Currently, synaptic

elimination has only focused on complement components upstream of C3, therefore the role of the terminal pathways in the modulation of synapses is unclear. Evidence of terminal complement activation is observed in the AD brain, primarily through immunohistochemistry evidence (Hakobyan *et al.*, 2016). Collectively, it is becoming increasingly clear that complement has a role in contributing to and exacerbating disease severity in AD.

In the developing retina, the complement system is necessary for appropriate RGC function. C1q is found to tag RGC synaptic terminals in the lateral geniculate nucleus (dLGN) where RGC axons terminate (Stevens *et al.*, 2007). In models of glaucoma, in which RGC dendritic complexity is degenerated, inhibition or deficiency of C1q, the initiator of the classical complement cascade, reduces the extent of RGC dendritic loss offering neuronal protection (Williams *et al.*, 2016). These studies have empathised the role of complement across the CNS highlighting the critical importance during normal development and in models of neurodegeneration.

In this chapter, I describe the impact of various complement deficiencies on RGC dendritic complexity and CA1 hippocampal dendritic spines. Additionally, in the 3xTg-AD model I assessed whether therapeutically inhibiting C5 or deficiency of C3 and C6 offered neuroprotection. The findings in this chapter provide further insights into the role of complement in refining neuronal networks across the CNS.

5.2 Experimental Setup

This chapter assesses the role of the complement system on modulating RGC dendritic complexity and CA1 hippocampal dendritic spines. The data is separated into three sections, the effect of complement deficiency in adult mice, the impact of C3 and C6 deficiency in the 3xTg-AD model and C5 antibody inhibition (mAb BB5.1) in 3xTg-AD mice. Figure 5.1 summarises the experimental plan. Chapter 2 provides a detailed description of the protocols used to assess RGC dendritic complexity and spine densities.

The first section assessed complement related deficiencies $C1q^{-/-}$, $C3^{-/-}$, $C3aR^{-/-}$, and $TREM2^{-/-}$ in wildtype mice. $C1q^{-/-}$ mice are deficient in the C1q protein, the initiator of the classical complement cascade. $C3^{-/-}$ mice are deficient in C3 protein, the central component of the complement system. $C3aR^{-/-}$ mice are deficient in the receptor for C3a. $TREM2^{-/-}$ mice are deficient in a receptor important in binding complement regulators. All models were aged over 3 months and maintained on homozygous lines after several generations. Previously, others report synaptic modulation in the brain of these models during development, it is uncertain whether these are present during adulthood (Ma *et al.*, 2013; Lian *et al.*, 2015; Filipello *et al.*, 2018).

The second section expands on the data generated from Chapter 3 and Chapter 4 in 3xTg-AD model. In the earlier chapters, 3xTg-AD mice displayed excessive RGC dendritic pruning and CA1 hippocampal spine loss. The importance of the complement system in modulating synaptic elimination, both during development and related to pathological changes, is now clear; complement tags synapses for elimination through microglial engulfment of synaptic elements (Stevens *et al.*, 2007). These studies have primarily focused on the classical complement system and upstream complement components. Recently, deficiency of C3 was shown to protect against cognitive decline in AD mice and opened the door to the potential role of downstream complement components in modulating the process of neurodegeneration (Shi *et al.*, 2017). In this section, I assessed whether C3 deficiency could offer protection against 3xTg-AD driven hippocampal CA1 spine density and RGC dendritic degeneration. Although modulation around C3, the central complement component is of therapeutic interest, it remains plausible that terminal complement activation (possibly sub-lytic activation) could have a role in synaptic elimination. I therefore assessed whether C6 deficiency could offer protection

against 3xTg-AD driven hippocampal and RGC degeneration. Due to animal availability, only male mice at 12 months old were analysed.

The last section, in a collaboration with Dr Johnathan Winter, Dr Alison Costigan, Professor B. Paul Morgan and Dr Tim Hughes as part of a GlaxoSmithKline (GSK) funded project, C5 was therapeutically inhibited with the mAb BB5.1 (Frei *et al.*, 1987), in 3xTg-AD female mice. Antibody preparation, administration, animal housing, health checks and other experimental readouts were performed by Dr Tim Hughes, Dr Alison Costigan and Dr Johnathan Winter. This thesis only investigated the impact of C5 inhibition on CA1 dendritic spines in 3xTg-AD mice. BB5.1, or isotype control, was administered twice weekly (0.5mg/animal/dose) via intraperitoneal injections to trigger sustained C5 inhibition between the ages of 6 and 12 months. BB5.1 biweekly dosage administration was necessary based on haemolytic assays (performed by Dr Winter) which supported this schedule for consistent and sustained blockage of systemic levels of C5 in the circulation of 3xTg-AD mice. BB5.1 and isotype control were grown and purified in house with functionality verified through *in vitro* haemolysis assays demonstrating inhibition of C5 with BB5.1.

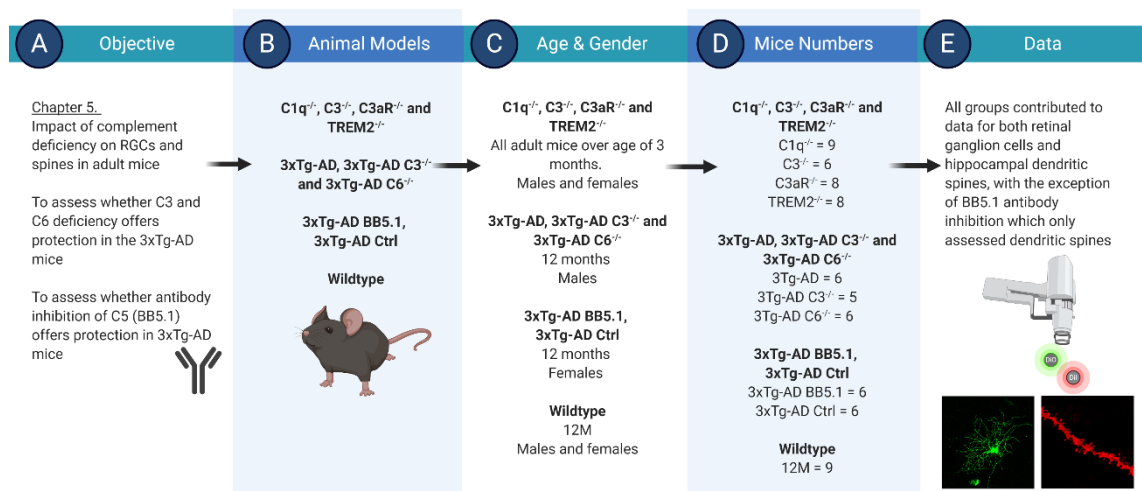


Figure 5.1 Experimental overview of Chapter 5 addressing the impact of the complement system on RGC dendritic complexity and CA1 hippocampal dendritic spine coverage. (A) Main objectives for Chapters 5. (B) The different animal models used. (C) More details on the animal models including ages and genders. (D) Number of total mice analysed that were subjected to DiOlistic labelling. (E) All groups were analysed for RGC dendrites and CA1 hippocampal dendritic spines, except for C5 inhibition which only assessed spine densities. Illustration created in BioRender.

5.3 Results

5.3.1 C1q^{-/-}, C3^{-/-}, C3aR^{-/-} and TREM2^{-/-} mice

In the retina, RGCs were labelled with DiI and DiO in C1q^{-/-}, C3^{-/-}, C3aR^{-/-} and TREM2^{-/-} adult mice. C1q^{-/-} mice were comparable to wildtype up to the peak of the Sholl curve. However, significantly fewer distal dendrites were present and corresponded to a reduced Sholl AUC (between 80 and 150 μm , $p < 0.05$; Figure 5.2A-E). In C3^{-/-} mice, RGC complexity was consistently reduced although not significantly lower than wildtypes. The cumulative decrease in C3^{-/-} RGC complexity subsequently resulted in a significant reduction in the Sholl AUC (11%, $p = 0.0372$) and total dendritic length (13%, $p = 0.0117$), whilst retaining the peak of the Sholl curve (Figure 5.3A-E). In C3aR^{-/-} mice, RGC dendritic complexity was significantly larger than wildtypes. The increased dendritic coverage was localised around the mid-branches (between 40 and 100 μm , $p < 0.05$), which corresponded to a significantly greater Sholl AUC, higher peak of the Sholl curve and greater total dendritic length (Figure 5.4A-E). Finally, TREM2^{-/-} mice displayed RGCs comparable to wildtypes based on the Sholl curve and related parameters (Figure 5.5A-E). Collectively these data highlight that deficiencies in certain components of the complement system can influence RGC dendritic complexity in adult mice.

Next, I assessed in the same mice, CA1 dendritic spines in C1q^{-/-}, C3^{-/-}, C3aR^{-/-} and TREM2^{-/-} mice (Figure 5.6A-E). C1q^{-/-} mice demonstrated significantly greater spine densities (8%, $p = 0.0375$) compared to wildtype. Based on spine subtype classification the increase was accounted for by mushroom spines alone, whilst the number of stubby and thin spines were comparable to wildtype. Conversely, C3^{-/-} mice displayed an overall significant reduction in dendritic spines (18%, $p = 0.0065$), which corresponded to fewer stubby and thin spines compared to wildtype. In C3aR^{-/-} and TREM2^{-/-} mice the density of spines remained constant and did not reveal any significant differences compared to wildtype. These findings demonstrate and emphasise that certain components related to the complement system have the capacity to modulate synaptic densities in the hippocampus of adult mice.

5.3.2 3xTg-AD C3^{-/-} and 3xTg-AD C6^{-/-} mice

Previous data in Chapter 3 demonstrated that RGC dendritic complexity is reduced in the retina of aged 3xTg-AD mice. In this chapter RGCs were morphologically assessed in twelve month 3xTg-AD mice deficient in C3 or C6 of the complement system (Figure 5.7). RGCs in the baseline 3xTg-AD model displayed excessive dendritic pruning with a reduced Sholl curve that represented the entire dendritic field in comparison to wildtypes. Excessive RGC dendritic pruning in the 3xTg-AD mice occurred from the tertiary dendritic level and corresponded to significant reductions in the Sholl AUC, the peak number of Sholl intersections and the total length of all the dendrites. These findings reinforce earlier data, supporting the observation of RGC dendritic loss in 3xTg-AD mice.

In 3xTg-AD mice deficient in C3, RGC dendrites were protected compared to 3xTg-AD mice (Figure 5.7). The Sholl curve was comparable to 3xTg-AD mice up to 60 μm however after this point, 3xTg-AD mice deficient in C3 had a significantly higher Sholl curve ($p < 0.05$), indicating an increased dendritic coverage. Compared to 3xTg-AD, RGCs in the 3xTg-AD C3^{-/-} mice had significantly increased Sholl AUC, maximum number of Sholl intersections and total dendritic length. Despite the greater dendritic complexity in RGCs in 3xTg-AD C3^{-/-} mice, the dendritic field and Sholl curve did not entirely match wildtype mice. Suggesting only a partial protection against excessive RGC dendritic pruning in 3xTg-AD mice deficient in C3.

Similar effects were seen in 3xTg-AD mice deficient in C6, with significantly higher Sholl curve compared to 3xTg-AD mice (Figure 5.7). Dendritic coverage was comparable to 3xTg-AD mice proximal to the cell body; however, dendritic complexity increased for the remaining Sholl curve (between 70 and 160 μm , $p < 0.05$). These changes coincided with significant increases in the Sholl AUC, the maximum number of Sholl intersections and the total dendritic length. Despite the increased RGCs dendritic complexity in 3xTg-AD C6^{-/-} mice, the Sholl curve did not entirely match wildtypes. Therefore, similar to 3xTg-AD C3^{-/-}, C6 deficiency only partially protected against excessive RGC dendritic pruning. Comparing RGCs between both lines of complement deficient 3xTg-AD mice showed that dendritic preservation was consistent. Despite the significantly improved dendritic morphologies, neither C3 nor C6 deficiencies provided total protection against excessive dendritic pruning.

Next, I assessed the dendritic spines on CA1 neurons in the same 3xTg-AD mice deficient in C3 or C6^{-/-} (Figure 5.8A-I). Spine loss was clear in the 3xTg-AD mice as described earlier in Chapter 4, which primarily corresponded with fewer stubby and thin spines whilst the mushroom spines remained similar to wildtype. 3xTg-AD C3^{-/-} mice displayed a slight but non significant increase in dendritic spines compared to 3xTg-AD mice. Conversely, 3xTg-AD C6^{-/-} mice showed notable and significant increase (16%, $p = 0.0003$) in spine densities compared to 3xTg-AD mice. The spine coverage in the 3xTg-AD C6^{-/-} were comparable to typical wildtype levels. On closer inspection of the different spine types, the extent of thin spine loss in 3xTg-AD mice was prevented in the 3xTg-AD C6^{-/-}. However, the number of stubby and mushroom spines remained constant. Together, these results demonstrate that deficiency in C6, rather than C3, provides protection against CA1 hippocampal synaptic pruning in the 3xTg-AD model.

5.3.3 3xTg-AD C5 antibody therapeutic inhibition with BB5.1

Twelve-month female 3xTg-AD mice treated with the C5-blocking mAb BB5.1, or isotype control, for 6 months between 6 and 12 months were assessed for CA1 dendritic spine density (Figure 5.9A-I). Isotype control-treated 3xTg-AD mice displayed prominent dendritic spine loss which corresponded to fewer thin spines in comparison to wildtype. These reduced spine densities were similar to the observed 3xTg-AD mice in Chapter 4. In 3xTg-AD mice treated with BB5.1 mAb between the ages of 6 and 12 months, dendritic spine coverage was significantly improved compared to isotype control-treated (19%, $p < 0.0001$). The spine density in BB5.1 treated 3xTg-AD mice was typical of the densities expected from wildtype mice. Spine subtype classification revealed significantly greater mushroom (33%, $p < 0.0001$) and thin spines (27%, $p = 0.0001$) whilst the number of stubby spines were unchanged compared to isotype control 3xTg-AD mice. These data demonstrate that inhibiting C5 in 3xTg-AD mice has the capacity to prevent CA1 dendritic spine loss in the hippocampus, providing support for inhibition of downstream components of the complement system to impact pathological synaptic pruning.

5.3.4 Figures

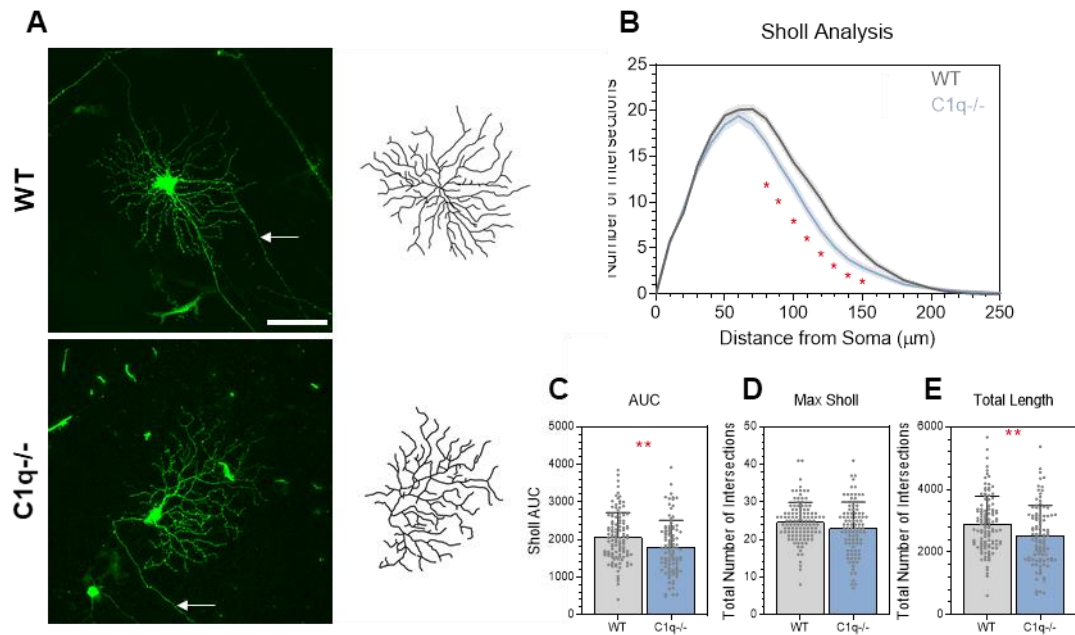


Figure 5.2 RGC dendritic complexity in C1q^{-/-} mice. (A) DiOlistic labelled RGCs from WT and C1q^{-/-} mice and corresponding dendritic reconstructions. Arrows indicate RGC axon. Scale bar 100 μm . (B) Sholl analysis of reconstructed RGCs. Line represents mean of group at each interval, shaded error zones \pm SEM. Two-tailed Mann-Whitney U test at each interval distance, * = $p < 0.05$. (C) Area under the Sholl curve. (D) Peak number of Sholl intersections. (E) Total dendritic length. Column Scatterplots: data represent individual cells and error bars correspond to SD. WT: $n = 114$ cells (10 mice, 5 male/5 female) and C1q^{-/-}: $n = 98$ cells (9 female mice). All mice adults older than three months. Two group comparisons were made using the Mann-Whitney U test comparing deficient mice to wildtype, * = $p < 0.05$, ** = $p < 0.01$, *** = $p < 0.001$, **** = $p < 0.0001$. Abbreviations: WT, wildtype; AUC, area under the Sholl curve.

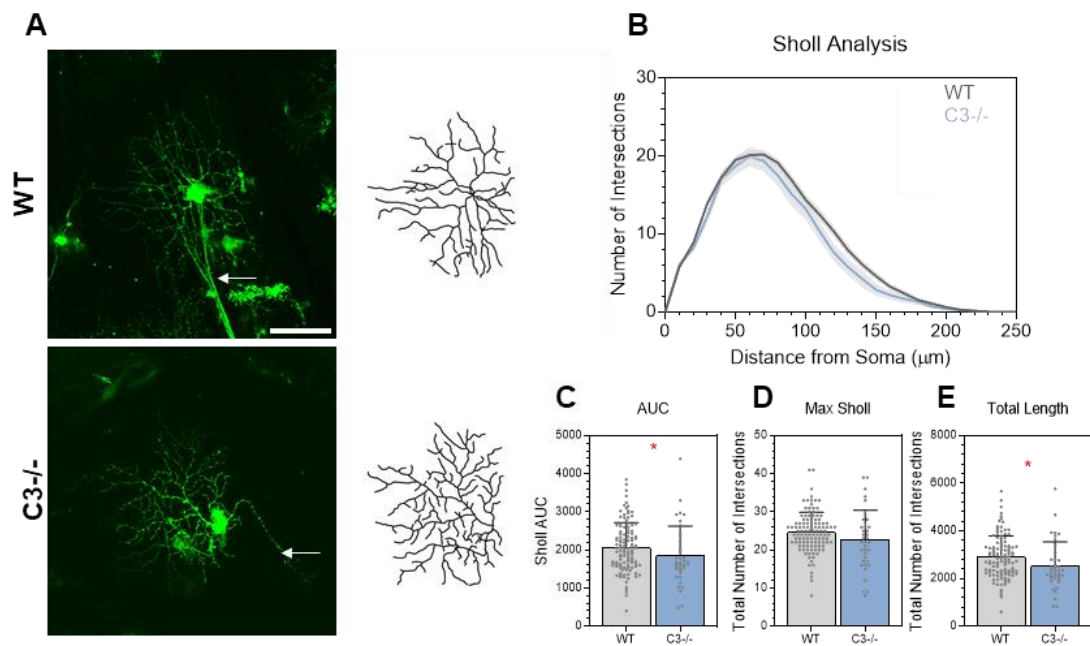


Figure 5.3 RGC dendritic complexity in C3^{-/-} mice. (A) DiOlistic labelled RGCs from WT and C3^{-/-} mice and corresponding dendritic reconstructions. Arrows indicate RGC axon. Scale bar 100 μm . (B) Sholl analysis of reconstructed RGCs. Line represents mean of group at each interval, shaded error zones \pm SEM. Two-tailed Mann-Whitney U test at each interval distance, * = $p < 0.05$. (C) Area under the Sholl curve. (D) Peak number of Sholl intersections. (E) Total dendritic length. Column Scatterplots: data represent individual cells and error bars correspond to SD. WT: $n = 114$ cells (10 mice, 5 male/5 female) and C3^{-/-}: $n = 38$ cells (6 male mice). All mice adults older than three months. Two group comparisons were made using the Mann-Whitney U test comparing deficient mice to wildtype, * = $p < 0.05$, ** = $p < 0.01$, *** = $p < 0.001$, **** = $p < 0.0001$. Abbreviations: WT, wildtype; AUC, area under the Sholl curve.

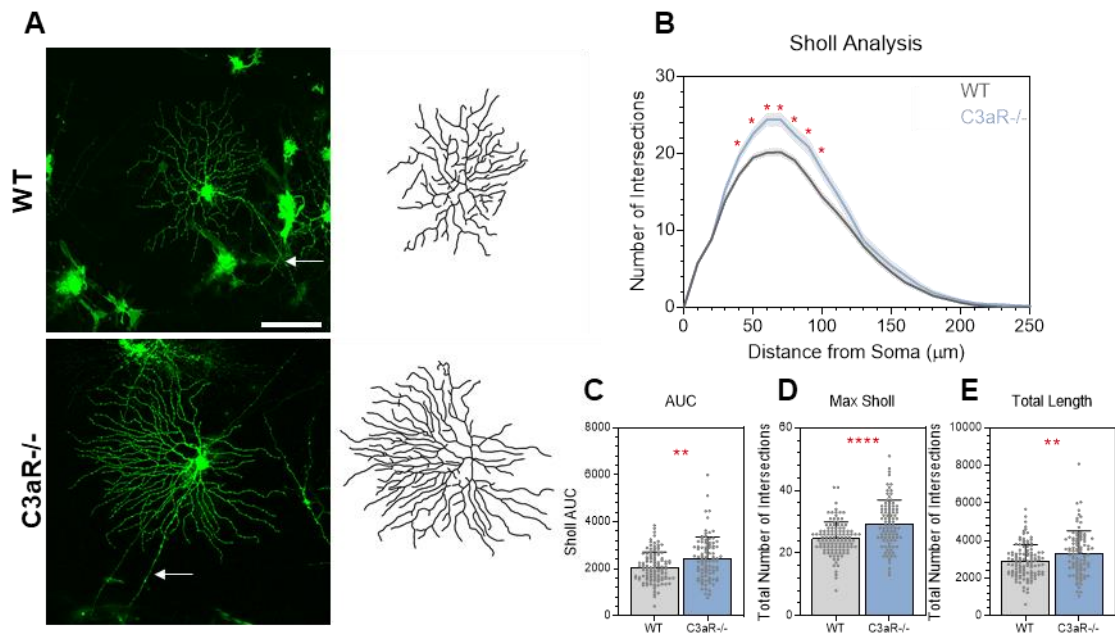


Figure 5.4 RGC dendritic complexity in C3aR^{-/-} mice. (A) DiOleistic labelled RGCs from WT and C3aR^{-/-} mice and corresponding dendritic reconstructions. Arrows indicate RGC axon. Scale bar 100 μm . (B) Sholl analysis of reconstructed RGCs. Line represents mean of group at each interval, shaded error zones \pm SEM. Two-tailed Mann-Whitney U test at each interval distance, * = $p < 0.05$. (C) Area under the Sholl curve. (D) Peak number of Sholl intersections. (E) Total dendritic length. Column Scatterplots: data represent individual cells and error bars correspond to SD. WT: $n = 114$ cells (10 mice, 5 male/5 female) and C3aR^{-/-}: $n = 93$ cells (8 mice, 3 male/5 female). All mice adults older than three months. Two group comparisons were made using the Mann-Whitney U test comparing deficient mice to wildtype, * = $p < 0.05$, ** = $p < 0.01$, *** = $p < 0.001$, **** = $p < 0.0001$. Abbreviations: WT, wildtype; AUC, area under the Sholl curve.

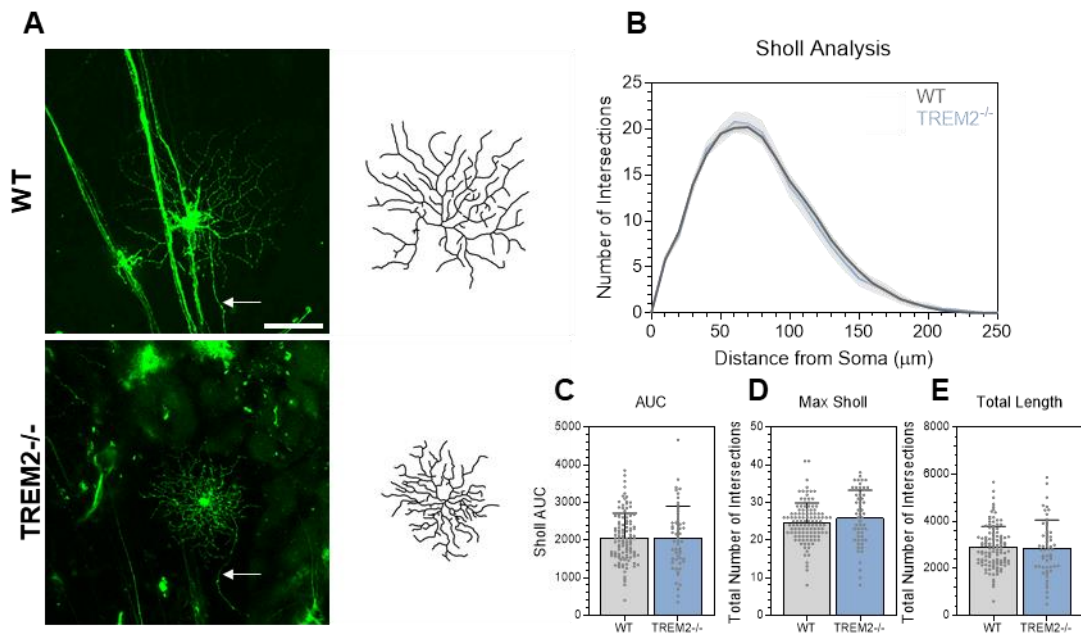


Figure 5.5 RGC dendritic complexity in TREM2^{-/-} mice. (A) DiOlistic labelled RGCs from WT and TREM2^{-/-} mice and corresponding dendritic reconstructions. Arrows indicate RGC axon. Scale bar 100 μ m. (B) Sholl analysis of reconstructed RGCs. Line represents mean of group at each interval, shaded error zones \pm SEM. Two-tailed Mann-Whitney U test at each interval distance, * = $p < 0.05$. (C) Area under the Sholl curve. (D) Peak number of Sholl intersections. (E) Total dendritic length. Column Scatterplots: data represent individual cells and error bars correspond to SD. WT: $n = 114$ cells (10 mice, 5 male/5 female) and TREM2^{-/-}: $n = 54$ cells (7 mice, 4 male/3 female). All mice adults older than three months. Two group comparisons were made using the Mann-Whitney U test comparing deficient mice to wildtype, * = $p < 0.05$, ** = $p < 0.01$, *** = $p < 0.001$, **** = $p < 0.0001$. Abbreviations: WT, wildtype; AUC, area under the Sholl curve.

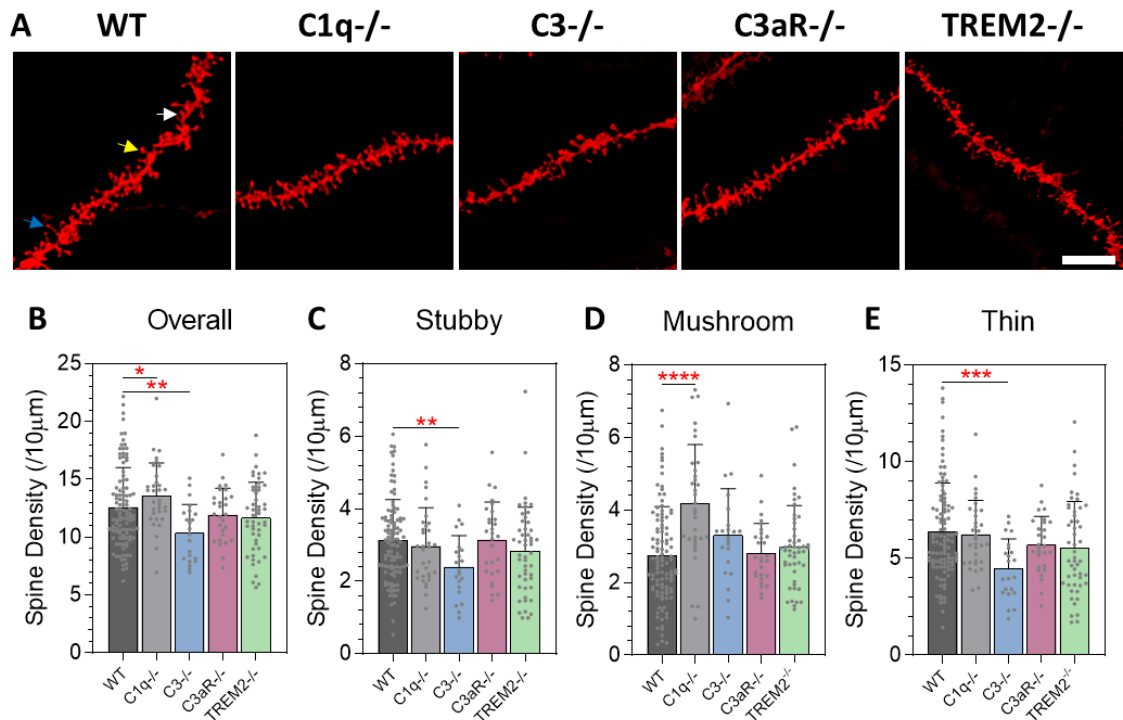


Figure 5.6 CA1 dendritic spines in C1q^{-/-}, C3^{-/-}, C3aR^{-/-} and TREM2^{-/-} mice. (A-D) Representative confocal images of CA1 dendritic segments from WT, C1q^{-/-}, C3^{-/-}, C3aR^{-/-} and TREM2^{-/-}. Arrows indicate spine morphology: stubby (white arrows), mushroom (yellow arrows), thin (blue arrows). Scale bar 5 μ m. Spine densities were analysed from dendritic segments of at least 30 μ m. (E-H) Spine densities across all dendritic segments for overall, stubby, mushroom and thin groups. Column Scatterplot (C-F): data points represent individual cells and error bars correspond to SD. WT: n = 106 dendrites (7 mice, 4 male 3 female), C1q^{-/-}: n = 33 dendrites (5 mice, 5 female), C3^{-/-}: n = 22 dendrites (3 mice, 3 male), C3aR^{-/-}: n = 28 dendrites (3 mice, 3 male) and TREM2^{-/-}: n = 50 dendrites (7 mice, 4 male 3 female). Two-tailed Mann-Whitney U test comparing deficient mice to wildtype, * = $p < 0.05$, ** = $p < 0.01$, *** = $p < 0.001$, **** = $p < 0.0001$. All mice adults older than three months. Abbreviations: WT, wildtype.

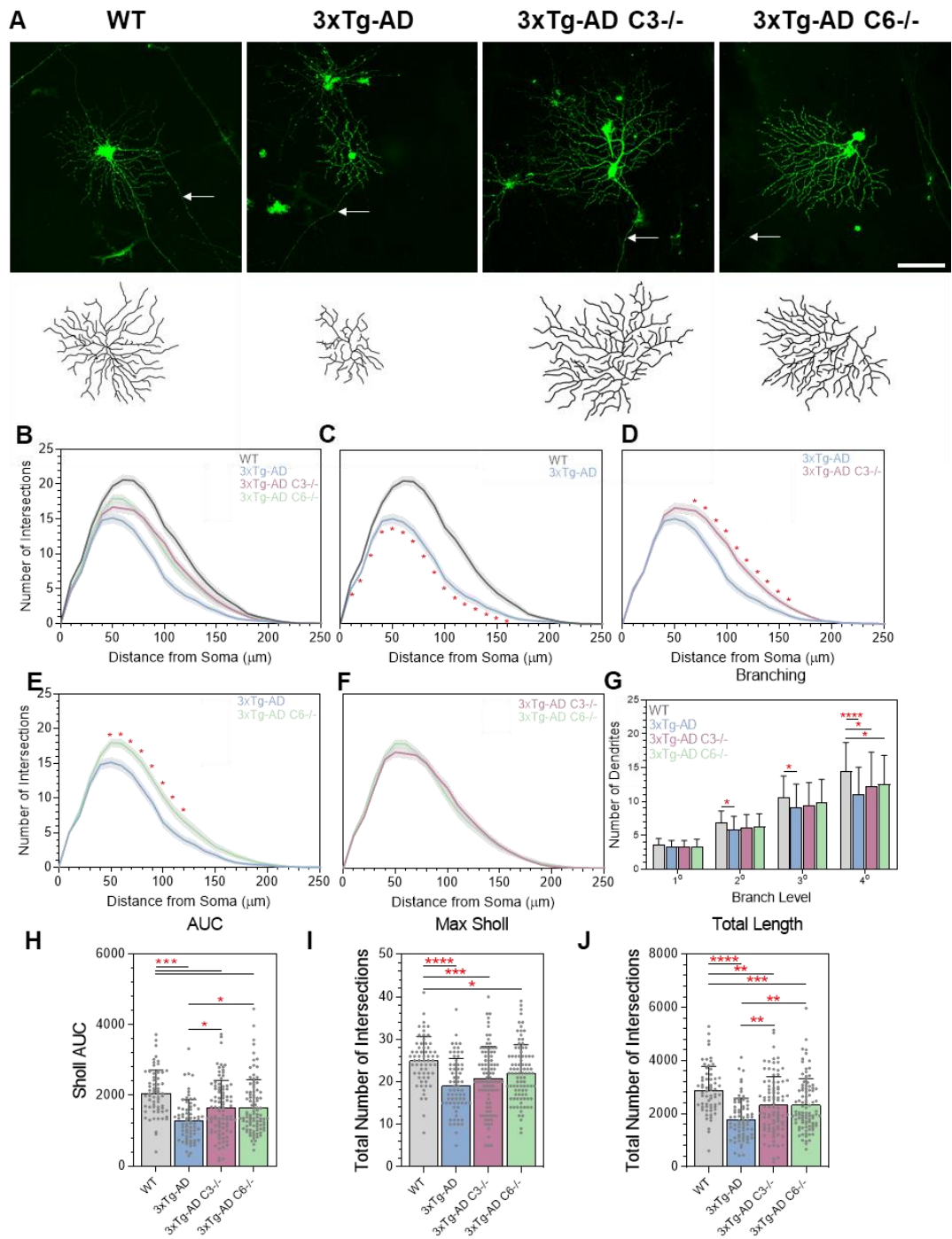


Figure 5.7 Complement C3 and C6 offers protection from RGC dendritic loss in 3xTg-AD mice. (A) Representative RGC examples from wildtype 3xTg-AD, 3xTg-AD C3^{-/-} and 3xTg-AD C6^{-/-}. (B-F) Sholl analysis of all reconstructed RGCs. Line represents mean of group at each interval, shaded error zones represent \pm SEM. Two-tailed Mann-Whitney U test at each interval distance, * = $p < 0.05$, (G) Number of dendrites at each branching level proximal to the cell body. Error bars correspond to SD. Column Plots (G): bars represent mean from individual cells and error bars correspond to SD. Column Scatterplots (H-J): data points represent individual cells and error bars correspond to SD. WT: $n = 64$ cells (5 mice), 3xTg-AD: $n = 69$ cells (6 mice), 3xTg-AD C3^{-/-}: $n = 92$ cells (5 mice) and 3xTg-AD C6^{-/-}: $n = 94$ cells (6 mice). Four groups were compared by nonparametric one-way analysis of variance (Kruskal-Wallis test) using Dunn multiple comparisons post-test, * = $p < 0.05$, ** = $p < 0.01$, *** = $p < 0.001$, **** = $p < 0.0001$. All male mice aged twelve months. Abbreviations: WT, wildtype; AUC, area under the Sholl curve.

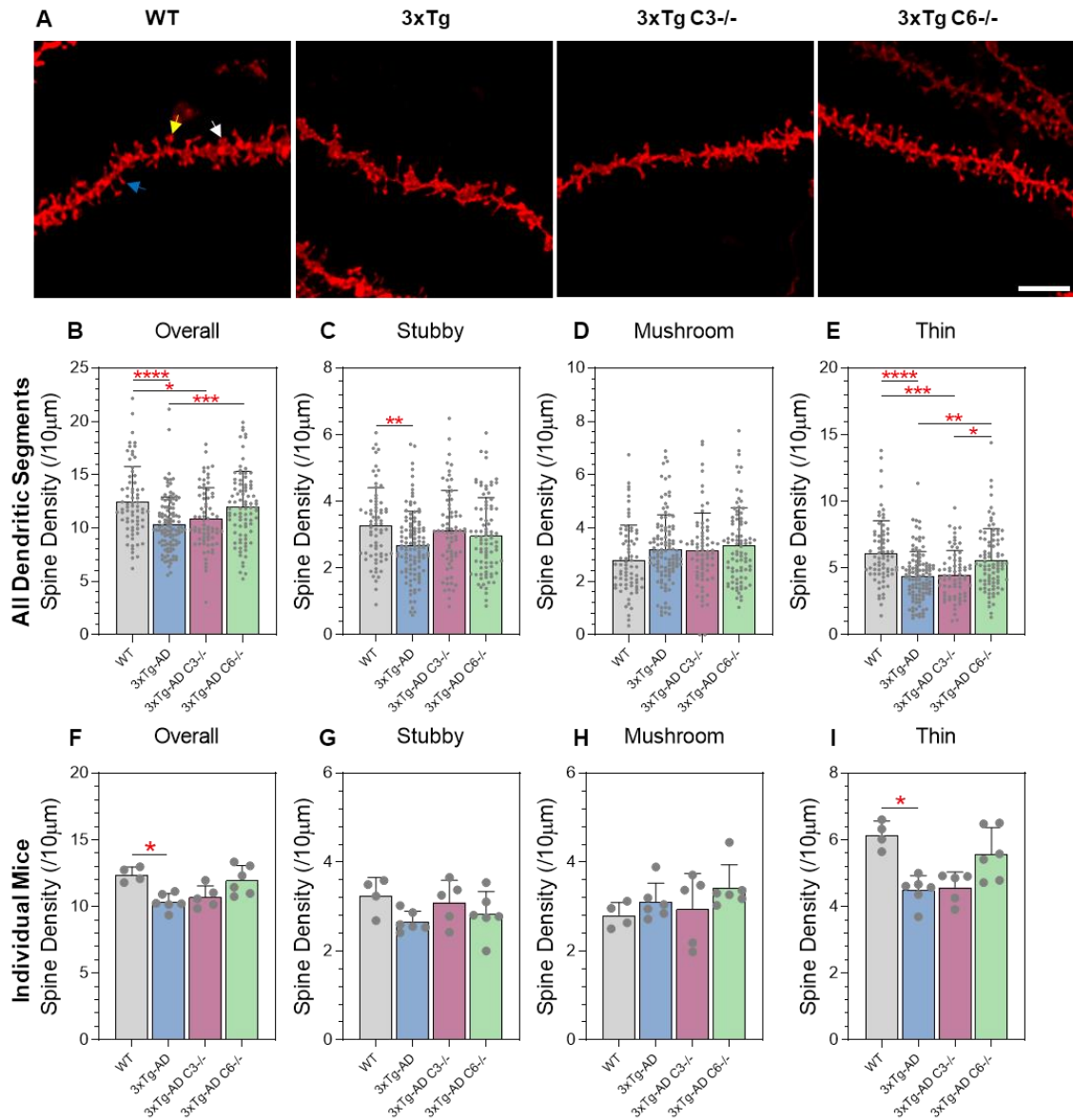


Figure 5.8 Complement C6 rather than C3 offers protection from hippocampal CA1 dendritic spine loss in 3xTg-AD mice. (A–D) Representative confocal images of DiI labelled dendritic segments of CA1 segments from WT, 3xTg-AD, 3xTg-AD C3^{-/-} and 3xTg-AD C6^{-/-}. Arrows indicate spine morphology: stubby (white arrows), mushroom (yellow arrows), thin (blue arrows). Spine densities collected from an average of 30 µm dendritic segments. Scale bar 5 µm. (C–F) Spine densities across all dendritic segments and (G–J) spine densities across all individual mice for overall, stubby, mushroom and thin groups. Column Scatterplot (C–F): data represent individual cells and error bars correspond to SD. Column Scatterplots (G–J): bars, mean of group; data represent the mean spine density from individual mice and error bars correspond to SD. WT: $n = 71$ dendrites (4 mice), 3xTg-AD: $n = 112$ dendrites (6 mice), 3xTg-AD C3^{-/-}: $n = 70$ dendrites (5 mice) and 3xTg-AD C6^{-/-}: $n = 86$ dendrites (6 mice). Multiple groups were compared by nonparametric one-way analysis of variance (Kruskal–Wallis test) using Dunn multiple comparisons post-test, * = $p < 0.05$, ** = $p < 0.01$, *** = $p < 0.001$, **** = $p < 0.0001$. All male mice aged twelve months. Abbreviations: WT, wildtype.

5.4 Discussion

Complement activation is associated with amyloid plaques and microglial activation in the AD brain. Components of the complement system have been reported to have key roles in the pruning of dendrites and synapses/ spines in AD mouse models (Veerhuis *et al.*, 2011; Hong *et al.*, 2016). In this chapter, I demonstrate that modulation of the complement system influences RGC dendritic complexity and CA1 hippocampal dendritic spines in wildtype and in 3xTg-AD mice. Using two models featuring complement deficiencies, I observed partial protection against RGC dendritic complexity in 3xTg-AD mice deficient in C3 or C6; C6 deficiency also protected against CA1 hippocampal dendritic spine loss. Inhibition of C5 with the BB5.1 mAb also protected CA1 dendritic spines in 3xTg-AD mice. In wildtype mice, deficiencies of C1q and C3 resulted in a decrease in RGC dendritic complexity, whereas, a deficiency of C3aR resulted in a marked enlargement of RGC dendritic coverage. In relation to CA1 dendritic spine densities, deficiency of C1q resulted in an increased spine density, whereas, a deficiency of C3 resulted in a decrease. This chapter reinforces the role of the complement system in the modulation and refinement of dendritic and synaptic neuronal networks.

Complement-mediated synaptic pruning is a feature in the developing CNS and in ageing in AD mouse models which is thought to arise based on neuronal activity. Synaptic loss correlated with the deposition of amyloid in the brain, the status of neuroinflammation and the burden of cognitive decline (Schafer *et al.*, 2012; Shi *et al.*, 2017). Current evidence supports upstream complement components such as C1q, the initiator of the classical complement cascade, and C3, the central component of the complement system, in the recruitment and activation of microglia, and the tagging and elimination of synapses (Stevens *et al.*, 2007). In Chapter 3, I reported that the retina of 3xTg-AD mice displays excessive RGC dendritic pruning in age-dependent process. In this chapter, I demonstrate that dendritic complexity is rescued, although not completely to wildtype levels, in 3xTg-AD mice deficient in C3. These findings are in agreement with other studies that demonstrate a role for C3 deficiency to protect against neurodegeneration (Perez-Alcazar *et al.*, 2014; Shi *et al.*, 2015). These findings suggest that C3 has an important role in the refinement of RGC dendritic complexity, and in the absence of C3, provides protection in mouse models of AD. In the brain, C3 deficiency has previously been found to protect

synapses in AD models (Shi *et al.*, 2017). In Tg2576 mice, C3 and C4 deposition is found to increase with age and localise on amyloid plaques (Zhou *et al.*, 2008). However, in contrast to these studies, I observed that a deficiency of C3 did not prevent dendritic spine loss in the hippocampus of 3xTg-AD mice.

It is uncertain whether downstream components of C3 in the complement system play a role in the pruning of synapses. The terminal pathway of the complement system leads to the formation of the membrane attack complex (MAC) which can trigger cell lysis. I observed that a deficiency of C6, a component required for the formation of MAC, rescued RGC dendritic complexity in 3xTg-AD mice, similar to a deficiency of C3. In contrast to C3, where CA1 spine density was not protected, the absence of C6 also prevented CA1 hippocampal dendritic spine loss in 3xTg-AD mice. These findings demonstrating that C6, part of the complement terminal pathway, is involved in neuronal refinement, suggests further complement therapeutic targets.

Complement therapeutics targeting neurodegeneration has supported the role of complement-mediated dendritic and synaptic pruning. Inhibition of C1q protects against excessive RGC dendritic atrophy in glaucoma models (Williams *et al.*, 2016). Whereas, in a tauopathy models (P301S), inhibition of C1q prevents microglial-engulfment of synapses and rescues synaptic function (Dejanovic *et al.*, 2018). Activation of C5 of the complement system triggers the release of the pro-inflammatory anaphylatoxin C5a fragment, which recruits and activates microglia, triggering the initiation of the terminal pathway. C5 has therefore been highlighted for its potential role for an anti-complement drugs (Zelek *et al.*, 2019). In 3xTg-AD model between the ages of 6 and 12 months, I observed that therapeutically inhibiting C5 (BB5.1 mAb) protected against CA1 hippocampal dendritic spine loss. These findings are in agreement with similar studies that report block C5a receptor, or receptor knockout mice, preserved synapses, reduced neuroinflammation and improves cognition (Fonseca *et al.*, 2009; Hernandez *et al.*, 2017; Panayiotou *et al.*, 2019). Collectively, these support the role of modulating the complement system to reduce C5 activation as a potential therapeutic target against synaptic elimination in AD mouse models.

With the current data it is unclear whether these improvements in CA1 hippocampal synaptic density are a consequence of local blockage of C5 within the CNS. Only a very small percentage (possibly less than 0.1%) of antibody drug treatments given systemically

have the capacity to pass the blood brain barrier, it is uncertain whether significant levels of BB5.1 entered the brain of the mice analysed. At this stage in the disease progression of the 3xTg-AD mice, it is unlikely that the blood brain barrier would be significantly disrupted, although this may be the case later in the disease (Chiquita, Ribeiro, *et al.*, 2019). Administered BB5.1 may therefore act systemically, lowering/blocking the levels of C5 in circulation with the observed changes in the brain a beneficial outcome. In the current study it was not possible to locally administer BB5.1 to the brain (or retina), however, such studies could provide more relevant information regarding direct effects of the antibody treatments on the CNS.

In development of the CNS, complement is known to have crucial roles in refining neuronal networks. However, it is unclear whether complement is involved during adulthood. In the development of the olfactory bulb circuitry in postnatal mice, deficiency of C1q and C3 lead to the improper refinement of the retinogeniculate system (Stevens *et al.*, 2007; Lehmann *et al.*, 2018). In adult mice deficient in C1q, I observed a reduction in RGC dendritic complexity compared to mice wildtypes. A decrease in complexity was unexpected due to previous reports supporting the impact of C1q deficiency leading to under-pruned dendritic fields (Zhang *et al.*, 2019). These observations do however support the role of C1q in influencing RGC dendritic structure. In the cortex, C1q deficiency associates with a failure to prune synapses and leads to an increase in dendritic complexity (Ma *et al.*, 2013). In contrast, in mice deficient in C3aR the receptor for the C3a anaphylatoxin fragment, RGCs were underpruned and displayed enlarged dendritic fields indicating a role for the C3a-C3aR axis in neuronal refinement. In tauopathy models, absence of C3aR is also found to reduce tau pathology and decrease neuroinflammation and synaptic elimination (Litvinchuk *et al.*, 2018). These discrepancies between the different complement models may arise due to potential compensatory mechanisms involved in RGC synaptic connections (Tripodi *et al.*, 2008).

In the hippocampus, a deficiency of C1q resulted in increased dendritic spine coverage, reinforcing the role of C1q in complement-mediated synaptic pruning (Ma *et al.*, 2013). C1q is found to accumulate in postsynaptic densities and is linked to microglial engulfment of synapses, decreasing synaptic density (Dejanovic *et al.*, 2018). Despite C1q being associated with synaptic loss, C1q also has protective role in the CNS by enhancing the clearance of apoptotic neurons (Fraser *et al.*, 2010; Györfy *et al.*, 2018).

In C3^{-/-} and C3aR^{-/-} mice the density of CA1 dendritic spines were similar to wildtype mice, in contrast with others that report blocking this part of the complement system conferred neuronal protection (Lian *et al.*, 2015). In mice lacking TREM2, the receptor involved in binding to complement regulators, others have demonstrated abnormal dendritic spine elimination in development (Filipello *et al.*, 2018). However, in adult mice, there was no evidence that deficiency of TREM2 altered the coverage of CA1 dendritic spines. Collectively, these findings highlight that different components of the complement system are involved in synaptic elimination and that some components have more central roles.

To conclude, in this chapter I demonstrate that the complement system influences RGC dendritic complexity and CA1 hippocampal dendritic spines in wildtype and AD model mice. These findings demonstrate that downstream components of C3 are involved in refining neuronal networks.

Chapter 6. The impact of bacterial and viral infections on retinal ganglion cells and CA1 hippocampal dendritic spines in wildtype and 3xTg-AD mice.

6.1 Introduction

In the previous chapters, I presented evidence supporting excessive RGC dendritic pruning and CA1 synaptic loss in 3xTg-AD mice. I also identified that deficiencies in the complement system, an important component of the innate immune system, conferred neuronal protection. Peripheral inflammation, outside of the CNS, is thought to contribute to the burden of neurodegeneration and associates with cognitive deficits in AD (Brown, 2019; Giridharan *et al.*, 2019). In this chapter, I explored the impact on RGC dendrites and CA1 hippocampal dendritic spines by initiating systemic inflammation, here mimicked bacterial and viral infections, in wildtype and 3xTg-AD mice.

AD pathology is closely linked to neuroinflammation, particularly in the early stages of the disease whereby, activation of microglia triggers excessive elimination of synapses prior to the observation of substantial neuronal loss. Chronic inflammation in the CNS of AD individuals associates with microglial activation and leads to a worse disease prognosis (Keenan A Walker *et al.*, 2019). In the AD brain, inflammation occurs in response to amyloid, however infectious agents, outside of the CNS, can influence and trigger alterations in the brain. In compromised individuals, those most at risk of neurodegenerative diseases, additional co-morbidities may contribute to an increased burden and accelerated pathology (Mawanda and Wallace, 2013; Sochocka *et al.*, 2017). Persistent inflammation in the periphery throughout life is a known contributor to the status of neuroinflammation, correlating with an increased synapse elimination and neuronal dysfunction (Sheppard *et al.*, 2019). Similar to that observed in human studies, animal models often describe similar effects in response to infectious agents in driving neuropathology (Brown, 2019).

In vivo models that investigate systemic inflammation mimic bacterial infections by the administration of the potent gram-negative bacterial endotoxin lipopolysaccharide (LPS). Low concentrations of LPS, less than 1 mg/kg, are commonly used to initiate an

inflammatory response without triggering sepsis, although more commonly, concentrations of 500 µg/kg better mimic chronic levels of inflammation. The lower dosages enable assessment of the impact of chronic inflammation several weeks post-infection, rather than changes occurring during the acute phases (Torvell *et al.*, 2019).

LPS-driven peripheral inflammation triggers neuroinflammation in the CNS, with *in vivo* models frequently reporting microglial activation and an increased production of pro-inflammatory cytokines (Chugh *et al.*, 2013). Chronic neuroinflammation, in response to LPS, associates with priming of the immune response leading to excessive microglial-mediated synaptic pruning which correlates with an increase in cognitive deficits in wildtype and disease models (Moraes *et al.*, 2015; Sheppard *et al.*, 2019). In the AD models, LPS also modulates the classical hallmarks of AD pathology altering the burden of amyloid plaques and neurofibrillary tangles (Kitazawa *et al.*, 2005). The effect of LPS on the retina is less described, although there are many similarities with the observed findings occurring in the brain. LPS administration into postnatal mice has recently demonstrated substantial remodeling of RGC dendritic complexity (Gao *et al.*, 2018). Other infectious agents such as viruses also trigger peripheral inflammation, although are less described, have suggested a role for viral-driven peripheral inflammation to exacerbate CNS pathology. Notably, herpes simplex virus (HSV), Cytomegalovirus (CMV) and Hepatitis C virus (HCV) reactivate during latent infection and are observed in the AD brain. Viral infections in AD models trigger intraneuronal disruption, with viral products detected in amyloid plaques and their presence correlating with the extent of cognitive impairment (Chiu *et al.*, 2014; Barnes *et al.*, 2015; Mangold and Szpara, 2019).

In this chapter, I assessed the impact of systemic inflammation mimicked by bacterial products and viral infections on RGC dendritic complexity and CA1 hippocampal dendritic spines in wildtype and 3xTg-AD mice. Bacterial infection was mimicked by i.p. injection of LPS (500 µg/kg) as either a single or triple insult in 6-month-old mice and analysed one month post initial injection. Viral infection was initiated by i.p. injection of MCMV (murine cytomegalovirus) (5×10^4 pfu) in 2-month-old mice and analysed at 9 months. The data in this chapter provides further insights into the role of systemic inflammation in driving CNS neurodegeneration.

6.2 Experimental Setup

This chapter assesses the impact of systemic inflammation triggered by mimicking bacterial and viral infection on RGC dendrites and CA1 dendritic spines in wildtype and 3xTg-AD mice. Figure 6.1 presents an overview of the methods used in this chapter with Chapter 2 providing a detailed description on the protocols used to assess RGC dendritic complexity and CA1 dendritic spines.

Bacterial infection was mimicked in female wildtype and 3xTg-AD mice at 6 months by i.p. injection with the endotoxin, lipopolysaccharide (LPS, Sigma Aldrich product code: L2880), either as a single dose (1xLPS) or once a week for three weeks (3xLPS) and compared to saline injections. All mice were analysed one month post initial injection. LPS was dissolved in 0.9% NaCl, yielding a 5 mg/ml LPS stock solution. On the day of injection, the LPS stock solution was diluted in 0.9% NaCl to a working concentration of 100 µg/ml and i.p. injected at 0.5µg of LPS per gram of body weight, or the equivalent volume of saline. Typically, a 30 g mouse required a volume of 150 µl of either saline or LPS working concentration. The dosage of LPS sufficiently induces an immune response without inducing sepsis and is used in other AD related studies (Torvell *et al.*, 2019). Following all injections, animals were health checked to assess any adverse effects and frequently weighed. Typically, LPS triggered 10-20% weight loss up to 48 hours post-injection. In the 3xLPS groups, LPS was injected once a week for three weeks, ensuring a recovery period whereby the observed LPS induced weight loss was either stable or recovered to baseline.

Viral infections were initiated using MCMV in female wildtype and 3xTg-AD mice. MCMV was prepared by sorbital gradient purification as described previously (Stacey *et al.*, 2014) with 3×10^4 pfu i.p. injected into mice as a single injection at 2 months. Virally infected mice were housed in pathogen-free scintainer ventilated cages and analysed at 9 months of age. MCMV preparation, MCMV administration, animal housing, health checks and other experimental readouts were performed by Dr Mathew Clement. The work presented in this thesis only investigated the impact of MCMV on RGC dendrites and CA1 hippocampal dendritic spines.

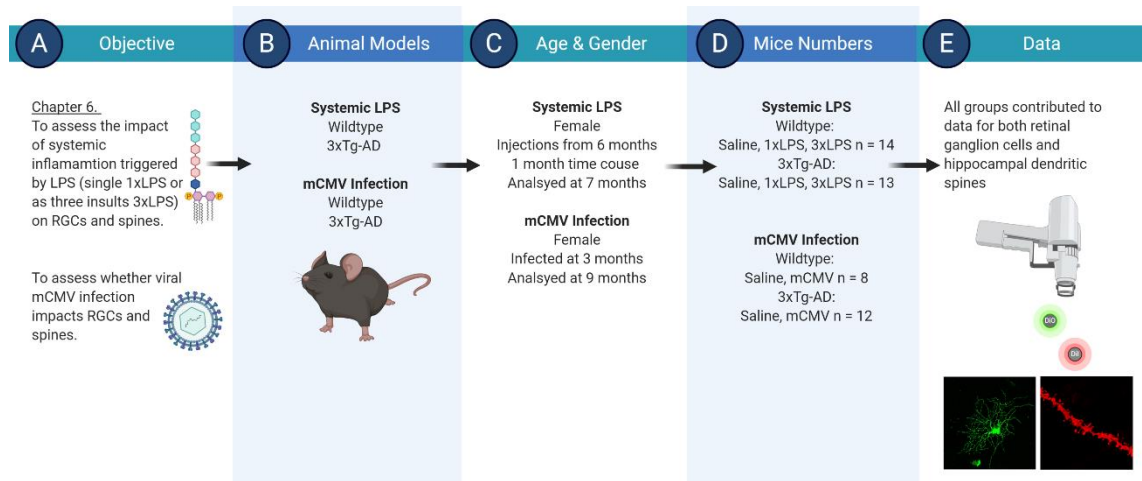


Figure 6.1 Experimental overview for Chapter 6 addressing the impact of systemic inflammation triggered by bacterial (LPS) and viral (MCMV) infection on RGC dendritic arborisation and CA1 hippocampal dendritic spines. **(A)** Main objectives for Chapter 6. **(B)** The different animal models used. **(C)** More details on the animal model's age, gender and time course. **(D)** Number of mice analysed that were subjected to DiOlistic labelling. **(E)** All groups in Chapter 6 were analysed for RGC dendrites and CA1 hippocampal dendritic spine coverage. Illustration created in BioRender.

6.3 Results

6.3.1 Systemic LPS

6.3.1.1 Weight Monitoring

To determine the impact of LPS on RGCs and CA1 hippocampal spines, firstly, evidence of inflammation was required. Weight monitoring is a useful method to monitor the health of mice following injection of LPS (Figure 6.2).

In wildtype mice (Figure 6.2A), the initial injection of saline resulted in slight weight loss that peaked at 24 hrs post-injection, with mice returning to baseline weight in the subsequent days. The second saline injection triggered a further slight loss of weight peaking at 24 hrs post-injection. Wildtype mice subsequently gained weight above the initial baseline between the second and third saline injections. In line with the previous injections, the final saline injection also triggered weight loss which peaked at 24 hrs post injection followed by weight gain in subsequent days. Wildtype mice injected with a single insult of LPS (1xLPS), displayed weight loss that peaked at 24 hrs post-injection. In comparison to the baseline weight, 1xLPS triggered a reduction of approximately 10%, however weights returned to baseline within a week. For wildtype mice injected with three insults of LPS (3xLPS), mice displayed a similar initial response to the 1xLPS wildtype mice with weight returning to baseline before further injections. The second and final LPS injections showed similar trends following injections. The 3xLPS wildtype mice subsequently returned to baseline before culling and were comparable to the saline group upon final weighing.

In 3xTg-AD mice (Figure 6.2B), an initial injection of saline resulted in slight weight loss that peaked at 48 hrs post-injection and did not return to baseline, instead remained stable. The second saline injection in 3xTg-AD mice did not display any weight loss and gained weight after 24 hrs, which decreased to the constant level before the third injection. The final saline injection in 3xTg-AD mice also did not trigger weight loss, with mice gaining weight and returning to and above the initial baseline. For 3xTg-AD mice injected with a single dose of LPS (1xLPS), mice displayed weight loss that peaked at 24 hours post-injection. 3xTg-AD 1xLPS mice displayed gradual weight gain, however, did not return

to baseline within a week post-injection. For 3xTg-AD mice injected with three doses of LPS (3xLPS), mice exhibited an initial weight loss that peaked at 48 hrs post injection and remained stable until the second injection. The second round of LPS triggered further weight loss, that peaked at 48 hrs post-injection with subsequent weight gain. The final LPS insult in 3xTg-AD mice inflicted similar weight loss at 24 hrs post-injection which was accompanied by a gradual return to baseline weight. These observations identifying fluctuations in weight following LPS injections indicates the successful administration of LPS in triggering systemic inflammation in both wildtype and 3xTg-AD mice.

6.3.1.2 Wildtype

To study the effect of mimicked bacterial infection in the retina of wildtype mice at 6 months, RGC dendritic morphology was quantified from saline, single (1xLPS) and triple LPS insults (3xLPS) (Figure 6.3A). Wildtype mice injected with saline revealed a Sholl profile and associated parameters typical of previous descriptions reported in Chapter 3. The insult of a single or triple doses of LPS resulted in a minimal changes to RGC dendritic complexity in wildtype mice (Figure 6.3B-D). A reduced LPS associated Sholl profile was only detected in wildtype 3xLPS group with a lowered peak of the Sholl curve compared to saline (between 40 and 80 μm , $p < 0.05$) and 1xLPS (at 70 μm , $p < 0.05$) groups. However, these changes were subtle and did not reflect any differences in the Sholl AUC, the maximum number of intersections or in the overall total length of the dendrites (Figure 6.3E-G). These data demonstrate that in wildtype mice at 6 months, a single or repeated insult of LPS throughout a month time course has a minimal effect on the dendritic complexity of RGCs.

As reported in Chapter 3, classification of RGC receptive field highlighted possible susceptibility of ON-centre RGCs. These observations were similar in 1xLPS wildtype mice with ON-centre RGCs displaying a reduced Sholl profile with fewer distal dendrites (between 90 and 120 μm , $p < 0.05$; Figure 6.4A). Additionally, ON-centre RGCs in 3xLPS wildtype mice also displayed similar distal dendritic loss (fewer intersections at 40 and 80 to 120 μm , $p < 0.05$); although, there were no differences between the two LPS groups (Figure 6.4B-C). Quantification of the Sholl AUC supported these findings; though, statistical significance was not reached when comparing all the groups (Figure 6.4D). Dendritic changes in OFF-centre RGCs, in line with previous data in earlier

chapters, was less pronounced in wildtype mice (Figure 6.4E-G). Wildtype LPS groups for OFF-centre RGCs did not demonstrate any overall differences in the Sholl curve. However, in the 3xLPS wildtype mice, OFF-centre RGCs possibly indicated a reduced Sholl curve at the point of highest complexity, compared to 1xLPS OFF-centre RGCs, although no statistical significance was obtained. These observations were highlighted by similarities with the Sholl AUC (Figure 6.4H). These findings suggest that LPS may affect ON-centre RGCs more than OFF-centre RGCs in wildtype mice.

In the same LPS treated wildtype mice, the impact on CA1 hippocampal dendritic spine density and morphology was also assessed (Figure 6.5A-E). Wildtype mice injected with saline revealed spine densities typical to expected normal levels. In contrast, wildtype mice injected with LPS revealed that 1xLPS showed an overall trend for fewer total spines with reduced number of stubby spines, whilst retaining mushroom and thin spines. However, such spine loss was not observed in the wildtype mice injected with 3xLPS and resulted in minimal effects on dendritic spine density. These differences highlight conflicting results for the impact of LPS on dendritic spines in wildtype mice. Previous data in earlier chapters indicated that the number of thin spines was a good indication of spine loss and was the most affected spine subtype. In the LPS treated wildtype mice, only a reduction in the number of stubby spines was observed in the 1xLPS group (225, $p = 0.0009$). This may be attributed to the limited number of mice analysed, although it is likely that in wildtype mice there is a minimal effect of LPS in modulating CA1 hippocampal dendritic spines.

6.3.1.3 3xTg-AD

To investigate the effect of LPS-mimicked bacterial infection in the retina of 3xTg-AD mice at 6 months, RGCs were morphologically quantified for their dendritic fields from saline, single (1xLPS) and triple LPS (3xLPS) insults (Figure 6.6A). 3xTg-AD mice injected with saline revealed a Sholl profile that was marginally decreased compared with wildtype mice (data comparison not shown). However, 3xTg-AD mice administered with either 1xLPS and 3xLPS resulting in minimal to no impact on the RGC dendritic complexity (Figure 6.6B-D). No significant changes were observed in 3xTg-AD LPS groups for the Sholl analysis or related parameters (Figure 6.6E-G). Therefore, these data indicate that at 6 months, for the one-month time course assessed, 3xTg-AD mice insulted with LPS either as a single or repeated injection do not develop exacerbated RGC dendritic pruning.

Classification of RGCs based on their receptive field, i.e ON and OFF centre, revealed subtle shifts within the groups. ON-centre RGCs from 3xTg-AD mice demonstrated that 1xLPS 3xTg-AD mice had slightly increased proximal dendritic coverage compared to saline (at 10, 20 and 40 μm $p < 0.05$) and 3xLPS (between 10 and 50 μm , $p < 0.05$) groups (Figure 6.7A-C). Although, no statistical differences were detected in the Sholl AUC (Figure 6.7D). In agreement with earlier data, changes to OFF-centre RGCs were less pronounced with no differences between the groups based on the Sholl curves and Sholl AUC (Figure 6.7E-H). These findings suggest that LPS in 3xTg-AD mice, during the one-month time course, does not impact RGC dendritic complexity.

In the same 3xTg-AD mice assessed for RGC dendritic complexity, CA1 hippocampal dendritic spines were analysed (representative examples, Figure 6.8A). 3xTg-AD mice injected with saline revealed spine densities typical of 3xTg-AD mice at this age with signs of early spine loss compared to wildtype mice, data comparison not shown. 3xTg-AD mice injected with a single incidence of LPS (1xLPS) were unaffected with no signs of overall or subtype spine loss. However, 3xLPS resulted in an overall significant reduction in spine density compared to 3xTg-AD injected with saline (14%, $p < 0.0001$) or 1xLPS groups (21%, $p = 0.0144$) (Figure 6.8B). Spine classification revealed only thin spines were significantly reduced in 3xTg-AD mice inflicted with 3xLPS compared to saline (16%, $p = 0.0086$) and 1xLPS (36%, $p = 0.0006$) (Figure 6.8C-E). These

observations are in agreement with previous chapters and demonstrate that repeated LPS insults exacerbates spine loss in 3xTg-AD mice.

6.3.1.4 Figures

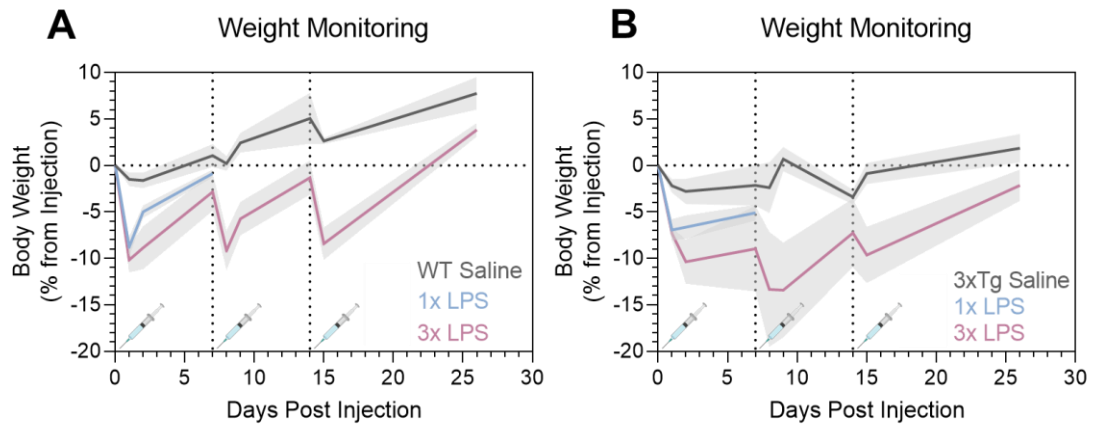


Figure 6.2 LPS triggers weight loss in wildtype and 3xTg-AD mice. **(A)** Body weight monitoring of wildtype mice compared to baseline (before injection) for saline, single (1xLPS) or repeated (3xLPS) insults of LPS. **(B)** Body weight monitoring of 3xTg-AD mice compared to baseline for saline, single (1xLPS) or repeated (3xLPS) insults of LPS. Injected days, indicated on each graph, correspond to day 0, 7 and 14 with 1x LPS only receiving day 0 injection. Mice were analysed in the 4th week post initial injection. All mice were female and aged 6 months at initial injection. Abbreviation: WT, wildtype; LPS, Lipopolysaccharide; 1xLPS, single LPS injection; 3xLPS, 3 LPS injections.

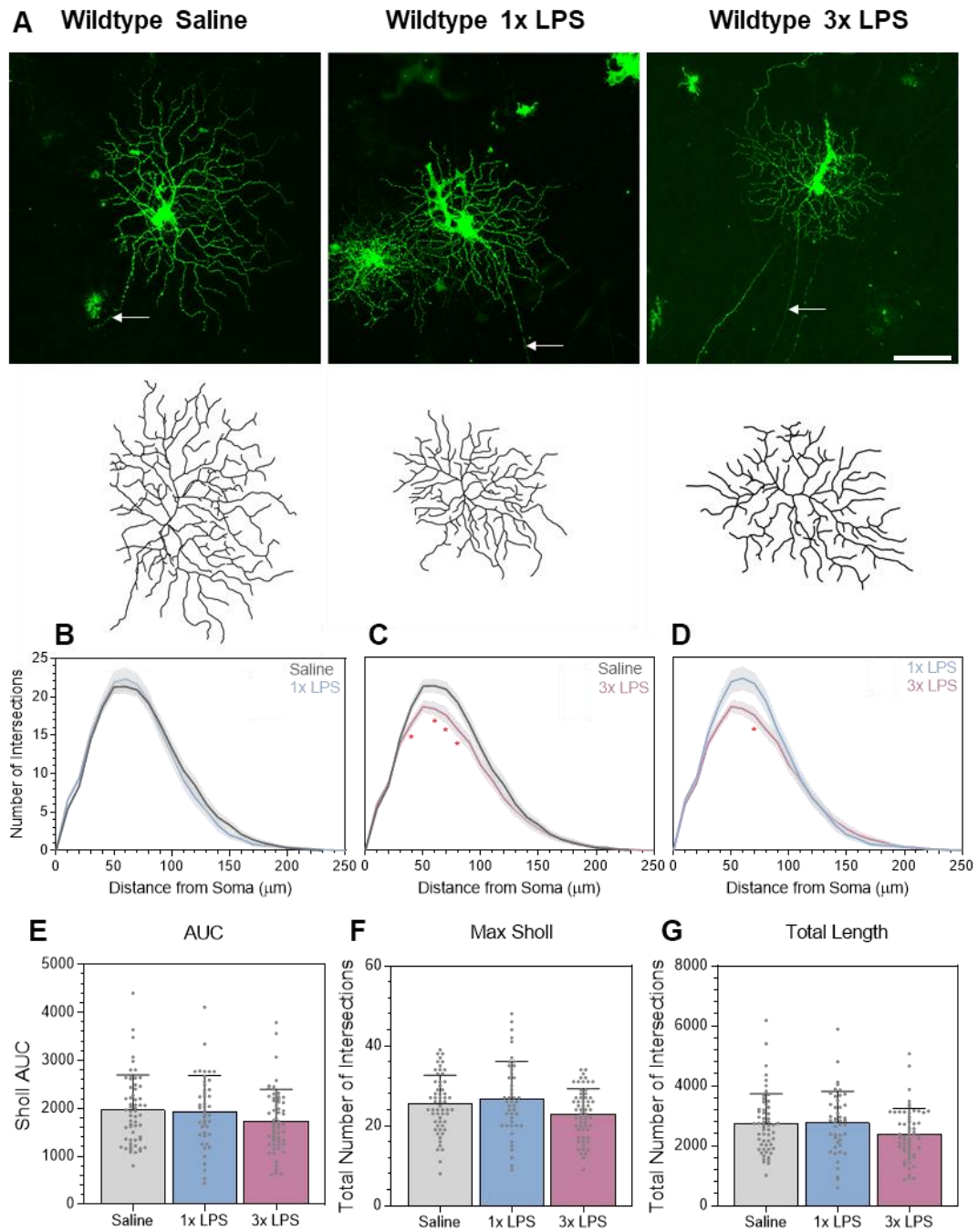


Figure 6.3 RGC dendritic complexity in LPS insulted wildtype mice. (A) Representative RGC examples from wildtype mice injected with either saline, 1 or 3 insults of LPS with the corresponding dendritic reconstructions. Arrows indicate RGC axon. Scale bar 100 μ m (B-D) Sholl analysis of RGCs. Line represents mean of group at each interval, shaded error zones \pm SEM. Two-tailed Mann-Whitney U test at each interval distance, * = $p < 0.05$. (E) Area under Sholl curve. (F) Maximum number of Sholl intersections. (G) Total length of all dendrites. Column Scatterplots: data represent individual cells and error bars correspond to SD. Saline: $n = 58$ cells (6 mice), 1xLPS: $n = 45$ cells (3 mice) and 3xLPS: $n = 59$ cells (3 mice). (E-G) Three groups were compared by nonparametric one-way analysis of variance (Kruskal–Wallis test) using Dunn multiple comparisons post-test, * = $p < 0.05$, ** = $p < 0.01$, *** = $p < 0.001$, **** = $p < 0.0001$. All female mice aged at 6 months at initial injection and analysed at 7 months. Abbreviations: WT, wildtype; AUC, area under the Sholl curve; 1xLPS, single LPS injection; 3xLPS, 3 LPS injections.

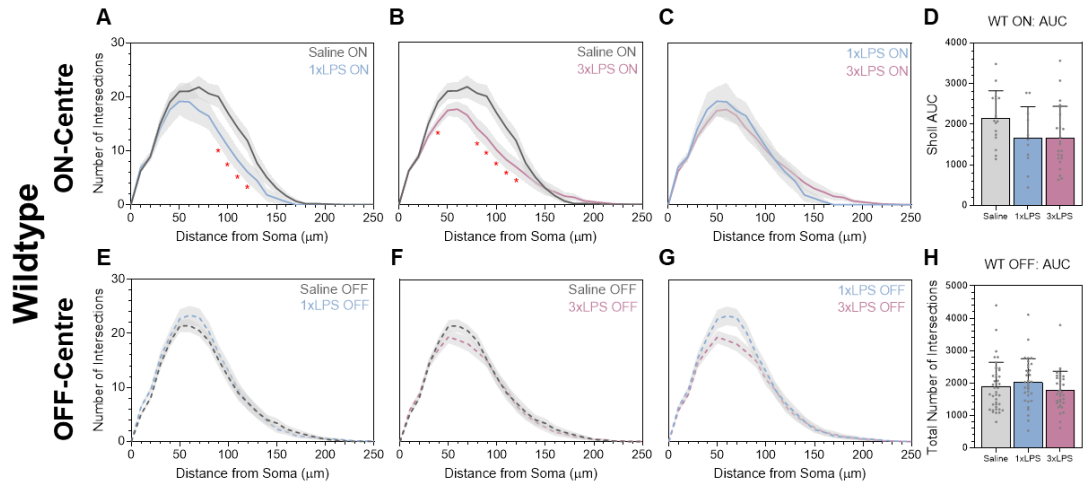


Figure 6.4 ON-centre vulnerability in LPS insulted wildtype mice. (A-C) Sholl analysis of ON-centre RGCs from wildtype mice subjected to saline, 1xLPS or 3xLPS injections. Line represents mean of group at each interval, shaded error zones \pm SEM. Two-tailed Mann-Whitney U test at each interval distance, $* = p < 0.05$. (D) Area under Sholl curve for ON-centre RGCs. (E-G) Sholl analysis for OFF-centre RGCs from wildtype mice subjected to saline, 1xLPS or 3xLPS injections. Line represents mean of group at each interval, shaded error zones \pm SEM. (H) Area under the Sholl curve for OFF-centre RGCs. Column Scatterplots (D, H): data represent individual cells and error bars correspond to SD. ON-Centre- Saline: $n = 16$ cells (6 mice), 1xLPS: $n = 11$ cells (3 mice) and 3xLPS: $n = 23$ cells (3 mice). OFF-Centre- Saline: $n = 42$ cells (6 mice), 1xLPS: $n = 34$ cells (3 mice) and 3xLPS: $n = 36$ cells (3 mice). All female mice aged at 6 at initial injection and analysed at 7 months. Abbreviations: WT, wildtype; AUC, area under the Sholl curve; 1xLPS, single LPS injection; 3xLPS, 3 LPS injections.

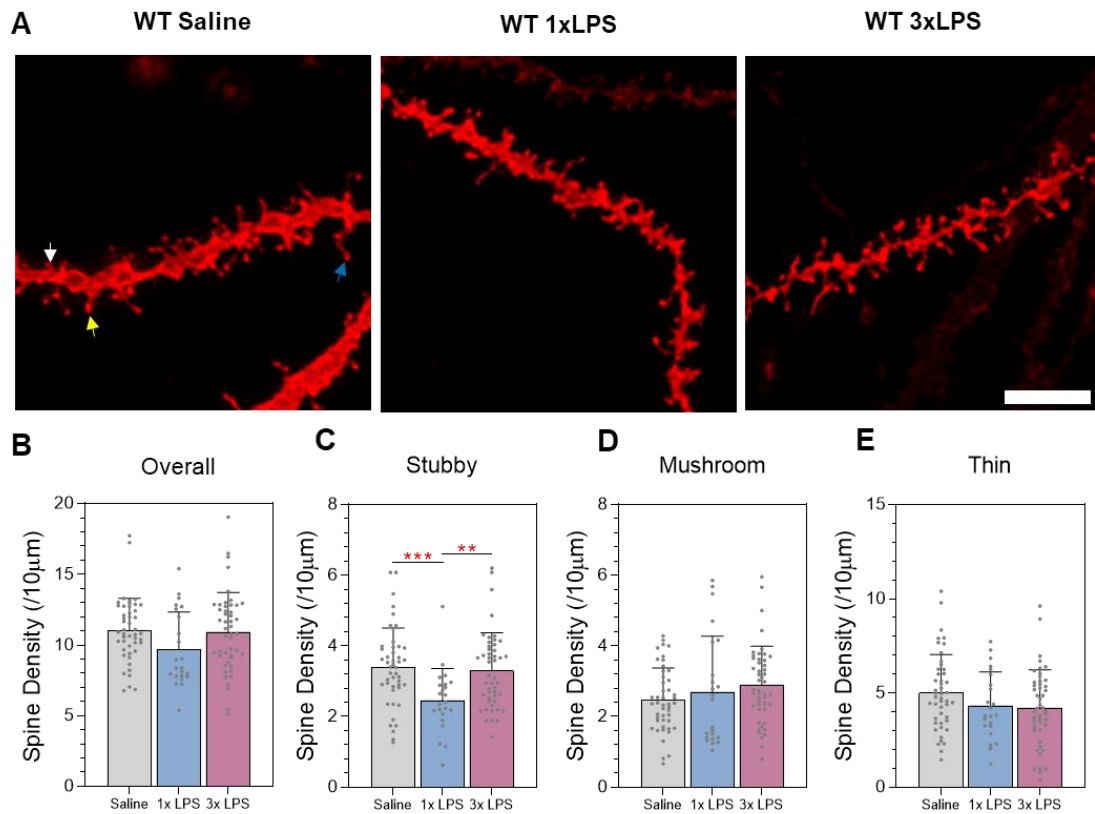


Figure 6.5 CA1 dendritic spine density in LPS insulted wildtype mice. (A) Representative confocal images of DiI labelled CA1 dendritic segments from WT, 1xLPS and 3xLPS. Arrows indicate spine morphology: stubby (white arrows), mushroom (yellow arrows), thin (blue arrows). Scale bar 5 μ m. Spine densities were analysed from dendritic segments of at least 30 μ m. (B-E) Spine densities across all dendritic segments for overall, stubby, mushroom and thin groups. Column Scatterplot: data represent individual cells and error bars correspond to SD. Saline: $n = 47$ dendrites (5 mice), 1xLPS: $n = 23$ dendrites (3 mice) and 3xLPS: $n = 48$ dendrites (3 mice). Three groups were compared by nonparametric one-way analysis of variance (Kruskal–Wallis test) using Dunn multiple comparisons post-test, $* = p < 0.05$, $** = p < 0.01$, $*** = p < 0.001$, $**** = p < 0.0001$. All female mice aged at 6 at initial injection and analysed at 7 months. Abbreviations: WT, wildtype; 1xLPS, single LPS injection; 3xLPS, 3 LPS injections.

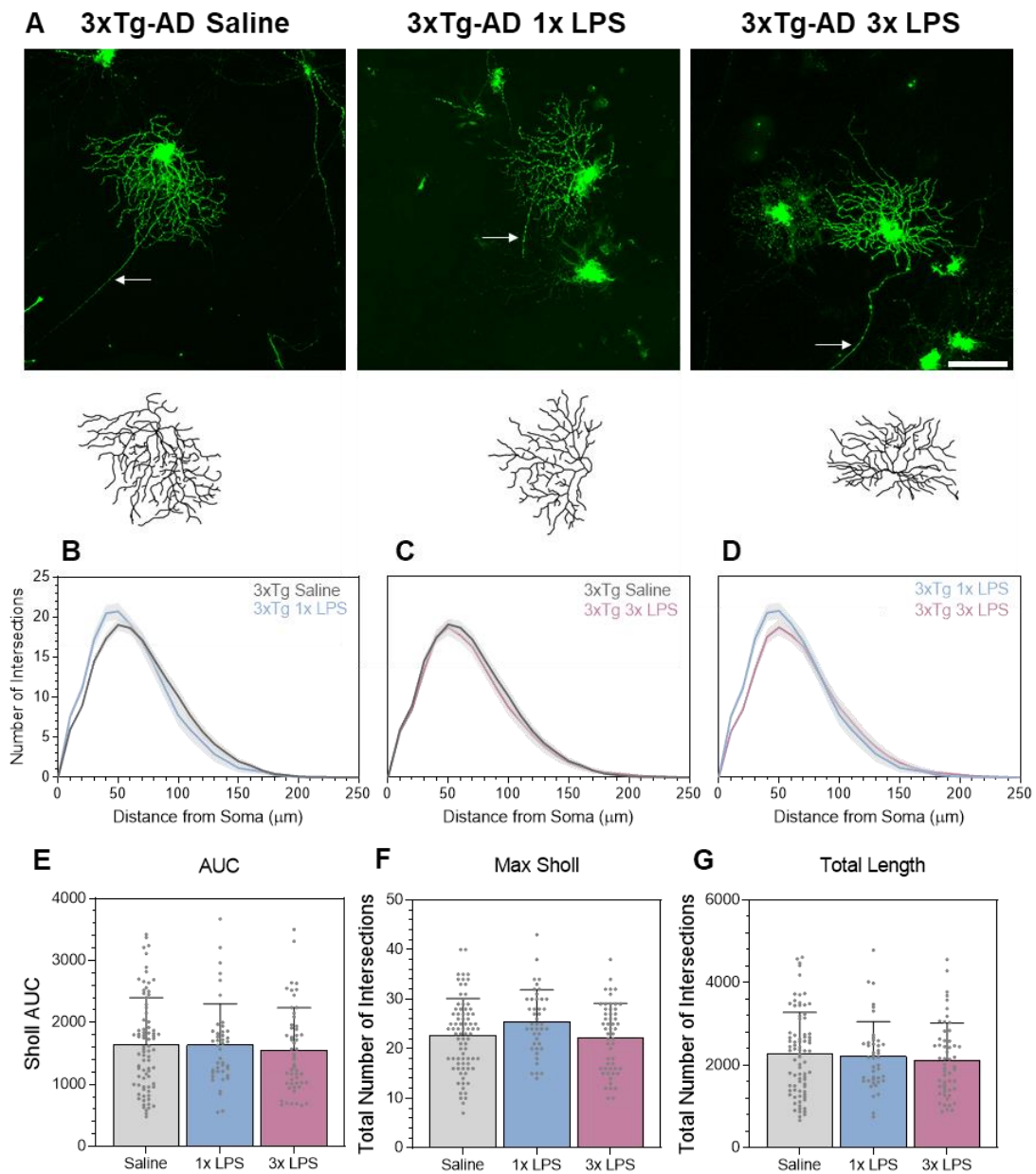


Figure 6.6 RGC dendritic complexity in LPS insulted 3xTg-AD mice. (A) Representative RGC examples from wildtype mice injected with either saline, 1 or 3 insults of LPS with the corresponding dendritic reconstructions. Arrows indicate RGC axon. Scale bar: 100 μm . (B-D) Sholl analysis of RGCs. Line represents mean of group at each interval, shaded error zones \pm SEM. Two-tailed Mann-Whitney U test at each interval distance, * = $p < 0.05$. (E) Area under Sholl curve. (F) Maximum number of Sholl intersections. (G) Total length of all dendrites. Column Scatterplots: data represent individual cells and error bars correspond to SD. Saline: $n = 81$ cells (5 mice), 1xLPS: $n = 43$ cells (4 mice) and 3xLPS: $n = 54$ cells (3 mice). (E-G) Three groups were compared by nonparametric one-way analysis of variance (Kruskal–Wallis test) using Dunn multiple comparisons post-test, * = $p < 0.05$, ** = $p < 0.01$, *** = $p < 0.001$, **** = $p < 0.0001$. All female mice aged at 6 at initial injection and analysed at 7 months. Abbreviations: AUC, area under the Sholl curve; 1xLPS, single LPS injection; 3xLPS, 3 LPS injections.

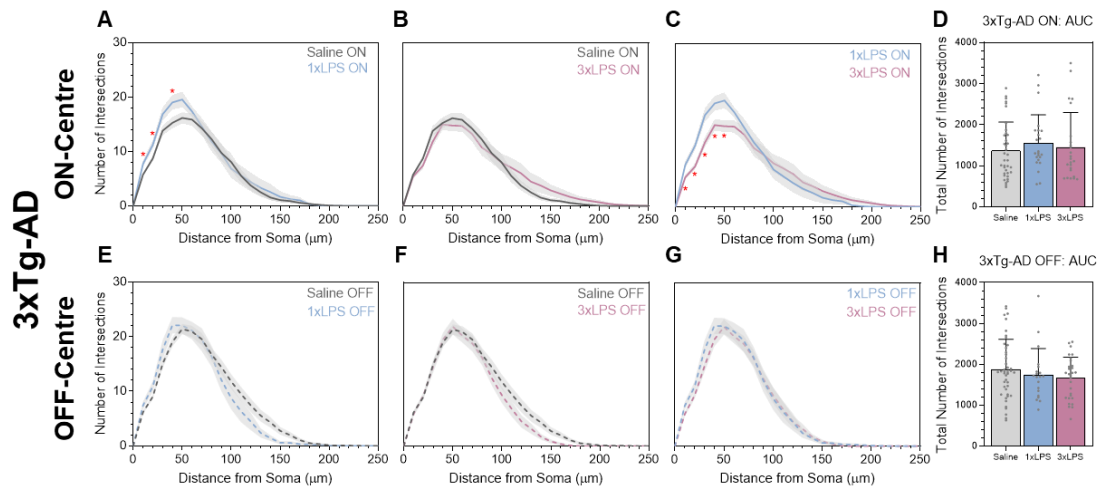


Figure 6.7 RGC receptive field classification in LPS insulted 3xTg-AD mice. (A-C) Sholl analysis of ON-centre RGCs from 3xTg-AD mice subjected to saline, 1xLPS or 3xLPS injections. Line represents mean of group at each interval, shaded error zones \pm SEM. Two-tailed Mann-Whitney U test at each interval distance, $* = p < 0.05$. (D) Area under Sholl curve for ON-centre RGCs. (E-G) Sholl analysis for OFF-centre RGCs from 3xTg-AD mice subjected to saline, 1xLPS or 3xLPS injections. Line represents mean of group at each interval, shaded error zones \pm SEM. (H) Area under the Sholl curve for OFF-centre RGCs. Column Scatterplots: data represent individual cells and error bars correspond to SD. ON-Centre- Saline: $n = 37$ cells (5 mice), 1xLPS: $n = 23$ cells (4 mice) and 3xLPS: $n = 25$ cells (3 mice). OFF-Centre- Saline: $n = 44$ cells (5 mice), 1xLPS: $n = 20$ cells (4 mice) and 3xLPS: $n = 29$ cells (3 mice). All female mice aged at 6 at initial injection and analysed at 7 months. Abbreviations: AUC, area under the Sholl curve; 1xLPS, single LPS injection; 3xLPS, 3 LPS injections.

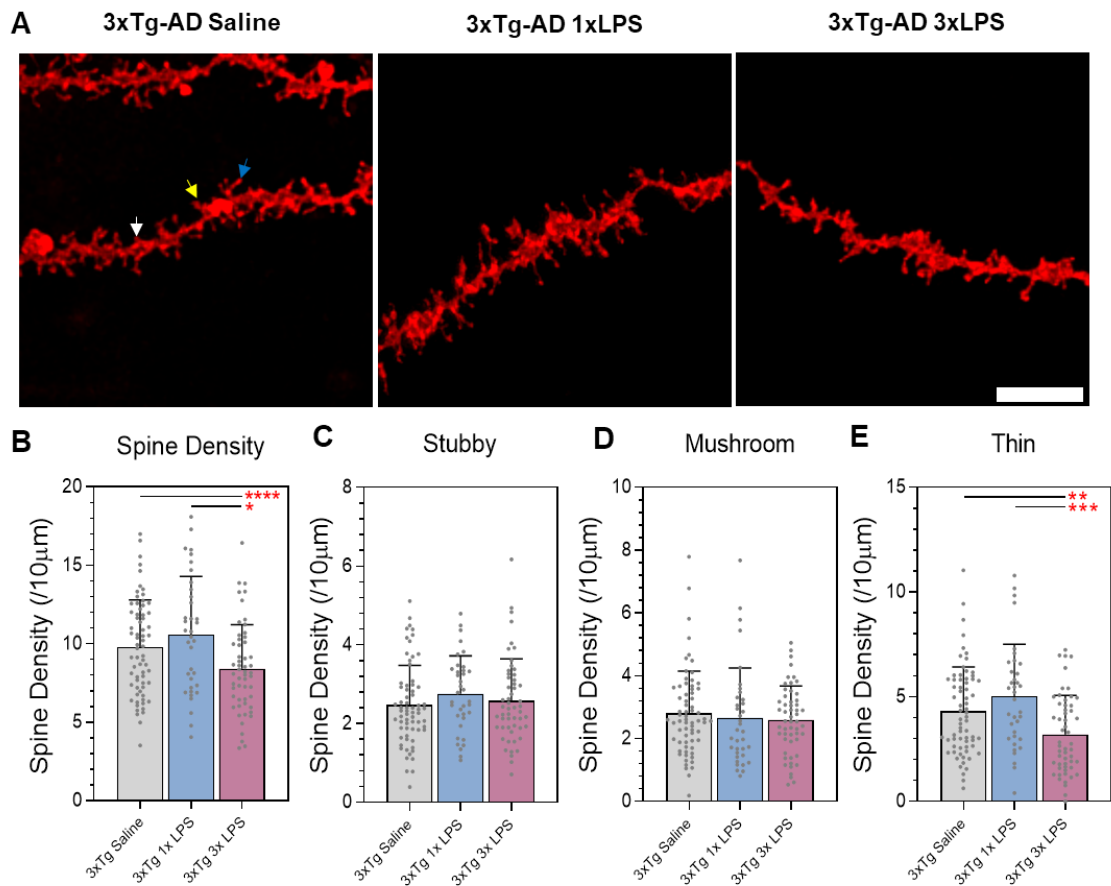


Figure 6.8 Repeated LPS insults triggers CA1 dendritic spine loss in 3xTg-AD mice. (A) Representative confocal images of DiI labelled CA1 dendritic segments from 3xTg-AD, 1xLPS and 3xLPS. Arrows indicate spine morphology: stubby (white arrows), mushroom (yellow arrows), thin (blue arrows). Scale bar 5 μ m. Spine densities were analysed from dendritic segments of at least 30 μ m. (B-E) Spine densities across all dendritic segments for overall, stubby, mushroom and thin groups. Column Scatterplot: data represent individual cells and error bars correspond to SD. Saline: $n = 68$ dendrites (5 mice), 1xLPS: $n = 36$ dendrites (3 mice) and 3xLPS: $n = 54$ dendrites (3 mice). Three groups were compared by nonparametric one-way analysis of variance (Kruskal–Wallis test) using Dunn multiple comparisons post-test, * = $p < 0.05$, ** = $p < 0.01$, *** = $p < 0.001$, **** = $p < 0.0001$. All female mice aged at 6-7 months. Abbreviations: 1xLPS, single LPS injection; 3xLPS, 3 LPS injections.

6.3.2 MCMV

6.3.2.1 Wildtype

To assess the impact of MCMV infection on RGC dendritic complexity, wildtype mice were assessed at 9 months. Wildtype mice injected with saline revealed a Sholl profile and accompanying parameters typical of previous wildtype descriptions. In contrast, wildtype mice infected with MCMV had a minimal effect on RGC dendritic complexity (representative examples, Figure 6.9A). Although not attaining statistical significance, the Sholl curve was reduced between 100 and 150 μm in the MCMV infected wildtype mice (Figure 6.9B). No statistical differences were identified in the Sholl AUC, the maximum number of intersections or in the overall total length of the dendrites (Figure 6.9C-E). It was not feasible based on the number of RGCs collected to separate the data based on receptive field classification. These data demonstrate that wildtype mice infected with MCMV does not trigger excessive pruning of RGC dendrites.

In the same wildtype mice, hippocampal CA1 dendritic spines were also analysed to assess the impact of MCMV infection (representative examples, Figure 6.10A). Wildtype mice injected with saline revealed spine densities both overall and classified based on subtype typical of normal levels previously described in earlier chapters. In the wildtype mice infected with MCMV, no effects were observed on the total spine density, nor in the spine subtypes (Figure 6.10B-I). These data demonstrate that MCMV infection in wildtype mice does not trigger dendritic spine loss on CA1 hippocampal neurons.

6.3.2.2 3xTg-AD

To assess the impact of MCMV infection on RGC dendritic complexity, 3xTg-AD mice were assessed at 9 months (representative examples, Figure 6.11A). 3xTg-AD mice injected with saline revealed a Sholl profile that was typical of 3xTg-AD mice at this age point, with modest reductions in dendritic complexity compared to wildtypes (data comparison not shown). In 3xTg-AD mice infected with MCMV, there was a consistent, but subtle, decrease in RGC dendritic complexity ($p < 0.05$ only at 40 and 50 μm) (Figure 6.11B). These changes were supported by significantly reduced Sholl AUC (16%, $p < 0.0423$) and decreased maximum number of intersections (13%, $p = 0.0223$) (Figure 6.11C-D). However, the total number length of all the dendrites was reduced in MCMV infected 3xTg-AD mice, although the changes were not significant (Figure 6.11E). Similar to the wildtype mice, it was not feasible based on the number of RGCs collected to separate the data based on receptive field classification. These data demonstrate that at 9 months, 3xTg-AD mice infected with MCMV trigger excessive RGC dendritic pruning.

In the same mice, hippocampal CA1 dendritic spines were also analysed in the 3xTg-AD model (representative examples, Figure 6.12A). 3xTg-AD mice injected with saline revealed spine densities typical of 3xTg-AD mice at this age, similar to previously reported findings in Chapter 4, with spine density reduced compared to wildtypes. In 3xTg-AD mice infected with MCMV there was a significant decrease in the overall spine density (14%, $p = 0.0058$), with a decrease in all spine subtypes, although alone these subtypes did not attain statistical significance (Figure 6.12B-I). These data demonstrate that MCMV infection in 3xTg-AD mice exacerbates hippocampal CA1 dendritic spine density.

6.3.2.3 Figures

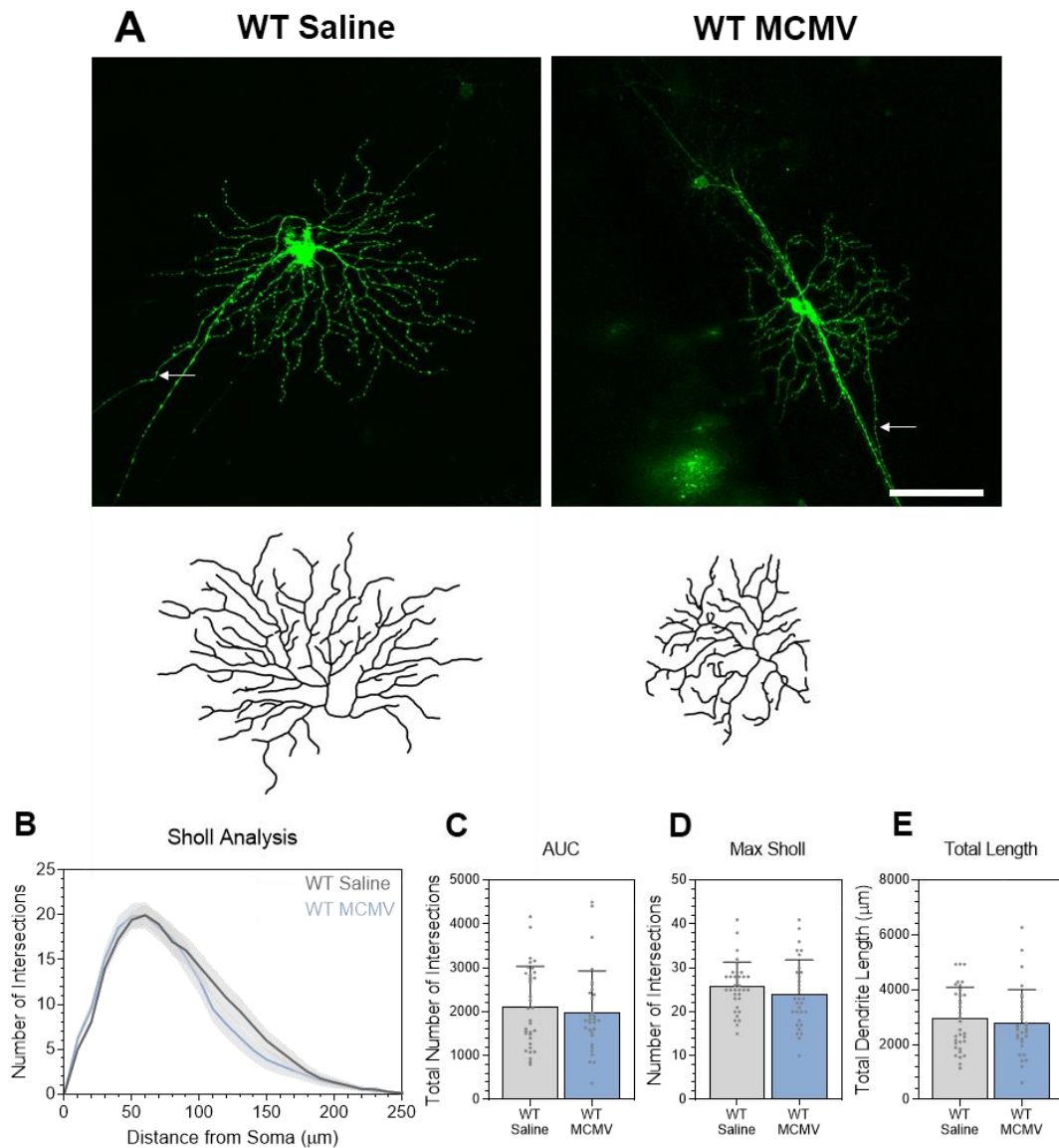


Figure 6.9 RGC dendritic complexity in MCMV infected wildtype mice. (A) Representative RGC examples from wildtype mice injected with either saline or MCMV with the corresponding dendritic reconstructions. Arrows indicate RGC axon. Scale bar: 100 μm . (B) Sholl analysis of RGCs. Line represents mean of group at each interval, shaded error zones \pm SEM. Two-tailed Mann-Whitney U test at each interval distance, * = $p < 0.05$. (C) Area under Sholl curve. (D) Maximum number of Sholl intersections. (E) Total length of all dendrites. Column Scatterplots: data represent individual cells and error bars correspond to SD. WT saline: $n = 35$ cells (4 mice), WT MCMV: $n = 31$ cells (4 mice). (C-E) Two group comparisons were made using the Mann-Whitney U test, * = $p < 0.05$, ** = $p < 0.01$, *** = $p < 0.001$, **** = $p < 0.0001$. All female mice aged at 9 months. Abbreviations: WT, wildtype; AUC, area under the Sholl curve.

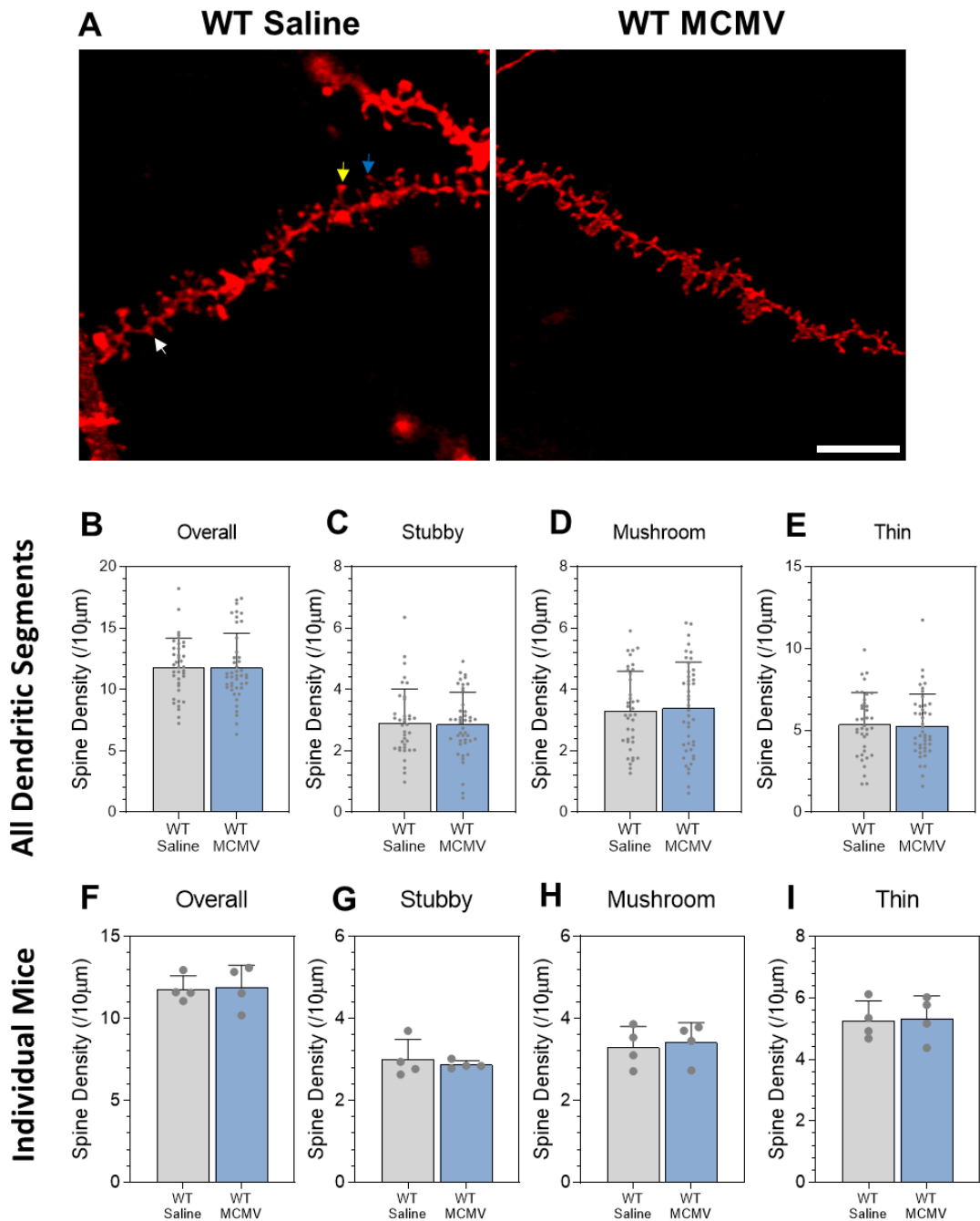


Figure 6.10 CA1 dendritic spines in MCMV infected wildtype mice. (A) Representative confocal images of DiI labelled CA1 dendritic segments from wildtype mice treated with saline or MCMV. Arrows indicate spine morphology: stubby (white arrows), mushroom (yellow arrows), thin (blue arrows). Scale bar 5 μm . Spine densities collected from an average of 30 μm dendritic segments. (B-E) Spine densities across all dendritic segments and (F-I) spine densities across all individual mice for overall, stubby, mushroom and thin groups. Column Scatterplots (B-E): data represent individual cells and error bars correspond to SD. Column Scatterplots (F-I): bars, mean of group; data represent the mean spine density from individual mice and error bars correspond to SD. WT saline: $n = 38$ dendrites (4 mice) and WT MCMV: $n = 44$ dendrites (4 mice). Two group comparisons were made using the Mann-Whitney U test., * = $p < 0.05$, ** = $p < 0.01$, *** = $p < 0.001$, **** = $p < 0.0001$. All female mice aged at 9 months. Abbreviations: WT, wildtype.

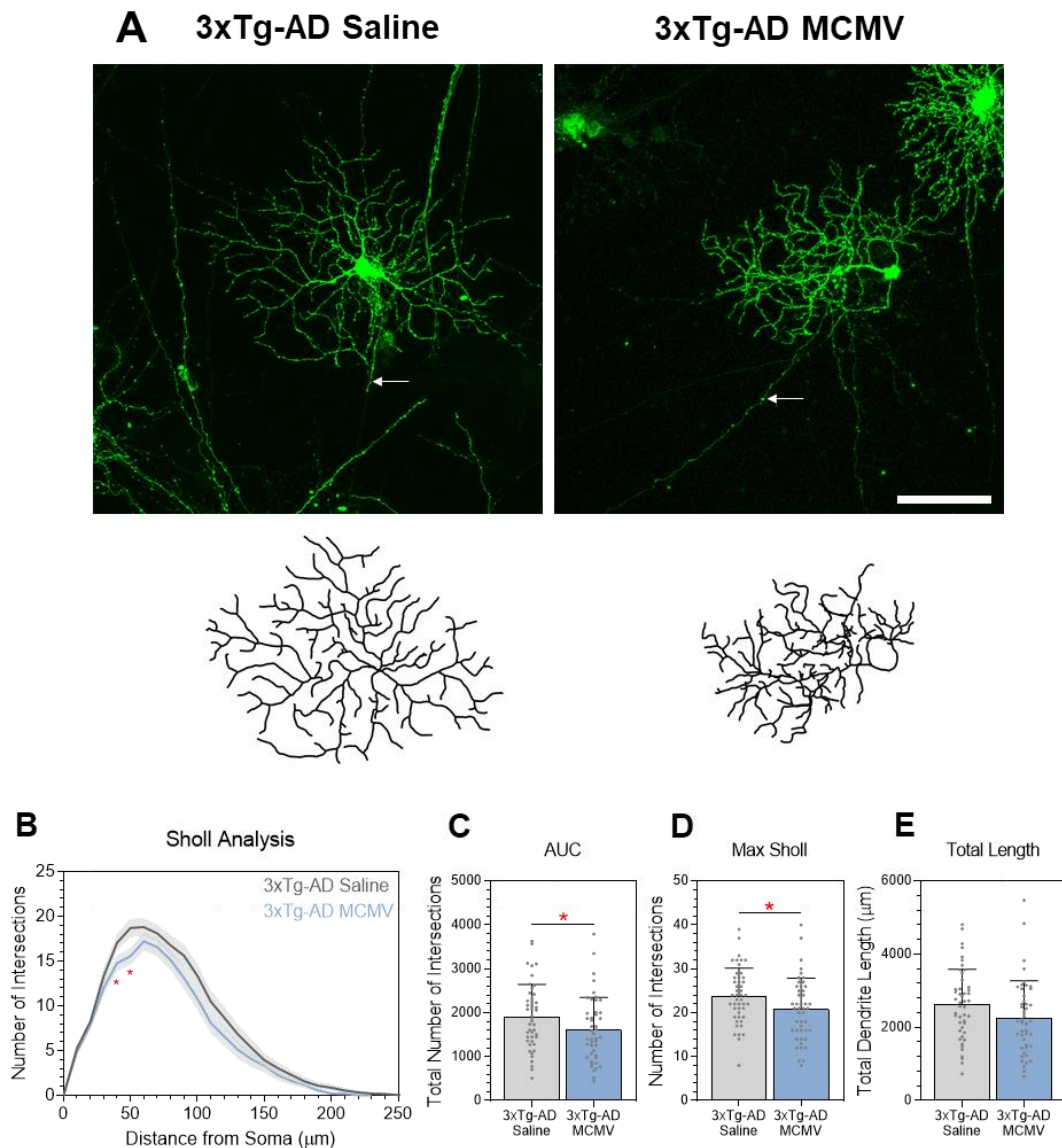


Figure 6.11 RGC dendritic complexity in MCMV infected 3xTg-AD mice. (A) Representative RGC examples from 3xTg-AD mice injected with either saline or MCMV with the corresponding dendritic reconstructions. Arrows indicate RGC axon. Scale bar: 100 μ m. (B) Sholl analysis of RGCs. Line represents mean of group at each interval, shaded error zones \pm SEM. Two-tailed Mann-Whitney U test at each interval distance, * = $p < 0.05$. (C) Area under Sholl curve. (D) Maximum number of Sholl intersections. (E) Total length of all dendrites. Column Scatterplots (C-E): data represent individual cells and error bars correspond to SD. 3xTg-AD saline: $n = 47$ cells (6 mice) and 3xTg-AD MCMV: $n = 46$ cells (6 mice). (C-E) Two group comparisons were made using the Mann-Whitney U test., * = $p < 0.05$, ** = $p < 0.01$, *** = $p < 0.001$, **** = $p < 0.0001$. All female mice aged at 9 months. Abbreviations: AUC, area under the Sholl curve.

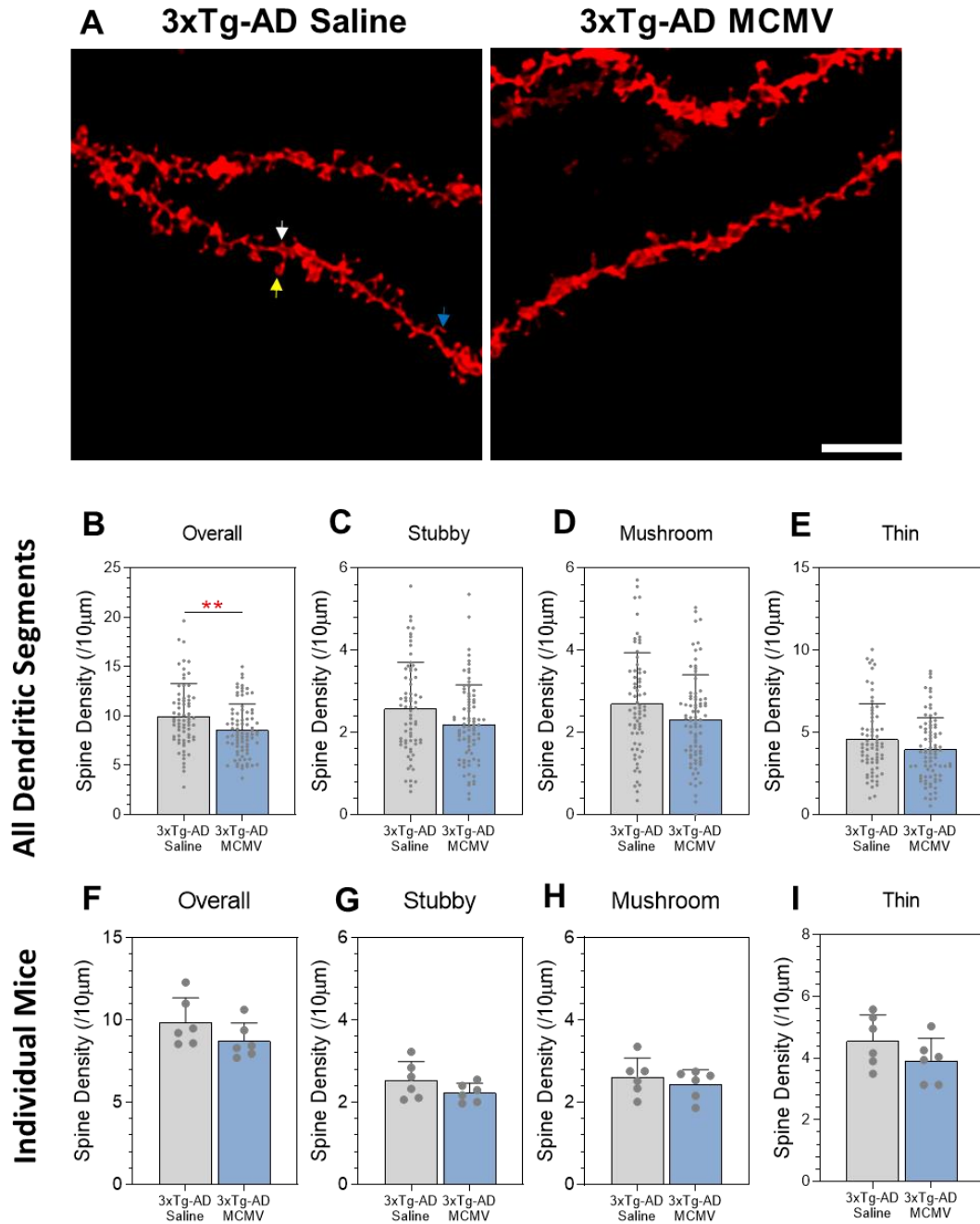


Figure 6.12 CA1 dendritic spines in MCMV infected 3xTg-AD mice. (A) Representative confocal images of DiI labelled CA1 dendritic segments from 3xTg-AD mice treated with saline or MCMV. Arrows indicate spine morphology: stubby (white arrows), mushroom (yellow arrows), thin (blue arrows). Scale bar 5 μ m. Spine densities collected from an average of 30 μ m dendritic segments. (B-E) Spine densities across all dendritic segments and (F-I) spine densities across all individual mice for overall, stubby, mushroom and thin groups. Column Scatterplot (B-E): data represent individual cells and error bars correspond to SD. Column Scatterplots (F-I): bars, mean of group; data represent the mean spine density from individual mice and error bars correspond to SD. 3xTg-AD PBS: $n = 70$ dendrites (6 mice) and 3xTg-AD CMV: $n = 82$ dendrites (6 mice). Two group comparisons were made using the Mann-Whitney U test., * = $p < 0.05$, ** = $p < 0.01$, *** = $p < 0.001$, **** = $p < 0.0001$. All female mice aged at 9 months.

6.4 Discussion

Inflammation is necessary to efficiently respond to damage and invading pathogens; however, chronic sustained inflammation associates with many diseases. The neuroinflammatory component of AD, including microglial activation, is closely linked to the development of pathology and cognitive deficits (Cunningham and Hennessy, 2015). Peripheral inflammation, outside of the CNS, can be chronic and affect the extent of neuroinflammation in AD associating with a worse prognosis (Brown, 2019). However, it is uncertain to what extent peripheral inflammation is a factor in driving neurodegeneration in AD. This chapter assessed the impact of systemic inflammation triggered by mimicked bacterial (LPS) and viral (MCMV) infections in wildtype and 3xTg-AD mice and determined the impact on RGC dendritic complexity and CA1 hippocampal dendritic spines. Peripheral inflammation driven by these infectious agents had the capacity to influence subtle changes to RGC dendritic complexity and CA1 hippocampal dendritic spines in AD mice. These findings are in support with the current understandings that inflammation outside of the CNS can contribute to the burden of neurodegeneration.

While infections alone may not cause AD pathology, their presence is increasingly associated with neuroinflammation, exacerbated disease severity and progression of the disease. Systemic inflammation can trigger cognitive dysfunction and lead to long-term cognitive impairment (Giridharan *et al.*, 2019). In the blood circulation of AD individuals it is common to detect proinflammatory markers, therefore demonstrating its potential significance and role in contributing to AD pathology (Zetterberg and Burnham, 2019). In AD mouse models, whereby bacterial infections are commonly mimicked through the administration of LPS, mice display an increased amyloid deposition in the brain, particularly in the hippocampus and cortex (Lee *et al.*, 2008). In models featuring LPS-driven inflammation, LPS triggers microglial activation and promotes the clearance of diffuse amyloid, whilst in models harvesting tau mutations, LPS exacerbates tau pathology (DiCarlo *et al.*, 2001; Herber *et al.*, 2004; Kitazawa *et al.*, 2005; Herber *et al.*, 2007; Lee *et al.*, 2010; Sy *et al.*, 2011).

As previously discussed, synaptic loss correlates with AD severity and progression. LPS-driven inflammation alters synaptic plasticity, triggers excessive synaptic pruning,

remodels neuronal networks and is linked to the observed cognitive impairments (Commins *et al.*, 2001; Kondo *et al.*, 2011). These LPS-related changes are found to have long-lasting effects on synaptic networks, and are detected from a single LPS exposure (Kondo *et al.*, 2011). Although the underlying mechanisms are unclear, these changes are linked to IL-1 β associated microglial activation and dysfunctional mitochondria, corresponding to the associated cognitive deficits (Moraes *et al.*, 2015; He *et al.*, 2019; Sheppard *et al.*, 2019; Zhao *et al.*, 2019).

In this chapter, wildtype and 3xTg-AD mice were treated with LPS, mimicking bacterial infections. Wildtype mice demonstrated exacerbated RGC dendritic pruning when subjected to multiple doses of LPS rather than a single dose. These suggest that in the absence of disease, RGCs are potentially vulnerable to repeated and sustained systemic inflammation. In previous chapters, classification of RGC's based on the dendritic lamination highlighted potential susceptibility of ON-centre classified RGCs rather than OFF-centre RGCs. These findings were also observed in the wildtype mice challenged with LPS. A recent study also reports excessive RGC dendritic pruning in response to LPS, although these observations were obtained from postnatal mice, suggesting the role of peripheral inflammation to influence RGC dendritic architecture (Gao *et al.*, 2018). In the 3xTg-AD model, LPS driven RGC dendritic pruning was less apparent. At the age point analysed, 6-7 months, 3xTg-AD mice display RGC dendritic profiles similar to wildtypes. In contrast, RGCs in the 3xTg-AD model did not display exacerbated dendritic pruning as a result of a single or multiple LPS dose. As reported in Chapter 3, excessive RGC dendritic pruning in the 3xTg-AD model is more prominent around the ages of 12 months. Despite the absence of exacerbated RGC pruning in the 3xTg-AD mice in response to LPS, it may remain possible for these early markers of neurodegeneration to become apparent later in the disease when pathology has advanced.

In earlier chapters I demonstrated that dendritic spines decorating CA1 hippocampal neurons are vulnerable to excessive pruning in AD mouse models, especially in older mice with a more advanced pathology. In the same LPS insulted mice assessed for RGC dendritic complexity, CA1 dendritic spine densities were quantified at 6-7 months. In wildtypes, the impact of LPS on CA1 hippocampal dendritic spine densities demonstrated mixed results. A single LPS insult in wildtype mice, rather than repeated doses, triggered overall dendritic spine loss, however on closer inspection of the spine subtypes, only

immature stubby spines were reduced. In the control wildtype mice injected with saline in revealed spine densities that were typical of previously discussed wildtype mice. These observations are in contrast to previous data that pinpointed the vulnerability of thin spines (Chugh *et al.*, 2013). These findings suggest that LPS driven inflammation in wildtype mice may trigger hippocampal dendritic spine alterations, however changes are subtle and absent in mice repeatedly exposed to LPS.

Administration of LPS in AD mouse models associate with accelerated pathology and further cognitive function. In 3xTg-AD mice at 6-7 months, the onset of detectable pathological changes, a single insult of LPS did not affect spine coverage; however, multiple LPS doses triggered CA1 hippocampal dendritic spine loss. The sustained elevation of systemic inflammation, which may arise from the multiple doses of LPS, corresponded to a reduction in thin spines. These observed decrease of dendritic spines, particularly of thin spines are in agreement with previous data in earlier chapters and data of others reporting a reduction in dendritic spines in the brain due to LPS-driven inflammation (Sheppard *et al.*, 2019). The changes in response to repeated systemic LPS injections has previously been reported an increase in microglial activation, classical complement activation and induction of neuronal loss, with a single dose unable to trigger such effects (Bodea *et al.*, 2014). Synapse loss as a result of LPS triggers microglial activation and initiates microglial-mediated synaptic engulfment. Both single and multiple LPS insults remodel synaptic networks, alter learning capacity, and triggers depression-like behaviour in mice (Sparkman *et al.*, 2005; Zhang *et al.*, 2014). In sepsis models, which feature higher concentrations of LPS, LPS elicits synaptic disruption and is associated with a marked increased production of proinflammatory cytokines (Moraes *et al.*, 2015; Lin *et al.*, 2019). Collectively, these findings demonstrate that peripheral inflammation caused by mimicking bacterial infection, has the capacity to influence the burden of synaptic loss in the brain of AD mouse models.

Viral infections are another source of potential triggers of systemic inflammation and similarly impact neuroinflammation in the CNS. Reactivation of latent viral infections triggers priming and activation of microglia, and in AD, viral seropositivity associates with an increased risk of a more severe pathology and cognitive deficits (Chiu *et al.*, 2014; Barnes *et al.*, 2015). To explore the role of viral infection on the RGC dendrites and hippocampal dendritic spines, both wildtype and 3xTg-AD mice were infected with

MCMV (5×10^4 pfu). In wildtypes virally infected, the effect on RGC dendritic complexity was unaltered. In contrast, 3xTg-AD mice demonstrated subtle but a significant and consistent reduction in dendritic complexity. These findings demonstrate that viral infections have the capacity to exacerbate neurodegeneration in the retina of 3xTg-AD mice. In the same MCMV infected mice, CA1 hippocampal dendritic spines were analysed. In wildtype mice, viral infection did not alter CA1 spine density and therefore mice displayed similar spine densities to saline and typical wildtype mice. In contrast, virally infected 3xTg-AD mice triggered a reduction in the number of dendritic spines. Although, it was unclear whether a particular spine subtype was driving this spine loss. Similar observation of synaptic loss in response to viral infections has previously been reported in wildtype mice (Sobue *et al.*, 2018). Therefore, the data in this chapter provides initial evidence supporting the role and impact of viral infections in triggering excessive synaptic loss in the hippocampus of AD mouse models.

To conclude, I demonstrate that systemic inflammation mimicked by bacterial and viral infections, can contribute to excessive RGC dendritic pruning and CA1 dendritic spine loss. Although changes were subtle and did not extensively remodel neurons, the observed impacts reinforce the role of peripheral inflammation influencing the burden of neurodegeneration in the CNS.

Chapter 7. The impact of probiotic supplementation on retinal ganglion cells and CA1 hippocampal dendritic spines in the 3xTg-AD model.

7.1 Introduction

In the preceding chapters, I reported that RGC dendritic complexity, and hippocampal CA1 dendritic spines are vulnerable to excessive pruning in AD mouse models. These were affected by changes to the innate immune system whereby deficiencies of the complement system offered neuronal protection, in contrast, infectious agents triggered exacerbated pruning. These findings demonstrated that inflammation in the periphery has a crucial role in modulating, at least in part, the status of neurodegeneration in both the retina and hippocampus of AD mouse models. An alternative source of peripheral inflammation, which can be chronic and sustained for long periods, relates to changes in the gut microbiome. Dysbiosis, is an increasingly reported feature in neurological and neurodevelopmental disorders, although the exact mechanisms are unclear (Grigg and Sonnenberg, 2017). Therapeutically altering the composition of the microbiome, particularly during early stages of diseases, may offer an opportunity to modulate the status of dysbiosis in order to reduce the status of circulating inflammation, a contributing factor in neurodegenerative diseases (Westfall *et al.*, 2017).

A healthy gut is typically stable however is closely influenced by a person's diet, particularly a diet high in fat, infections throughout life, and ageing to name a few. Although the exact mechanisms are unknown, the gut microbiome can affect cognitive function. Dysregulation of the gut microbiome is linked to several neurological disorders, including depression, stress and autism (O'Hagan *et al.*, 2017). Dysbiosis has also been found as an emerging comorbidity in neurodegenerative diseases, including AD (Sy *et al.*, 2011). Dysbiosis can lead to chronic increases in peripheral inflammation that is sustained for many years (Saiyasit *et al.*, 2020). As discussed earlier, peripheral inflammation is an associating factor on the burden of neuroinflammation and correlates with AD pathology. Therefore, modulation of the gut microbiome is a realistic and

attractive therapeutic strategy against the inflammatory component of AD (Li *et al.*, 2019).

Probiotics, such as *Bifidobacterium* and *Lactobacillus*, are regarded as beneficial bacteria that have the ability to modulate the gut microbiome and restore homeostasis. Recently, probiotics have demonstrated positive effects in the brain including against depression and neurodegenerative diseases (Roy Sarkar and Banerjee, 2019). *In vitro* and *in vivo* studies have highlighted the roles of probiotics for modulation of the immune system, anti-apoptotic properties, protects against oxidative damage, and improves cognitive function (Nimgampalle and Yellamma, 2017). AD models and human AD studies have recently demonstrated that probiotic supplementation decreases the abundance of amyloid pathology, reduces oxidative stress and reduces inflammatory markers (Akbari *et al.*, 2016; Abraham *et al.*, 2019). However, it remains unclear to what extent probiotics modulate synaptic plasticity.

In this chapter, in collaboration with Cultech Ltd, I assessed the impact of probiotic dietary supplementation on RGC dendritic complexity and hippocampal CA1 dendritic spines in 3xTg-AD mice on a normal chow diet and a high-fat diet.

7.2 Experimental Setup

This chapter assessed the potential of probiotic dietary supplementation to provide neuroprotection against excessive RGC dendritic pruning and hippocampal CA1 spine loss in the 3xTg-AD model. Two probiotic consortia, Lab4b and Lab4p were analysed in 3xTg-AD mice on a normal chow and a high-fat diet. Lab4b comprises of *Lactobacillus salivarius* CUL61, *Lactobacillus paracasei* CUL21, *Bifidobacterium animalis subsp. lactis* CUL34 and *Bifidobacterium bifidum* CUL20, whereas Lab4p comprises *Lactobacillus acidophilus* CUL60 and CUL21, *Bifidobacterium bifidum* CUL20, *Bifidobacterium animalis subsp. lactis* CUL34 and *Lactobacillus plantarum* CUL66. Figure 7.1 provides an overview of the experimental setup.

Mice were assessed on a normal chow diet at 9 and 12 months. Both probiotic groups consisted of 3-month probiotic supplementation before analysis, i.e. 6-9 and 9-12 months, respectively. The second section in this chapter assessed the potential of probiotic supplementation in 3xTg-AD mice on a high-fat diet (21% (w/w) pork lard supplemented with 0.15% (w/w) cholesterol (Special Diets Services, Witham, U.K; product code: 821424)). The high fat diet and probiotic supplementation were administered for three months prior to analysis at 6 months, i.e. 3-6 months. All probiotic supplements consisted of 5×10^8 cfu/mouse/day, with mice fed 10 g/cage/day (44.50 kcal/cage/day). All mice in this chapter were male, and for all groups, both RGCs and hippocampal CA1 dendritic spines were assessed from the same animals. Access to wildtype mice was unavailable for all groups in this chapter, therefore the data only represents changes in respect to the 3xTg-AD model. Administration of probiotics, dietary changes, health checks and other data collections were performed by Dr Tim Hughes and Dr Tom Davies (Cultech Ltd). This thesis only investigated the impact of probiotics on RGC dendritic complexity and CA1 spine densities.

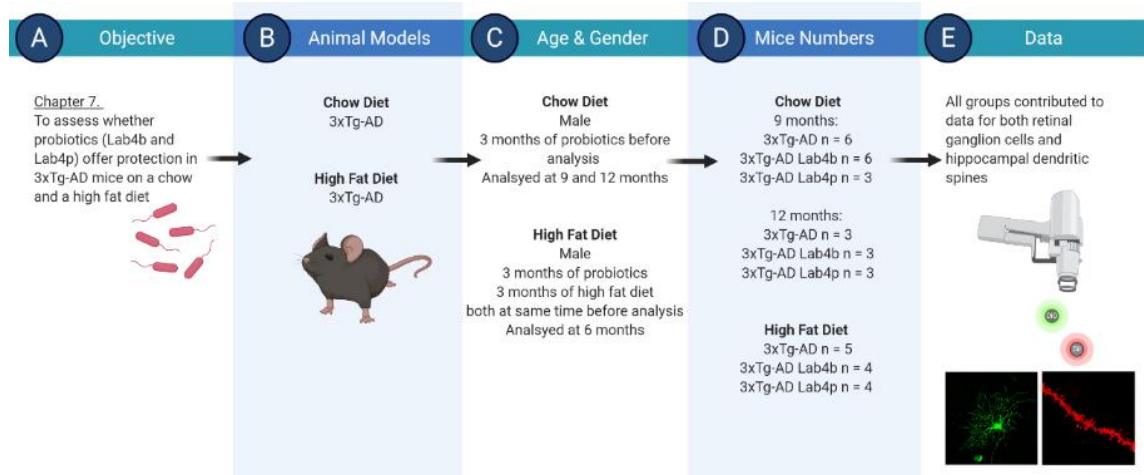


Figure 7.1 Experimental overview for Chapter 7 addressing the impact of probiotics in 3xTg-AD mice on a chow and a high fat diet for RGC dendritic complexity and CA1 hippocampal dendritic spine coverage. **(A)** Main objectives for Chapters 7. **(B)** The different animal models used in this chapter. **(C)** More details on the animal models including ages analysed and genders available. **(D)** Number of total mice analysed that were subjected to DiOlistic labelling. **(E)** All groups in Chapter 7 were analysed for RGC dendrites and hippocampal dendritic spine coverage. Illustration created in BioRender.

7.3 Results

7.3.1 Chow Diet

In 3xTg-AD mice on a normal chow diet without probiotic supplements, RGC dendritic complexity based on the Sholl profile and associated parameters, displayed minimal dendritic loss at 9 months, expected at this time point of the disease. Supplementation of Lab4b and Lab4p probiotics in 3xTg-AD mice analysed at 9 months showed no beneficial effects on RGC dendritic complexity (Figure 7.2A-I). As RGC dendritic loss is more apparent in 3xTg-AD mice at 12 months, probiotics were assessed in mice given 3 months of supplements between 9 and 12 months. Similarly, at 12 months neither Lab4b or Lab4p offered any beneficial effects on RGC dendritic complexity in 3xTg-AD mice based on Sholl analysis and the associated parameters (Figure 7.3A-I). These suggest that probiotic dietary supplementation, at the time points analysed, does not offer protection against excessive RGC dendritic pruning in the 3xTg-AD model.

In the same mice analysed at 9 and 12 months, CA1 hippocampal dendritic spine density and spine subtypes were collected. 3xTg-AD mice on a normal diet at 9 months without any probiotics display overall dendritic spine loss compared to typical wildtype densities. These correspond primarily to the loss of thin spines which agrees with previous data in earlier chapters. Both Lab4b and Lab4p probiotic supplementation in 3xTg-AD mice analysed at 9 months prevented CA1 dendritic spine loss (increase of 21% and 27% $p < 0.0001$, respectively), maintaining similar densities expected from wildtype mice (Figure 7.4A-I). In both probiotic groups, the densities of mushroom and thin spines were increased. Importantly, the number of thin spines was increased compared to the baseline 3xTg-AD mice however did not reach the density expected at from wildtypes. The number of mushroom spines were elevated above typical wildtype levels. In contrast, 3xTg-AD mice at 12 months, where the disease is more advanced, the beneficial effects of the two probiotics were less pronounced (Lab4b: 14% $p = 0.0669$, Lab4p: 28% $p = 0.0122$) (Figure 7.5A-I). These demonstrate that probiotics dietary supplementation in the 3xTg-AD model has beneficial effects on CA1 hippocampal dendritic spines, although only in the early stages of the disease.

7.3.2 HFD Diet

Following the promising findings for probiotics in 3xTg-AD mice on a normal diet, mice were fed a high fat diet and assessed for RGC dendritic complexity and CA1 hippocampal spines. A high fat diet is known to accelerate disease onset and pathology in AD mice (Knight *et al.*, 2014). 3xTg-AD mice were analysed at 6 months with 3 months prior dietary change and probiotic supplementation.

In the retina, 3xTg-AD mice at 6 months old on a high fat diet without probiotic supplementation displayed excessive dendritic loss compared to 3xTg-AD mice on a normal chow diet, which at this age is comparable to wildtype (representative examples, Figure 7.6A). Reductions were observed in the Sholl analysis (between 70 and 110 μm $p < 0.05$), AUC and the peak of the Sholl curve (Figure 7.6B-I). However similar to the data on 3xTg-AD mice on a normal diet, neither probiotics offered any protection against excessive RGC dendritic pruning the high-fat diet 3xTg-AD mice (Figure 7.6B-I). These findings further suggest that probiotic supplementation does not offer protection from excessive RGC dendritic pruning in the 3xTg-AD retina.

In the same high-fat diet 3xTg-AD mice, CA1 hippocampal dendritic spines were analysed for the overall density and subtype classification (Figure 7.7A-I). The high-fat diet resulted in significant overall spine loss compared to 3xTg-AD mice on a normal chow diet (24% $p < 0.0001$), which at this age is comparable to wildtype. Based on spine morphology the high-fat diet triggered a decrease in the number of stubby and thin spines, the latter, in agreement with earlier chapters highlighting the vulnerability of this spine type. Both probiotics, Lab4b and Lab4p, offered protection against spine loss in the 3xTg-AD mice on a high-fat diet (Lab4b: 20% $p = 0.0116$; Lab4p: 29% $p < 0.0001$). In both instances the observed thin spine loss was comparable to 3xTg-AD mice on a normal chow diet which is similar to wildtype densities (Figure 7.7). These demonstrate that in 3xTg-AD mice on a high-fat diet, CA1 hippocampal dendritic spine loss is exacerbated, however, probiotic supplementation offers protection against these changes.

7.3.3 Figures

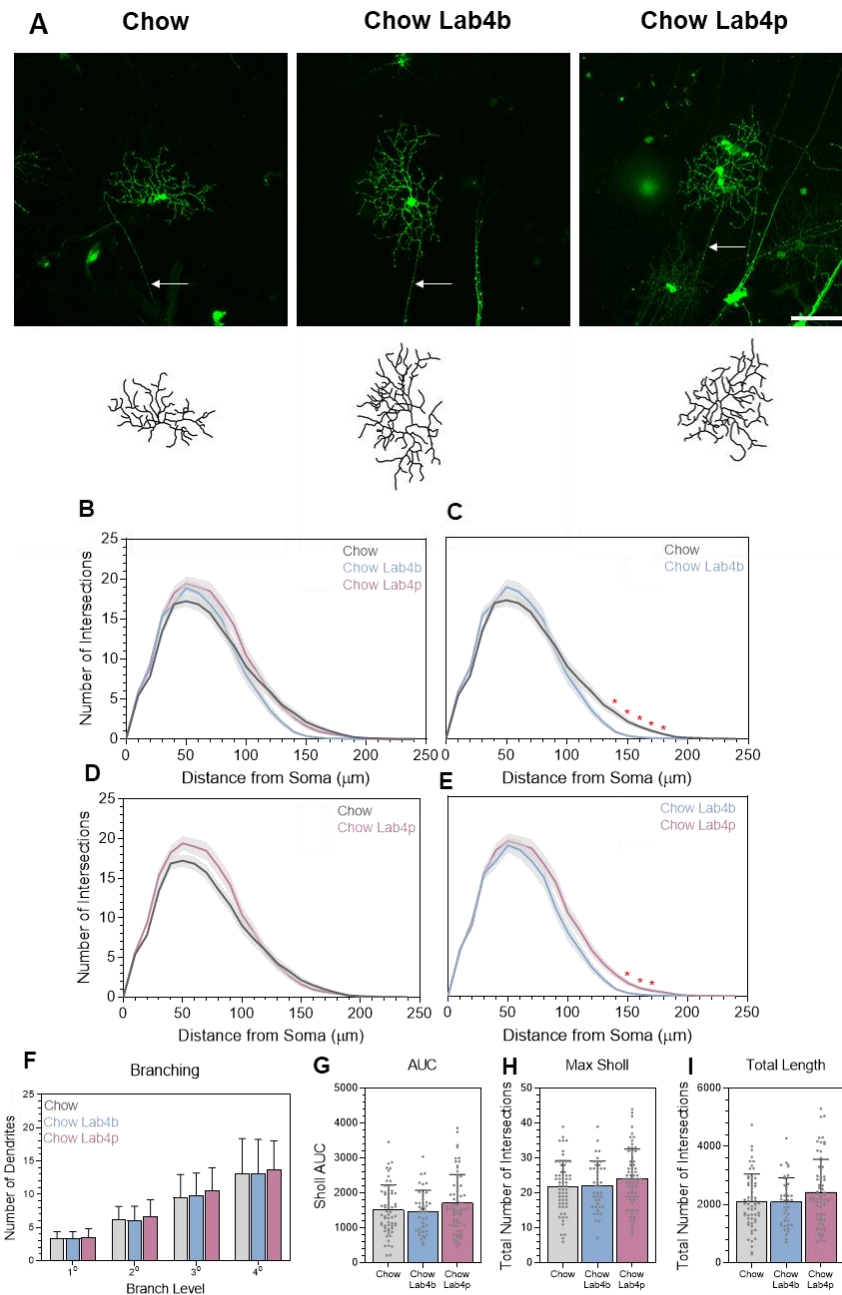


Figure 7.2 Probiotic supplementation in 3xTg-AD mice: RGC dendrites at 9 months. (A) Representative RGC examples from 3xTg-AD mice on a chow diet with Lab4b or Lab4p probiotics and corresponding dendritic reconstructions. Arrows indicate RGC axon. Scale bar: 100 μm . (B-E) Sholl analysis of RGCs. Line represents mean of group at each interval, shaded error zones \pm SEM. Two-tailed Mann-Whitney U test at each interval distance, $* = p < 0.05$. (F) Number of dendrites at each branching level proximal to the cell body. Error bars correspond to SD. (G) Area under Sholl curve. (H) Maximum number of Sholl intersections. (I) Total length of all dendrites. Column Scatterplots: data represent individual cells and error bars correspond to SD. Chow: $n = 80$ cells (6 mice), 3xTg-AD Lab4b: $n = 42$ cells (3 mice) and Chow Lab4p: $n = 67$ cells (3 mice). (F-I) Three groups were compared by nonparametric one-way analysis of variance (Kruskal–Wallis test) using Dunn multiple comparisons post-test, $* = p < 0.05$, $** = p < 0.01$, $*** = p < 0.001$, $**** = p < 0.0001$. All male mice aged at 9 months. Abbreviations: AUC, area under the Sholl curve.

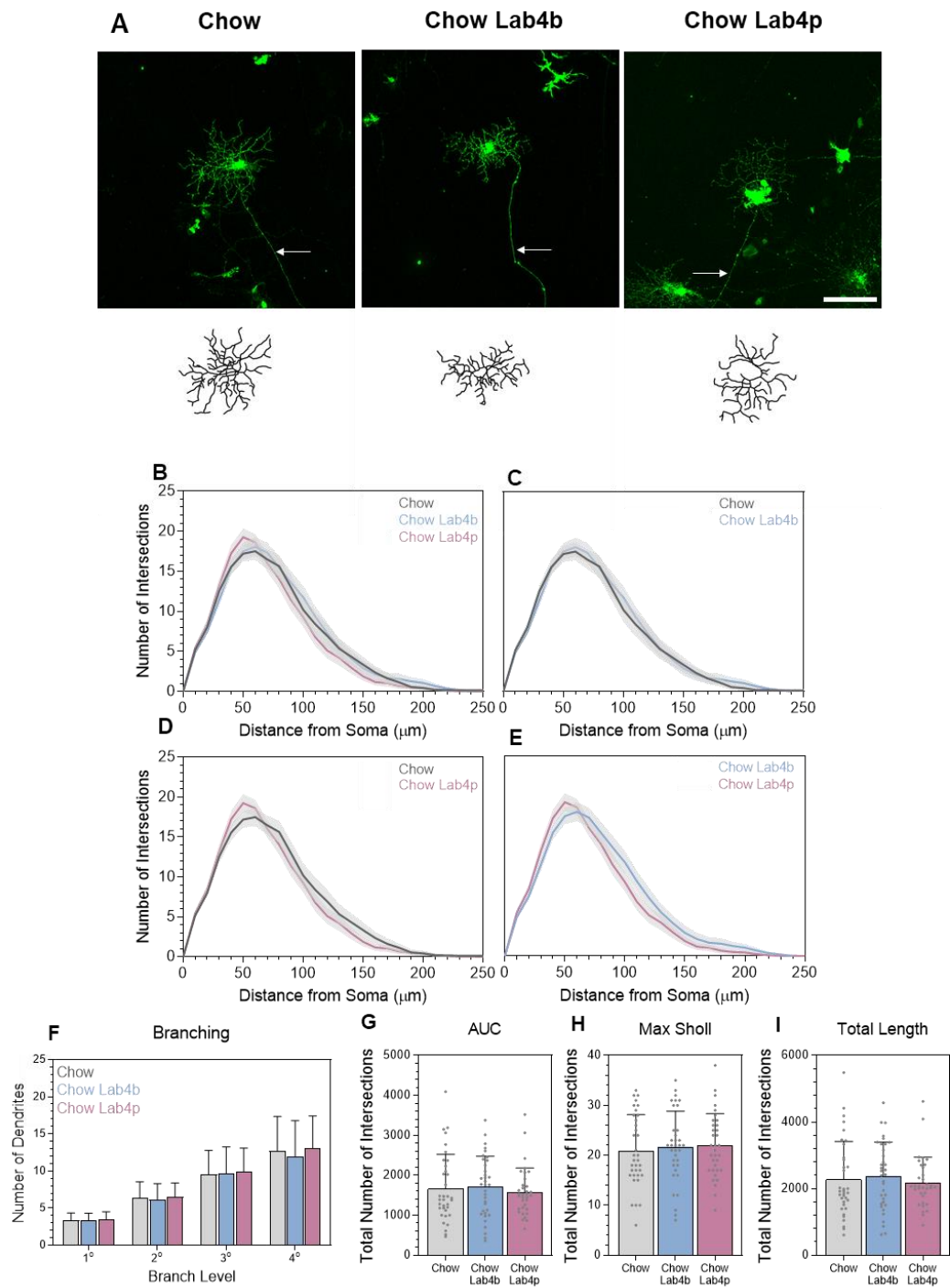


Figure 7.3 Probiotic supplementation in 3xTg-AD mice: RGC dendrites at 12 months. (A) Representative RGC examples from 3xTg-AD mice on a chow diet with Lab4b or Lab4p probiotics with the corresponding dendritic reconstructions. Arrows indicate RGC axon. Scale bar: 100 μm . (B-E) Sholl analysis of RGCs. Line represents mean of group at each interval, shaded error zones \pm SEM. Two-tailed Mann-Whitney U test at each interval distance, $* = p < 0.05$. (F) Number of dendrites at each branching level proximal to the cell body. Error bars correspond to SD. (G) Area under Sholl curve. (H) Maximum number of Sholl intersections. (I) Total length of all dendrites. Column Scatterplots: data represent individual cells and error bars correspond to SD. Chow: $n = 35$ cells (3 mice), 3xTg-AD Lab4b: $n = 35$ cells (3 mice) and Chow Lab4p: $n = 34$ cells (3 mice). (F-I) Three groups were compared by nonparametric one-way analysis of variance (Kruskal–Wallis test) using Dunn multiple comparisons post-test, $* = p < 0.05$, $** = p < 0.01$, $*** = p < 0.001$, $**** = p < 0.0001$. All male mice aged at 9 months. Abbreviations: AUC, area under the Sholl curve.

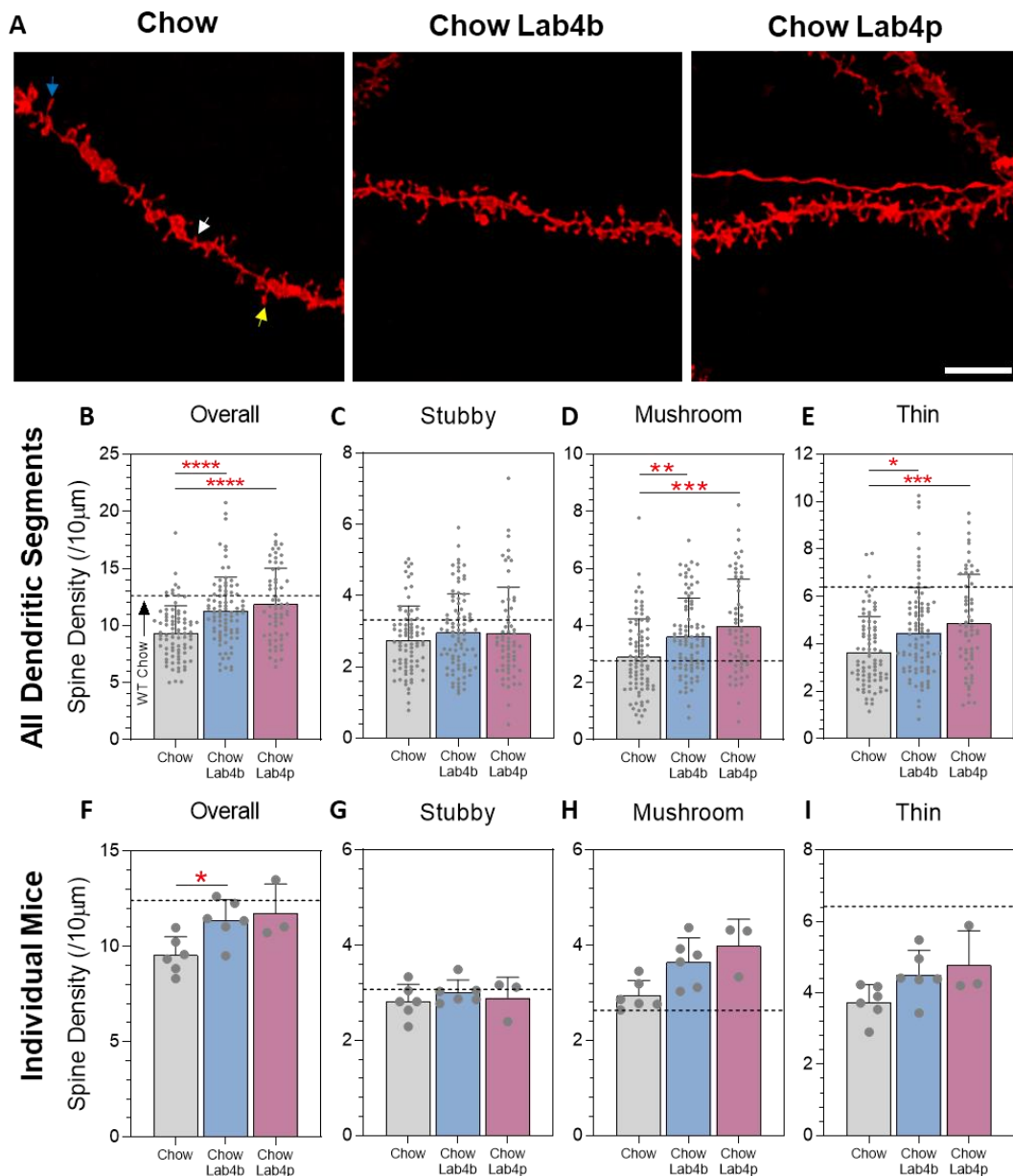


Figure 7.4 Probiotic supplementation in 3xTg-AD mice: CA1 hippocampal dendritic spines at 9 months. (A) Representative confocal images of DiI labelled CA1 dendritic segments from 3xTg-AD mice treated with Lab4b and Lab4p. Arrows correspond to example spine types: stubby (white arrows), mushroom (yellow arrows), thin (blue arrows). Scale bar 5 µm. (B-E) Spine densities across all dendritic segments and (F-I) spine densities across all individual mice for overall, stubby, mushroom and thin groups. Column Scatterplot (B-E): data represent individual cells and error bars correspond to SD. Column Scatterplots (F-I): bars, mean of group; data represent the mean spine density from individual mice and error bars correspond to SD. Chow: $n = 81$ dendrites (3 mice), Chow Lab4b: $n = 87$ dendrites (3 mice) and Chow Lab4p: $n = 62$ dendrites (3 mice). Three groups were compared by nonparametric one-way analysis of variance (Kruskal–Wallis test) using Dunn multiple comparisons post-test, * = $p < 0.05$, ** = $p < 0.01$, *** = $p < 0.001$, **** = $p < 0.0001$. All male mice aged 9 months. Dashed line corresponds to reference spine density from wildtype mice aged at 12 months. Abbreviations: WT, wildtype.

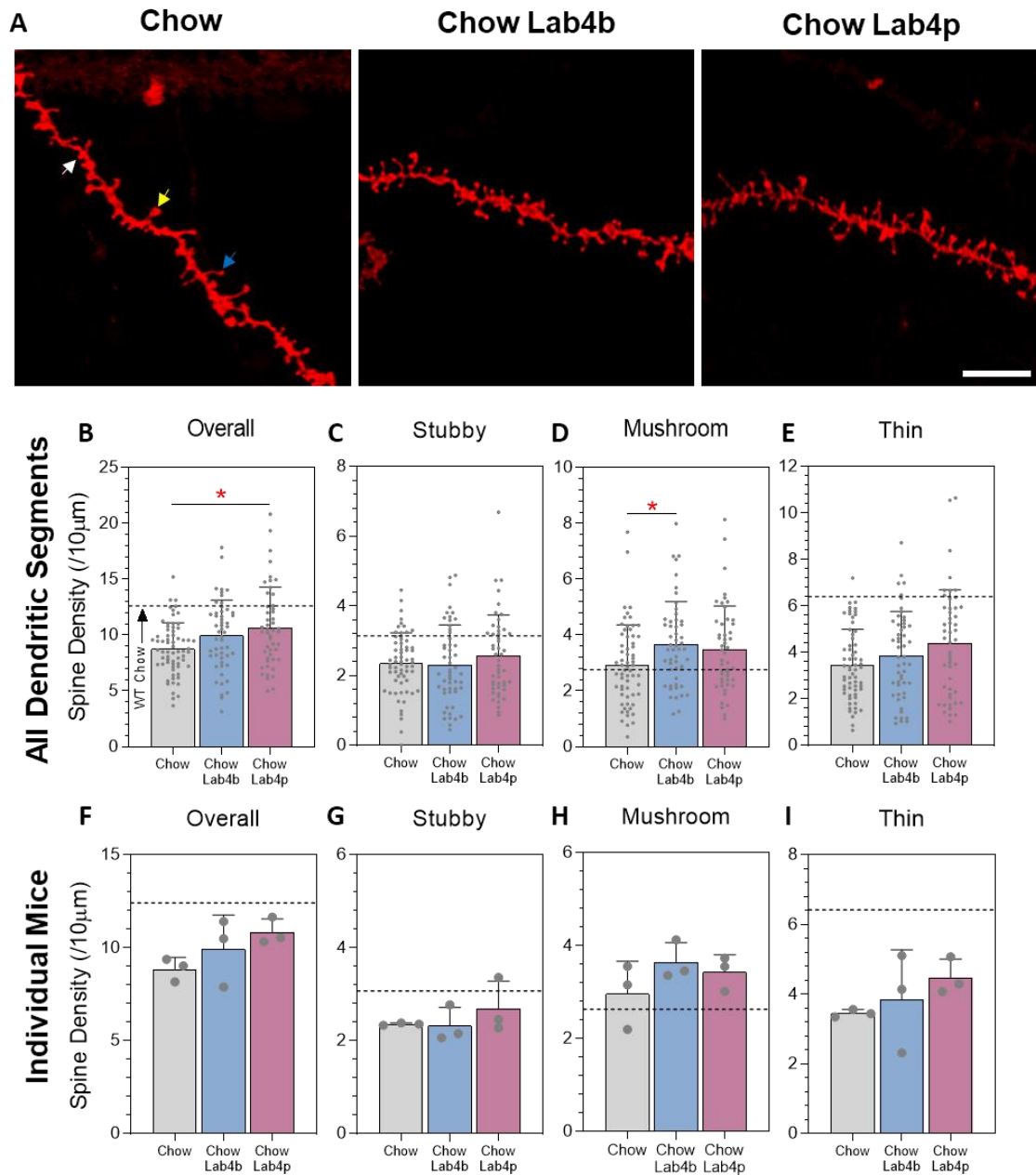


Figure 7.5 Probiotic supplementation in 3xTg-AD mice: CA1 hippocampal dendritic spines at 12 months. (A) Representative confocal images of DiI labelled CA1 dendritic segments from 3xTg-AD mice treated with Lab4b and Lab4p. Arrows correspond to example spine types: stubby (white arrows), mushroom (yellow arrows), thin (blue arrows). Scale bar 5 μm. (B-E) Spine densities across all dendritic segments and (F-I) spine densities across all individual mice for overall, stubby, mushroom and thin groups. Column Scatterplot (B-E): data represent individual cells and error bars correspond to SD. Column Scatterplots (F-I): bars, mean of group; data represent the mean spine density from individual mice and error bars correspond to SD. Chow: $n = 67$ dendrites (3 mice), Chow Lab4b: $n = 52$ dendrites (3 mice) and Chow Lab4p: $n = 49$ dendrites (3 mice). Three groups were compared by nonparametric one-way analysis of variance (Kruskal–Wallis test) using Dunn multiple comparisons post-test, $* = p < 0.05$, $** = p < 0.01$, $*** = p < 0.001$, $**** = p < 0.0001$. All male mice aged 12 months. Dashed line corresponds to reference spine density from wildtype mice aged at 12 months. Abbreviations: WT, wildtype.

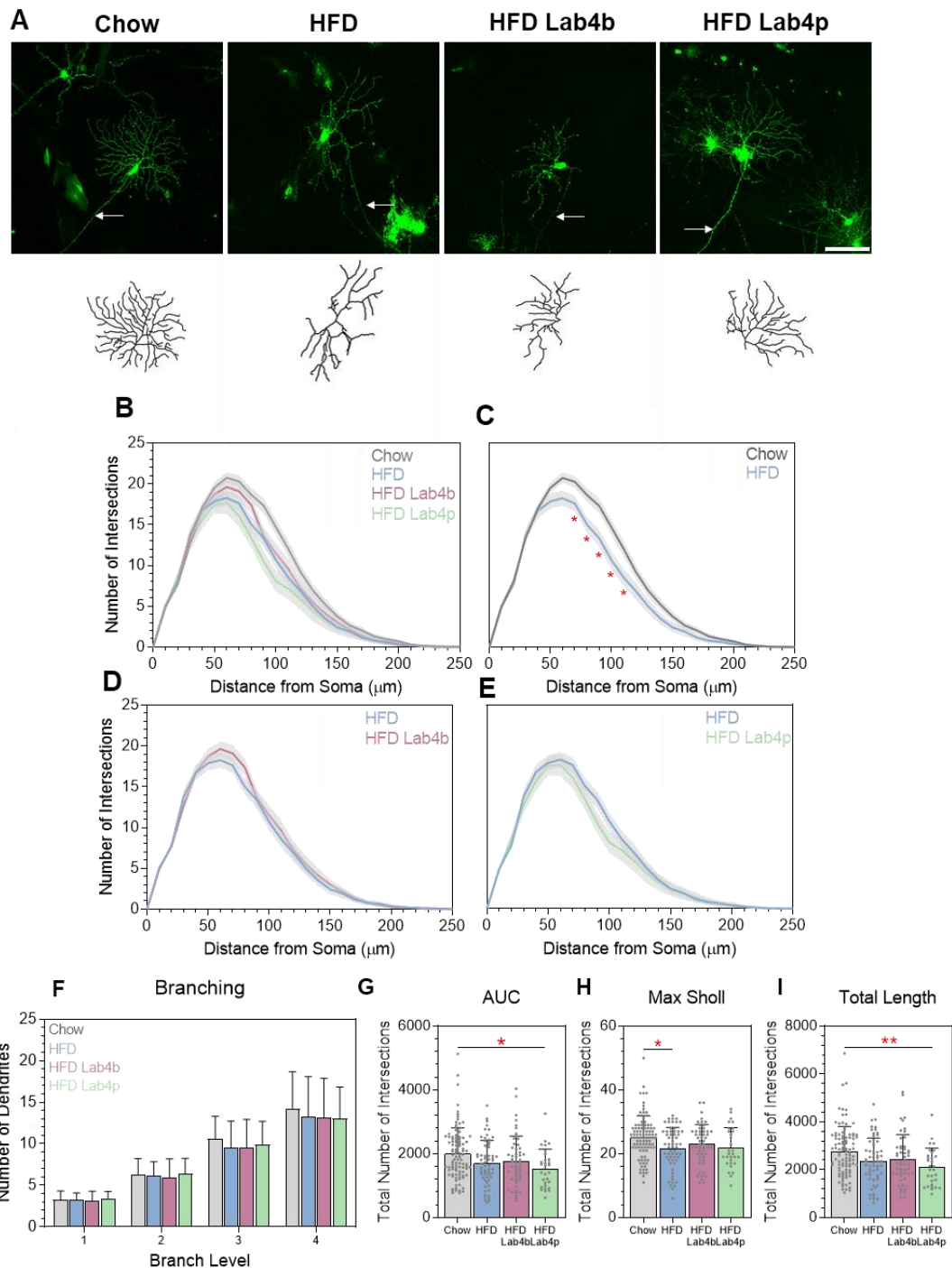


Figure 7.6 Probiotic supplementation in 3xTg-AD mice on a high-fat diet: RGC dendrites at 6 months. (A) Representative RGC examples from 3xTg-AD mice on a high-fat diet with Lab4b or Lab4p probiotics with the corresponding dendritic reconstructions. Arrows indicate RGC axon. Scale bar: 100 μm . (B-E) Sholl analysis of RGCs. Line represents mean of group at each interval, shaded error zones \pm SEM. Two-tailed Mann-Whitney U test at each interval distance, * = $p < 0.05$. (F) Number of dendrites at each branching level proximal to the cell body. Error bars correspond to SD. (G) Area under Sholl curve. (H) Maximum number of Sholl intersections. (I) Total length of all dendrites. Column Scatterplots: data represent individual cells and error bars correspond to SD. Chow: $n = 99$ cells (9 mice), HFD: $n = 60$ cells (5 mice), HFD Lab4b: $n = 53$ cells (4 mice) and HFD Lab4p: $n = 30$ cells (4 mice). (F-I) Three groups were compared by nonparametric one-way analysis of variance (Kruskal–Wallis test) using Dunn multiple comparisons post-test, * = $p < 0.05$, ** = $p < 0.01$, *** = $p < 0.001$, **** = $p < 0.0001$. All male mice aged at 9 months. Abbreviations: AUC, area under the Sholl curve; HFD, high-fat diet.

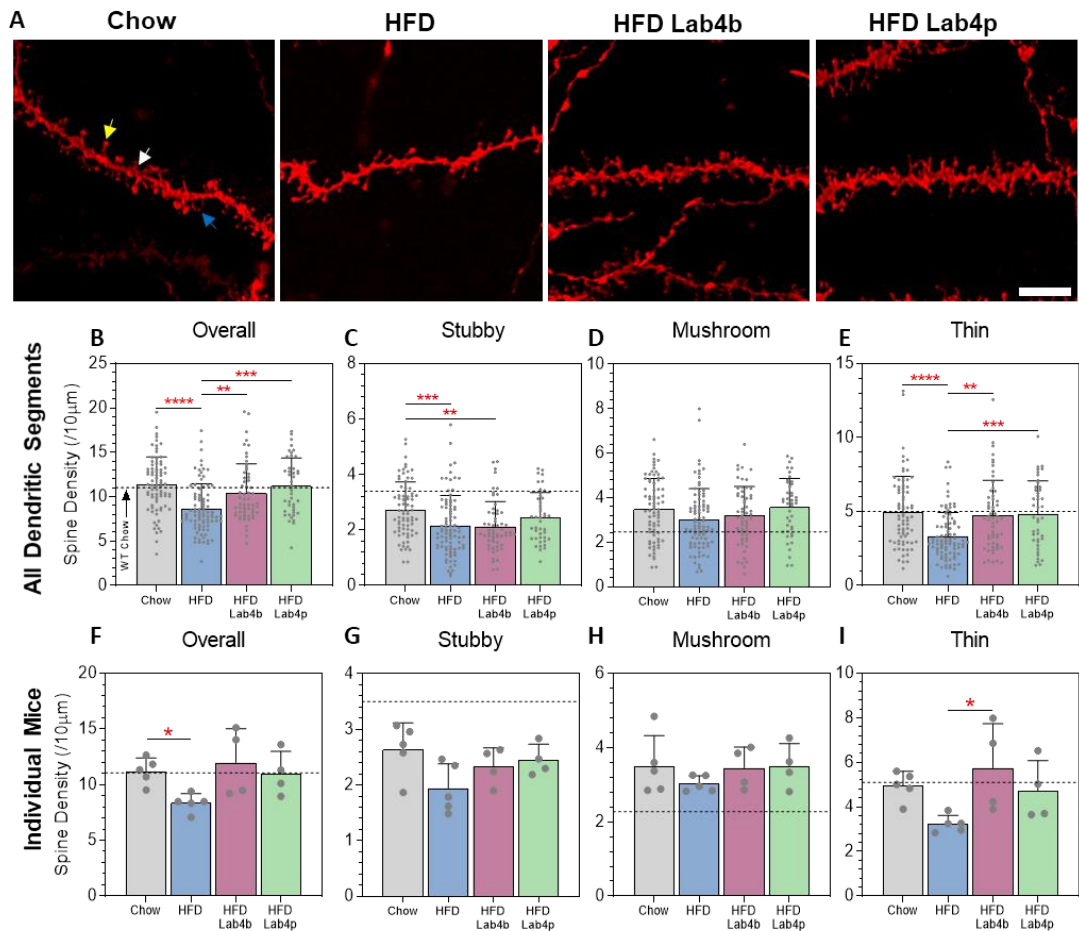


Figure 7.7 Probiotic supplementation in 3xTg-AD mice on a high-fat diet: CA1 hippocampal dendritic spines at 6 months. (A) Representative confocal images of DiI labelled CA1 dendritic segments from 3xTg-AD mice treated with Lab4b and Lab4p. Arrows correspond to example spine types: stubby (white arrows), mushroom (yellow arrows), thin (blue arrows). Scale bar 5 µm. (B-E) Spine densities across all dendritic segments and (F-I) spine densities across all individual mice for overall, stubby, mushroom and thin groups. Column Scatterplot (B-E): data represent individual cells and error bars correspond to SD. Column Scatterplots (F-I): bars, mean of group; data represent the mean spine density from individual mice and error bars correspond to SD. Chow: $n = 77$ dendrites (5 mice), HFD: $n = 87$ dendrites (5 mice), HFD Lab4b: $n = 58$ dendrites (4 mice) and HFD Lab4p: $n = 43$ dendrites (4 mice). Groups were compared by nonparametric one-way analysis of variance (Kruskal–Wallis test) using Dunn multiple comparisons post-test, * = $p < 0.05$, ** = $p < 0.01$, *** = $p < 0.001$, **** = $p < 0.0001$. All male mice aged 6 months. Dashed line corresponds to reference spine density from wildtype mice aged at 6 months. Abbreviations: WT, wildtype; HFD, high-fat diet.

7.4 Discussion

The cognitive deficits observed in AD mouse models are driven, at least in part, by neuroinflammation which is influenced by circulating inflammation (Cunningham and Hennessy, 2015). Infections are a major source of systemic inflammation, however, there are additional routes that can lead to inflammatory events such as changes to the gut microbiome (Westfall *et al.*, 2017). Dysbiosis, changes to the gut microbiome from homeostasis, can trigger sustained and chronic systemic inflammation, which in neurodegenerative diseases such as AD is linked to worse severity and accelerated progression. Therefore, modulation of the gut microbiome in AD is a realistic therapeutic option to reduce the burden of circulating inflammation (Ni *et al.*, 2019). This chapter explored the impact of probiotic dietary supplementation in the 3xTg-AD model on a normal chow and on a high-fat diet against excessive RGC dendritic pruning and hippocampal CA1 dendritic spine loss. I demonstrate that diet high in fat is capable of exacerbating RGC dendritic pruning and CA1 spine loss and report that probiotics are neuroprotective against spine loss; however, were unable to prevent the excessive RGC dendritic pruning in the 3xTg-AD model.

Recent studies have demonstrated beneficial effects of probiotics in amyloid AD models to have the capacity to modulate dysbiosis, reduce peripheral inflammation, decrease serum cholesterol, lower inflammatory markers and overall improve cognitive function (Rezaeiasl *et al.*, 2019; Mehrabadi and Sadr, 2020). Modulation of the microbiome, through antibiotics, in transgenic AD models has demonstrated reductions in amyloid pathology and microglial activation (Dodiya *et al.*, 2019). Such changes also correlate with decreases in hippocampal neurogenesis and memory function (Möhle *et al.*, 2016). When assessing the impact of probiotics, others report that ability to suppress amyloid induced hippocampal inflammation and reverse the deficits triggered by the bacterial dysbiosis (Kobayashi *et al.*, 2017; Lee *et al.*, 2019). In AD models, probiotics are found to attenuate oxidative stress and peripheral inflammation, improve senescence, reduce the pathological burden related to synaptic loss and provide improvements to cognition (Bonfili *et al.*, 2017; Bonfili *et al.*, 2018; Ni *et al.*, 2019; Wang *et al.*, 2020). In LPS-induced inflammation, probiotics have demonstrated that ability to lower the status of pro-inflammatory cytokines whilst increasing the expression of neurotrophic factors

(Mohammadi *et al.*, 2019). In the retina, although less described, probiotics also prevent chronic inflammation and reduce age-associated RGC loss (Morita *et al.*, 2018).

The probiotic consortia assessed in this thesis have previously been demonstrated to offer beneficial effects in the brain with roles in neuroprotection and to improving cognitive function (Michael *et al.*, 2019). I demonstrate that probiotic supplementation, specifically the consortia of Lab4b and Lab4p, offer neuroprotective roles during the early stages of against hippocampal CA1 dendritic spine loss in the 3xTg-AD model. This supports and indicate the potential benefit of targeting the disease before the onset of pathology. Such findings are in agreement with others that report synaptic improvements in other AD models (Rezaeiasl *et al.*, 2019). However, in more severe amyloid AD models with more advanced pathology, such as the APP^{NL-G-F} model, probiotics decrease peripheral inflammation whilst unable to decrease the burden of amyloid pathology and neuroinflammation (Kaur *et al.*, 2020).

Neurodegenerative diseases are increasingly found to present as a multifactorial disease, that is influenced by many factors that can lead to accelerated disease onset and increased pathological burden. In transgenic AD models, simply alternating feeding regimens is found to exacerbate neuropathology, with every-other-day feeding triggering inflammation and neuronal deficits in the 5XFAD mouse model (Lazic *et al.*, 2020). Diet, especially high in fat, shifts pathology onset to occur several months sooner than expected timelines, increases neuroinflammation and worsens the trajectory of the disease (Westfall *et al.*, 2017). In diabetes induced 3xTg-AD mice, modulation of the diet results in an increased amyloid deposition in the subiculum and hippocampal regions without further cognitive deficits (Hayashi-Park *et al.*, 2017). In studies using the 3xTg-AD model and APP knock-in mice, a diet high in fat diet causes memory impairments and deficits in hippocampal LTP, which are independent of both amyloid and tau pathology (Knight *et al.*, 2014; Salas *et al.*, 2018).

A diet high in fat elevates the status of systemic inflammation. I found that RGC dendritic complexity and hippocampal CA1 dendritic spines were vulnerable to excessive pruning in the 3xTg-AD model. These observations agree with the findings in the preceding chapters that demonstrated the role of peripheral inflammation in influencing the status of early stage neurodegeneration in the retina and hippocampus of AD mouse models. In the 3xTg-AD mice on a high fat diet, I observed that probiotic supplementation prevented

hippocampal CA1 dendritic spine loss and maintained densities similar to wildtype mice on a normal chow diet, effectively preventing neurodegeneration. Two other AD studies also report the role of a high-fat diet in exacerbating synaptic degeneration and report accelerated onset of pathology, increased microglial activation, and further cognitive impairments. However, these changes occurred irrespective to the core AD neuropathology load (Knight *et al.*, 2014; Salas *et al.*, 2018).

Despite the encouraging outcomes indicating the potential neuroprotection against CA1 synaptic loss, beneficial effects were absent when assessing RGC dendritic complexity in the same mice. 3xTg-AD mice on a normal chow and on a high-fat diet both demonstrated RGC dendritic pruning; however, neither probiotic supplementation prevented or reduced the extent of dendritic loss. Suggesting that simply modifying the gut microbiome through probiotics may not provide a viable option to prevent RGC degeneration. The absence of probiotic RGC dendritic protection may empathise the less neuronal plasticity in the retina, compared with neurons in the brain. Therefore, protecting RGCs against degeneration may require a more direct route of potential therapeutics rather than just modifying the status of systemic inflammation. This chapter did however present with some noticeable limitations. It was not feasible to assess the impact of probiotic supplementation and a high-fat diet in wildtype mice. Therefore, all the observed effects are unlikely to be AD specific. Additionally, probiotic treatment may have provided further indications of neuroprotection if the treatment windows were tested for longer than 3 months.

To conclude, I demonstrate that in 3xTg-AD mice on a normal chow diet or a high fat diet, probiotic dietary supplementation protected against CA1 dendritic spine loss, although could not protect against excessive RGC dendritic pruning. 3xTg-AD mice on a high-fat diet were also found to display exacerbated RGC dendritic pruning and hippocampal CA1 dendritic spine loss. These suggest that probiotics may have a beneficial impact in reducing the extent of neurodegeneration in the hippocampus of AD mouse models.

Chapter 8. Discussion

Dendritic and synaptic loss are among the earliest detectable events in the progressive stages of neurodegeneration. While the AD brain, specifically regions including the hippocampus and cortex, are the primary sites for detecting and monitoring pathology, other parts of the CNS, including the retina demonstrate key hallmark pathology (Hart *et al.*, 2016; Lim *et al.*, 2016). Imaging innovations in AD mouse models, and in the human disease, have recently offered the prospect of non-invasive monitoring of pathological changes through the retina (Chidlow *et al.*, 2017). However, there are inconsistent reports documenting retinal pathology and an urgent need to better characterise the pathological events particularly in AD models. A better understanding of retinal neurodegeneration may deliver as a potential biomarker for AD severity and progression. The principle aim of this study was to assess whether excessive RGC dendritic pruning is a robust readout that reflects synaptic density in the hippocampus in mouse models of AD, and to explore the impact of complement deficiency, peripheral inflammation and probiotic interventions.

Several AD mouse models successfully recapitulate aspects of human AD pathology in the brain. Amyloid plaques, neurofibrillary tangles and synaptic loss are some of the most commonly reported changes in AD models; however, the extent and severity of these depend on the model in question. Recently, prominent retinal pathology has been reported in AD mouse models. Studies published by the research group led by Koronyo-Hamaoui have provided several fundamental observations that support the detection of retinal pathology, particularly in AD mouse models (Koronyo-Hamaoui *et al.*, 2011; Koronyo *et al.*, 2012). Amyloid plaques were found in the retinal layers and in some instances were detectable earlier than plaques occurring in the brain. Increased retinal amyloid deposition was also associated with the development of the disease and could be noninvasively detected through curcumin labelling. Recently, the same group has also reported an increase in vascular amyloidosis and pericyte loss in the human AD retina, implying a compromised blood-retina barrier (Shi *et al.*, 2020).

Despite these promising observations, these findings are not always recapitulated, and therefore, there is a search for a more robust marker of AD-related retinal pathology. Monitoring neurodegeneration during the early stages of the disease, prior to neuron loss, has pinpointed dendritic and synaptic loss to be the strongest link to disease progression

and severity. In the retina, there are many different neuronal populations that are susceptible to neurodegeneration, with RGCs a specific target in a number of retinal diseases. In other retinal degeneration models that feature RGC degeneration, RGCs display a marked reduction in the dendritic arborisation prior to cell loss. The reduction in RGC dendritic complexity also correlates with the severity of the disease, with models of glaucoma highlighting the vulnerability of these neurons (Williams, Howell, *et al.*, 2013). In AD, degeneration of RGC's is a feature of the post mortem AD retina (Blanks *et al.*, 1989), although the extent of RGC degeneration in AD models is unclear. In 2013, Williams *et al.*, reported for the first time, that in the Tg2576 AD mouse model, a model that addresses the amyloid component of AD, there was a marked reduction in RGC dendritic complexity that was similar to other studied retinal degeneration models (Williams, Thirgood, *et al.*, 2013). Since this study, although referenced many times, no other group has recapitulated or expanded on these observations.

In Chapter 3, I replicated the previously reported reduction of RGC dendritic complexity in 12-month Tg2576 AD mice. In addition, the excessive RGC dendritic pruning was also a prominent feature in the retina of 3xTg-AD and APP^{NL-G-F} mice. In the three AD models analysed, ON-centre specific RGC degeneration was a consistent feature, whereas only APP^{NL-G-F} mice has significant OFF-centre RGC degeneration. The burden of dendritic loss progressively worsened with age, and in the 3xTg-AD model there was a clear greater overall excessive pruning in male mice. Gender variations are known to occur in the 3xTg-AD model; however, these studies relate to pathology in the brain where females display more consistent phenotypes (Belfiore *et al.*, 2019). It is unclear why the gender effects are opposite (worse in males) for RGC degeneration in this model; this requires further analysis. In Chapter 4, I demonstrated that RGC changes in the 3xTg-AD and APP^{NL-G-F} models correlated with ongoing synaptic loss in the hippocampus as demonstrated by fewer CA1 dendritic spines, particularly thin subtype classification.

The identification of excessive RGC dendritic loss in the different AD models, implies that RGC dendritic degeneration is a robust feature in the retina of AD mice. The inclusion of the APP^{NL-G-F} model removes the underlying confounding factor of overexpression present in other AD models. Overexpression of AD transgenes may cause with artefactual phenotypes; retinal pathology has previously been attributed to these (Chintapaludi *et al.*, 2020). Thus, the data provided in this thesis give supporting evidence

to reinforce the potential of analysing the retina to monitor neurodegeneration, particularly during the early stages, in AD mouse models.

This thesis demonstrates morphological differences between the RGC dendritic complexity within the AD mouse models compared to wildtype; however it is unclear what is driving this retinal phenotype. It is likely that the expression of retinal toxic amyloid peptides, which may aggregate into plaque structures later in disease, is one driver of early neurodegeneration (Vandenabeele *et al.*, 2020). Although not assessed, it is also plausible that RGC dendritic loss may, at least in part, be driven by retrograde signals due to the far higher abundance of amyloid pathology elsewhere in the CNS. Placing the observed RGC changes on the expected disease progression timelines for the AD models, it is likely that retinal pathology may occur at a slower rate and following synaptic loss in the brain.

RGC dendritic loss may be attributed to intrinsic degeneration, rather than extrinsic pruning. Glaucoma models, which feature RGC dendritic loss, support both scenarios (Risner *et al.*, 2018). Energy metabolism disruption may be a driver for dendritic loss by decreasing mitochondrial membrane potentials, resulting in mitochondrial depolarisation and an energy deficit that is normally required to produce the dendritic growth cone. Consequently triggering reduced synaptic activity, mitochondrial reshuffling towards the cell body from the dendrites and dendritic (Beckers and Moons, 2019). Despite this, extrinsic factors also drive RGC dendritic loss. Inhibition, or deficiency, of C1q a key component identified in microglial-mediated synaptic engulfment, prevents RGC dendritic loss in models of glaucoma (Williams *et al.*, 2016; Zhang *et al.*, 2019). Therefore, acting similarly to the processes of active pruning of synapses and dendrites elsewhere in the CNS.

Improving understandings of the mechanisms underlying the early stages of neurodegeneration is gaining increasing interest as a way to identify potential targets to combat neurodegenerative diseases. The complement system, an integral part of the innate immune system is involved in the removal of debris and pathogens; however, it is also critical in the process of refining neuronal networks (Veerhuis *et al.*, 2011; Hong *et al.*, 2016). Studies led by Stevens *et al* in recent years has eloquently demonstrated the role of complement mediated synaptic pruning during neuronal development and in AD models (Stevens *et al.*, 2007; Schafer *et al.*, 2012). The absence of C1q, the initiator of

the classical complement cascade, or C3, the central converging molecule, in AD models caused synaptic and neuronal protection, associated with improved cognitive function, irrespective of impact on the hallmark amyloid pathology (Perez-Alcazar *et al.*, 2014; Shi *et al.*, 2015; Shi *et al.*, 2017). Inhibition, or deletion of components of the complement system has previously been shown to confer protection against excessive RGC dendritic pruning in models of glaucoma (Williams *et al.*, 2016).

In Chapter 5, I demonstrated that complement has a key role in the elimination of synapses and pruning of dendrites in the hippocampus and retina respectively. In the 3xTg-AD model, deficiency of either C3 or C6 significantly reduced the degree of excessive RGC dendritic pruning, although levels of pruning were still increased compared to wildtypes. In contrast, only C6 deficiency conferred protection against hippocampal CA1 dendritic spine loss in the 3xTg-AD model. Therapeutic blockade of C5 in 3xTg-AD mice also protected dendritic spines. These observations demonstrate new roles of the complement system, in particular the downstream components that assemble the MAC, in the refinement and modulation of neuronal networks.

AD neuropathology is closely associated with neuroinflammation; however, roles of peripheral inflammation in driving events in the CNS are increasingly reported. Chronic inflammation in the periphery may be sustained for many years and may contribute to the development of neurodegenerative diseases (Cunningham and Hennessy, 2015). There are several sources of inflammatory triggers that associate with AD and pose as potential target to reduce the burden of neuropathology, particularly during the early stages of the disease. In studies that use systemic LPS dosing to mimic bacterial infection, amyloid deposition and tau pathology increased, microglia were activated, synapses were excessively pruned and mice displayed more severe cognitive impairments (DiCarlo *et al.*, 2001; Herber *et al.*, 2004; Kitazawa *et al.*, 2005; Herber *et al.*, 2007; Lee *et al.*, 2010; Sy *et al.*, 2011; Torvell *et al.*, 2019). Although less well documented, viral infections also contribute to the status of microglial activation and associate with worse cognitive deficits in AD (Westman *et al.*, 2014; Garré *et al.*, 2017). Recent studies in AD models and wildtype mice have shown that a diet high in fat can drive neuroinflammation, synaptic loss and cognitive impairments (Salas *et al.*, 2018; Lazic *et al.*, 2020). Dysbiosis, is another factor that can trigger chronic levels of circulating inflammation and is linked to several neurological disorders (Roy Sarkar and Banerjee, 2019). Recently, microbiome

modulators (antibiotics and probiotics) have been shown to reduce the extent of neuroinflammation, amyloid deposition, oxidative damage, neurodegeneration and cognitive impairments in AD mouse models (Akbari *et al.*, 2016; Nimgampalle and Yellamma, 2017; Abraham *et al.*, 2019).

In Chapter 6 and Chapter 7, I have provided evidence linking infectious/inflammatory agents with excessive RGC dendritic pruning and hippocampal spine loss. LPS administration was associated with excessive RGC dendritic pruning and CA1 dendritic spine loss in 3xTg-AD mice. In MCMV virally infected 3xTg-AD mice, similar effects were observed with infected mice displaying increased loss of both RGC dendrites and CA1 spines compared to non-infected controls. In 3xTg-AD mice, simply modifying the diet to increase fat content was associated with increased loss of RGC dendrites and CA1 spines. Notably, treatment with probiotics reduced hippocampal CA1 dendritic spine loss in 3xTg-AD mice either on a high fat or normal chow diet. These positive effects were limited to the hippocampus and were not reflected in altered RGC dendritic pruning. Although the exact mechanisms linking peripheral inflammation, neuroinflammation and other changes occurring in the CNS remain unclear, modulation of systemic inflammation, particularly during the early stages of the disease, may be a tractable and realistic therapeutic target in AD.

This thesis proposes several new insights into the potential mechanisms of neurodegeneration in AD mouse models by modulating the status of circulating systemic inflammation through inflammatory triggers and anti-inflammatory applications (probiotics), deficiencies/ blockage of the complement system and their potential relevance to the human disease. RGC dendritic loss was a robust and consistent feature in the retina of AD mice, although the exact mechanisms are unclear; detection of similar events *in vivo* in humans may be of clinical significance, aiding diagnosis and monitoring of AD. The identified changes, loss of RGC dendritic complexity, can be observed by optical imaging of the IPL, the layer into which RGCs project their dendrites. A few earlier studies have described IPL changes in AD models (Song *et al.*, 2020); however, the identification here of consistent ON-centre RGC degeneration (dendrites in sublamina b of the IPL) should enable better optimisation of optical imaging studies in order to detect changes *in vivo* in patients. Although ongoing excessive RGC dendritic pruning in the retina of AD mice is a common finding across AD models, it is unclear what is driving

dendritic loss; the demonstration here of a role for complement raises the prospect of using therapeutics that target the complement system and the status of systemic inflammation in protecting RGCs as well as neurons in the brain.

I propose that further studies should now be undertaken to determine the potential translational capability of these robust RGC dendritic degeneration observed in AD model mice. It would be beneficial to explore, various retinal *in vivo* imaging techniques, to assess, at ‘high resolution’, texture changes of the IPL rather than gross thickness measurements currently employed to the human AD retina. Additionally, it will be important to determine the underlying mechanisms involved in driving these neurodegenerative events. The data presented in this thesis, and published literature, implicate the involvement of the complement system and circulating inflammation in exacerbating synaptic plasticity and pruning (Hong *et al.*, 2016; Williams *et al.*, 2016; Shi *et al.*, 2017). It will be important to determine whether these factors have direct effects within the CNS, or if simply modifying the levels of peripheral inflammation may be sufficient to modify pathology during the early stages of the disease in AD models.

In conclusion, I have shown that excessive RGC dendritic pruning is a robust feature in the retinas of overexpressing and knock-in AD mouse models, and that RGC dendritic loss mirrors synaptic loss in the hippocampus of AD models. I have also shown that these are impacted by manipulating the complement system using knockouts or blocking antibodies, by systemic inflammation, by diet modification and by probiotics to modulate the gut microbiome. The identification of excessive RGC dendritic pruning in the retina of knock-in APP^{NL-G-F} mice, currently the best available amyloidosis model for the human disease because it lacks overexpression artefacts, supports the relevance of the findings and enhances the potential for translation. Although there are obvious limitations in extrapolating observations from mouse models to the human disease, these findings may, at least in part, reflect changes that occur in the human AD retina. This thesis therefore supports the prospective monitoring of RGCs and the potential of clinical imaging strategies to non-invasively detect early stages of neurodegeneration that may mirror ongoing synaptic degeneration elsewhere in the CNS.

References

- Abraham, D., Feher, J., Scuderi, G.L., Szabo, D., Dobolyi, A., Cservenak, M., *et al.* (2019) Exercise and probiotics attenuate the development of Alzheimer's disease in transgenic mice: Role of microbiome. *Exp Gerontol* **115**: 122–131.
- Akbari, E., Asemi, Z., Kakhaki, R.D., Bahmani, F., Kouchaki, E., Tamtaji, O.R., *et al.* (2016) Effect of probiotic supplementation on cognitive function and metabolic status in Alzheimer's disease: A randomized, double-blind and controlled trial. *Front Aging Neurosci* **8**: 1–8.
- Alexandrova, P.N., Pogueb, A., Bhattacharjee, S., and Lukiwb, W.J. (2011) Retinal amyloid peptides and complement factor H in transgenic models of Alzheimer's disease. *Neuroreport* **22**: 623–627.
- Altuna-Azkargorta, M., and Mendioroz-Iriarte, M. (2020) Blood biomarkers in Alzheimer's disease. *Neurología* **1207**: 1–7.
- Arikkath, J. (2012) Molecular mechanisms of dendrite morphogenesis. *Front Cell Neurosci* **6**: 1–14.
- Baazaoui, N., Flory, M., and Iqbal, K. (2017) Synaptic Compensation as a Probable Cause of Prolonged Mild Cognitive Impairment in Alzheimer's Disease: Implications from a Transgenic Mouse Model of the Disease. *J Alzheimer's Dis* **56**: 1385–1401.
- Baden, T., Berens, P., Franke, K., Rosón, M.R., Bethge, M., and Euler, T. (2016) The functional diversity of retinal ganglion cells in the mouse. *Nature* **529**: 345–350.
- Baglietto-Vargas, D., Chen, Y., Suh, D., Ager, R.R., Carlos, J., Mederios, R., *et al.* (2016) Short-term modern life-like stress exacerbates A β -pathology and synapse loss in 3xTg-AD mice. *J Neurochem* **134**: 915–926.
- Bales, K.R., O'Neill, S.M., Pozdnyakov, N., Pan, F., Caouette, D., Pi, Y., *et al.* (2016) Passive immunotherapy targeting amyloid- β reduces cerebral amyloid angiopathy and improves vascular reactivity. *Brain* **139**: 563–577.
- Barnes, L.L., Capuano, A.W., Aiello, A.E., Turner, A.D., Yolken, R.H., Torrey, E.F., and Bennett, D.A. (2015) Cytomegalovirus infection and risk of alzheimer disease in older black and white individuals. *J Infect Dis* **211**: 230–237.
- Basu, J., and Siegelbaum, S.A. (2015) The corticohippocampal circuit, synaptic plasticity, and memory. *Cold Spring Harb Perspect Biol* **7**: 1–26.
- Basu, S., Saha, P.K., Roszkowska, M., Magnowska, M., Baczynska, E., Das, N., *et al.* (2018) Quantitative 3-D morphometric analysis of individual dendritic spines. *Sci Rep* **8**: 1–13.
- Beckers, A., and Moons, L. (2019) Dendritic shrinkage after injury: A cellular killer or a necessity for axonal regeneration? *Neural Regen Res* **14**: 1313–1316.
- Bekris, L.M., Yu, C.-E., Bird, T.D., and Tsuang, D.W. (2010) Genetics of Alzheimer's disease. *J Geriatr Psychiatry Neurol* **23**: 213–227.

-
- Belfiore, R., Rodin, A., Ferreira, E., Velazquez, R., Branca, C., Caccamo, A., and Oddo, S. (2019) Temporal and regional progression of Alzheimer's disease-like pathology in 3xTg-AD mice. *Aging Cell* **18**: 1–13.
- Belkaid, Y., and Hand, T.W. (2014) Role of the microbiota in immunity and inflammation. *Cell* **157**: 121–141.
- Berry, K.P., and Nedivi, E. (2017) Spine Dynamics: Are They All the Same? *Neuron* **96**: 43–55.
- Billings, L.M., Oddo, S., Green, K.N., McGaugh, J.L., and LaFerla, F.M. (2005) Intraneuronal A β causes the onset of early Alzheimer's disease-related cognitive deficits in transgenic mice. *Neuron* **45**: 675–688.
- Binder, L.I., Guillozet-Bongaarts, A.L., Garcia-Sierra, F., and Berry, R.W. (2005) Tau, tangles, and Alzheimer's disease. *Biochim Biophys Acta* **1739**: 216–223.
- Bittner, T., Fuhrmann, M., Burgold, S., Ochs, S.M., Hoffmann, N., Kretzschmar, H., *et al.* (2010) Multiple Events Lead to Dendritic Spine Loss in Triple Transgenic Alzheimer's Disease Mice. *PLoS One* **5**: 1–9.
- Blanks, J.C., Hinton, D.R., Sadun, A.A., and Miller, C.A. (1989) Retinal ganglion cell degeneration in Alzheimer's disease. *Brain Res* **501**: 364–372.
- Blanks, J.C., Schmidt, S.Y., Torigoe, Y., Porrello, K. V., Hinton, D.R., and Blanks, R.H.I. (1996) Retinal pathology in Alzheimer's disease. II. Regional neuron loss and glial changes in GCL. *Neurobiol Aging* **17**: 385–395.
- Blázquez, G., Cañete, T., Tobeña, A., Giménez-Llort, L., and Fernández-Teruel, A. (2014) Cognitive and emotional profiles of aged Alzheimer's disease (3 \times TgAD) mice: Effects of environmental enrichment and sexual dimorphism. *Behav Brain Res* **268**: 185–201.
- Boche, D., Denham, N., Holmes, C., and Nicoll, J.A.R. (2010) Neuropathology after active A β 42 immunotherapy: Implications for Alzheimer's disease pathogenesis. *Acta Neuropathol* **120**: 369–384.
- Bodea, L.-G., Wang, Y., Linnartz-Gerlach, B., Kopatz, J., Sinkkonen, L., Musgrove, R., *et al.* (2014) Neurodegeneration by Activation of the Microglial Complement-Phagosome Pathway. *J Neurosci* **34**: 8546–8556.
- Bodnarenko, S.R., and Chalupa, L.M. (1993) Stratification of ON and OFF ganglion cell dendrites depends on glutamate-mediated afferent activity in the developing retina. *Nature* **364**: 144–146.
- Bonfili, L., Cecarini, V., Berardi, S., Scarpona, S., Suchodolski, J.S., Nasuti, C., *et al.* (2017) Microbiota modulation counteracts Alzheimer's disease progression influencing neuronal proteolysis and gut hormones plasma levels. *Sci Rep* **7**: 1–21.
- Bonfili, L., Cecarini, V., Cuccioloni, M., Angeletti, M., Berardi, S., Scarpona, S., *et al.* (2018) SLAB51 Probiotic Formulation Activates SIRT1 Pathway Promoting Antioxidant and Neuroprotective Effects in an AD Mouse Model. *Mol Neurobiol* **55**: 7987–8000.

- Boros, B.D., Greathouse, K.M., Gentry, E.G., Curtis, K.A., Birchall, E.L., Gearing, M., and Herskowitz, J.H. (2017) Dendritic spines provide cognitive resilience against Alzheimer's disease. *Ann Neurol* **82**: 602–614.
- Bourne, J.N., and Harris, K.M. (2008) Balancing Structure and Function at Hippocampal Dendritic Spines. *Annu Rev Neurosci* **31**: 47–67.
- Braak, H., and Tredici, K. Del (2018) Spreading of tau pathology in sporadic Alzheimer's disease along cortico-cortical top-down connections. *Cereb Cortex* **28**: 3372–3384.
- Brown, G.C. (2019) The endotoxin hypothesis of neurodegeneration. *J Neuroinflammation* **16**: 1–10.
- Buckingham, B.P., Inman, D.M., Lambert, W., Oglesby, E., Calkins, D.J., Steele, M.R., et al. (2008) Progressive ganglion cell degeneration precedes neuronal loss in a mouse model of glaucoma. *J Neurosci* **28**: 2735–2744.
- Carroll, J.C., Rosario, E.R., Kreimer, S., Villamagna, A., Gentschein, E., Stanczyk, F.Z., and Pike, C.J. (2010) Sex differences in β -amyloid accumulation in 3xTg-AD mice: Role of neonatal sex steroid hormone exposure. *Brain Res* **1366**: 233–245.
- Chapman, P.F., White, G.L., Jones, M.W., Cooper-Blacketer, D., Marshall, V.J., Irizarry, M., et al. (1999) Impaired synaptic plasticity and learning in aged amyloid precursor protein transgenic mice. *Nat Neurosci* **2**: 271–276.
- Charidimou, A., Boulouis, G., Gurol, M.E., Ayata, C., Bacsikai, B.J., Frosch, M.P., et al. (2017) Emerging concepts in sporadic cerebral amyloid angiopathy. *Brain* **140**: 1829–1850.
- Chen, W., Abud, E.A., Yeung, S.T., Lakatos, A., Nassi, T., Wang, J., et al. (2016) Increased tauopathy drives microglia-mediated clearance of beta-amyloid. *Acta Neuropathol Commun* **4**: 63.
- Cheng, C., Trzcinski, O., and Doering, L.C. (2014) Fluorescent labeling of dendritic spines in cell cultures with the carbocyanine dye “Dil.” *Front Neuroanat* **8**: 1–8.
- Chiasseu, M., Alarcon-Martinez, L., Belforte, N., Quintero, H., Dotigny, F., Destroismaisons, L., et al. (2017) Tau accumulation in the retina promotes early neuronal dysfunction and precedes brain pathology in a mouse model of Alzheimer's disease. *Mol Neurodegener* **12**: 58.
- Chidlow, G., Wood, J.P.M., Manavis, J., Finnie, J., and Casson, R.J. (2017) Investigations into Retinal Pathology in the Early Stages of a Mouse Model of Alzheimer's Disease. *J Alzheimer's Dis* **56**: 655–675.
- Chintapaludi, S., Carter, A.U., Jackson, H., Acklin, C., Wang, X., Sasner, M., et al. (2020) Staging Alzheimer's disease in the brain and retina of B6.APP/PS1 mice by transcriptional profiling. *J Alzheimer's Dis* **73**: 1421–1434.
- Chiquita, S., Campos, E.J., Castellano, J., Ribeiro, M., Sereno, J., Moreira, P.I., et al. (2019) Retinal thinning of inner sub-layers is associated with cortical atrophy in a mouse model of Alzheimer's disease: A longitudinal multimodal in vivo study. *Alzheimer's Res Ther* **11**: 1–16.

- Chiquita, S., Ribeiro, M., Castelhana, J., Oliveira, F., Sereno, J., Batista, M., *et al.* (2019) A longitudinal multimodal in vivo molecular imaging study of the 3xTg-AD mouse model shows progressive early hippocampal and taurine loss. *Hum Mol Genet* **28**: 2174–2188.
- Chiquita, S., Rodrigues-Neves, A.C., Baptista, F.I., Carecho, R., Moreira, P.I., Castelo-Branco, M., and Ambrósio, A.F. (2019) The Retina as a Window or Mirror of the Brain Changes Detected in Alzheimer’s Disease: Critical Aspects to Unravel. *Mol Neurobiol* **56**: 5416–5435.
- Chiu, W.C., Tsan, Y.T., Tsai, S.L., Chang, C.J., Wang, J.D., and Chen, P.C. (2014) Hepatitis C viral infection and the risk of dementia. *Eur J Neurol* **21**: 1–9.
- Chklovskii, D.B. (2004) Synaptic connectivity and neuronal morphology: Two sides of the same coin. *Neuron* **43**: 609–617.
- Chovatiya, R., and Medzhitov, R. (2014) Stress, inflammation, and defense of homeostasis. *Mol Cell* **54**: 281–288.
- Chugh, D., Nilsson, P., Afjei, S.A., Bakochi, A., and Ekdahl, C.T. (2013) Brain inflammation induces post-synaptic changes during early synapse formation in adult-born hippocampal neurons. *Exp Neurol* **250**: 176–188.
- Colom-Cadena, M., Spires-Jones, T., Zetterberg, H., Blennow, K., Caggiano, A., Dekosky, S.T., *et al.* (2020) The clinical promise of biomarkers of synapse damage or loss in Alzheimer’s disease. *Alzheimer’s Res Ther* **12**: 1–12.
- Commins, S., O’Neill, L.A.J., and O’Mara, S.M. (2001) The effects of the bacterial endotoxin lipopolysaccharide on synaptic transmission and plasticity in the CA1-subiculum pathway in vivo. *Neuroscience* **102**: 273–280.
- Cook, T., Botto, M., Walport, M.J., Fossati-Jimack, L., Cortes-Hernandez, J., Daniel, H., *et al.* (2002) Expression Effects of Genetic Background on Disease C1q Deficiency and Autoimmunity: The. *J Immunol Ref* **168**: 2538–2543.
- Criscuolo, C., Cerri, E., Fabiani, C., Capsoni, S., Cattaneo, A., and Domenici, L. (2018) The retina as a window to early dysfunctions of Alzheimer’s disease following studies with a 5xFAD mouse model. *Neurobiol Aging* **67**: 181–188.
- Cunningham, C., and Hennessy, E. (2015) Co-morbidity and systemic inflammation as drivers of cognitive decline: New experimental models adopting a broader paradigm in dementia research. *Alzheimer’s Res Ther* **7**: 1–13.
- Czirr, E., Castello, N.A., Mosher, K.I., Castellano, J.M., Hinkson, I. V., Lucin, K.M., *et al.* (2017) Microglial complement receptor 3 regulates brain A β levels through secreted proteolytic activity. *J Exp Med* **214**: 1081–1092.
- Dejanovic, B., Huntley, M.A., Mazière, A. De, Meilandt, W.J., Wu, T., Srinivasan, K., *et al.* (2018) Changes in the Synaptic Proteome in Tauopathy and Rescue of Tau-Induced Synapse Loss by C1q Antibodies. *Neuron* **100**: 1–15.
- Dekeyser, S., Kock, I. De, Nikoubashman, O., Bossche, S. Vanden, Eetvelde, R. Van, Groote, J. De, *et al.* (2017) “Unforgettable” – a pictorial essay on anatomy and pathology

of the hippocampus. *Insights Imaging* **8**: 199–212.

Deture, M.A., and Dickson, D.W. (2019) The neuropathological diagnosis of Alzheimer's disease. *Mol Neurodegener* **14**: 1–18.

DiCarlo, G., Wilcock, D., Henderson, D., Gordon, M., and Morgan, D. (2001) Intrahippocampal LPS injections reduce A β load in APP+PS1 transgenic mice. *Neurobiol Aging* **22**: 1007–1012.

Dodiya, H.B., Kuntz, T., Shaik, S.M., Baufeld, C., Leibowitz, J., Zhang, Xulun, *et al.* (2019) Sex-specific effects of microbiome perturbations on cerebral A-beta amyloidosis and microglia phenotypes. *J Exp Med* **216**: 1–19.

Dorostkar, M.M., Zou, C., Blazquez-Llorca, L., and Herms, J. (2015) Analyzing dendritic spine pathology in Alzheimer's disease: problems and opportunities. *Acta Neuropathol* **130**: 1–19.

Doustar, J., Torbati, T., Black, K.L., Koronyo, Y., and Koronyo-Hamaoui, M. (2017) Optical coherence tomography in Alzheimer's disease and other neurodegenerative diseases. *Front Neurol* **8**: 1–13.

Driscoll, I., and Troncoso, J. (2011) Asymptomatic Alzheimer's Disease: A Prodrome or a State of Resilience? *Curr Alzheimer Res* **999**: 1–6.

Dubois, B., Feldman, H.H., Jacova, C., DeKosky, S.T., Barberger-Gateau, P., Cummings, J., *et al.* (2007) Research criteria for the diagnosis of Alzheimer's disease: revising the NINCDS-ADRDA criteria. *Lancet Neurol* **6**: 734–746.

Dubois, B., Hampel, H., Feldman, H.H., Scheltens, P., Andrieu, S., Bakardjian, H., *et al.* (2016) Preclinical Alzheimer's disease: Definition, natural history, and diagnostic criteria. *Alzheimers Dement* **12**: 292–323.

Dutescu, R.M., Li, Q.-X., Crowston, J., Masters, C.L., Baird, P.N., and Culvenor, J.G. (2009) Amyloid precursor protein processing and retinal pathology in mouse models of Alzheimer's disease. *Graefes Arch Clin Exp Ophthalmol* **247**: 1213–21.

Edwards, M.M., Rodríguez, J.J., Gutierrez-Lanza, R., Yates, J., Verkhratsky, A., and Luty, G.A. (2014) Retinal macroglia changes in a triple transgenic mouse model of Alzheimer's disease. *Exp Eye Res* **127**: 252–260.

Ehlers, M.D., Heine, M., Groc, L., Lee, M.C., and Choquet, D. (2007) Diffusional Trapping of GluR1 AMPA Receptors by Input-Specific Synaptic Activity. *Neuron* **54**: 447–460.

Eikelenboom, P., and Veerhuis, R. (1996) The Role of Complement and Activated Microglia in the Pathogenesis of Alzheimer's Disease. *Neurobiol Aging* **17**: 673–680.

Eimer, W.A., and Vassar, R. (2013) Neuron loss in the 5XFAD mouse model of Alzheimer's disease correlates with intraneuronal A β 42 accumulation and Caspase-3 activation. *Mol Neurodegener* **8**: 1–12.

Elahi, F.M., and Miller, B.L. (2017) A clinicopathological approach to the diagnosis of dementia. *Nat Rev Neurol* **13**: 457–476.

-
- Emoto, K. (2011) Dendrite remodeling in development and disease. *Dev Growth Differ* **53**: 277–286.
- Evans, C.E., Miners, J.S., Piva, G., Willis, C.L., Heard, D.M., Kidd, E.J., *et al.* (2020) ACE2 activation protects against cognitive decline and reduces amyloid pathology in the Tg2576 mouse model of Alzheimer's disease. *Acta Neuropathol* **139**: 485–502.
- Fiandaca, M.S., Mapstone, M.E., Cheema, A.K., and Federoff, H.J. (2014) The critical need for defining preclinical biomarkers in Alzheimer's disease. *Alzheimer's Dement* **10**: 196–212.
- Fijan, S. (2014) Microorganisms with claimed probiotic properties: An overview of recent literature. *Int J Environ Res Public Health* **11**: 4745–4767.
- Filipello, F., Morini, R., Corradini, I., Zerbi, V., Canzi, A., Michalski, B., *et al.* (2018) The Microglial Innate Immune Receptor TREM2 Is Required for Synapse Elimination and Normal Brain Connectivity. *Immunity* **48**: 979–991.
- Fonseca, M.I., Ager, R.R., Chu, S., Yazan, O., Sanderson, S.D., LaFerla, F.M., *et al.* (2009) Treatment with a C5aR Antagonist Decreases Pathology and Enhances Behavioral Performance in Murine Models of Alzheimer's Disease. *J Immunol* **23**: 1–7.
- Fonseca, M.I., Chu, S., Berci, A.M., Benoit, M.E., Peters, D.G., Kimura, Y., and Tenner, A.J. (2011) Contribution of complement activation pathways to neuropathology differs among mouse models of Alzheimer's disease. *J Neuroinflammation* **8**: 1–12.
- Fonseca, M.I., Zhou, J., Botto, M., and Tenner, A.J. (2004) Absence of C1q Leads to Less Neuropathology in Transgenic Mouse Models of Alzheimer's Disease. *J Neurosci* **24**: 6457–6465.
- Fraser, D.A., Pisalyaput, K., and Tenner, A.J. (2010) C1q enhances microglial clearance of apoptotic neurons and neuronal blebs, and modulates subsequent inflammatory cytokine production. *J Neurochem* **112**: 733–743.
- Freeman, S.A., and Grinstein, S. (2014) Phagocytosis: Receptors, signal integration, and the cytoskeleton. *Immunol Rev* **262**: 193–215.
- Frei, Y., Lambris, J.D., and Stockinger, B. (1987) Generation of a monoclonal antibody to mouse C5 application in an ELISA assay for detection of anti-CS antibodies. *Mol Cell Probes* **1**: 141–149.
- Frisoni, G., Fox, N., Jack, C., Scheltens, P., and Thompson, P. (2010) The clinical use of structural MRI in Alzheimer disease. *Nat Rev Neurol* **6**: 67–77.
- Frost, S., Kanagasingam, Y., Sohrabi, H., Vignarajan, J., Bourgeat, P., Salvado, O., *et al.* (2013) Retinal vascular biomarkers for early detection and monitoring of Alzheimer's disease. *Transl Psychiatry* **3**: e233.
- Galasko, D., Xiao, M., Xu, D., Smirnov, D., Salmon, D.P., Dewit, N., *et al.* (2019) Synaptic biomarkers in CSF aid in diagnosis, correlate with cognition and predict progression in MCI and Alzheimer's disease. *Alzheimer's Dement Transl Res Clin Interv* **5**: 871–882.

-
- Galloway, D.A., Phillips, A.E.M., Owen, D.R.J., and Moore, C.S. (2019) Phagocytosis in the brain: Homeostasis and disease. *Front Immunol* **10**: 1–15.
- Gan, W.-B.B., Grutzendler, J., Wong, W.T., Wong, R.O., and Lichtman, J.W. (2000) Multicolor “DiOlistic” labeling of the nervous system using lipophilic dye combinations. *Neuron* **27**: 219–225.
- Gao, L., Chen, X., Tang, Y., Zhao, J., Li, Q., Fan, X., *et al.* (2015) Neuroprotective effect of memantine on the retinal ganglion cells of APP^{swe}/PS1^{ΔE9} mice and its immunomodulatory mechanisms. *Exp Eye Res* **135**: 47–58.
- Gao, Y., Hu, S., Li, Q., Wang, M., Zhi, Z., Kuang, X., *et al.* (2018) Neonatal inflammation induces reorganization in dendritic morphology of retinal ganglion cells but not their retinogeniculate projection in mice. *Neurosci Lett* **676**: 34–40.
- Garré, J.M., Silva, H.M., Lafaille, J.J., and Yang, G. (2017) CX3CR1⁺ monocytes modulate learning and learning-dependent dendritic spine remodeling via TNF- α . *Nat Med* **23**: 714–722.
- Gasparini, L., Anthony Crowther, R., Martin, K.R., Berg, N., Coleman, M., Goedert, M., and Spillantini, M.G. (2011) Tau inclusions in retinal ganglion cells of human P301S tau transgenic mice: Effects on axonal viability. *Neurobiol Aging* **32**: 419–433.
- Gipson, C.D., and Olive, M.F. (2017) Structural and functional plasticity of dendritic spines – root or result of behavior? *Genes Brain Behav* **16**: 101–117.
- Giridharan, V. V., Masud, F., Petronilho, F., Dal-Pizzol, F., and Barichello, T. (2019) Infection-induced systemic inflammation is a potential driver of Alzheimer’s disease progression. *Front Aging Neurosci* **11**: 1–5.
- Goaillard, J.M., Moubarak, E., Tapia, M., and Tell, F. (2020) Diversity of Axonal and Dendritic Contributions to Neuronal Output. *Front Cell Neurosci* **13**: 1–21.
- Gool, W.A. van, Beek, D. van de, and Eikelenboom, P. (2010) Systemic infection and delirium: when cytokines and acetylcholine collide. *Lancet* **375**: 773–775.
- Graewe, B., Lemos, R., Ferreira, C., Santana, I., Farivar, R., Weerd, P. De, and Castelo-Branco, M. (2013) Impaired processing of 3D motion-defined faces in mild cognitive impairment and healthy aging: An fMRI study. *Cereb Cortex* **23**: 2489–2499.
- Grigg, J.B., and Sonnenberg, G.F. (2017) Host-Microbiota Interactions Shape Local and Systemic Inflammatory Diseases. *J Immunol* **198**: 564–571.
- Grimaldi, A., Brighi, C., Peruzzi, G., Ragozzino, D., Bonanni, V., Limatola, C., *et al.* (2018) Inflammation, neurodegeneration and protein aggregation in the retina as ocular biomarkers for Alzheimer’s disease in the 3xTg-AD mouse model. *Cell Death Dis* **9**: 1–10.
- Grimaldi, A., Pediconi, N., Oieni, F., Pizzarelli, R., Rosito, M., Giubettini, M., *et al.* (2019) Neuroinflammatory Processes, A1 Astrocyte Activation and Protein Aggregation in the Retina of Alzheimer’s Disease Patients, Possible Biomarkers for Early Diagnosis. *Front Neurosci* **13**: 1–11.

-
- Gu, L., and Guo, Z. (2013) Alzheimer's A β 42 and A β 40 peptides form interlaced amyloid fibrils. *J Neurochem* **126**: 305–311.
- Guerreiro, R., Wojtas, A., Bras, J., Carrasquillo, M., Rogaeva, E., Majounie, E., *et al.* (2013) TREM2 variants in Alzheimer's disease. *N Engl J Med* **368**: 117–127.
- Gupta, V.K.V.B., Chitranshi, N., Gupta, V.K.V.B., Golzan, M., Dheer, Y., Wall, R. Vander, *et al.* (2016) Amyloid β accumulation and inner retinal degenerative changes in Alzheimer's disease transgenic mouse. *Neurosci Lett* **623**: 52–56.
- Györfy, B.A., Kun, J., Török, G., Bulyáki, É., Borhegyi, Z., Gulyácssy, P., *et al.* (2018) Local apoptotic-like mechanisms underlie complement-mediated synaptic pruning. *Proc Natl Acad Sci U S A* **115**: 6303–6308.
- Haan, J. den, Morrema, T.H.J., Verbraak, F.D., Boer, J.F. de, Scheltens, P., Rozemuller, A.J., *et al.* (2018) Amyloid-beta and phosphorylated tau in post-mortem Alzheimer's disease retinas. *Acta Neuropathol Commun* **6**: 1–11.
- Hadoux, X., Hui, F., Lim, J.K.H., Masters, C.L., Pébay, A., Chevalier, S., *et al.* (2019) Non-invasive in vivo hyperspectral imaging of the retina for potential biomarker use in Alzheimer's disease. *Nat Commun* **10**: 1–12.
- Hakobyan, S., Harding, K., Aiyaz, M., Hye, A., Dobson, R., Baird, A., *et al.* (2016) Complement Biomarkers as Predictors of Disease Progression in Alzheimer's Disease. *J Alzheimer's Dis* **54**: 707–716.
- Hall, J.H., Wiseman, F.K., Fisher, E.M.C., Tybulewicz, V.L.J., Harwood, J.L., and Good, M.A. (2016) Tc1 mouse model of trisomy-21 dissociates properties of short- and long-term recognition memory. *Neurobiol Learn Mem* **130**: 118–128.
- Hardy, J.A., and Higgins, G.A. (1992) Alzheimer's Disease: The Amyloid Cascade Hypothesis. *Science (80-)* **256**: 184–185.
- Harold, D., Abraham, R., Hollingworth, P., Sims, R., Hamshere, M., Pahwa, J.S., *et al.* (2009) Genome-Wide Association Study Identifies Variants at CLU and PICALM Associated with Alzheimer's Disease, and Shows Evidence for Additional Susceptibility Genes. *Nat Genet* **41**: 1088–1093.
- Hart, N.J., Koronyo, Y., Black, K.L., and Koronyo-Hamaoui, M. (2016) Ocular indicators of Alzheimer's: exploring disease in the retina. *Acta Neuropathol* **132**: 767–787.
- Hayashi-Park, E., Ozment, B.N., Griffith, C.M., Zhang, H., Patrylo, P.R., and Rose, G.M. (2017) Experimentally induced diabetes worsens neuropathology, but not learning and memory, in middle aged 3xTg mice. *Behav Brain Res* **322**: 280–287.
- He, J., Zhao, C., Dai, J., Weng, C.H., Bian, B.S.J., Gong, Y., *et al.* (2019) Microglia Mediate Synaptic Material Clearance at the Early Stage of Rats With Retinitis Pigmentosa. *Front Immunol* **10**: 1–17.
- Heesterbeek, D.A.C., Angelier, M.L., Harrison, R.A., and Rooijackers, S.H.M. (2018) Complement and Bacterial Infections: From Molecular Mechanisms to Therapeutic Applications. *J Innate Immun* **10**: 455–464.

- Helmy, K.Y., Katschke, K.J., Gorgani, N.N., Kljavin, N.M., Elliott, J.M., Diehl, L., *et al.* (2006) CR1g: A macrophage complement receptor required for phagocytosis of circulating pathogens. *Cell* **124**: 915–927.
- Hemonnot, A.L., Hua, J., Ulmann, L., and Hirbec, H. (2019) Microglia in Alzheimer disease: Well-known targets and new opportunities. *Front Cell Infect Microbiol* **9**: 1–20.
- Henneman, W.J.P., Sluimer, J.D., Barnes, J., Flier, W.M. Van Der, Sluimer, I.C., Fox, N.C., *et al.* (2009) Hippocampal atrophy rates in Alzheimer disease: Added value over whole brain volume measures. *Neurology* **72**: 999–1007.
- Henry, C.J., Huang, Y., Wynne, A.M., and Godbout, J.P. (2009) Peripheral LPS challenge promotes microglial hyperactivity in aged mice that is associated with exaggerated induction of both proinflammatory IL1 β and antiinflammatory IL10 cytokines.pdf. *Brain Behav Immun* **23**: 309–317.
- Herber, D.L., Mercer, M., Roth, L.M., Symmonds, K., Maloney, J., Wilson, N., *et al.* (2007) Microglial activation is required for A β clearance after intracranial injection of lipopolysaccharide in APP transgenic mice. *J Neuroimmune Pharmacol* **2**: 222–231.
- Herber, D.L., Roth, L.M., Wilson, D., Wilson, N., Mason, J.E., Morgan, D., and Gordon, M.N. (2004) Time-dependent reduction in A β levels after intracranial LPS administration in APP transgenic mice. *Exp Neurol* **190**: 245–253.
- Hernandez, M.X., Jiang, S., Cole, T.A., Chu, S.H., Fonseca, M.I., Fang, M.J., *et al.* (2017) Prevention of C5aR1 signaling delays microglial inflammatory polarization, favors clearance pathways and suppresses cognitive loss. *Mol Neurodegener* **12**: 1–19.
- Hinton, D.R., Sadun, A.A., Blanks, J.C., and Miller, C.A. (1986) Optic-nerve degeneration in Alzheimer's Disease. *N Engl J Med* **314**: 1547–1552.
- Ho, C.Y., Troncoso, J.C., Knox, D., Stark, W., and Eberhart, C.G. (2014) Beta-amyloid, phospho-tau and alpha-synuclein deposits similar to those in the brain are not identified in the eyes of Alzheimer's and Parkinson's disease patients. *Brain Pathol* **24**: 25–32.
- Hong, S., Beja-glasser, V.F., Nfonoyim, B.M., Frouin, A., Ramakrishnan, S., Merry, K.M., *et al.* (2016) Complement and Microglia Mediate Early Synapse Loss in Alzheimer Mouse Models. *Science (80-)* **352**: 712–716.
- Hoon, M., Okawa, H., Santina, L. Della, and Wong, R.O.L. (2014) Functional architecture of the retina: Development and disease. *Prog Retin Eye Res* **42**: 44–84.
- Hsiao, K., Chapman, P., Nilsen, S., Eckman, C., Harigaya, Y., Younkin, S., *et al.* (1996a) Correlative Memory Deficits, A β Elevation, and Amyloid Plaques in Transgenic Mice. *Science (80-)* **274**: 99–102.
- Hsiao, K., Chapman, P., Nilsen, S., Eckman, C., Harigaya, Y., Younkin, S., *et al.* (1996b) Amyloid Plaques in Transgenic Mice. *Science (80-)* **274**: 99–102.
- Huang, W., Fileta, J., Guo, Y., and Grosskreutz, C.L. (2006) Downregulation of Thy1 in retinal ganglion cells in experimental glaucoma. *Curr Eye Res* **31**: 265–271.
- Humbles, A.A., Lu, B., Nilsson, C.A., Lilly, C., Israel, E., Fujiwara, Y., *et al.* (2000) A

role for the C3a anaphylatoxin receptor in the effector phase of asthma. *Nature* **406**: 998–1001.

Iqbal, K., Liu, F., Gong, C.-X., and Grundke-Iqbal, I. (2010) Tau in Alzheimer Disease and Related Tauopathies Khalid. *Curr Alzheimer Res* **7**: 656–664.

Irizarry, M.C., McNamara, M., Fedorchak, K., Hsiao, K., and Hyman, B.T. (1997) APP(Sw) transgenic mice develop age-related A β deposits and neuropil abnormalities, but no neuronal loss in CA1. *J Neuropathol Exp Neurol* **56**: 965–973.

Isas, J.M., Luibl, V., Johnson, L. V, Kaye, R., Wetzel, R., Glabe, C.G., *et al.* (2010) Soluble and mature amyloid fibrils in drusen deposits. *Investig Ophthalmol Vis Sci* **51**: 1304–1310.

Iseri, P.K., Altınış, Ö., Tokay, T., and Yüksel, N. (2006) Relationship between cognitive impairment and retinal morphological and visual functional abnormalities in Alzheimer disease. *J Neuro-Ophthalmology* **26**: 18–24.

Ito, Y.A., and Polo, A. Di (2017) Mitochondrial dynamics, transport, and quality control: A bottleneck for retinal ganglion cell viability in optic neuropathies. *Mitochondrion* **36**: 186–192.

Izumi, H., Sato, K., Kojima, K., Saito, T., Saido, T.C., and Fukunaga, K. (2020) Oral glutathione administration inhibits the oxidative stress and the inflammatory responses in AppNL–G-F/NL–G-F knock-in mice. *Neuropharmacology* **168**: 1–11.

Jacobsen, J.S., Wu, C.C., Redwine, J.M., Comery, T.A., Arias, R., Bowlby, M., *et al.* (2006) Early-onset behavioral and synaptic deficits in a mouse model of Alzheimer's disease. *Proc Natl Acad Sci U S A* **103**: 5161–5166.

Jáñez-Escalada, L., Jáñez-García, L., Salobrar-García, E., Santos-Mayo, A., Hoz, R. de, Yubero, R., *et al.* (2019) Spatial analysis of thickness changes in ten retinal layers of Alzheimer's disease patients based on optical coherence tomography. *Sci Rep* **9**: 1–14.

Jankowsky, J.L., and Zheng, H. (2017) Practical considerations for choosing a mouse model of Alzheimer's disease. *Mol Neurodegener* **12**: 1–22.

Javaid, F.Z., Brenton, J., Guo, L., and Cordeiro, M.F. (2016) Visual and ocular manifestations of Alzheimer's disease and their use as biomarkers for diagnosis and progression. *Front Neurol* **7**: 1–11.

Jaworski, T., Lechat, B., Demedts, D., Gielis, L., Devijver, H., Borghgraef, P., *et al.* (2011) Dendritic degeneration, neurovascular defects, and inflammation precede neuronal loss in a mouse model for tau-mediated neurodegeneration. *Am J Pathol* **179**: 2001–2015.

Johnson, K.A., Fox, N.C., Sperling, R.A., and Klunk, W.E. (2012) Brain imaging in Alzheimer disease. *Cold Spring Harb Perspect Med* **2**: 1–24.

Joly, S., Lamoureux, S., and Pernet, V. (2017) Nonamyloidogenic processing of amyloid beta precursor protein is associated with retinal function improvement in aging male APP^{swe}/PS1 Δ E9 mice. *Neurobiol Aging* **53**: 181–191.

- Jonsson, T., Stefansson, H., Steinberg, S., Jonsdottir, I., Jonsson, P. V., Snaedal, J., *et al.* (2013) Variant of TREM2 Associated with the Risk of Alzheimer's Disease. *N Engl J Med* **368**: 107–116.
- Katz, B., Rimmer, S., Iragui, V., and Katzman, R. (1989) Abnormal pattern electroretinogram in Alzheimer's disease: Evidence for retinal ganglion cell degeneration? *Ann Neurol* **26**: 221–225.
- Kaur, H., Nagamoto-Combs, K., Golovko, S., Golovko, M.Y., Klug, M.G., and Combs, C.K. (2020) Probiotics ameliorate intestinal pathophysiology in a mouse model of Alzheimer's disease. *Neurobiol Aging* **92**: 114–134.
- Kavalali, E.T. (2015) The mechanisms and functions of spontaneous neurotransmitter release. *Nat Rev Neurosci* **16**: 5–16.
- Kennedy, M.B. (2016) Synaptic signaling in learning and memory. *Cold Spring Harb Perspect Biol* **8**: 1–16.
- Kent, S.A., Spires-Jones, T.L., and Durrant, C.S. (2020) The physiological roles of tau and A β : implications for Alzheimer's disease pathology and therapeutics. *Acta Neuropathol* <http://link.springer.com/10.1007/s00401-020-02196-w>.
- Kim, M., Suh, J., Romano, D., Truong, M.H., Mullin, K., Hooli, B., *et al.* (2009) Potential late-onset Alzheimer's disease-associated mutations in the ADAM10 gene attenuate α -secretase activity. *Hum Mol Genet* **18**: 3987–3996.
- Kim, S.M., Mun, B.R., Lee, S.J., Joh, Y., Lee, H.Y., Ji, K.Y., *et al.* (2017) TREM2 promotes A β phagocytosis by upregulating C/EBP α -dependent CD36 expression in microglia. *Sci Rep* **7**: 1–12 <http://dx.doi.org/10.1038/s41598-017-11634-x>.
- Kima, B.G., Daia, H.-N., McAtee, M., Vicinib, S., and Bregman, B. (2007) Labeling of dendritic spines with the carbocyanine dye. *J Neurosci Methods* **15**: 237–243.
- Kitazawa, M., Oddo, S., Yamasaki, T.R., Green, K.N., and LaFerla, F.M. (2005) Lipopolysaccharide-induced inflammation exacerbates tau pathology by a cyclin-dependent kinase 5-mediated pathway in a transgenic model of Alzheimer's disease. *J Neurosci* **25**: 8843–8853.
- Knight, E.M., Martins, I.V.A., Gümüşgöz, S., Allan, S.M., and Lawrence, C.B. (2014) High-fat diet-induced memory impairment in triple-transgenic Alzheimer's disease (3xTgAD) mice is independent of changes in amyloid and tau pathology. *Neurobiol Aging* **35**: 1821–1832.
- Kobayashi, Y., Sugahara, H., Shimada, K., Mitsuyama, E., Kuhara, T., Yasuoka, A., *et al.* (2017) Therapeutic potential of Bifidobacterium breve strain A1 for preventing cognitive impairment in Alzheimer's disease. *Sci Rep* **7**: 1–10.
- Kondo, S., Kohsaka, S., and Okabe, S. (2011) Long-term changes of spine dynamics and microglia after transient peripheral immune response triggered by LPS in vivo. *Mol Brain* **4**: 1–16.
- Koronyo-Hamaoui, M., Koronyo, Y., Ljubimov, A. V., Miller, C.A., Ko, M.K., Black, K.L., *et al.* (2011) Identification of amyloid plaques in retinas from Alzheimer's patients

and noninvasive in vivo optical imaging of retinal plaques in a mouse model. *Neuroimage* **54**: S204–S217.

Koronyo, Y., Biggs, D., Barron, E., Boyer, D.S., Pearlman, J.A., Au, W.J., *et al.* (2017) Retinal amyloid pathology and proof-of-concept imaging trial in Alzheimer's disease. *JCI insight* **2**: 196–208.

Koronyo, Y., Salumbides, B.C., Black, K.L., and Koronyo-Hamaoui, M. (2012) Alzheimer's disease in the retina: Imaging retinal A β plaques for early diagnosis and therapy assessment. *Neurodegener Dis* **10**: 285–293.

Krasodomska, K., Lubiński, W., Potemkowski, A., and Honczarenko, K. (2010) Pattern electroretinogram (PERG) and pattern visual evoked potential (PVEP) in the early stages of Alzheimer's disease. *Doc Ophthalmol* **121**: 111–121.

Krstic, D., and Knuesel, I. (2013) Deciphering the mechanism underlying late-onset Alzheimer disease. *Nat Rev Neurol* **9**: 25–34.

Kumar, A. (2011) Long-term potentiation at CA3-CA1 hippocampal synapses with special emphasis on aging, disease, and stress. *Front Aging Neurosci* **3**: 1–20.

LaFerla, F.M., and Green, K.N. (2012) Animal models of Alzheimer disease. *Cold Spring Harb Perspect Med* **2**: 1–13.

Langa, K.M., and Levine, D.A. (2014) The diagnosis and management of mild cognitive impairment: A clinical review. *JAMA - J Am Med Assoc* **312**: 2551–2561.

Lanz, T.A., Carter, D.B., and Merchant, K.M. (2003) Dendritic spine loss in the hippocampus of young PDAPP and Tg2576 mice and its prevention by the ApoE2 genotype. *Neurobiol Dis* **13**: 246–253.

Latif-Hernandez, A., Sabanov, V., Ahmed, T., Craessaerts, K., Saito, T., Saido, T., and Balschun, D. (2020) The two faces of synaptic failure in App NL-G-F knock-in mice. *Alzheimer's Res Ther* **12**: 1–15.

Latif-Hernandez, A., Shah, D., Craessaerts, K., Saido, T., Saito, T., Strooper, B. De, *et al.* (2019) Subtle behavioral changes and increased prefrontal-hippocampal network synchronicity in APP NL-G-F mice before prominent plaque deposition. *Behav Brain Res* **364**: 431–441.

Lazic, D., Tesic, V., Jovanovic, M., Brkic, M., Milanovic, D., Zlokovic, B. V., *et al.* (2020) Every-other-day feeding exacerbates inflammation and neuronal deficits in 5XFAD mouse model of Alzheimer's disease. *Neurobiol Dis* **136**: 1–15.

Lebovitz, Y., Kowalski, E.A., Wang, X., Kelly, C., Lee, M., McDonald, V., *et al.* (2019) Lactobacillus rescues postnatal neurobehavioral and microglial dysfunction in a model of maternal microbiome dysbiosis. *Brain Behav Immun* **81**: 617–629.

Lee, D.C., Rizer, J., Selenica, M.L.B., Reid, P., Kraft, C., Johnson, A., *et al.* (2010) LPS-induced inflammation exacerbates phospho-tau pathology in rTg4510 mice. *J Neuroinflammation* **7**: 1–16.

Lee, H.J., Lee, K.E., Kim, J.K., and Kim, D.H. (2019) Suppression of gut dysbiosis by

Bifidobacterium longum alleviates cognitive decline in 5XFAD transgenic and aged mice. *Sci Rep* **9**: 1–12.

Lee, J.W., Lee, Y.K., Yuk, D.Y., Choi, D.Y., Ban, S.B., Oh, K.W., and Hong, J.T. (2008) Neuro-inflammation induced by lipopolysaccharide causes cognitive impairment through enhancement of beta-amyloid generation. *J Neuroinflammation* **5**: 1–14.

Leffler, J., Bengtsson, A.A., and Blom, A.M. (2014) The complement system in systemic lupus erythematosus: An update. *Ann Rheum Dis* **73**: 1601–1606.

Leger, F., Fernagut, P.O., Canron, M.H., Léoni, S., Vital, C., Tison, F., *et al.* (2011) Protein aggregation in the aging retina. *J Neuropathol Exp Neurol* **70**: 63–68.

Lehmann, K., Wood, A., Cummings, D., Bai, L., Stevens, B., and Belluscio, L. (2018) Complement 3 signaling is necessary for the developmental refinement of olfactory bulb circuitry. *bioRxiv, Preprint* 1–28.

Lemos, R., Figueiredo, P., Santana, I., Simões, M.R., and Castelo-Branco, M. (2012) Temporal integration of 3D coherent motion cues defining visual objects of unknown orientation is impaired in amnesic mild cognitive impairment and Alzheimer's disease. *J Alzheimer's Dis* **28**: 885–896.

Leuzy, A., Heurling, K., Ashton, N.J., Schöll, M., and Eduardo, R. (2018) In vivo Detection of Alzheimer's Disease. *Yale J Biol Med* **91**: 291–300.

Lewis, L.A., and Ram, S. (2014) Meningococcal disease and the complement system. *Virulence* **5**: 98–126.

Li, B., He, Y., Ma, J., Huang, P., Du, J., Cao, L., *et al.* (2019) Mild cognitive impairment has similar alterations as Alzheimer's disease in gut microbiota. *Alzheimer's Dement* **15**: 1357–1366.

Li, H., Xue, X., Li, L., Li, Y., Wang, Yanni, Huang, T., *et al.* (2020) Aluminum-Induced Synaptic Plasticity Impairment via PI3K-Akt-mTOR Signaling Pathway. *Neurotox Res* **37**: 996–1008.

Li, L., Luo, J., Chen, D., Tong, J. Bin, Zeng, L.P., Cao, Y.Q., *et al.* (2016) BACE1 in the retina: A sensitive biomarker for monitoring early pathological changes in Alzheimer's disease. *Neural Regen Res* **11**: 447–453.

Lian, H., Yang, L., Cole, A., Sun, L., Chiang, A.C.A., Fowler, S.W., *et al.* (2015) NFkB-Activated Astroglial Release of Complement C3 Compromises Neuronal Morphology and Function Associated with Alzheimer's Disease. *Neuron* **85**: 101–116.

Liao, H., Zhu, Z., and Peng, Y. (2018) Potential Utility of Retinal Imaging for Alzheimer's Disease: A Review. *Front Aging Neurosci* **10**: 1–16.

Lim, J.K.H., Li, Q.X., He, Z., Vingrys, A.J., Wong, V.H.Y., Currier, N., *et al.* (2016) The eye as a biomarker for Alzheimer's disease. *Front Neurosci* **10**: 1–14.

Lin, L., Chen, X., Zhou, Q., Huang, P., Jiang, S., Wang, H., and Deng, Y. (2019) Synaptic structure and alterations in the hippocampus in neonatal rats exposed to lipopolysaccharide. *Neurosci Lett* **709**: 1–10.

-
- Litvinchuk, A., Wan, Y.W., Swartzlander, D.B., Chen, F., Cole, A., Propson, N.E., *et al.* (2018) Complement C3aR Inactivation Attenuates Tau Pathology and Reverses an Immune Network Deregulated in Tauopathy Models and Alzheimer's Disease. *Neuron* **100**: 1337–1353.
- Liu, Y.L., Hsieh, Y.T., Chen, T.F., Chiou, J.M., Tsai, M.K., Chen, J.H., and Chen, Y.C. (2019) Retinal ganglion cell–inner plexiform layer thickness is nonlinearly associated with cognitive impairment in the community-dwelling elderly. *Alzheimer's Dement Diagnosis, Assess Dis Monit* **11**: 19–27.
- Loffler, K.U., Edward, D.P., and Tso, M.O.M. (1995) Immunoreactivity against tau, amyloid precursor protein, and beta-amyloid in the human retina. *Investig Ophthalmol Vis Sci* **36**: 24–31.
- London, A., Benhar, I., and Schwartz, M. (2013) The retina as a window to the brain - From eye research to CNS disorders. *Nat Rev Neurol* **9**: 44–53.
- M, O., Franco, A.P. Del, and Gipson, C.D. (2018) Diolistic Labeling and Analysis of Dendritic Spines. *Methods Mol Biol* **1727**: 179–200.
- Ma, Q., Xing, C., Long, W., Wang, H.Y., Liu, Q., and Wang, R.F. (2019) Impact of microbiota on central nervous system and neurological diseases: The gut-brain axis. *J Neuroinflammation* **16**: 1–14.
- Ma, Y., Ramachandran, A., Ford, N., Parada, I., and Prince, D.A. (2013) Remodeling of dendrites and spines in the C1q knockout model of genetic epilepsy. *Epilepsia* **54**: 1232–1239.
- Mahajan, D., and Votruba, M. (2017) Can the retina be used to diagnose and plot the progression of Alzheimer's disease? *Acta Ophthalmol* **95**: 768–777.
- Maier, M., Peng, Y., Jiang, L., Seabrook, T.J., Carroll, M.C., and Lemere, C.A. (2008) Complement C3 deficiency leads to accelerated amyloid β plaque deposition and neurodegeneration and modulation of the microglia/macrophage phenotype in amyloid precursor protein transgenic mice. *J Neurosci* **28**: 6333–6341.
- Mangold, C.A., and Szpara, M.L. (2019) Persistent infection with herpes simplex virus 1 and Alzheimer's disease—a call to study how variability in both virus and host may impact disease. *Viruses* **11**: 1–22.
- Marquié, M., Castilla-Martí, M., Valero, S., Martínez, J., Sánchez, D., Hernández, I., *et al.* (2019) Visual impairment in aging and cognitive decline: experience in a Memory Clinic. *Sci Rep* **9**: 1–10.
- Masland, R.H. (2012) The Neuronal Organization of the Retina. *Neuron* **76**: 266–280.
- Mastrangelo, M.A., and Bowers, W.J. (2008) Detailed immunohistochemical characterization of temporal and spatial progression of Alzheimer's disease-related pathologies in male triple-transgenic mice. *BMC Neurosci* **9**: 1–31.
- Masuda, A., Kobayashi, Y., Kogo, N., Saito, T., Saido, T.C., and Itohara, S. (2016) Cognitive deficits in single App knock-in mouse models. *Neurobiol Learn Mem* **135**: 73–82.

- Matias, I., Morgado, J., and Gomes, F.C.A. (2019) Astrocyte Heterogeneity: Impact to Brain Aging and Disease. *Front Aging Neurosci* **11**: 1–18.
- Mawanda, F., and Wallace, R. (2013) Can infections cause Alzheimer's disease? *Epidemiol Rev* **35**: 161–180.
- Mehla, J., Lacoursiere, S.G., Lapointe, V., McNaughton, B.L., Sutherland, R.J., McDonald, R.J., and Mohajerani, M.H. (2019) Age-dependent behavioral and biochemical characterization of single APP knock-in mouse (APPNL-G-F/NL-G-F) model of Alzheimer's disease. *Neurobiol Aging* **75**: 25–37.
- Mehrabadi, S., and Sadr, S.S. (2020) Assessment of probiotics mixture on memory function, inflammation markers, and oxidative stress in an Alzheimer's disease model of rats. *Iran Biomed J* **24**: 220–228.
- Mendell, A.L., Creighton, S.D., Wilson, H.A., Jardine, K.H., Isaacs, L., Winters, B.D., and MacLusky, N.J. (2020) Inhibition of 5 α Reductase Impairs Cognitive Performance, Alters Dendritic Morphology and Increases Tau Phosphorylation in the Hippocampus of Male 3xTg-AD Mice. *Neuroscience* **429**: 185–202.
- Mendez, M.F. (2017) Early-Onset Alzheimer Disease. *Neurol Clin* **35**: 263–281.
- Merlini, M., Rafalski, V.A., Rios Coronado, P.E., Gill, T.M., Ellisman, M., Muthukumar, G., *et al.* (2019) Fibrinogen Induces Microglia-Mediated Spine Elimination and Cognitive Impairment in an Alzheimer's Disease Model. *Neuron* **101**: 1099-1108.e6.
- Michael, D.R., Davies, T.S., Loxley, K.E., Allen, M.D., Good, M.A., Hughes, T.R., and Plummer, S.F. (2019) In vitro neuroprotective activities of two distinct probiotic consortia. *Benef Microbes* **10**: 437–447.
- Miller, A.A., and Spencer, S.J. (2014) Obesity and neuroinflammation: A pathway to cognitive impairment. *Brain Behav Immun* **42**: 10–21.
- Mohammadi, G., Dargahi, L., Peymani, A., Mirzanejad, Y., Alizadeh, S.A., Naserpour, T., and Nassiri-Asl, M. (2019) The Effects of Probiotic Formulation Pretreatment (Lactobacillus helveticus R0052 and Bifidobacterium longum R0175) on a Lipopolysaccharide Rat Model. *J Am Coll Nutr* **38**: 209–217.
- Möhle, L., Mattei, D., Heimesaat, M.M., Bereswill, S., Fischer, A., Alutis, M., *et al.* (2016) Ly6Chi Monocytes Provide a Link between Antibiotic-Induced Changes in Gut Microbiota and Adult Hippocampal Neurogenesis. *Cell Rep* **15**: 1945–1956.
- Moraes, C.A., Santos, G., Spohr, T.C.L.S., D'Avila, J.C., Lima, F.R.S., Benjamim, C.F., *et al.* (2015) Activated Microglia-Induced Deficits in Excitatory Synapses Through IL-1 β : Implications for Cognitive Impairment in Sepsis. *Mol Neurobiol* **52**: 653–663.
- More, S.S., Beach, J.M., McClelland, C., Mokhtarzadeh, A., and Vince, R. (2019) In Vivo Assessment of Retinal Biomarkers by Hyperspectral Imaging: Early Detection of Alzheimer's Disease. *ACS Chem Neurosci* **10**: 4492–4501.
- More, S.S., and Vince, R. (2015) Hyperspectral imaging signatures detect amyloidopathy in alzheimers mouse retina well before onset of cognitive decline. *ACS Chem Neurosci* **6**: 306–315.

- Morgan, B.P. (2003) The Complement System: An Overview. *Complement Methods Protoc* **150**: 1–13.
- Morgan, B.P. (2018) Complement in the pathogenesis of Alzheimer's disease. *Semin Immunopathol* **40**: 113–124.
- Morgia, C. La, Ross-Cisneros, F.N., Koronyo, Y., Hannibal, J., Gallassi, R., Cantalupo, G., *et al.* (2016) Melanopsin retinal ganglion cell loss in Alzheimer disease. *Ann Neurol* **79**: 90–109.
- Morita, Y., Jounai, K., Sakamoto, A., Tomita, Y., Sugihara, Y., Suzuki, H., *et al.* (2018) Long-term intake of *Lactobacillus paracasei* KW3110 prevents age-related chronic inflammation and retinal cell loss in physiologically aged mice. *Aging (Albany NY)* **10**: 2723–2740.
- Mu, Y., and Gage, F.H. (2011) Adult hippocampal neurogenesis and its role in Alzheimer's disease. *Mol Neurodegener* **6**: 1–9.
- Mukhin, V.N., Pavlov, K.I., and Klimenko, V.M. (2017) Mechanisms of Neuron Loss in Alzheimer's Disease. *Neurosci Behav Physiol* **47**: 508–516.
- Nakada, T., Matsuzawa, H., Igarashi, H., Fujii, Y., and Kwee, I.L. (2008) In vivo visualization of senile-plaque-like pathology in Alzheimer's disease patients by mr microscopy on a 7T system. *J Neuroimaging* **18**: 125–129.
- Nelson, P.T., Alafuzoff, I., Bigio, E.H., Bouras, C., Braak, H., Cairns, N.J., *et al.* (2012) Correlation of Alzheimer Disease Neuropathologic Changes With Cognitive Status: A Review of the Literature. *J Neuropathol Exp Neurol* **71**: 362–381.
- Neuner, S.M., TCW, J., and Goate, A.M. (2020) Genetic architecture of Alzheimer's disease. *Neurobiol Dis* **143**: 1–18.
- Ni, Y., Yang, X., Zheng, L., Wang, Z., Wu, L., Jiang, J., *et al.* (2019) *Lactobacillus* and *Bifidobacterium* Improves Physiological Function and Cognitive Ability in Aged Mice by the Regulation of Gut Microbiota. *Mol Nutr Food Res* **63**: 1–14.
- Niccoli, T., and Partridge, L. (2012) Ageing as a risk factor for disease. *Curr Biol* **22**: R741–R752.
- Nilsson, P., Saito, T., and Saido, T.C. (2014) New mouse model of Alzheimer's. *ACS Chem Neurosci* **5**: 499–502.
- Nimgampalle, M., and Yellamma, K. (2017) Anti-Alzheimer properties of probiotic, *Lactobacillus plantarum* MTCC 1325 in Alzheimer's disease induced albino rats. *J Clin Diagnostic Res* **11**: KC01–KC05.
- Ning, A., Cui, J., To, E., Ashe, K.H., and Matsubara, J. (2008) Amyloid-beta deposits lead to retinal degeneration in a mouse model of Alzheimer disease. *Invest Ophthalmol Vis Sci* **49**: 5136–5143.
- Nunes, A., Silva, G., Duque, C., Januário, C., Santana, I., Ambrósio, A.F., *et al.* (2019) Retinal texture biomarkers may help to discriminate between Alzheimer's, Parkinson's, and healthy controls. *PLoS One* **14**: 1–13.

- O'Hagan, C., Li, J. V., Marchesi, J.R., Plummer, S., Garaiova, I., and Good, M.A. (2017) Long-term multi-species Lactobacillus and Bifidobacterium dietary supplement enhances memory and changes regional brain metabolites in middle-aged rats. *Neurobiol Learn Mem* **144**: 36–47.
- O'Shea, A., Cohen, R.A., Porges, E.C., Nissim, N.R., and Woods, A.J. (2016) Cognitive aging and the hippocampus in older adults. *Front Aging Neurosci* **8**: 1–8.
- Oddo, S., Caccamo, A., Shepherd, J.D., Murphy, M.P., Golde, T.E., Kaye, R., *et al.* (2003) Triple-transgenic model of Alzheimer's Disease with plaques and tangles: Intracellular A β and synaptic dysfunction. *Neuron* **39**: 409–421.
- Olsen, I., and Singhrao, S.K. (2015) Can oral infection be a risk factor for Alzheimer's disease? *J Oral Microbiol* **7**: 1–16.
- Olsen, I., and Singhrao, S.K. (2020) Is there a link between genetic defects in the complement cascade and Porphyromonas gingivalis in Alzheimer's disease? *J Oral Microbiol* **12**: 1–10.
- Ostroff, L.E., Fiala, J.C., Allwardt, B., and Harris, K.M. (2002) Polyribosomes redistribute from dendritic shafts into spines with enlarged synapses during LTP in developing rat hippocampal slices. *Neuron* **35**: 535–545.
- Panayiotou, E., Fella, E., Andreou, S., Papacharalambous, R., Gerasimou, P., Costeas, P., *et al.* (2019) C5aR agonist enhances phagocytosis of fibrillar and non-fibrillar A β amyloid and preserves memory in a mouse model of familial Alzheimer's disease. *PLoS One* **14**: 1–22.
- Parnell, M., Guo, L., Abdi, M., and Cordeiro, M.F. (2012) Ocular manifestations of Alzheimer's disease in animal models. *Int J Alzheimers Dis* **2012**: 1–13.
- Pedrini, S., Gupta, V.B., Hone, E., Doecke, J., O'Bryant, S., James, I., *et al.* (2017) A blood-based biomarker panel indicates IL-10 and IL-12/23p40 are jointly associated as predictors of β -amyloid load in an AD cohort. *Sci Rep* **7**: 1–12.
- Perea, J.R., Llorens-Martín, M., Ávila, J., and Bolós, M. (2018) The role of microglia in the spread of Tau: Relevance for tauopathies. *Front Cell Neurosci* **12**: 1–8.
- Perez-Alcazar, M., Daborg, J., Stokowska, A., Wasling, P., Björefeldt, A., Kalm, M., *et al.* (2014) Altered cognitive performance and synaptic function in the hippocampus of mice lacking C3. *Exp Neurol* **253**: 154–164.
- Perez, S.E., Lumayag, S., Kovacs, B., Mufson, E.J., Shunbin, Xu, and Xu, S. (2009) β -Amyloid Deposition and Functional Impairment in the Retina of the APP^{swe}/PS1 Δ E9 Transgenic Mouse Model of Alzheimer's Disease. *Investig Ophthalmol Vis Sci* **50**: 793–800.
- Pocock, J.M., and Kettenmann, H. (2007) Neurotransmitter receptors on microglia. *Trends Neurosci* **30**: 527–535.
- Price, K.A., Varghese, M., Sowa, A., Yuk, F., Brautigam, H., Ehrlich, M.E., and Dickstein, D.L. (2014) Altered synaptic structure in the hippocampus in a mouse model of Alzheimer's disease with soluble amyloid- β oligomers and no plaque pathology. *Mol*

Neurodegener **9**: 41.

Prince, M., Ali, G.C., Guerchet, M., Prina, A.M., Albanese, E., and Wu, Y.T. (2016) Recent global trends in the prevalence and incidence of dementia, and survival with dementia. *Alzheimer's Res Ther* **8**: 1–13.

Prince, M., Bryce, R., Albanese, E., Wimo, A., Ribeiro, W., and Ferri, C.P. (2013) The global prevalence of dementia: A systematic review and metaanalysis. *Alzheimer's Dement* **9**: 63–75.

Qin, L., Liu, Y., Hong, J.-S., and Crews, F.T. (2013) NADPH oxidase and aging drive microglial activation, oxidative stress and dopaminergic neurodegeneration following systemic LPS administration. *Glia* **61**: 855–868.

Qin, L., Wu, X., Block, M.L., Liu, Y., Breese, G.R., Hong, J.-S., *et al.* (2007) Systemic LPS Causes Chronic Neuroinflammation and Progressive Neurodegeneration. *Glia* **55**: 453–462.

Querfurth, H.W., and Laferla, F.M. (2010) Alzheimer's Disease. *N Engl J Med* **362**: 329–344.

Ran, C., Xu, X., Raymond, S.B., Ferrara, B.J., Neal, K., Bacskai, B.J., *et al.* (2009) Design, synthesis, and testing of difluoroboron derivatized curcumins as near infrared probes for in vivo detection of amyloid- β deposits. *J Am Chem* **131**: 15257–15261.

Rezaeiasl, Z., Salami, M., and Sepehri, G. (2019) The effects of probiotic *Lactobacillus* and *Bifidobacterium* strains on memory and learning behavior, long-term potentiation (LTP), and some biochemical parameters in β -amyloid-induced rat's model of Alzheimer's disease. *Prev Nutr Food Sci* **24**: 265–273.

Ricklin, D., Hajishengallis, G., Yang, K., and Lambris, J.D. (2010) Complement: A key system for immune surveillance and homeostasis. *Nat Immunol* **11**: 785–797.

Ricobaraza, A., Cuadrado-Tejedor, M., Marco, S., Pérez-Otaño, I., and García-Osta, A. (2012) Phenylbutyrate rescues dendritic spine loss associated with memory deficits in a mouse model of Alzheimer disease. *Hippocampus* **22**: 1040–1050.

Risner, M.L., Pasini, S., Cooper, M.L., Lambert, W.S., and Calkins, D.J. (2018) Axogenic mechanism enhances retinal ganglion cell excitability during early progression in glaucoma. *Proc Natl Acad Sci U S A* **115**: E2393–E2402.

Rodriguez de Cordoba, S., Tortajada, A., Harris, C.L., and Morgan, B.P. (2012) Complement dysregulation and disease: From genes and proteins to diagnostics and drugs. *Immunobiology* **217**: 1034–1046.

Roy Sarkar, S., and Banerjee, S. (2019) Gut microbiota in neurodegenerative disorders. *J Neuroimmunol* **328**: 98–104.

Safieh, M., Korczyn, A.D., and Michaelson, D.M. (2019) ApoE4: an emerging therapeutic target for Alzheimer's disease. *BMC Med* **17**: 1–17.

Saito, T., Matsuba, Y., Mihira, N., Takano, J., Nilsson, P., Itohara, S., *et al.* (2014) Single App knock-in mouse models of Alzheimer's disease. *Nat Neurosci* **17**: 661–663.

- Saiyasit, N., Chunchai, T., Prus, D., Suparan, K., Pittayapong, P., Apaijai, N., *et al.* (2020) Gut dysbiosis develops before metabolic disturbance and cognitive decline in high-fat diet-induced obese condition. *Nutrition* **69**: 1–10.
- Sakakibara, Y., Sekiya, M., Saito, T., Saido, T.C., and Iijima, K.M. (2018) Cognitive and emotional alterations in App knock-in mouse models of A β amyloidosis. *BMC Neurosci* **19**: 1–17.
- Salas, I.H., Weerasekera, A., Ahmed, T., Callaerts-Vegh, Z., Himmelreich, U., D’Hooge, R., *et al.* (2018) High fat diet treatment impairs hippocampal long-term potentiation without alterations of the core neuropathological features of Alzheimer disease. *Neurobiol Dis* **113**: 82–96.
- Salobarra-García, E., Rodrigues-Neves, A.C., Ramírez, A.I., Hoz, R. de, Fernández-Albarral, J.A., López-Cuenca, I., *et al.* (2020) Microglial activation in the retina of a triple-transgenic alzheimer’s disease mouse model (3xTg-AD). *Int J Mol Sci* **21**: 1–15.
- Sambasivarao, S. V (2001) Dendritic spine geometry is critical for AMPA receptor expression in hippocampal CA1 pyramidal neurons. *Nat Neurosci* **4**: 1086–1092.
- Sanes, J.R., and Masland, R.H. (2015) The Types of Retinal Ganglion Cells: Current Status and Implications for Neuronal Classification. *Annu Rev Neurosci* **38**: 221–246.
- Santinaa, L. Della, and Ou, Y. (2017) Who’s lost first? Susceptibility of retinal ganglion cell types in experimental glaucoma. *Exp Eye Res* **158**: 43–50.
- Sarma, J.V., and Ward, P. a (2011) The Complement System. *Cell Tissue Res* **343**: 227–235.
- Sasaguri, H., Nilsson, P., Hashimoto, S., Nagata, K., Saito, T., Strooper, B. De, *et al.* (2017) APP mouse models for Alzheimer’s disease preclinical studies. *EMBO J* **36**: 2473–2487.
- Schafer, D.P., Lehrman, E.K., Kautzman, A.G., Koyama, R., Mardinly, A.R., Yamasaki, R., *et al.* (2012) Microglia Sculpt Postnatal Neural Circuits in an Activity and Complement-Dependent Manner. *Neuron* **74**: 691–705.
- Scheff, S.W., Neltner, J.H., and Nelson, P.T. (2014) Is synaptic loss a unique hallmark of Alzheimer’s disease? *Biochem Pharmacol* **88**: 517–528.
- Scheltens, P., Blennow, K., Breteler, M.M.B., Strooper, B. de, Frisoni, G.B., Salloway, S., and Flier, W.M. Van der (2016) Alzheimer’s disease. *Lancet* **388**: 505–517.
- Schlamp, C.L., Johnson, E.C., Li, Y., Morrison, J.C., and Nickells, R.W. (2001) Changes in Thy1 gene expression associated with damaged retinal ganglion cells. *Mol Vis* **7**: 192–201.
- Schön, C., Hoffmann, N.A., Ochs, S.M., Burgold, S., Filser, S., Steinbach, S., *et al.* (2012) Long-Term In Vivo Imaging of Fibrillar Tau in the Retina of P301S Transgenic Mice. *PLoS One* **7**: 1–9.
- Schultz, N., Byman, E., and Wennström, M. (2020) Levels of Retinal Amyloid- β Correlate with Levels of Retinal IAPP and Hippocampal Amyloid- β in

- Neuropathologically Evaluated Individuals. *J Alzheimers Dis* **73**: 1201–1209.
- Serrano-Pozo, A., Frosch, M.P., Masliah, E., and Hyman, B.T. (2011) Neuropathological Alterations in Alzheimer Disease. *Cold Spring Harb Perspect Med* **1**: 1–23.
- Sheng, J.G., Bora, S.H., Xu, G., Borchelt, D.R., Price, D.L., and Koliatsos, V.E. (2003) Lipopolysaccharide-induced-neuroinflammation increases intracellular accumulation of amyloid precursor protein and amyloid β peptide in APP^{swe} transgenic mice. *Neurobiol Dis* **14**: 133–145.
- Sheppard, O., Coleman, M.P., and Durrant, C.S. (2019) Lipopolysaccharide-induced neuroinflammation induces presynaptic disruption through a direct action on brain tissue involving microglia-derived interleukin 1 beta. *J Neuroinflammation* **16**: 1–13.
- Shi, H., Koronyo, Y., Rentsendorj, A., Regis, G.C., Sheyn, J., Fuchs, D.T., *et al.* (2020) Identification of early pericyte loss and vascular amyloidosis in Alzheimer's disease retina. *Acta Neuropathol* **139**: 813–836.
- Shi, Q., Chowdhury, S., Ma, R., Le, K.X., Hong, S., Caldarone, B.J., *et al.* (2017) Complement C3 deficiency protects against neurodegeneration in aged plaque-rich APP/PS1 mice. *Sci Transl Med* **9**: 1–14.
- Shi, Q., Colodner, K.J., Matousek, S.B., Merry, K., Hong, S., Kenison, J.E., *et al.* (2015) Complement C3-deficient mice fail to display age-related hippocampal decline. *J Neurosci* **35**: 13029–13042.
- Sholl, D.A. (1953) Dendritic organization in the neurons of the visual and motor cortices of the cat. *J Anat* **87**: 387–406.
- Sierksma, A., Lu, A., Mancuso, R., Fattorelli, N., Thrupp, N., Salta, E., *et al.* (2020) Novel Alzheimer risk genes determine the microglia response to amyloid- β but not to TAU pathology. *EMBO Mol Med* **12**: e10606.
- Silver, R.A. (2010) Neuronal arithmetic. *Nat Rev Neurosci* **11**: 474–489.
- Sipe, G.O., Lowery, R.L., Tremblay, M., Kelly, E.A., Lamantia, C.E., and Majewska, A.K. (2016) Microglial P2Y₁₂ is necessary for synaptic plasticity in mouse visual cortex. *Nat Commun* **7**: 1–15.
- Siracusa, R., Fusco, R., and Cuzzocrea, S. (2019) Astrocytes: Role and functions in brain pathologies. *Front Pharmacol* **10**: 1–10.
- Šišková, Z., Justus, D., Kaneko, H., Friedrichs, D., Henneberg, N., Beutel, T., *et al.* (2014) Dendritic structural degeneration is functionally linked to cellular hyperexcitability in a mouse model of alzheimer's disease. *Neuron* **84**: 1023–1033.
- Sobue, A., Ito, N., Nagai, T., Shan, W., Hada, K., Nakajima, A., *et al.* (2018) Astroglial major histocompatibility complex class I following immune activation leads to behavioral and neuropathological changes. *Glia* **66**: 1034–1052.
- Sochocka, M., Zwolińska, K., and Leszek, J. (2017) The Infectious Etiology of Alzheimer's Disease. *Curr Neuropharmacol* **15**: 996–1009.

- Song, G., Steelman, Z.A., Finkelstein, S., Yang, Z., Martin, L., Chu, K.K., *et al.* (2020) Multimodal Coherent Imaging of Retinal Biomarkers of Alzheimer's Disease in a Mouse Model. *Sci Rep* **10**: 1–11.
- Sparkman, N.L., Kohman, R.A., Garcia, A.K., and Boehm, G.W. (2005) Peripheral lipopolysaccharide administration impairs two-way active avoidance conditioning in C57BL/6J mice. *Physiol Behav* **85**: 278–288.
- Spires-Jones, T.L., and Hyman, B.T. (2014) The Intersection of Amyloid Beta and Tau at Synapses in Alzheimer's Disease. *Neuron* **82**: 756–771.
- Spires, T.L., Meyer-Luehmann, M., Stern, E.A., McLean, P.J., Skoch, J., Nguyen, P.T., *et al.* (2005) Dendritic spine abnormalities in amyloid precursor protein transgenic mice demonstrated by gene transfer and intravital multiphoton microscopy. *J Neurosci* **25**: 7278–7287.
- Sri, S., Pegasiou, C.M., Cave, C.A., Hough, K., Wood, N., Gomez-Nicola, D., *et al.* (2019) Emergence of synaptic and cognitive impairment in a mature-onset APP mouse model of Alzheimer's disease. *Acta Neuropathol Commun* **7**: 25.
- Stacey, M.A., Marsden, M., Pham N, T.A., Clare, S., Dolton, G., Stack, G., *et al.* (2014) Neutrophils recruited by IL-22 in peripheral tissues function as TRAIL-dependent antiviral effectors against MCMV. *Cell Host Microbe* **15**: 471–483.
- Staffend, N.A., and Meisel, R.L. (2011) Diolistic labeling in fixed brain slices: Phenotype, morphology, and dendritic spines. *Curr Protoc Neurosci* **April**: 1–23.
- Stevens, B., Allen, N.J., Vazquez, L.E., Howell, G.R., Christopherson, K.S., Nouri, N., *et al.* (2007) The Classical Complement Cascade Mediates CNS Synapse Elimination. *Cell* **131**: 1164–1178.
- Stover, K.R., Campbell, M.A., Winssen, C.M. Van, and Brown, R.E. (2015) Early detection of cognitive deficits in the 3xTg-AD mouse model of Alzheimer's disease. *Behav Brain Res* **289**: 29–38.
- Strange, B.A., Witter, M.P., Lein, E.S., and Moser, E.I. (2014) Functional organization of the hippocampal longitudinal axis. *Nat Rev Neurosci* **15**: 655–669.
- Strien, N.M. Van, Cappaert, N.L.M., and Witter, M.P. (2009) The anatomy of memory: An interactive overview of the parahippocampal- hippocampal network. *Nat Rev Neurosci* **10**: 272–282.
- Strooper, B. De, and Karran, E. (2016) The Cellular Phase of Alzheimer's Disease. *Cell* **164**: 603–615.
- Sy, M., Kitazawa, M., Medeiros, R., Whitman, L., Cheng, D., Lane, T.E., and LaFerla, F.M. (2011) Inflammation induced by infection potentiates tau pathological features in transgenic mice. *Am J Pathol* **178**: 2811–2822.
- Tampellini, D. (2015) Synaptic activity and Alzheimer's disease: A critical update. *Front Neurosci* **9**: 1–7.
- Tatsumi, S., Uchihara, T., Aiba, I., Iwasaki, Y., Mimuro, M., Takahashi, R., and Yoshida,

- M. (2014) Ultrastructural differences in pretangles between Alzheimer disease and corticobasal degeneration revealed by comparative light and electron microscopy. *Acta Neuropathol Commun* **161**: 1–11.
- Thal, D.R., Capetillo-Zarate, E., Tredici, K. Del, and Braak, H. (2006) The development of amyloid beta protein deposits in the aged brain. *Sci Aging Knowledge Environ* **6**: 52–54.
- Thanos, S., Kacza, J., Seeger, J., and Mey, J. (1994) Old dyes for new scopes: the phagocytosis-dependent long-term fluorescence labelling of microglial cells in vivo. *Trends Neurosci* **17**: 177–182.
- Torvell, M., Hampton, D.W., Connick, P., MacLulich, A.M.J., Cunningham, C., and Chandran, S. (2019) A single systemic inflammatory insult causes acute motor deficits and accelerates disease progression in a mouse model of human tauopathy. *Alzheimer's Dement Transl Res Clin Interv* **5**: 579–591.
- Tripodi, M., Evers, J.F., Mauss, A., Bate, M., and Landgraf, M. (2008) Structural homeostasis: Compensatory adjustments of dendritic arbor geometry in response to variations of synaptic input. *PLoS Biol* **6**: 2172–2187.
- Tyng, C.M., Amin, H.U., Saad, M.N.M., and Malik, A.S. (2017) The influences of emotion on learning and memory. *Front Psychol* **8**: 1–22.
- Uribe-Querol, E., and Rosales, C. (2020) Phagocytosis: Our Current Understanding of a Universal Biological Process. *Front Immunol* **11**: 1–13.
- Vandenabeele, M., Veys, L., Lemmens, S., Hadoux, X., Gelders, G., Serneels, L., *et al.* (2020) The App NL-G-F mouse retina is a site for preclinical Alzheimer ' s disease diagnosis and research. *bioRxiv* .
- Varatharaj, A., and Galea, I. (2017) The blood-brain barrier in systemic inflammation. *Brain Behav Immun* **60**: 1–12.
- Vecino, E., Rodriguez, F.D., Ruzafa, N., Pereiro, X., and Sharma, S.C. (2016) Glia-neuron interactions in the mammalian retina. *Prog Retin Eye Res* **51**: 1–40.
- Veerhuis, R., Nielsen, H.M., and Tenner, A.J. (2011) Complement in the brain. *Mol Immunol* **48**: 1592–1603.
- Walker, Keenan A, Ficek, B.N., and Westbrook, R. (2019) Understanding the Role of Systemic Inflammation in Alzheimer's Disease. *ACS Chem Neurosci* **10**: 3340–3342.
- Walker, Keenan A., Gottesman, R.F., Wu, A., Knopman, D.S., Gross, A.L., Mosley, T.H., *et al.* (2019) Systemic inflammation during midlife and cognitive change over 20 years: The ARIC Study. *Neurology* **92**: 1–13.
- Walker, K.A., Hoogeveen, R.C., Folsom, A.R., Ballantyne, C.M., Knopman, D.S., Windham, B.G., *et al.* (2017) Midlife systemic inflammatory markers are associated with late-life brain volume: The ARIC study. *Neurology* **89**: 2262–2270.
- Wang, Q.J., Shen, Y.E., Wang, X., Fu, S., Zhang, X., Zhang, Y.N., and Wang, R.T. (2020) Concomitant memantine and lactobacillus plantarum treatment attenuates cognitive

impairments in APP/PS1 mice. *Aging (Albany NY)* **12**: 1–22.

Weinhard, L., Bartolomei, G. Di, Bolasco, G., Machado, P., Schieber, N.L., Neniskyte, U., *et al.* (2018) Microglia remodel synapses by presynaptic trogocytosis and spine head filopodia induction. *Nat Commun* **9**: 1–14.

Westfall, S., Lomis, N., Kahouli, I., Dia, S.Y., Singh, S.P., and Prakash, S. (2017) Microbiome, probiotics and neurodegenerative diseases: deciphering the gut brain axis. *Cell Mol Life Sci* **74**: 3769–3787.

Westman, G., Berglund, D., Widén, J., Ingelsson, M., Korsgren, O., Lannfelt, L., *et al.* (2014) Increased inflammatory response in cytomegalovirus seropositive patients with Alzheimer's disease. *PLoS One* **9**: 1–9.

Williams, E.A., McGuone, D., Frosch, M.P., Hyman, B.T., Laver, N., and Stemmer-Rachamimov, A. (2017) Absence of Alzheimer disease neuropathologic changes in eyes of subjects with Alzheimer disease. *J Neuropathol Exp Neurol* **76**: 376–383.

Williams, P.A., Howell, G.R., Barbay, J.M., Braine, C.E., Sousa, G.L., John, S.W.M., and Morgan, J.E. (2013) Retinal ganglion cell dendritic atrophy in DBA/2J glaucoma. *PLoS One* **8**: 1–10.

Williams, P.A., Morgan, J.E., and Votruba, M. (2010) Opa1 deficiency in a mouse model of dominant optic atrophy leads to retinal ganglion cell dendropathy. *Brain* **133**: 2942–2951.

Williams, P.A., Piechota, M., Ruhland, C. Von, Taylor, E., Morgan, J.E., and Votruba, M. (2012) Opa1 is essential for retinal ganglion cell synaptic architecture and connectivity. *Brain* **135**: 493–505.

Williams, P.A., Thirgood, R.A., Oliphant, H., Frizzati, A., Littlewood, E., Votruba, M., *et al.* (2013) Retinal ganglion cell dendritic degeneration in a mouse model of Alzheimer's disease. *Neurobiol Aging* **34**: 1799–1806.

Williams, P.A., Tribble, J.R., Pepper, K.W., Cross, S.D., Morgan, B.P., Morgan, J.E., *et al.* (2016) Inhibition of the classical pathway of the complement cascade prevents early dendritic and synaptic degeneration in glaucoma. *Mol Neurodegener* **11**: 1–13.

Wozniak, M., Mee, A., and Itzhaki, R. (2009) Herpes simplex virus type 1 DNA is located within Alzheimer's disease amyloid plaques. *J Pathol* **217**: 231–241.

Wyk, M. Van, Wässle, H., and Taylor, W.R. (2009) Receptive field properties of ON- and OFF-ganglion cells in the mouse retina. *Vis Neurosci* **26**: 297–308.

Xu, B., Sun, A., He, Y., Qian, F., Xi, S., Long, D., and Chen, Y. (2018) Loss of thin spines and small synapses contributes to defective hippocampal function in aged mice. *Neurobiol Aging* **71**: 91–104.

Xu, H., and Chen, M. (2016) Targeting the complement system for the management of retinal inflammatory and degenerative diseases. *Eur J Pharmacol* **787**: 94–104.

Yasuhara, O., Kawamata, T., Aimi, Y., McGeer, E.G., and McGeer, P.L. (1994) Two types of dystrophic neurites in senile plaques of Alzheimer disease and elderly non-

demented cases. *Neurosci Lett* **171**: 73–76.

Yu, D.Y., Cringle, S.J., Balaratnasingam, C., Morgan, W.H., Yu, P.K., and Su, E.N. (2013) Retinal ganglion cells: Energetics, compartmentation, axonal transport, cytoskeletons and vulnerability. *Prog Retin Eye Res* **36**: 217–246 <http://dx.doi.org/10.1016/j.preteyeres.2013.07.001>.

Zelek, W.M., Xie, L., Morgan, B.P., and Harris, C.L. (2019) Compendium of current complement therapeutics. *Mol Immunol* **114**: 341–352.

Zetterberg, H., and Burnham, S.C. (2019) Blood-based molecular biomarkers for Alzheimer's disease. *Mol Brain* **12**: 1–7.

Zhang, H., Wu, L., Pchitskaya, E., Zakharova, O., Saito, T., Saido, T., and Bezprozvanny, I. (2015) Neuronal store-operated calcium entry and mushroom spine loss in amyloid precursor protein knock-in mouse model of Alzheimer's disease. *J Neurosci* **35**: 13275–13286.

Zhang, J., Anderson, S.R., Kautzman, A.G., Vetter, M.L., Schafer, D.P., Steele, M.R., and Romero, C.O. (2019) Complement targets newborn retinal ganglion cells for phagocytic elimination by microglia. *J Neurosci* **39**: 1854–18.

Zhang, J.C., Wu, J., Fujita, Y., Yao, W., Ren, Q., Yang, C., *et al.* (2014) Antidepressant effects of TrkB ligands on depression-like behavior and dendritic changes in mice after inflammation. *Int J Neuropsychopharmacol* **18**: 1–12.

Zhao, W., Xu, Z., Cao, J., Fu, Q., Wu, Y., Zhang, Xiaoying, *et al.* (2019) Elamipretide (SS-31) improves mitochondrial dysfunction, synaptic and memory impairment induced by lipopolysaccharide in mice. *J Neuroinflammation* **16**: 1–19.

Zhou, J., Fonseca, M.I., Pisalyaput, K., and Tenner, A.J. (2008) Complement C3 and C4 expression in C1q sufficient and deficient mouse models of Alzheimer's Disease. *J Neurochem* **106**: 2080–2092.